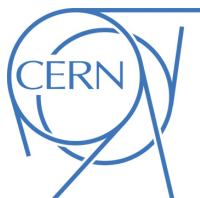




ATLAS NOTE

23rd July 2017



Draft version 0.2

Search for massive supersymmetric particles in multijet final states produced in pp collisions at $\sqrt{s} = 13$ TeV using the ATLAS detector at the LHC

Brian Amadio^a, Samuel Bright-Thonney^a, Ian Hinchliffe^a, Simone Pagan-Griso^a, Marjorie Shapiro^a, Sicong Lu^a, Erfei Wang^a, Haichen Wang^a

^a*Lawrence Berkeley National Laboratory*

^b*The Chinese University of Hong Kong*

Abstract

Results of a search for supersymmetric gluino pair productions with subsequent R -parity-violating decays to quarks are presented. This search uses 36.1 fb^{-1} of data collected by the ATLAS detector in proton-proton collisions with a center-of-mass energy of $\sqrt{s} = 13$ TeV at the LHC. The analysis is performed using both a requirement on the number of jets and the number of jets tagged as containing a b -hadron as well as a topological observable formed from the scalar sum of large-radius jet masses in the event. No significant deviation is observed from the expected Standard Model backgrounds. Limits are set on the production of gluinos in the gluino direct and cascade decay models in the UDD scenarios of RPV SUSY. In the gluino cascade decay model, gluinos with masses up to 1000 GeV - 1920 GeV are excluded, depending on the neutralino mass; For the gluino direct decay model, the limit on the cross section times branching ratio varies between 0.80 fb^{-1} at $m_{\tilde{g}} = 900 \text{ GeV}$ and 0.011 fb^{-1} at $m_{\tilde{g}} = 1800 \text{ GeV}$. Model independent limits on the cross section of signal in the defined SRs are also reported.

24 **Contents**

25	1 Introduction	5
26	2 Data and Monte Carlo samples	6
27	2.1 Data	6
28	2.2 Signal simulation	6
29	2.3 Background simulation	6
30	3 Search strategy	9
31	3.1 Choice of discriminating variables	9
32	3.2 Event selection	12
33	4 Background estimation strategy	13
34	4.1 Overview	13
35	4.2 Implementation and systematic uncertainties	15
36	4.3 Definition of regions	16
37	4.4 Data-driven systematic uncertainty determination	18
38	4.4.1 Jet mass response	20
39	4.4.2 Estimate the systematic uncertainty with uncertainty determination regions	22
40	4.4.3 Systematic uncertainty determination	26
41	4.5 Prediction from the MC and data	29
42	4.5.1 Background estimation performance in Monte Carlo sample	29
43	4.6 Prediction in data	38
44	4.7 Signal contamination	43
45	5 Signal systematic uncertainties	46
46	6 Results	49
47	6.1 Summary of unblinded M_J^Σ distributions and event yields in the SRs	49
48	6.2 Likelihood function and statistical interpretation procedure	52
49	6.3 Expected sensitivity	53
50	6.4 Interpolation of result	54
51	6.5 Unblinded statistical interpretation	55
52	7 Conclusion	57
53	Appendix	58
54	A M_J^Σ, p_T, and η distributions vs $m_{\tilde{\chi}}$	58
55	B Background estimation result in Sherpa multijet sample	60
56	C Impact of $t\bar{t}$ events on the background estimation performance	63
57	D Trigger impact on the UDR	65
58	E Jet mass response in the UDR	75

59	E.1 Data	75
60	E.2 PYTHIA8 multijet plus $t\bar{t}$ sample	75
61	E.3 Herwigpp multijet plus $t\bar{t}$ sample	75
62	E.4 SHERPA multijet sample	75
63	F Systematic uncertainty vs signal injection	78
64	G Jet mass response between non-matched jets and b-matched jets	80
65	H Background estimation performance with alternative binning for control region	82
66	I Signal systematic uncertainties	86
67	J Expected signal yields in various regions at 36.1 fb^{-1}	93
68	K Implemnnetation of the background estimation method	100
69	K.1 Jet mass templates	100
70	K.2 Jet mass randomization	100
71	K.3 Dressed mass response	101
72	K.4 Dressed M_J^Σ distributions	101
73	K.5 Normalization	102
74	K.6 Systematic uncertainty	102
75	K.7 Propagation of uncertainty	102
76	K.8 Determining predicted M_J^Σ and uncertainties	102
77	L Predicted and observed M_J^Σ distributions in Herwigpp multijet plus $t\bar{t}$ MC samples	104
78	M Trigger impact on CR and UDRs	104
79	N Jet mass templates comparison between the b-matched jets and non-matched jets	105
80	O Jet mass PDFs comparison between CR and UDRs	115
81	P Jet mass PDFs comparison between CR and 4j and 5j regions	123
82	Q Jet mass templates comparison between the two leading jets and the third and fourth leading jets	127
84	R Packages and performance recommendations	130
85	S Sensitivity to the 6-quark model	131

86 List of contributions

Brian Amadio	Analysis framework, data processing, signal study, signal production, statistics interpretation, large-R jet performance study.
Samuel Bright-Thonney	evaluating signal systematic uncertainties and sensitivity
Ian Hinchliffe	Advising analysis team
Simone Pagan-Griso	advising analysis team
Marjorie Shapiro	Advising analysis team
87 Sicong Lu	running background estimation and statistical interpretation programs.
Erfei Wang	producing comparison plots for the signal and background estimation studies
Haichen Wang	Background estimation, signal study, statistics interpretation, analysis coordination, contact and editor.

Not reviewed, for internal circulation only

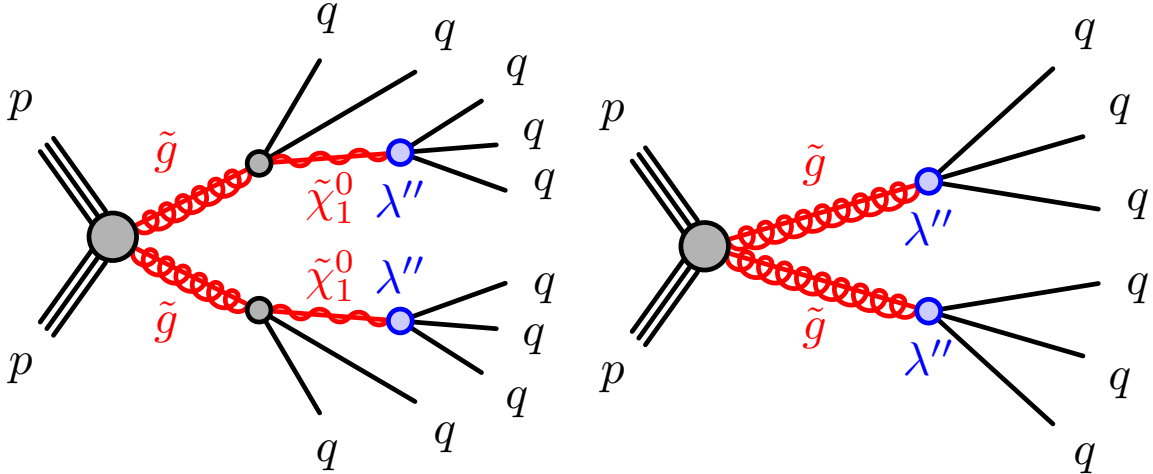


Figure 1: Diagrams for the benchmark processes considered for this analysis. The solid black lines represent Standard Model particles, the solid red lines represent SUSY partners, the gray shaded circles represent effective vertices that include off-shell propagators (e.g. heavy squarks coupling to a neutralino and a quark), and the blue shaded circles represent effective RPV vertices allowed by the baryon-number-violating λ_{00} couplings with off-shell propagators (e.g. heavy squarks coupling to two quarks).

89 1. Introduction

90 This note documents the search for R-Parity Violating (RPV) supersymmetry (SUSY) signal in the multijet
91 final state.

92 We present a search for the pair production of massive particles that subsequently cascade to a final state
93 characterized by a large number of quarks using the $\sqrt{s} = 13$ TeV data collected in 2015 and 2016. Such
94 high multiplicity final states are expected in some models of Supersymmetry (SUSY) when gluinos (\tilde{g}) are
95 pair produced and then decay via squarks to two quarks and a neutralino. In RPV scenarios, the neutralino
96 itself can then decay to three quarks via an RPV decay vertex with a Yukawa coupling strength denoted
97 by λ . Alternatively, the gluinos can directly decay to three quarks via the same RPV coupling. In both
98 scenarios, it is assumed that all other SUSY partners are “decoupled,” or so massive that their presence in
99 the decay chain of the gluino, or even direct production, is negligible. These processes are illustrated in
100 Figure 1.

101 The analysis strategy closely follows the one that was performed with the $\sqrt{s} = 8$ TeV data by ATLAS [1].
102 The high jet multiplicity in the signal event motivates the use of an event-level observable, the total jet
103 mass M_J^Σ , constructed from multiple individual large-radius jets. This provides significant discrimina-
104 tion between signal and background by capitalizing on the topological differences between them. The
105 background estimation relies on a “jet mass template” method, which was first proposed in Ref. [2]. The
106 predicted background total jet mass distribution is constructed from individual jet mass templates that are
107 obtained from data in control samples. Extensive studies have been done to validate this method with
108 several Monte Carlo samples as well as data validation regions. The systematic uncertainties associated
109 with this method are also understood and quantified from these studies.

¹¹⁰ The analysis uses data collected in 2015 and 2016, corresponding to an integrated luminosity of 36.1 fb^{-1} .
¹¹¹ The datasets taken in 2015 and 2016 are analyzed as one uniform sample.

¹¹² This note is organized as follows: Section 2 describes the data and Monte Carlo samples. Section 3
¹¹³ discusses the search strategy, presents the event selection and defines the control, validation and signal
¹¹⁴ regions. Section 4 explains the background estimation strategy, and in Section 4.6 the predicted M_j^Σ dis-
¹¹⁵ tribution and background yield in the signal regions are shown. Section 5 introduces the signal systematic
¹¹⁶ uncertainties. Section 6 presents the statistics analysis and interpretation.

¹¹⁷ 2. Data and Monte Carlo samples

¹¹⁸ 2.1. Data

¹¹⁹ This analysis uses data collected in 2015 and in 2016 up to the summer conference. The ALL_GOOD
¹²⁰ Good Run List (GRL) is used to select events with good data quality. The DS1 data sample is used for the
¹²¹ current version of the note. A total of 3.2 fb^{-1} 2015 data and a total of 32.9 fb^{-1} 2016 data are analyzed.

¹²² 2.2. Signal simulation

¹²³ Signal samples are generated at the leading order using MG5_aMC@NLO event generator [3] inter-
¹²⁴ faced to Pythia 8.186 [4]. The A14 [5] set of tuned parameters (tune) is used for underlying event together
¹²⁵ with the NNPDF2.3LO [6] parton distribution function (PDF) set. The EvtGen v1.2.0 program [7] is
¹²⁶ used to describe the properties of the b- and c- hadron decays in the signal samples and the background
¹²⁷ samples except those produced with Sherpa [8]. The signal cross-sections are calculated at next-to-leading
¹²⁸ order (NLO) in the strong coupling constant, adding the resummation of soft gluon emission at next-to-
¹²⁹ leading-logarithmic accuracy (NLO+NLL) [9–13]. The nominal cross-section is taken from an envelope
¹³⁰ of cross-section predictions using different PDF sets and factorization and renormalization scales, as
¹³¹ described in [14], considering only light-flavour quarks (u, d, s, c). Cross-sections are evaluated assuming
¹³² masses of 450 TeV for the light-flavour squarks in case of gluino-pair production.

¹³³ Signal samples are produced covering a wide range of both $m_{\tilde{g}}$ and $m_{\tilde{\chi}}$. In the six-quark direct gluino
¹³⁴ decay model, the gluino mass is varied from 900 to 1800 GeV with a step of 100 GeV. In the case of the
¹³⁵ cascade decays, for each gluino mass (1000 GeV to 2.1 TeV), separate samples are generated with multiple
¹³⁶ neutralino masses ranging from 50 GeV to 1.9 TeV, which is shown in Figure 2.

¹³⁷ It has been shown that the ATLFast II agrees with the full simulation very well in the kinematic region
¹³⁸ relevant to the RPV signals [15]. Therefore, ATLFast II samples are requested for all signal points,
¹³⁹ while full simulation samples are requested at a few representative points.

¹⁴⁰ 2.3. Background simulation

¹⁴¹ While a data-driven method is used to estimate the background, simulated events are used to establish, test
¹⁴² and validate the methodology of the analysis. Therefore, simulation is not required to accurately describe
¹⁴³ the background, but it should be sufficiently similar that the strategy can be tested before applying it to
¹⁴⁴ data. Multijet events constitute the dominant background in the search region, with small contributions

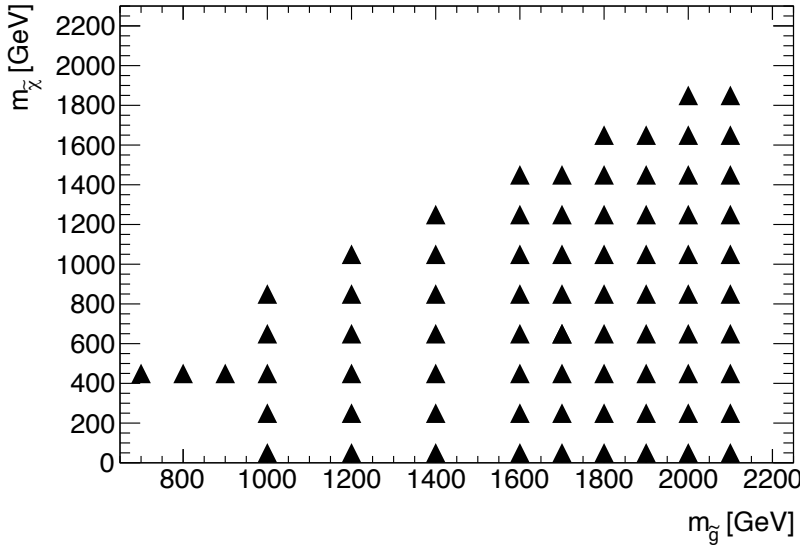


Figure 2: The grid of simulated signal samples for the 10-quark model.

Not reviewed, for internal circulation only

¹⁴⁵ from top-quark pair-production ($t\bar{t}$); $\gamma + \text{jets}$, $W + \text{jets}$, $Z + \text{jets}$, single-top quark, and diboson background
¹⁴⁶ contributions are negligible.

¹⁴⁷ The multi-jet background is generated with PYTHIA8 8.186 using the A14 underlying-event tune and
¹⁴⁸ the NNPDF2.3LO parton distribution functions. SHERPA multi-jet samples, with up to three partons
¹⁴⁹ included in the matrix-element calculation, are also generated and tested for the background estimationx.
¹⁵⁰ For the generation of $t\bar{t}$ processes the Powheg-Box v2 [16] generator is used with the CT10 PDF set [17].

¹⁵¹ The multijet samples (often known as the JZW samples in ATLAS) are created in 13 slices defined
¹⁵² by the leading jet p_T . The slice with the lowest jet p_T needed in the analysis is the JZ3 slice with a
¹⁵³ leading jet p_T between 160 GeV and 400 GeV. The Monte Carlo luminosity is 1.9 fb^{-1} and 3.6 fb^{-1} for
¹⁵⁴ the PYTHIA8 multijet sample and Herwigpp multijet sample, respectively. For the JZ4W slice, both
¹⁵⁵ PYTHIA8 and Herwigpp samples have an MC integrated luminosity at least three times that of data.
¹⁵⁶ Table 1 summarizes the information of the three multijet MC samples.

DSID	sample	events	MC luminosity
361021	mc15_13TeV.361021.Pythia8EvtGen_A14NNPDF23LO_jetjet_JZ1W.evgen.EVNT.e3569	15999000	0.0
361022	mc15_13TeV.361022.Pythia8EvtGen_A14NNPDF23LO_jetjet_JZ2W.evgen.EVNT.e3668	15989500	0.02
361023	mc15_13TeV.361023.Pythia8EvtGen_A14NNPDF23LO_jetjet_JZ3W.evgen.EVNT.e3668	15882500	1.88
361024	mc15_13TeV.361024.Pythia8EvtGen_A14NNPDF23LO_jetjet_JZ4W.evgen.EVNT.e3668	15983500	118.4
361025	mc15_13TeV.361025.Pythia8EvtGen_A14NNPDF23LO_jetjet_JZ5W.evgen.EVNT.e3668	15994500	3809.9
361026	mc15_13TeV.361026.Pythia8EvtGen_A14NNPDF23LO_jetjet_JZ6W.evgen.EVNT.e3569	17859000	73815.3
361027	mc15_13TeV.361027.Pythia8EvtGen_A14NNPDF23LO_jetjet_JZ7W.evgen.EVNT.e3668	15986000	2513966.94
361028	mc15_13TeV.361028.Pythia8EvtGen_A14NNPDF23LO_jetjet_JZ8W.evgen.EVNT.e3569	16000000	2517789.09
361029	mc15_13TeV.361029.Pythia8EvtGen_A14NNPDF23LO_jetjet_JZ9W.evgen.EVNT.e3569	15998500	67555778.44
361030	mc15_13TeV.361030.Pythia8EvtGen_A14NNPDF23LO_jetjet_JZ10W.evgen.EVNT.e3569	16000000	2268373246.28
361031	mc15_13TeV.361031.Pythia8EvtGen_A14NNPDF23LO_jetjet_JZ11W.evgen.EVNT.e3569	15998000	141400009484.0
361032	mc15_13TeV.361032.Pythia8EvtGen_A14NNPDF23LO_jetjet_JZ12W.evgen.EVNT.e3668	15996000	3.62941428448e+13
426043	mc15_13TeV.426043.HerwigppEvtGen_UEEE5_CTEQ6L1_jetjet_JZ3W.evgen.EVNT.e4410	15618500	3.67
426044	mc15_13TeV.426044.HerwigppEvtGen_UEEE5_CTEQ6L1_jetjet_JZ4W.evgen.EVNT.e4410	15647000	236.73
426045	mc15_13TeV.426045.HerwigppEvtGen_UEEE5_CTEQ6L1_jetjet_JZ5W.evgen.EVNT.e4410	15658000	7701.24
426046	mc15_13TeV.426046.HerwigppEvtGen_UEEE5_CTEQ6L1_jetjet_JZ6W.evgen.EVNT.e4410	3908000	32569.15
426047	mc15_13TeV.426047.HerwigppEvtGen_UEEE5_CTEQ6L1_jetjet_JZ7W.evgen.EVNT.e4410	3901500	1154204.14
426048	mc15_13TeV.426048.HerwigppEvtGen_UEEE5_CTEQ6L1_jetjet_JZ8W.evgen.EVNT.e4410	1963500	566055.81
426049	mc15_13TeV.426049.HerwigppEvtGen_UEEE5_CTEQ6L1_jetjet_JZ9W.evgen.EVNT.e4410	491000	3700042.34
426050	mc15_13TeV.426050.HerwigppEvtGen_UEEE5_CTEQ6L1_jetjet_JZ10W.evgen.EVNT.e4410	491000	127287866.54
426051	mc15_13TeV.426051.HerwigppEvtGen_UEEE5_CTEQ6L1_jetjet_JZ11W.evgen.EVNT.e4410	489500	8624206090.08
426052	mc15_13TeV.426052.HerwigppEvtGen_UEEE5_CTEQ6L1_jetjet_JZ12W.evgen.EVNT.e4410	488000	2.41659846758e+12
426133	mc15_13TeV.426133.Sherpa_CT10_jets_JZ3.evgen.EVNT.e4355	7975000	0.03
426134	mc15_13TeV.426134.Sherpa_CT10_jets_JZ4.evgen.EVNT.e4355	7987000	2.99
426135	mc15_13TeV.426135.Sherpa_CT10_jets_JZ5.evgen.EVNT.e4355	7999000	159.65
426136	mc15_13TeV.426136.Sherpa_CT10_jets_JZ6.evgen.EVNT.e4355	1999400	1102.81
426138	mc15_13TeV.426138.Sherpa_CT10_jets_JZ8.evgen.EVNT.e4635	1999000	412920.04
426139	mc15_13TeV.426139.Sherpa_CT10_jets_JZ9.evgen.EVNT.e4635	1986000	10979179.58
426141	mc15_13TeV.426141.Sherpa_CT10_jets_JZ11.evgen.EVNT.e4635	1979550	22272130962.5

Table 1: Information of the multijet Monte Carlo samples. The lowest relevant jet p_T slice is JZ3, which has a leading jet p_T filer of 160 GeV - 400 GeV. p_T slicing information of the multijet samples can be found [here](#).

157 **3. Search strategy**

158 **3.1. Choice of discriminating variables**

159 The search utilizes the large-R jet so that the jet mass template method can be implemented to estimate the
 160 background. The large-R jet is a trimmed Anti-kt jet with a radius of 1.0 (anti-kt 1.0 jet). The reconstructed
 161 anti-kt1.0 jet is first re-clustered with kt 0.2 sub-jets (radius = 0.2). If the transverse momentum of the
 162 sub-jet is less than 5% of transverse momnetum of the original jet, then the sub-jet is removed. The
 163 discriminating variable of this analysis, M_J^Σ , the sum of jet mass variable, is defined with largeR jet:

$$M_J^\Sigma = \sum_{i=1}^4 m_{jet}^i \quad (1)$$

164 where i is the index of the large-R jet ordered by p_T , and m_{jet}^i is the mass of the i -th large-R jet. In
 165 the case of 3-jet events, the M_J^Σ variable is calculated with all three large-R jets' masses in the event.
 166 Simulation studies show that M_J^Σ provides greater sensitivity than variables such as H_T , the scalar sum
 167 of jet p_T : the masses contain angular information about the events by definition, whereas a variable
 168 like H_T simply describes the energy (or transverse momentum) in the event. A large M_J^Σ implies not
 169 only high energy, but also rich angular structure. Previous studies at the Monte Carlo event generator
 170 level have demonstrated the power of the M_J^Σ variable in the high-multiplicity events that this analysis
 171 targets [18, 19]. Figure 3(a) presents examples of the discrimination that the M_J^Σ observable provides
 172 between the background (represented here by SHERPA and PYTHIA8 multi-jet MC simulation) and several
 173 signal samples, as well as the comparison of the data to the Monte Carlo multi-jet background.

174 Another discriminating variable that is independent of M_J^Σ is necessary in order to define suitable control
 175 and validation regions for the analysis. The signal is characterized by a considerably higher rate of central
 176 jet events as compared to the primary multi-jet background. This is expected due to the difference in the
 177 production processes that is predominantly s -channel for the signal, while the background can also be
 178 produced through u - and t -channel processes. Figure 3(b) shows the distribution of the pseudorapidity
 179 difference between the two leading large- R jets, $|\Delta\eta_{12}|$ for several signal and background Monte Carlo
 180 samples, as well as data. A high $|\Delta\eta_{12}|$ requirement can be applied to establish a control region or a
 181 validation region where the potential signal contamination needs to be suppressed.

182 The RPV signal events are expected to have a large number of jets, and therefore, the search will require a
 183 high large-R jet multiplicity. Figure 4(a) shows large- R jet multiplicity for signal and background multijet
 184 Monte Carlo samples, as well as data.

185 The RPV model considered by this analysis assumes that the decay branching ratio is identical for all
 186 possible final states, which leads to a large number of b-jets in the final state. The choice of equal
 187 coupling to the allowed UDD final states indicates the final states are likely to contain at least one third
 188 generation quarks. In some theoretical model, such as the Minimal Flavor Violating SUSY [20–24], the
 189 decays to final states containg third generation quarks are also favored. Figure 5 shows the number of
 190 reconstructed b-jets in events with ≥ 4 large- R jets for two representative RPV signal samples as well
 191 as the PYTHIA8 multijet MC sample. The search takes advantage of this characteristics by defining the
 192 signal region with a b-tagging requirement. The event should have at least one Anti-kt4 EMtopo jet that
 193 is b-tagged, but the b-tagged jet is not required to be matched to a selected large R jet.

Not reviewed, for internal circulation only

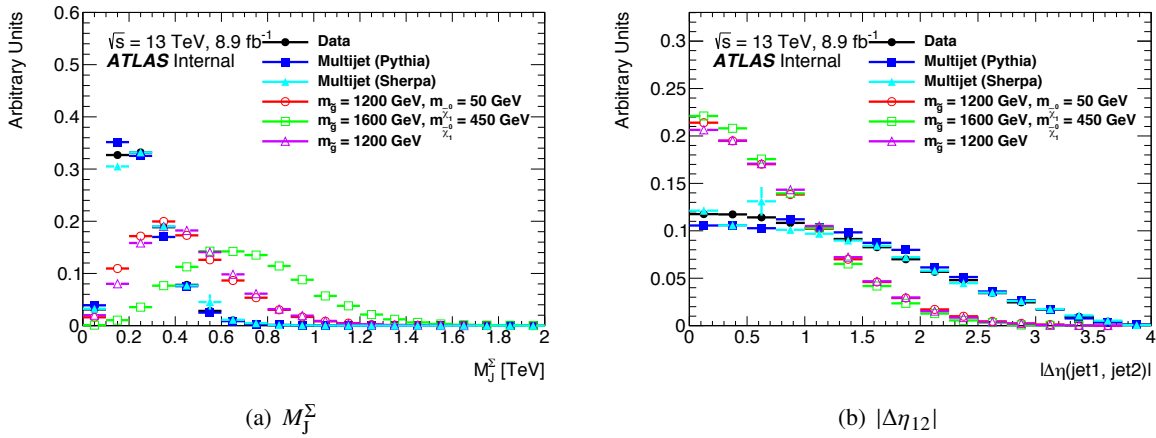


Figure 3: Comparison between signal sample and background dominant data control sample for (a) the scalar sum of the masses of the four leading large- R jets M_J^Σ and (b) the difference in pseudorapidity between the two leading large- R jets $|\Delta\eta_{12}|$. Several typical signal points are shown, as well as the distributions obtained from the data. All distributions are normalized to the same area. The selection requires four or more jets, and are inclusive in $|\Delta\eta_{12}|$ and have no b-tagging requirements.

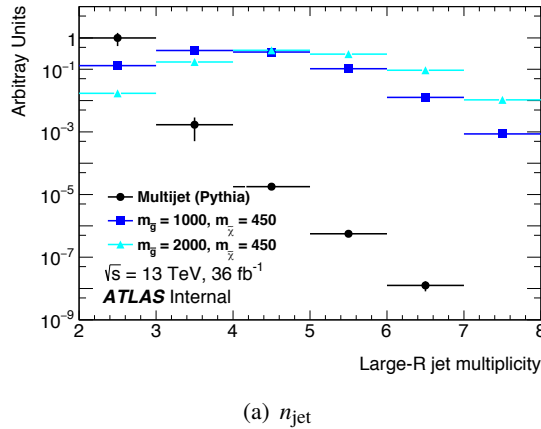


Figure 4: Comparison between signal sample and background dominant data control sample for the large- R jet multiplicity. Several typical signal points are shown, as well as the distributions obtained from the data. All distributions are normalized to the same area. The selection requires two or more jets, and are inclusive in $|\Delta\eta_{12}|$ and have no b-tagging requirements.

194 One additional variable that can be used to suppress signal contamination is the p_T of the leading large- R jet.
 195 Figure 6 shows distributions of leading jet p_T for signal and background MC samples. The p_T distribution
 196 strongly depends on the mass of gluino assumed in the signal model. For a signal of $m_{\tilde{g}} = 1000$ GeV and
 197 $m_{\tilde{\chi}} = 450$ GeV, its p_T distribution peaks at around 500 GeV with a steep turn-on between 200 GeV and 500
 198 GeV. For signals with a larger $m_{\tilde{g}}$ value, the peak and the turn-on region of the leading jet p_T distribution
 199 shift towards higher p_T ranges. This motivates to use a leading jet p_T veto in some cases to suppress signal
 200 contamination.

Not reviewed, for internal circulation only

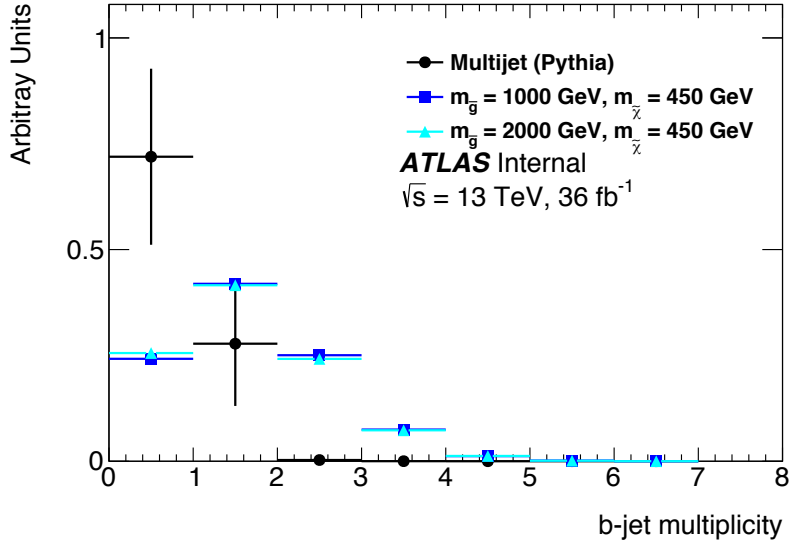


Figure 5: Reconstructed number of b-jets in the events with ≥ 4 large- R jets for two representative RPV signal samples as well as the PYTHIA8 multijet MC sample.

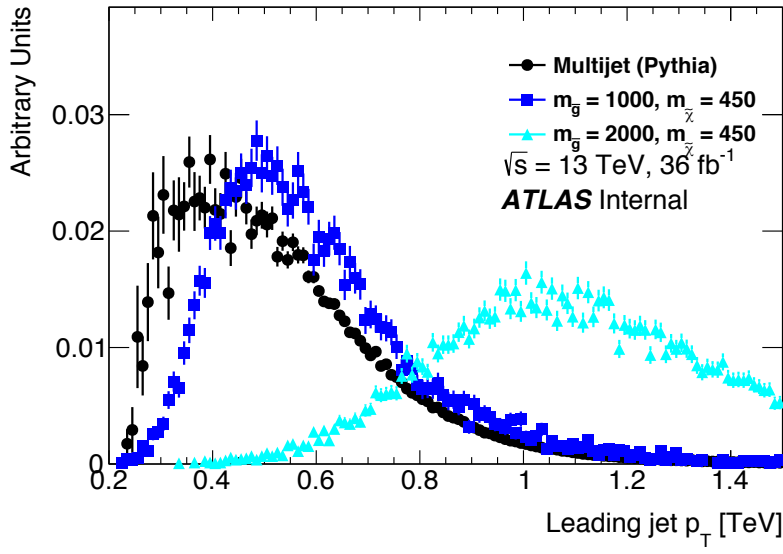


Figure 6: p_T of leading jet for events with four or more large- R jets. Distributions from the PYTHIA8 multijet MC sample and two signal samples are shown. The values of $m_{\tilde{g}} = 1000 \text{ GeV}$ and $m_{\tilde{g}} = 2000 \text{ GeV}$ represent the two extremes of the signal coverage of this analysis, with the former just beyond the limit set by the Run-1 analysis and the latter around the sensitivity reach of this analysis.

201 **3.2. Event selection**

202 The ALL_GOOD GRL is applied to select events in data. In addition, events must not have LAr/Tile/Core/SCT
 203 errors. Events used in the analysis are required to pass a H_T based trigger, seeded from a level-one jet
 204 with p_T greater than 100 GeV, the HLT_ht1000_L1J100 trigger. This is the lowest unprescaled H_T based
 205 trigger for the 2016 data taking ¹. AntiKt4EMTopoJets (anti-kt4-jets) are used to tag b-jet, and they
 206 are required to be within $|\eta| < 2.8$ and have a p_T greater than 50 GeV. An anti-kt4-jet is considered as a
 207 b-tagged jet if its $|\eta|$ is less than 2.5 and it passes the b-tagging requirement of fixed 70% working point of
 208 the MV2c10 tagger. AntiKt10LCTopoTrimmedPtFrac5SmallR20Jets (largeR jets) are used to define
 209 discriminating variables, such M_j^Σ and n_{jet} . These large-R jets must have a minimum p_T of 200 GeV and
 210 be within $|\eta| < 2.0$. To ensure the trigger is fully efficient for the offline analysis, a preselection requiring
 211 at least one large-R jet with a p_T greater than 440 GeV is applied. The following preselection is applied.

212 • **GRL ALL_GOOD**

213 • **Event quality** No LAr / Tile / Core / SCT

214 • **Trigger HLT_ht1000_J100**

215 • **Object definition**

216 – **Large-R jet** AntiKt10LCTopoTrimmedPtFrac5SmallR20Jets, $p_T > 200$ GeV, $|\eta| < 2.0$.

217 – **B-tagged jet** AntiKt4EMTopoJets, $p_T > 50$ GeV, $|\eta| < 2.5$. The selected AntiKt4EMTopoJet
 218 should pass the 70% fixed working point of MV2c10 tagger.

219 • **Categorization** Events are further classified into control, uncertainty determination, validation and
 220 signal regions.

221 Figure 7 shows the background trigger turn-on curves for events with five or more large- R jets and events
 222 with four or more large- R jets, which contain the signal regions that are defined later in the note. For
 223 events with five or more large- R jets, a jet p_T threshold at 200 GeV is fully efficient for offline analysis; for
 224 events with four or more large- R jets, the p_T threshold beyond which the offline analysis is fully efficient
 225 is slightly higher. The analysis addresses the inefficiency in events with four or more large- R jets by
 226 increasing leading jet p_T threshold to 400 GeV. Appendix M documents further checks to understand if
 227 trigger turn-on has any effect on various regions used in the analysis.

228 The large-R jet (AntiKt10LCTopoTrimmedPtFrac5SmallR20Jet) is trimmed from a regular anti-kt jet with
 229 a radius of $R = 1.0$. The clusters contained by the anti-kt 1.0 jet are regrouped to jets with $R = 0.2$ using
 230 the anti-kt algorithm (small-R jets). A small-R jet is removed if its p_T is less than 5% of the original anti-kt
 231 1.0 jet's p_T . The survived small-R jets are then rebuilt into an anti-kt jet with a radius of $R = 1.0$. This
 232 resulting jet is the large-R jet used in this analysis, and the standard large-R jet calibration is applied.

233 The fixed efficiency working point is chosen for b-tagging as its systematic uncertainties are already
 234 available. Results documented in earlier versions of the note used a flat efficiency working point. The 70%
 235 working point was chosen to achieve a balance between signal efficiency and background reduction. The
 236 choice of b-tagging working point can be further optimized, but this may be beyond the timescale of this
 237 analysis.

¹ For the 2015 data taking, the lowest unprescaled H_T based trigger is HLT_ht850_L1J100. For the sake of consistency between the two data taking periods, the HLT_ht1000_L1J100 trigger is chosen for both 2015 and 2016 data analyses.

Not reviewed, for internal circulation only

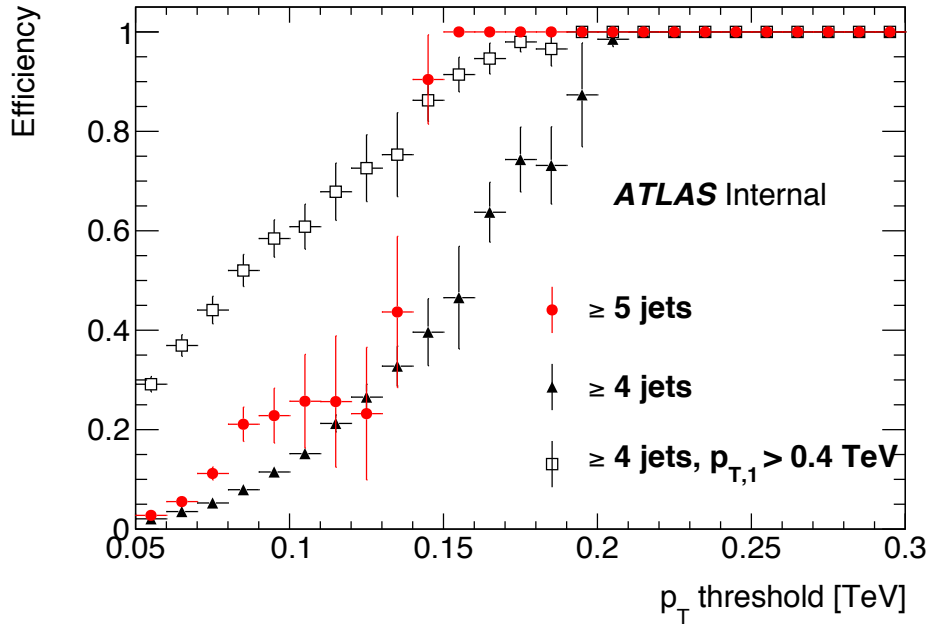


Figure 7: Trigger efficiency is shown as a function of large- R jet p_T threshold for events with our or more large- R jets events with five or more large- R jets.

238 4. Background estimation strategy

239 4.1. Overview

240 The use of M_j^Σ in this analysis provides an opportunity to employ the fully data-driven jet mass *template*
 241 *method* to estimate the background contribution in signal regions. The jet mass template method is
 242 discussed in great detail in [2], and its first experimental implementation is described in [1]. In this
 243 method, single jet mass templates are extracted from signal-depleted control regions, or *training samples*.
 244 These jet mass templates are created in bins of jet p_T and η , which effectively provides a *probability*
 245 *density function* (PDF) that describes the relative probability for a jet with a given p_T and η to have a
 246 certain mass. This method assumes that jet mass templates only depend on jet p_T and η and are the same
 247 between control regions and signal regions. A sample where the background M_j^Σ distribution needs to
 248 be estimated, such as a validation region or a signal region, is referred to as the *kinematic sample*. The
 249 only information used is the jet p_T and η , which are inputs to the templates. For each jet in the kinematic
 250 sample, the p_T - η dependent jet mass template is sampled to generate a random jet mass. A M_j^Σ distribution
 251 can be constructed from the randomized jet masses of the kinematic sample. This procedure is referred
 252 to as “dressing”, and the resulting sample is referred to as a *dressed sample*. If jet mass templates are
 253 created from a control sample of background events and the number of events in the kinematic sample is
 254 sufficiently large, then the M_j^Σ distribution constructed from randomized jet masses should reproduce the
 255 shape of background M_j^Σ distribution.

256 In practice, the jet mass templates are the templates of m/p_T , the jet mass normalized to its p_T . The
 257 randomized jet mass is then the product of the actual jet p_T and its randomized m/p_T . Using the

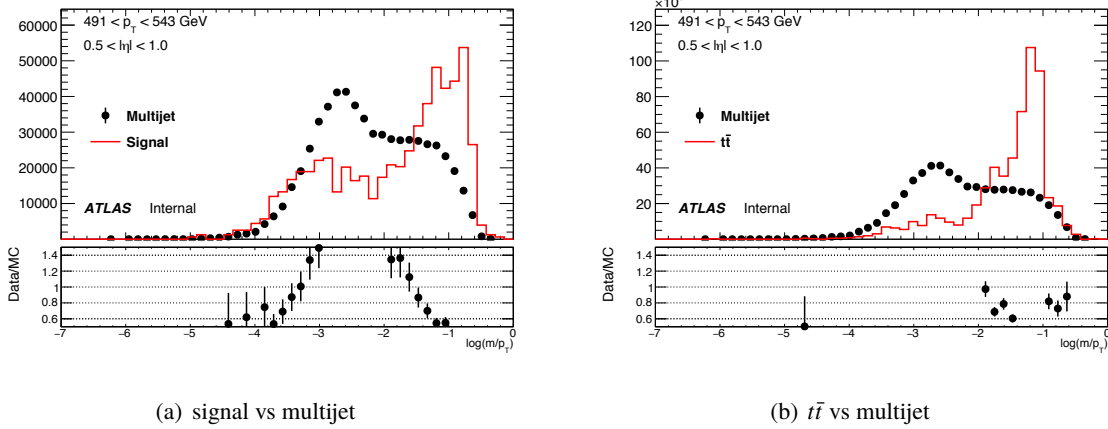


Figure 8: Example jet mass templates in the bin of $0.0 < |\eta| < 0.5$ and $491 \text{ GeV} < p_T < 543 \text{ GeV}$. Subfigure (a) compares the jet mass templates between RPV signal events and multijet events generated by PYTHIA8; subfigure (b) compares the jet mass templates between $t\bar{t}$ events generated by PowhegPYTHIA8 and multijet events generated by PYTHIA8.

Not reviewed, for internal circulation only

258 normalized jet mass, m/p_T , reduces the jet mass PDF's dependence on p_T . Figure 8(a) shows the jet mass
 259 templates in a particular bin of p_T and $|\eta|$ ($0.0 < |\eta| < 0.5$ and $491 \text{ GeV} < p_T < 543 \text{ GeV}$) for simulated
 260 signal and multijet background events generated by PYTHIA8. Figure 8(b) compares the jet mass PDFs
 261 between PYTHIA8 multijet events and $t\bar{t}$ events using the same p_T and $|\eta|$ bin, and it shows that the jet
 262 mass PDF in the $t\bar{t}$ events are different from that in the multijet events. $t\bar{t}$ events constitute less than 5% of
 263 background events in the analysis, and the $t\bar{t}$ MC sample is always included in the background estimation
 264 study in order to account for possible effect due to the presence of $t\bar{t}$ events. The kinks in the jet mass
 265 PDFs are due to the trimming applied to the large- R jets, and the position of the kink depends on the
 266 radius of the small-R jet (0.2) as well as the p_T fraction used in the trimming (5% in this case).

267 This analysis adopts basically the same procedure employed in the Run-1 analysis [1]. First, the statistical
 268 fluctuations in the jet mass templates is propagated to the prediction of background yield in the signal
 269 region, and therefore considered as a systematic uncertainty of the jet mass template method, whereas the
 270 Run-1 analysis smoothed the jet mass templates with a Gaussian kernel technique. Second, the predicted
 271 M_J^Σ distribution is normalized to the observation in $0.2 \text{ TeV} < M_J^\Sigma < 0.6 \text{ TeV}$, whereas the Run-1 analysis
 272 did not introduce any normalization region, effectively normalizing the prediction to the observation in
 273 the entire M_J^Σ range. In the region of $0.2 \text{ TeV} < M_J^\Sigma < 0.6 \text{ TeV}$, contamination from signal models not
 274 yet excluded by the ATLAS Run-1 search [1] is negligible compared to the statistical uncertainty of
 275 background.

276 Since the ICHEP CONF note [25] was released, a data driven method has been studied to estimate the
 277 systematic uncertainty of the jet mass template method. In this method, the predicted jet mass is compared
 278 to the observed jet mass in regions free of significant signal contamination (the uncertainty determination
 279 regions), and the difference between the prediction and the observation is used to estimate the systematic
 280 uncertainty. This uncertainty estimation method is tested in the Monte Carlo sample and found to cover
 281 the discrepancy between the prediction of the jet mass template method and the observation.

282 The impact of the $t\bar{t}$ contribution on the background estimation performance has been questioned in the
 283 past reviews of the analysis. In response, the standard MC results shown in this section include both

²⁸⁴ multijet and $t\bar{t}$ MC samples. Appendix C also shows that the background estimation performance is
²⁸⁵ essentially the same with or without including the $t\bar{t}$ contribution.

²⁸⁶ This section is organized as follows: Section 4.2 describes the implementation of the jet mass template
²⁸⁷ method. Section 4.3 defines the regions used in the analysis and briefly discusses the roles of these regions.
²⁸⁸ Section 4.4 describes the data driven determination of the systematic uncertainty. Section 4.5 presents the
²⁸⁹ result of the background estimation. Section 4.7 discusses the contribution to the predicted background
²⁹⁰ yield due to the presence of signal events.

²⁹¹ 4.2. Implementation and systematic uncertainties

²⁹² This section provides a concise description of the procedure used to generate the predicted M_J^Σ distribution
²⁹³ and then introduces the systematic uncertainties associated with the jet mass randomization. A more
²⁹⁴ detailed and technical description of how the jet mass template method is implemented can be found in
²⁹⁵ the Appendix K.

²⁹⁶ The jet mass templates are built from jets in a control region. Jets are binned in three dimensions, using
²⁹⁷ its p_T , $|\eta|$, and b-matching² information. In each bin, the distribution of jet mass over p_T is obtained, and
²⁹⁸ it is referred to jet mass PDF/template hereafter. For regions of interest, such as a signal region, the four
²⁹⁹ leading jets in p_T in an event are selected. For each selected jet, its jet mass PDF is retrieved and used to
³⁰⁰ generate a random number. The randomized jet mass is the product of this random number and the actual
³⁰¹ p_T of the jet. Then, the randomized total jet mass variable, M_J^Σ , can be calculated from the randomized jet
³⁰² masses, and repeating this procedure for all events in the region of interest yields a randomized jet mass
³⁰³ distribution.

³⁰⁴ Since the jet mass randomization is subject to statistical fluctuation, a large number of pseudo-experiments
³⁰⁵ (PEs) are generated, and each PE yields a randomized M_J^Σ distribution. For the purpose of presentation
³⁰⁶ and performing statistical test, the M_J^Σ distribution is binned. Each M_J^Σ bin has a distribution of event
³⁰⁷ yields from randomized M_J^Σ distributions in the PEs. The mean of this yield distribution and the RMS
³⁰⁸ are considered as the central value of the predicted yield and its statistical uncertainty, respectively. This
³⁰⁹ procedure produces a predicted M_J^Σ distribution with bin-by-bin statistical uncertainties. The predicted
³¹⁰ M_J^Σ distribution is further normalized to the observed M_J^Σ distribution in the region of $0.2 \text{ TeV} < M_J^\Sigma <$
³¹¹ 0.4 TeV .

³¹² The systematic uncertainty of this method has two components, one of statistical nature, the other of physics
³¹³ nature. First of all, the prediction of M_J^Σ distribution and the event yield in the signal region is subject
³¹⁴ to statistical uncertainty in the jet mass PDF and jet kinematics sample. The statistical uncertainty in
³¹⁵ the jet kinematics sample is quantified by pseudo-experiment procedure described above. The statistical
³¹⁶ uncertainty in the jet mass PDFs can be estimated by introducing Poisson fluctuations to the jet mass
³¹⁷ PDFs. In the implementation, these two sources of statistical uncertainty are estimated in one set of
³¹⁸ PE generation. In every PE, a bin-by-bin fluctuation is introduced to the jet mass PDF according to
³¹⁹ its statistical uncertainty; then, these fluctuated jet mass PDFs are used to randomize jet masses in the
³²⁰ kinematics sample. The statistical uncertainty determined in this ensemble of PEs reflects the total
³²¹ uncertainty of both sources.

² b-matching is referred to whether or not a large- R jet is matched to a b-tagged jet by requiring $\Delta R < 1.0$.

Not reviewed, for internal circulation only

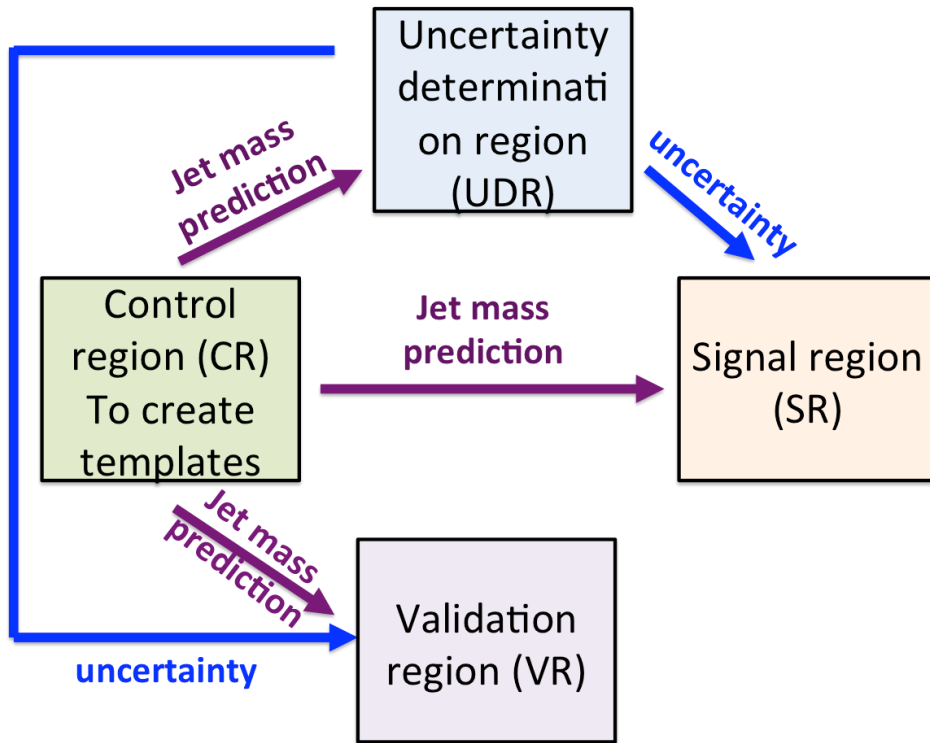


Figure 9: Workflow diagram that shows the role of various regions in the analysis.

322 The second component of the systematic uncertainty is related to the method's assumption on the jet mass
 323 PDF's dependence on a number of variables as well as the assumption that jets in the same events are
 324 uncorrelated. This is discussed in detail in Section 4.4.

325 **4.3. Definition of regions**

326 A number of regions serving different roles in the background estimation are defined. A Control Region
 327 (CR) is defined to create the jet mass templates. Then the jet mass templates are applied to predict
 328 masses of jets in Uncertainty Determination Regions (UDRs) where distributions of predicted jet mass
 329 and observed jet mass are compared, in order to understand the systematic uncertainty of the estimation;
 330 The jet mass templates are used to predict the M_j^{Σ} distributions in the signal and validation regions, where
 331 the systematic uncertainties are propagated from the jet mass estimation uncertainty determined in the
 332 UDRs. This workflow is illustrated by Figure 9.

333 The control region requires the event have exactly three large- R jets with $p_T > 200$ GeV, and in case that
 334 the event contains a b-jet, the $|\Delta\eta_{12}|$ of the event be greater than 1.4. The requirement on $|\Delta\eta_{12}|$ variable
 335 for b-tag events is introduced to suppress signal contamination. Jet mass templates are binned in p_T and η ,
 336 and created separately for b-matched jets and non-matched jets. In the Run-1 analysis, separate sets
 337 of jet mass templates are created for the first two leading jets and the third and fourth leading jets, and no
 338 speration in jet mass templates between b-matched jets and non-matched jets is made. Figure 10
 339 shows comparisons of jet mass templates between different types of jets in the PYTHIA8 multijet MC

Not reviewed, for internal circulation only

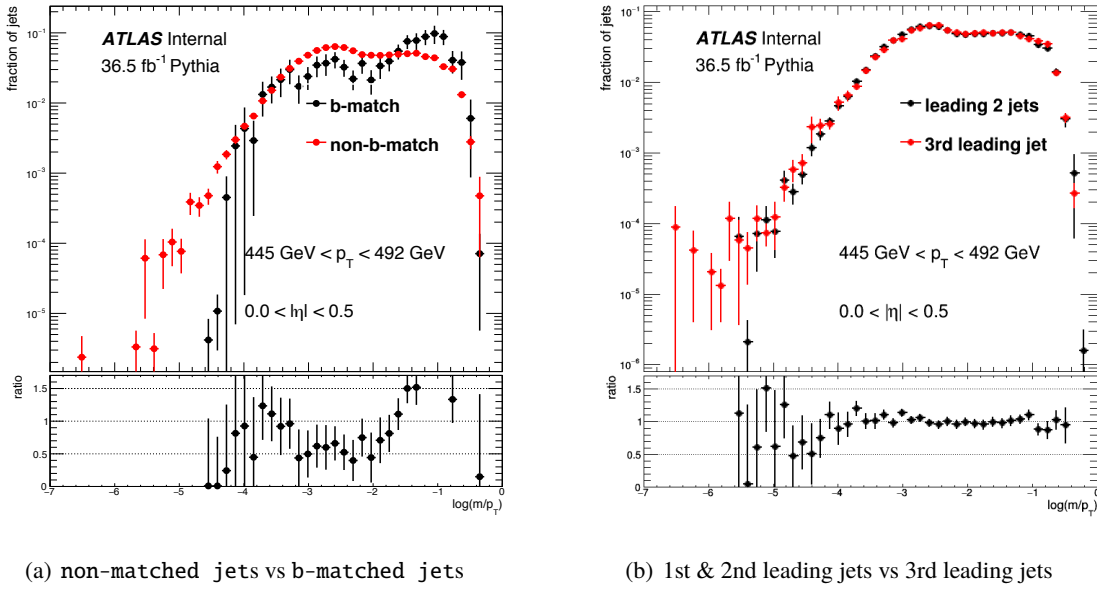


Figure 10: Jet mass template ($\log(m/p_T)$) comparison between the non-matched jets and b-matched jets ((a)), and between the two leading jets and the third leading jets ((b)), in PYTHIA8 multijet sample.

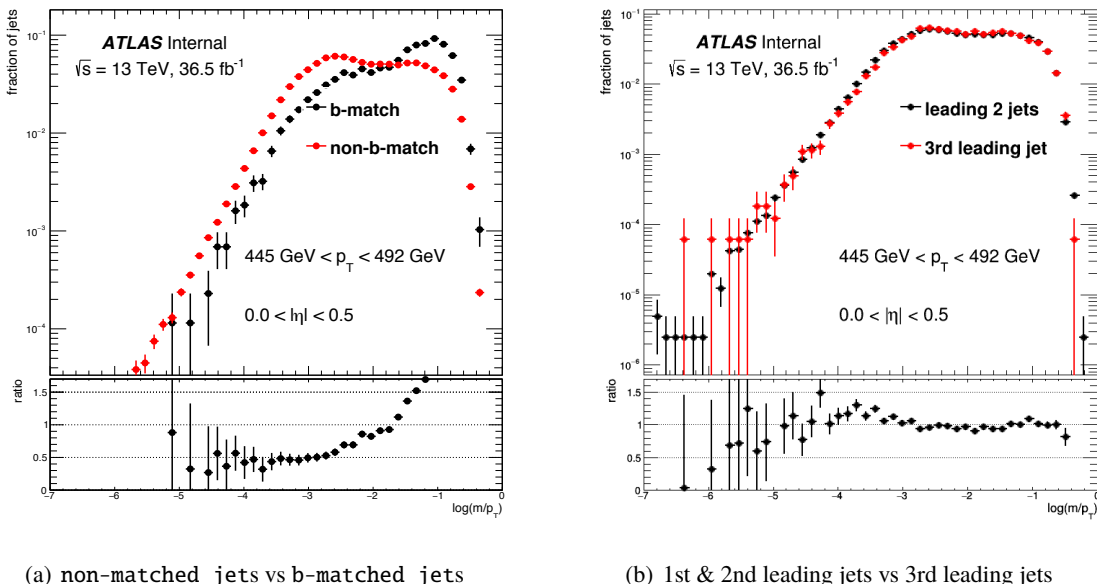


Figure 11: Jet mass template ($\log(m/p_T)$) comparison between the non-matched jets and b-matched jets ((a)), and between the two leading jets and the third leading jets ((b)), in data.

sample. The differences in the jet mass template shapes between b-matched jets and non-matched jets, as shown in Figure 10(a), are found to be larger than the differences between the two leading jets and the third leading jets, as shown in Figure 10(b). This observation is also confirmed in data, as shown by Figure 11. Appendices N and Q show all comparisons of jet mass templates between b-matched jets and non-matched jets, and between the two leading jets and the third and fourth leading jets, respectively. In this study, the differences in jet mass templates between b-matched jets and non-matched jets are found to be greater than the differences between the two leading jets and the third and fourth leading jets, which motivates the change in the binning of jets in the control region. The Run-1 binning is also implemented as a cross check and found not to improve the performance of the background estimation, as documented in Appendix H to be included.

To understand the systematic uncertainty of the jet mass template method, two Uncertainty Determination Region (UDR) are defined. The first UDR requires the events have exactly two large- R jets with $p_T > 200$ GeV; and the second UDR requires events have exactly four large- R jets with $p_T > 200$ GeV, and the leading jet p_T should be less than 400 GeV. The leading jet p_T cut is motivated by Figure 6, which indicates that a p_T veto significantly suppresses signal contribution in high jet multiplicity events. More detailed discussion of the UDRs can be found in Section 4.4.

The search is performed in multiple overlapping signal regions defined with jet multiplicity and b-matching requirements. The signal region with the best expected sensitivity to the RPV signals is selected for the model-dependent interpretation, while other signal regions are used for model independent statistical test. The first set of signal regions are defined with ≥ 4 large- R jets, $|\Delta\eta_{12}| < 1.4$, and a M_J^Σ cut³. One of the signal region requires the presence of a b-jet (4jSRb), while the other does not have any b-jet requirement (4jSR). The second set of signal regions are defined with ≥ 5 large- R jets, $|\Delta\eta_{12}| < 1.4$, and a M_J^Σ cut; the one requiring the presence of at least one b-jet is referred to as 5jSRb, and the one without a b-jet requirement is referred to as 5jSR.

To validate the performance of the background estimation, two Validation Regions (VRs) are defined corresponding to the two SRs. They are defined with the same requirements as the SRs except that the $|\Delta\eta_{12}|$ cut is reversed to be greater than 1.4. The two VRs, 5jVR and 5jVRb, are corresponding to the 5jSR and 5jSRb, respectively.

The event level and jet level requirements used to define various regions are summarized in Table 2.

The expected signal and background (as predicted by PYTHIA8 multijet samples) yields are calculated for all the regions defined in this section and shown in Tables 21 and 22 in the Appendix J. Figure 12 shows the expected background (PYTHIA8) and signal ($m_{\tilde{g}} = 1.0$ TeV, $m_{\tilde{\chi}} = 0.45$ TeV) yields and the signal-to-background ratios in various regions, at 36.1 fb^{-1} . The signal point ($m_{\tilde{g}} = 1.0$ TeV, $m_{\tilde{\chi}} = 0.45$ TeV) is at the limit set by the Run-1 analysis. For this signal point with very large cross section, there is no significant contamination in various control, validation and uncertainty determination regions. Figure 13 shows the same plot for a signal point with $m_{\tilde{g}} = 1.6$ TeV, $m_{\tilde{\chi}} = 0.45$ TeV, and the contamination becomes much smaller in all regions.

4.4. Data-driven systematic uncertainty determination

One of the background systematic uncertainty arises from the fundamental assumption that the jet mass template of background jets in the signal region follows the same template derived from the control region.

³ to be presented later

Not reviewed, for internal circulation only

		n_{jet}	b-tag	b-match	$p_{T,1}$	$ \Delta\eta_{12} $	M_J^Σ
CR	3jCRb	= 3	-	Yes	-	> 1.4	-
	3jCR	= 3	-	No	-	-	-
UDR	UDR1	= 2	-	-	> 400 GeV	-	-
	UDR2	= 4	-	-	< 400 GeV	-	-
VR	4jVRb	≥ 4	Yes	-	> 400 GeV	> 1.4	-
	5jVRb	≥ 5	Yes	-	-	> 1.4	-
	4jVR	≥ 4	-	-	> 400 GeV	> 1.4	-
	5jVR	≥ 5	-	-	-	> 1.4	-
SR	4jSRb	≥ 4	Yes	-	> 400 GeV	< 1.4	> 1.0 TeV
	5jSRb	≥ 5	Yes	-	-	< 1.4	> 0.8 TeV
	5jSR	≥ 5	Yes	-	-	< 1.4	> 0.6 TeV
	4jSR	≥ 4	-	-	> 400 GeV	< 1.4	> 1.0 TeV
	5jSR	≥ 5	-	-	-	< 1.4	> 0.8 TeV

Table 2: Summary of the event level and jet level requirements used to define various regions.

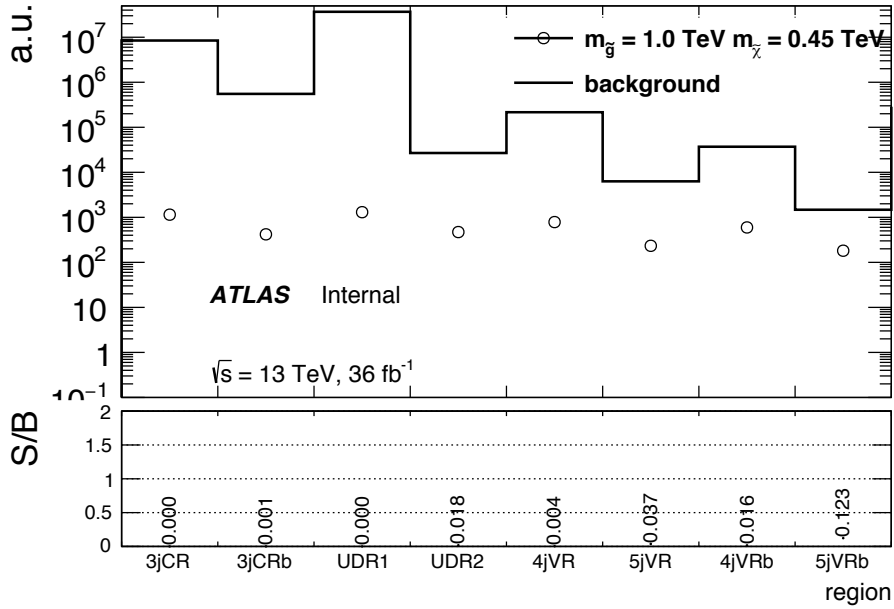


Figure 12: Expected background (PYTHIA8) and signal ($m_{\tilde{g}} = 1.0 \text{ TeV}$, $m_{\tilde{\chi}} = 0.45 \text{ TeV}$) yields and the signal-to-background ratios in various regions. The total yields of signal and background are normalized to 36.1 fb^{-1} .

Not reviewed, for internal circulation only

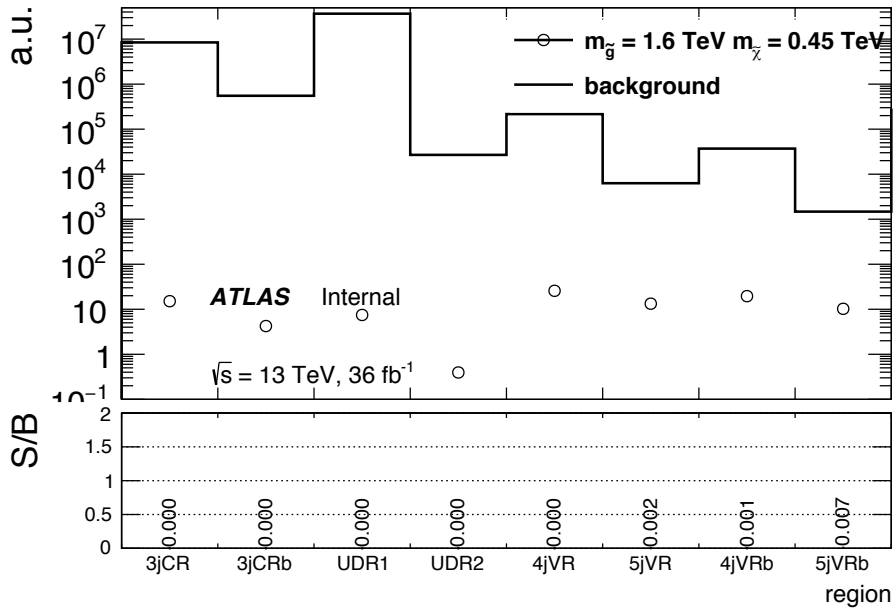


Figure 13: Expected background (PYTHIA8) and signal ($m_{\tilde{g}} = 1.6$ TeV, $m_{\tilde{\chi}} = 0.45$ TeV) yields and the signal-to-background ratios in various regions. The total yields of signal and background are normalized to 36.1 fb^{-1} .

380 To understand the systematic uncertainty associated with the assumption that the jet mass DPF is the same
 381 between the signal regions and the control region, a data-driven method is developed. This method studies
 382 the performance of the jet mass prediction using signal-depleted jet samples in data. The predicted and
 383 observed individual jet mass distributions are compared in p_T and $|\eta|$ in the UDRs. Specifically, the jet mass
 384 response, defined as the mean value of the jet mass distribution in a given p_T and $|\eta|$ bin, is used to quantify
 385 the performance of the jet mass template method. In the ideal scenario, Ideally, the jet mass response
 386 should be in agreement between the observed jet masses and predicted jet masses, and any discrepancy
 387 in the jet mass response between the observation and prediction indicates a non-closure of the jet mass
 388 template at the individual jet mass level, which is a metric to quantify the systematic uncertainty of the
 389 jet mass prediction. The uncertainties on individual jet mass can be propagated to the prediction of the
 390 M_J^Σ distribution and therefore the predicted background yield in the signal region.

391 As an example, Figure 14 shows the jet mass response for all jets in 3jCR region of the PYTHIA8 multijet
 392 and $t\bar{t}$ MC samples. In such a plot, the top pane shows the jet mass response for predicted jet masses
 393 (histogram with vertical lines connecting adjacent bins) and observed jet masses (histogram with horizontal
 394 error bars only), and the bottom pane shows the ratio of the observed jet mass response over the predicted
 395 jet mass response. A ratio over 1 in the bottom pane suggests an under-prediction of jet mass, while a
 396 ratio below 1 suggests an over-prediction.

397 4.4.1. Jet mass response

398 Plots like Figure 14 are the primary tool to understand the performance of the jet mass template method.
 399 For example, Figure 15 shows the predicted and observed jet mass responses of 3-jet events separately for

Not reviewed, for internal circulation only

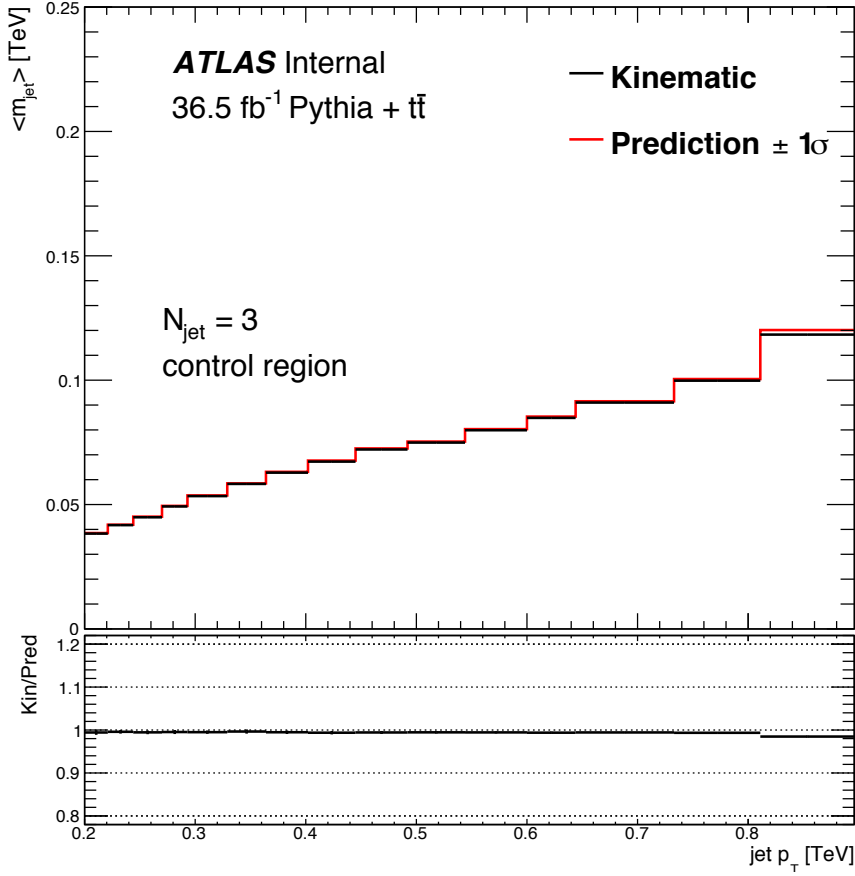


Figure 14: Jet mass response for jets in the 3jCR (control region) of the PYTHIA8 multijet plus $t\bar{t}$ MC samples. The jet mass response is defined as the mean of jet mass distribution in a given bin defined by p_T , $|\eta|$, and b-matching requirements. The black points with vertical and horizontal error bars are the observed jet mass response values, while the red histogram corresponds to the predicted jet mass response.

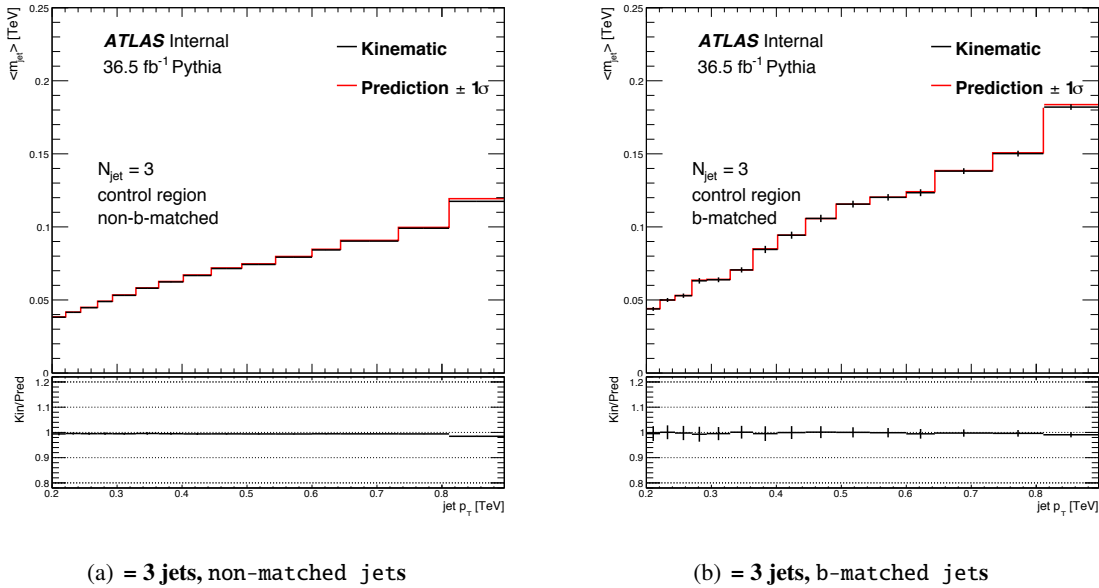


Figure 15: Jet mass response of 3-jet events for non-matched jets(15(a)) and b-matched jets(15(b)) in PYTHIA8 multijet MC sample.

400 non-matched jets(15(a)) and b-matched jets(15(b)) in PYTHIA8 multijet MC sample. The observed
 401 and predicted jet mass responses overlap in these plots, indicating a closure of the jet mass template
 402 method in the control region, as expected.

403 Figure 16 shows the observed and predicted jet mass response in ≥ 4 jets 16(a) and ≥ 5 jets 16(b) events
 404 in PYTHIA8 multijet plus $t\bar{t}$ MC samples. The result is statistics-limited, nevertheless, it appears that both
 405 ≥ 4 jets and ≥ 5 jets regions suffer a moderate over-prediction for jet with $p_T < 400$ GeV and a
 406 small under-prediction for jets with $p_T > 400$ GeV. A very similar trend is seen in the ≥ 4 jets region
 407 of Herwigpp multijet plus $t\bar{t}$ MC samples, as shown in Figure 17(a), while the response ratio in the \geq
 408 5 jets region (Figure 17(b)) is completely dominated by statistical fluctuation and thereorefre renders no
 409 information.

410 4.4.2. Estimate the systematic uncertainty with uncertainty determination regions

411 The jet mass template method involves two major assumptions: first, jet mass PDFs only depend on
 412 observables including jet p_T , η , and b-matching information; second, jets in the same event are uncorrelated
 413 and their masses can be modeled independently. Both assumptions are known to be invalid to some extent.
 414 For example, jet mass PDFs depend on the quark or gluon origin of jet, which cannot be determined
 415 experimentally on a jet-by-jet basis. In addition, jets in the same events are also not completely independent
 416 from each other at both particle level and reconstruction level.

417 This analysis develops an effective approach to probe the systematic uncertainty of the background
 418 estimation using data UDRs. The UDRs are defined by jet multiplicity and p_T in a way so that they
 419 contain jets that are different in origin. The jet mass prediction is tested in the UDRs, and the discrepancy
 420 between the observation and the prediction indicates the level of systematic uncertainty of the background

Not reviewed, for internal circulation only

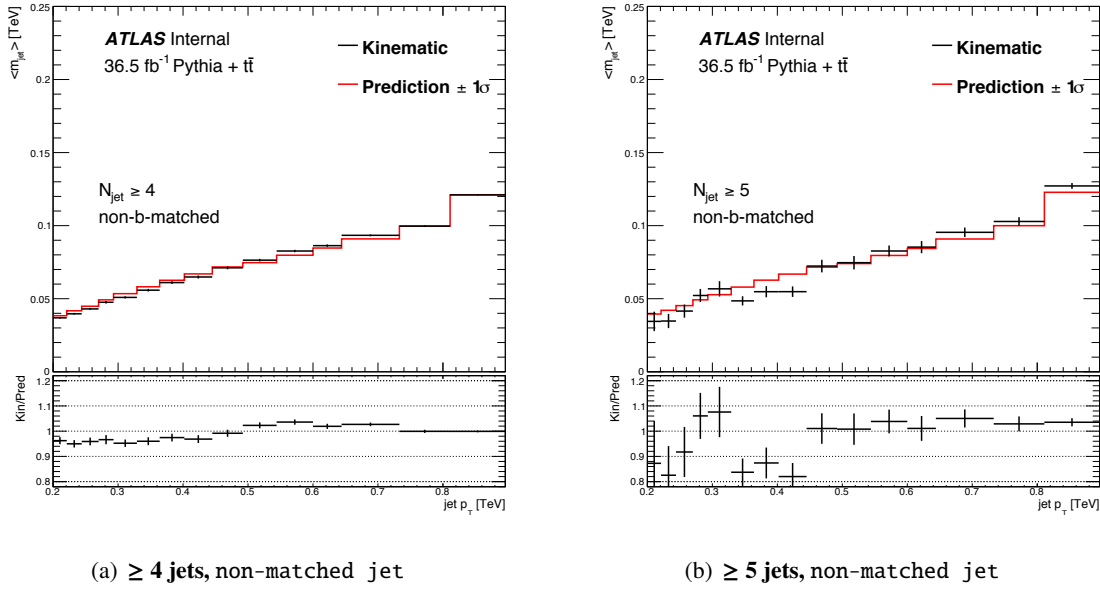


Figure 16: Observed and predicted jet mass response in ≥ 4 jets 16(a) and ≥ 5 jets 16(b) events in PYTHIA8 multijet plus $t\bar{t}$ MC samples.

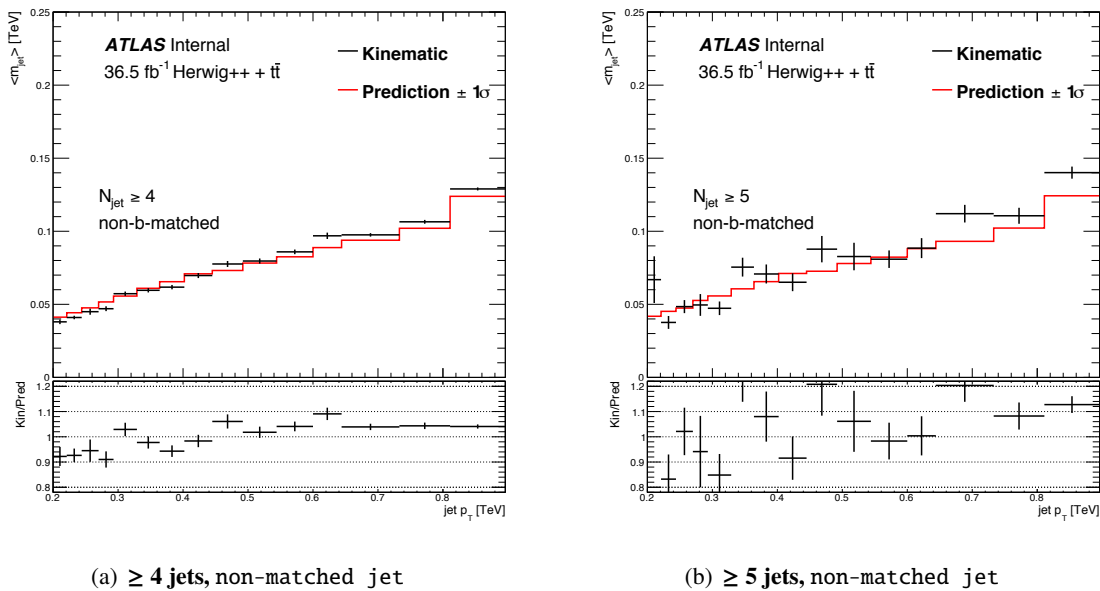
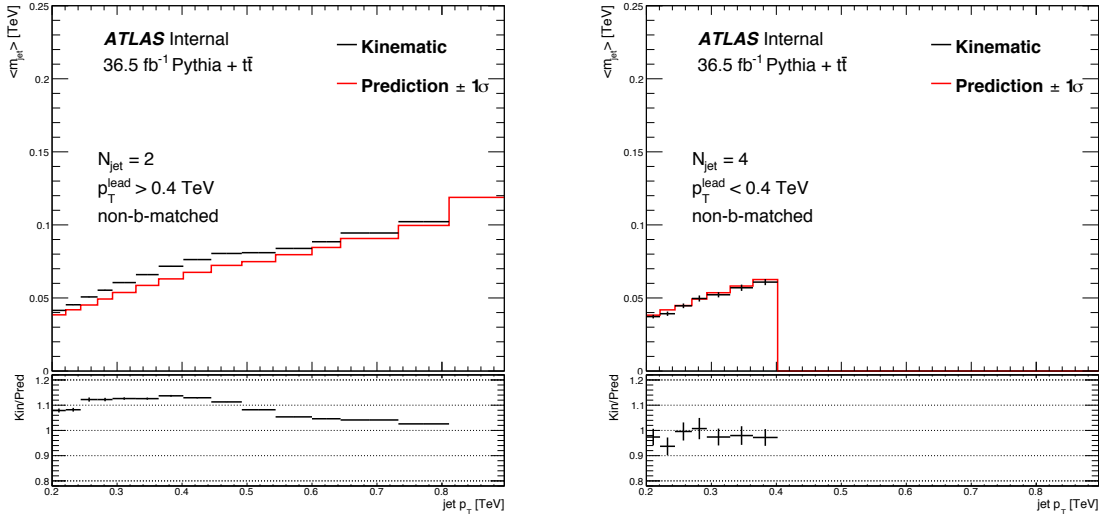


Figure 17: Observed and predicted jet mass response in ≥ 4 jets 17(a) and ≥ 5 jets 17(b) events in Herwigpp multijet plus $t\bar{t}$ MC samples.

Not reviewed, for internal circulation only



(a) = 2 jets, leading jet $p_T > 400$ GeV non-matched jet (b) = 4 jets, leading jet $p_T > 400$ GeV non-matched jet

Figure 18: Predicted and observed jet mass responses in the UDR1 (a) and UDR2 (b) with PYTHIA8 multijet plus $t\bar{t}$ MC samples.

estimation. These UDRs need to be orthogonal to signal and validation regions, and certain cuts may be introduced to suppress signal contamination.

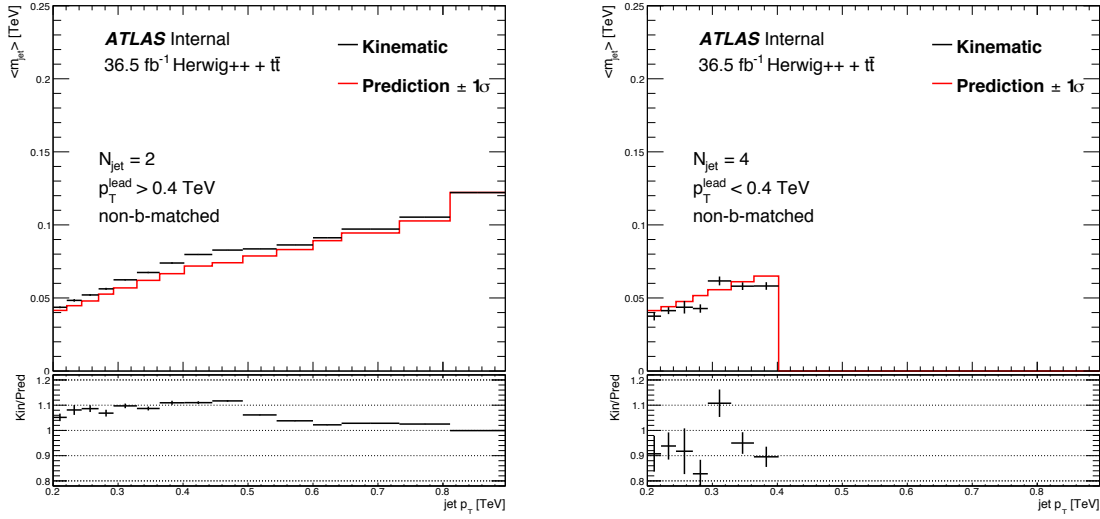
The 2 UDRs considered in the analysis are defined as follows:

- UDR1 2 large- R jets, the leading large- R jet $p_T > 400$ GeV.
- UDR2 4 large- R jets, the leading large- R jet $p_T < 400$ GeV.

In the UDR1, events are selected by requiring exactly two large- R jets. High p_T jets in the UDR1 are likely resulted from hadronization of an outgoing parton at the leading order (LO) of the parton scattering. Since all events are required to pass an `HLT_ht1000_L1J100` trigger, the outgoing partons at the leading order are unlikely to have a $p_T < 500$ GeV; at the reconstruction level, the large- R jets with $p_T < 400$ GeV are more likely to be resulted from partons radiated from the hard scattering at the LO. Similarly, jets in the UDR2, which is defined as events with four large- R jets with $200 \text{ GeV} < p_T < 400 \text{ GeV}$, are also likely to be associated with partons radiated from the LO hard scattering. The low p_T jets in the UDR1 and UDR2 may be similar in their origin, however, they are produced from every different types of events. The UDR1 events with a low p_T jet tend to be “imbalanced”, as there is a leading jet with $p_T > 400$ GeV and the H_T of the event needs to be greater than 1000 GeV. The events in the UDR2 should be more “balanced”, as they are selected by vetoing high p_T jets and requiring high multiplicity. The jet mass response distributions of the low p_T jets indeed exhibit different behaviors in the UDR1 and UDR2, as shown by Figures 18 and 19. This observation is confirmed by both PYTHIA8 and Herwigpp multijet samples, as well as data.

Figure 18 shows the jet mass responses in the two UDRs in the PYTHIA8 multijet plus $t\bar{t}$ MC samples. In the “low p_T ” range ($p_T < 400$ GeV), the UDR1 shows a sizable (10 - 15% level) under-prediction, while the UDR2 shows a small (~ 5% level) but systematic over-prediction. In the “high p_T ” range ($p_T > 400$ GeV

Not reviewed, for internal circulation only



(a) = 2 jets, leading jet $p_T > 400$ GeV non-matched jet (b) = 4 jets, leading jet $p_T > 400$ GeV non-matched jet

Figure 19: Predicted and observed jet mass responses in the UDR1 (a) and UDR2 (b) with Herwigpp multijet plus $t\bar{t}$ MC samples.

of the UDR1, there is a consistent under-prediction at 15% level starting from p_T just beyond 400 GeV and gradually dropping to just a few percents for $p_T > 600$ GeV. Very similar behaviors are also found in Herwigpp multijet sample, as shown in Figure 19. The discrepancy at the high p_T range appears to be qualitatively consistent with those in the high p_T part of ≥ 4 jets and ≥ 5 jets regions, as shown in Figure 16. The discrepancy at the low p_T range of UDR2 is also qualitatively consistent with those in the low p_T part of the ≥ 4 jets and ≥ 5 jets regions. The difference in the sign and size of the discrepancy for low p_T jets between the UDR1 and the UDR2 suggests that the jet mass PDF depends on factors beyond the origin of jets.

Jets collected by the UDRs correspond to some extreme scenarios, and the jets in the signal and validation regions are a mix of these different extremes. The discrepancies quantified by the UDRs can be considered as an upper limit of the discrepancy that may appear in the signal and validation regions. Using Monte Carlo samples, this assertion can be examined. Figure 16 suggests that for high p_T jets a 4-5% level of under-prediction exists for events with ≥ 4 (or 5) jets in the PYTHIA8 multijet MC sample. Figure 17, made with Herwigpp multijet sample, indicates similar behavior, especially in events with ≥ 4 jets. These discrepancies are indeed qualitatively consistent with the discrepancy seen in the high p_T region of UDR1, as shown in Figures 18(a) and 19(a). For low p_T jets in events with ≥ 4 jets, there is a systematic over-prediction shown in both PYTHIA8 (Figure 16) and Herwigpp (Figure 17) multijet samples. This is more consistent with the discrepancy seen in the UDR2. In events with ≥ 5 jets, these jet mass response plots are statistically inconclusive.

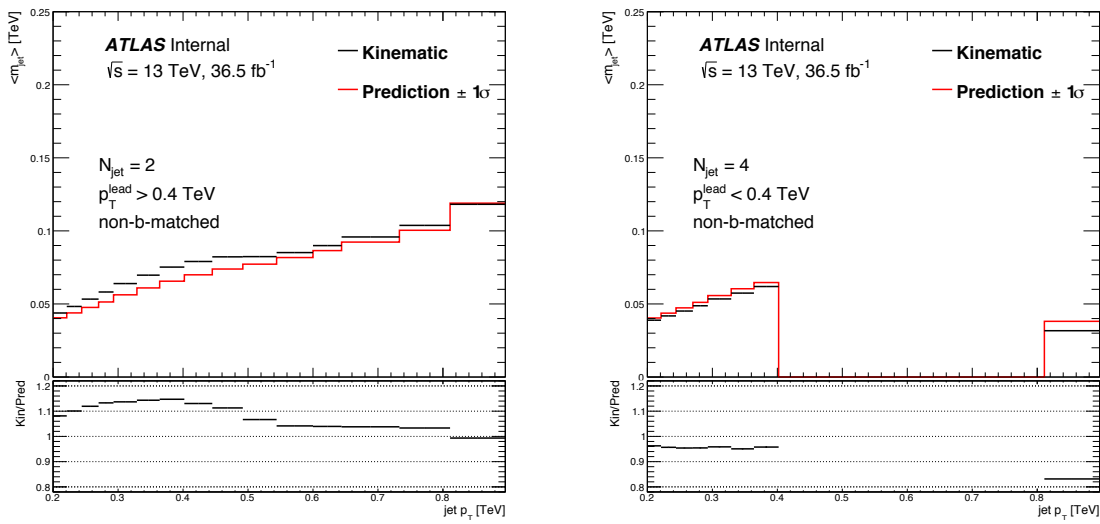
The jet mass response is further checked in data, as shown in Figure 20. The jet mass response in data is consistent with the jet mass response in the PYTHIA8 and Herwigpp multijet samples.

Table 3 summarizes the compatibility between the observed jet mass response and the prediction in various regions and different samples. In this table, the results from SHERPA multijet sample are also

	low p_T $< 400 \text{ GeV}$				intermediate p_T $400 \text{ GeV} - 600 \text{ GeV}$			high p_T $> 600 \text{ GeV}$		
	UDR1	UDR2	4j	5j	UDR1	4j	5j	UDR1	4j	5j
Data	↓	↑	-	-	↓	-	-	↓	-	-
PYTHIA8	↓	↑	↑	↑	↓	↓	×	↓	↓	↓
Herwigpp	↓	↑	↑	↑	↓	↓	×	↓	↓	↓
SHERPA	↓	✗	✗	✗	✗	✗	✗	↑	✗	✗

Table 3: A summary of compatibility between jet mass prediction and observation in various regions and different samples. In this table, the symbol \uparrow stands for over-prediction, \downarrow for under-prediction, \times for inconclusive due to low statistics, and “-” for not available.

Not reviewed, for internal circulation only



(a) = 2 jets, leading jet $p_T > 400 \text{ GeV}$ non-matched jet (b) = 4 jets, leading jet $p_T > 400 \text{ GeV}$ non-matched jet

Figure 20: Predicted and observed jet mass responses in the UDR1 ((a)) and UDR2 ((b)) with 36.1 fb^{-1} data.

465 listed, although they are statistically inconclusive in a few cases.

466 4.4.3. Systematic uncertainty determination

467 The jet mass response distributions in the UDR1 and UDR2 are used to estimate the uncertainty of jet mass
 468 prediction as a function of p_T and η of individual jets. In the prediction, the randomized jet mass value
 469 can be scaled up or down by the size of the discrepancy seen in the jet mass responses in the UDRs, and the
 470 M_J^Σ distributions resulted from the shifted randomized jet masses are used to determine the uncertainty
 471 on the predicted background yield in a signal region with a specific M_J^Σ cut. This implementation requires
 472 that the shift in jet mass response captures the main discrepancy in the jet mass PDF between different
 473 regions. Figure 21 compares the jet mass distributions between the CR and two UDRs in two example
 474 p_T - $|\eta|$ bins. While a simple scaling of jet mass may not completely correct the discrepancy at the tail part

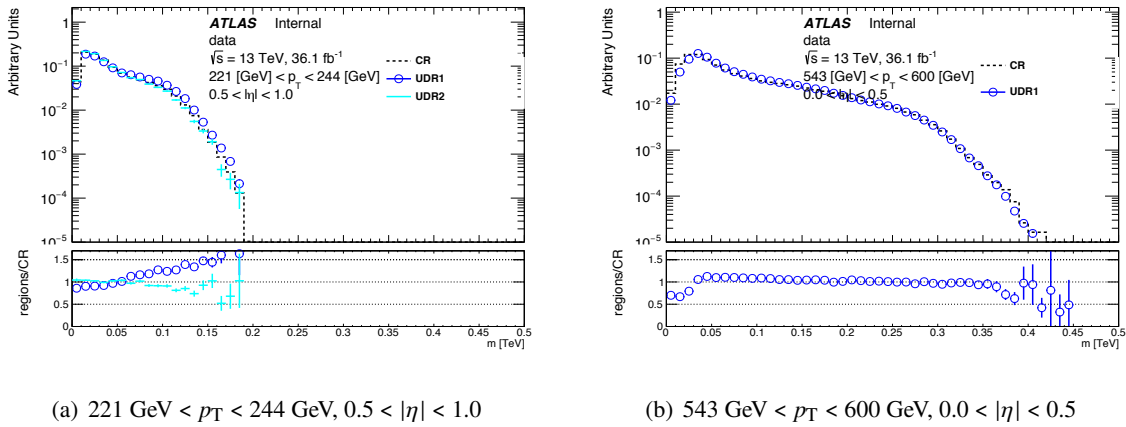


Figure 21: Jet mass distributions for the control region (dashed), UDR1 (open circle), and UDR2 (cyan cross) in two example p_T - $|\eta|$ bins, $221 \text{ GeV} < p_T < 244 \text{ GeV}, 0.5 < |\eta| < 1.0$ ((a)), and $543 \text{ GeV} < p_T < 600 \text{ GeV}, 0.0 < |\eta| < 0.5$ ((b)).

of the jet mass distribution, the discrepancy in the peak part of the jet mass distribution between these regions indeed can be captured by a shift in the jet mass. Appendix O presents the comparison plots for all p_T - $|\eta|$ bins.

The jet mass response distributions in four η regions for both UDRs are studied using PYTHIA8, Herwigpp, and SHERPA as well as data. Appendix E shows the jet mass response distributions in four η regions for both UDRs. The trends of the discrepancy between different η regions are very consistent. In each η region, the systematic uncertainty is determined in three different p_T ranges. For jets with $p_T < 400 \text{ GeV}$, the discrepancy is different in size and sign between the UDR1 and the UDR2, and the largest discrepancy observed in these two UDRs is considered as the systematic uncertainty. For jets with an intermediate p_T ($400 \text{ GeV} < p_T < 600 \text{ GeV}$), the discrepancy is dropping gradually over the p_T range, and the discrepancy observed at the bin right beyond $p_T = 400 \text{ GeV}$ is considered as the systematic uncertainty. For jets with $p_T > 600 \text{ GeV}$, the discrepancy is relatively flat in p_T and the average value is considered as the systematic uncertainty.

Tables 5 and 6 presents the systematic uncertainties determined with this procedure, for the PYTHIA8 multijet plus $t\bar{t}$ MC sample and the Herwigpp multijet plus $t\bar{t}$ MC sample, respectively. The uncertainty is relative to the jet mass and shown in four η regions and three p_T ranges.

The uncertainty on jet mass prediction is propagated to the prediction on background event yield in the signal region through pseudo-experiments. As described in Section 4.2, the nominal prediction of M_j^Σ is constructed from randomized jet masses in an ensemble of PEs; In the same ensemble of PEs, the randomized jet masses can be scaled up or down by the size of the jet mass prediction uncertainty determined here, and the resulting M_j^Σ distributions correspond to the $\pm 1 \sigma$ variation of the jet mass prediction uncertainty and can be used to derive the uncertainty on the predicted yield. This procedure is implemented separately for the “low p_T ” jet mass prediction uncertainty, which affects jets with a $p_T < 400 \text{ GeV}$, and the “high p_T ” jet mass prediction uncertainty, which affects jets with a $p_T > 400 \text{ GeV}$ and has different values for p_T ranges of $400 \text{ GeV} - 600 \text{ GeV}$ and $> 600 \text{ GeV}$.

In this uncertainty determination procedure, no separation between b-matched jets and non-matched

$ \eta $	low p_T	intermediate p_T	high p_T
$0 < \eta < .5$	10.96	10.63	2.31
$.5 < \eta < 1.0$	11.17	11.14	2.66
$1.0 < \eta < 1.5$	10.07	11.07	4.10
$1.5 < \eta < 2.0$	11.82	13.36	4.45

Table 4: Uncertainties (in percent) on predicted jet mass as determined from 36.1 fb^{-1} data.

$ \eta $	low p_T	intermediate p_T	high p_T
$0 < \eta < .5$	10.79	9.70	3.31
$.5 < \eta < 1.0$	9.99	13.14	3.95
$1.0 < \eta < 1.5$	9.56	11.32	3.65
$1.5 < \eta < 2.0$	10.60	11.70	4.19

Table 5: Uncertainties (in percent) on predicted jet mass as determined from PYTHIA8 and $t\bar{t}$ MC samples normalized to 36.1 fb^{-1} .

$ \eta $	low p_T	intermediate p_T	high p_T
$0 < \eta < .5$	6.41	8.74	1.82
$.5 < \eta < 1.0$	8.75	10.67	1.70
$1.0 < \eta < 1.5$	10.30	9.69	3.34
$1.5 < \eta < 2.0$	9.22	13.15	5.78

Table 6: Uncertainties (in percent) on predicted jet mass as determined from Herwigpp and $t\bar{t}$ MC samples normalized to 36.1 fb^{-1} .

501 jets is made. The jet mass response is checked separately for b-matched jets and non-matched jets
 502 in data and Monte Carlo samples and shown in Appendix G. In the UDR1, the discrepancies seen in
 503 the b-matched jets and non-matched jets are essentially the same, as shown by Figure 66. In the
 504 UDR2(67), PYTHIA8 multijet plus $t\bar{t}$ MC sample does not suggest significant discrepancy, and the jet mass
 505 response of b-matched jets is statistically limited; data suggest that there is an over-prediction at the
 506 level of 5 - 10% in both non-matched jets and b-matched jets, with the discrepancy in b-matched
 507 jets slightly larger. Since the larger discrepancy in the range of $p_T < 400 \text{ GeV}$ between the UDR1 and
 508 UDR2 is taken as the uncertainty and the discrepancy in the UDR1 is always larger than that in the UDR2, the
 509 merge of b-matched jets and non-matched jets does not yield any practical impact in the analysis.

510 Since UDR1 only requires two large- R jets, the HLT_ht1000_L1J100 trigger may not be fully efficient
 511 in this region. The inefficiency of UDR1 events in principle should not affect the estimation of the jet
 512 mass prediction uncertainty, as this uncertainty is at the individual jet level. The UDR2 also suffer from
 513 a small inefficiency, as suggested by Figure 7. To check if the trigger inefficiency can introduce any
 514 significant change in the UDRs, an offline $H_T > 1.0 \text{ TeV}$ requirement is included and the discrepancies in
 515 the UDRs are found to be consistent with or without this offline H_T cut. Appendix D includes figures of
 516 this comparison.

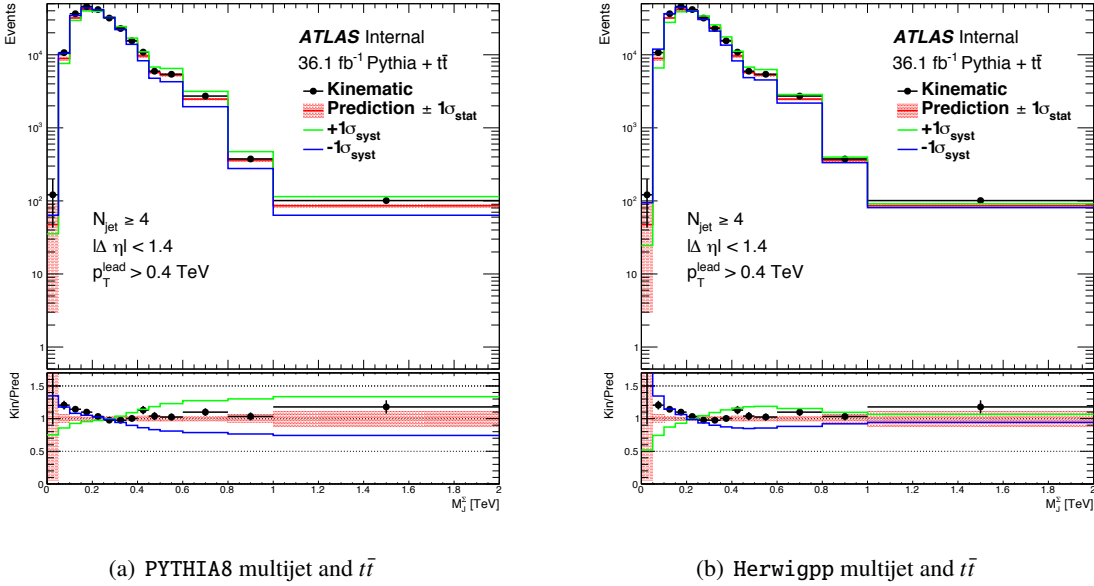


Figure 22: Example predicted and observed M_J^Σ distributions in Monte Carlo background samples. The events are selected by requiring four or more large- R jets and a leading large- R jet with $p_T > 400$ GeV. Results from PYTHIA8 multijet combined with $t\bar{t}$ sample are shown. (a) shows the systematic variation for the “high p_T ” component, and (b) shows systematic variation for the “low p_T ” component. The black dots with error bars indicate the observed M_J^Σ distribution and its statistical uncertainty. The solid red histogram with shaded bands indicate the predicted M_J^Σ distribution and its statistical uncertainty. The green and blue histograms correspond to $\pm 1 \sigma$ variation of one of the systematic uncertainties identified in the analysis. Additional systematic uncertainties are not included in these plots. The bottom pane show the ratio of the observed M_J^Σ distribution over the expected M_J^Σ distribution or its systematic variations. Both multijet MC samples are a combination of samples with different leading jet p_T requirements (known as the JZW samples in ATLAS), and the lowest MC luminosity of these samples is 1.8 fb^{-1} and 3.6 fb^{-1} for PYTHIA8 multijet sample and Herwigpp multijet sample, respectively.

517 4.5. Prediction from the MC and data

518 4.5.1. Background estimation performance in Monte Carlo sample

519 The full background estimation procedure is exercised on three multijet MC samples, including PYTHIA8,
 520 Herwigpp, and SHERPA. In certain regions, the samples are statistically limited. The equivalent MC
 521 integrated luminosity is as low as 1.9 fb^{-1} and 3.6 fb^{-1} for PYTHIA8 and Herwigpp samples. In the
 522 comparison of jet mass response in the CR and UDRs between SHERPA and data, it is found that the
 523 SHERPA multijet sample does not model data well, and therefore the SHERPA multijet sample is disfavored
 524 in this study.

525 Figures 23 - 26 show the predicted and observed M_J^Σ distributions in various signal regions using
 526 PYTHIA8 multijet and $t\bar{t}$ Monte Carlo background samples, while Figures 27 - 30 show the predicted
 527 and observed M_J^Σ distributions in various validation regions using the same samples. The equivalent of
 528 these figures produced from Herwigpp multijet plus $t\bar{t}$ samples can be found in Appendix L.

529 In the regions defined with five or more large- R jets, the Monte Carlo statistics is severely limited. The

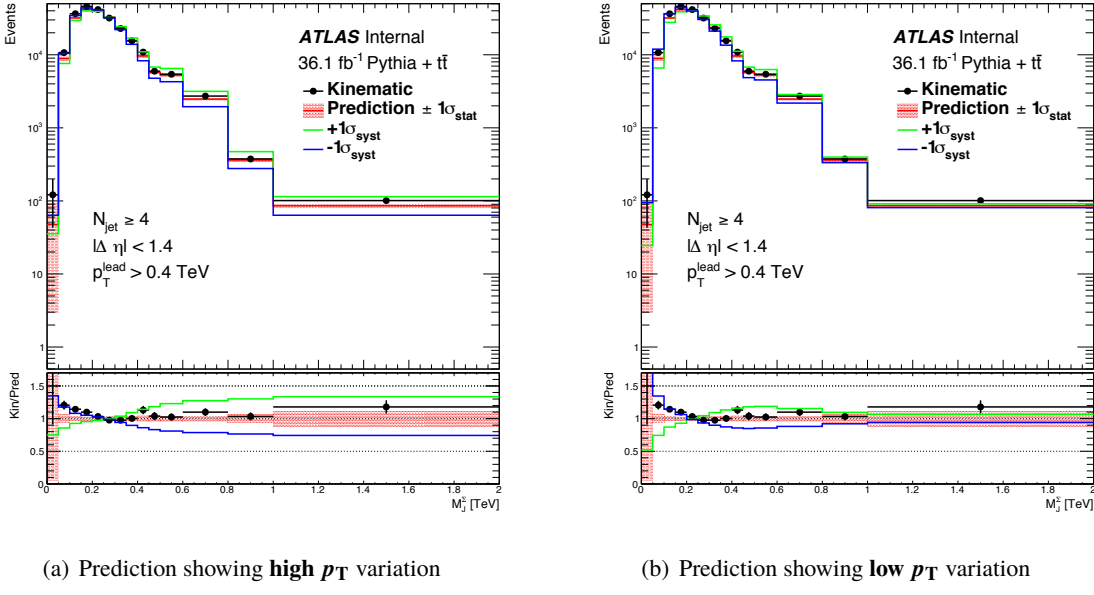


Figure 23: Predicted and observed M_J^Σ distributions in PYTHIA8 multijet and $t\bar{t}$ Monte Carlo background samples. The events are selected by requiring four or more large- R jets and a leading large- R jet with $p_T > 400$ GeV. The $|\Delta\eta_{12}|$ of the event is required to be less than 1.4. There is no requirement on the presence of a b-tagged jet. The black dots with error bars indicate the observed M_J^Σ distribution and its statistical uncertainty. The solid red histogram with shaded bands indicate the predicted M_J^Σ distribution and its statistical uncertainty. The green and blue histograms correspond to $\pm 1 \sigma$ variation of one of the systematic uncertainties identified in the analysis. Subfigure (a) shows variations of the “high p_T ” systematic uncertainty, while subfigure (b) shows variations of the “low p_T ” systematic uncertainty. The bottom pane show the ratio of the observed M_J^Σ distribution over the expected M_J^Σ distribution or its systematic variations. The PYTHIA8 multijet MC samples are a combination of samples with different leading jet p_T requirements (known as the JZW samples in ATLAS), and the lowest MC luminosity of these samples is 1.8 fb^{-1} .

prediction and observation agree within statistical uncertainty, which is much larger than the systematic uncertainties determined in the UDRs. In the regions defined with four or more large- R jets, the overall agreement is reasonable. In the low M_J^Σ region, there is a systematic excess regardless of the b-tagging requirement, while in the high M_J^Σ region, there is a modest excess that is at the level of statistical uncertainty. Overall, the predicted M_J^Σ distribution is “narrower” than the observed M_J^Σ distribution. The excess in the low M_J^Σ part suggests an over-prediction of jet mass, while the excess in the high M_J^Σ part suggests an under-prediction of jet mass. It is clear that a single one-sided shift of jet mass cannot account for such kind of discrepancy. This observation is indeed consistent with the observation in the UDRs. The UDR2 sees an over-prediction of jet mass for jet with $p_T < 400$ GeV, while the UDR1 sees an under-prediction of jet mass for the entire p_T range. Two uncorrelated systematic components are needed to account for the discrepancy seen in the M_J^Σ distributions.

The predicted and observed background yields in a region with $M_J^\Sigma > 0.8$ TeV are shown in Table 7 and Table 8 for PYTHIA8 multijet plus $t\bar{t}$ sample and Herwigpp multijet plus $t\bar{t}$ sample, respectively. In general, there is a good agreement between the prediction and the observation.

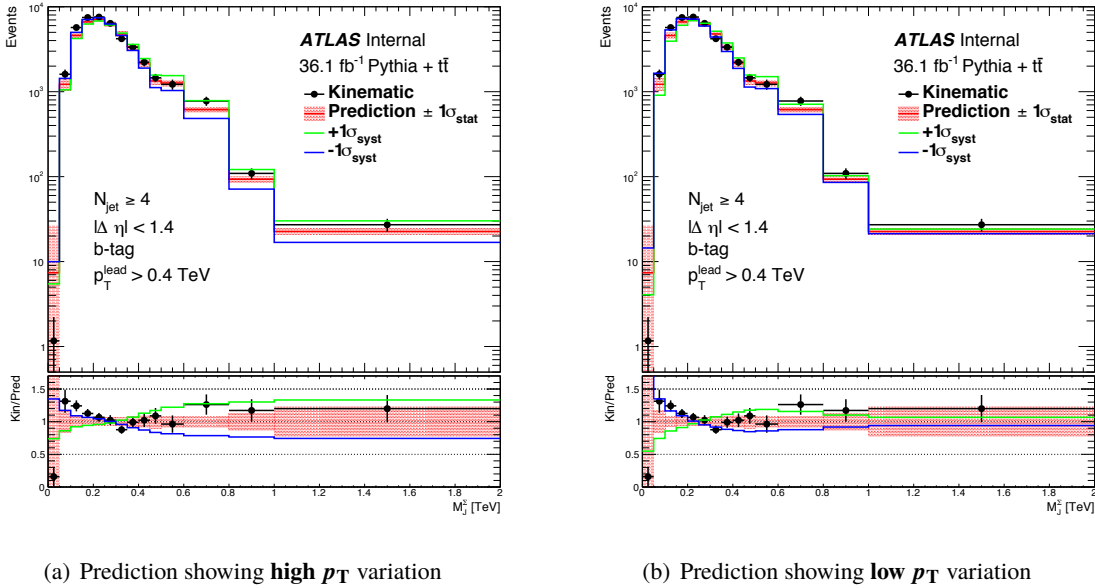


Figure 24: Predicted and observed M_J^Σ distributions in PYTHIA8 multijet and $t\bar{t}$ Monte Carlo background samples. The events are selected by requiring four or more large- R jets and a leading large- R jet with $p_T > 400$ GeV. The $|\Delta\eta_{12}|$ of the event is required to be less than 1.4. At least one b-tagged jet is required to be present in the event. The black dots with error bars indicate the observed M_J^Σ distribution and its statistical uncertainty. The solid red histogram with shaded bands indicate the predicted M_J^Σ distribution and its statistical uncertainty. The green and blue histograms correspond to $\pm 1 \sigma$ variation of one of the systematic uncertainties identified in the analysis. Subfigure (a) shows variations of the “high p_T ” systematic uncertainty, while subfigure (b) shows variations of the “low p_T ” systematic uncertainty. The bottom pane show the ratio of the observed M_J^Σ distribution over the expected M_J^Σ distribution or its systematic variations. The PYTHIA8 multijet MC samples are a combination of samples with different leading jet p_T requirements (known as the JZW samples in ATLAS), and the lowest MC luminosity of these samples is 1.8 fb^{-1} .

Region	$\geq M_J^\Sigma$ [TeV]	Observed	Expected ($\pm (\text{Stat.}) \pm (\text{High } p_T) \pm (\text{Low } p_T)$)
4jSRb	0.8	129.1 ± 15.8	$117.1 \pm 7.6 \pm 36.5 \pm 10.9$
5jSRb	0.8	6.0 ± 2.0	$6.3 \pm 1.6 \pm 2.0 \pm .5$
4jSR	0.8	454.5 ± 22.7	$452.8 \pm 13.7 \pm 140.9 \pm 41.3$
5jSR	0.8	29.8 ± 4.9	$24.6 \pm 3.4 \pm 7.7 \pm 1.9$

Table 7: Predicted and observed yields in various search regions in PYTHIA8 multijet and $t\bar{t}$ MC.

Region	$\geq M_J^\Sigma$ [TeV]	Observed	Expected ($\pm (\text{Stat.}) \pm (\text{High } p_T) \pm (\text{Low } p_T)$)
4jSRb	0.8	81.6 ± 20.1	$76.8 \pm 9.8 \pm 16.3 \pm 6.0$
5jSRb	0.8	4.8 ± 2.1	$3.7 \pm 1.4 \pm .8 \pm .2$
4jSR	0.8	419.9 ± 110.7	$304.0 \pm 18.5 \pm 64.8 \pm 21.9$
5jSR	0.8	16.7 ± 3.7	$18.3 \pm 4.1 \pm 4.1 \pm .9$

Table 8: Predicted and observed yields in various search regions in Herwigpp multijet and $t\bar{t}$ MC.

Not reviewed, for internal circulation only

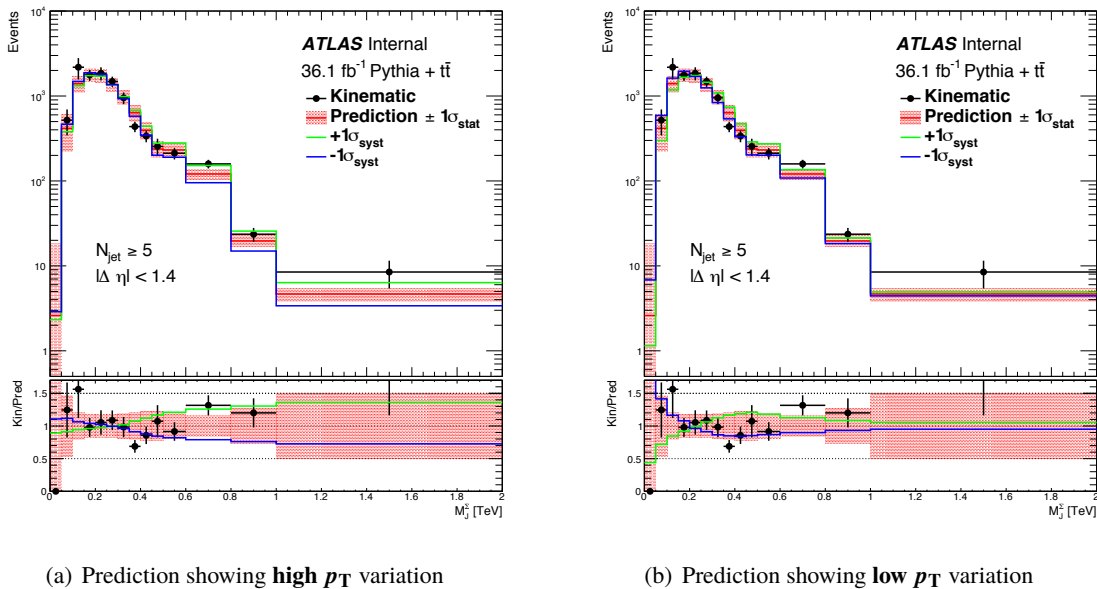


Figure 25: Predicted and observed M_j^Σ distributions in PYTHIA8 multijet and $t\bar{t}$ Monte Carlo background samples. The events are selected by requiring five or more large- R jets and a leading large- R jet with $p_T > 400$ GeV. The $|\Delta\eta_{12}|$ of the event is required to be less than 1.4. There is no requirement on the presence of a b-tagged jet. The black dots with error bars indicate the observed M_j^Σ distribution and its statistical uncertainty. The solid red histogram with shaded bands indicate the predicted M_j^Σ distribution and its statistical uncertainty. The green and blue histograms correspond to $\pm 1 \sigma$ variation of one of the systematic uncertainties identified in the analysis. Subfigure (a) shows variations of the “high p_T ” systematic uncertainty, while subfigure (b) shows variations of the “low p_T ” systematic uncertainty. The bottom pane show the ratio of the observed M_j^Σ distribution over the expected M_j^Σ distribution or its systematic variations. The PYTHIA8 multijet MC samples are a combination of samples with different leading jet p_T requirements (known as the JZW samples in ATLAS), and the lowest MC luminosity of these samples is 1.8 fb^{-1} .

Not reviewed, for internal circulation only

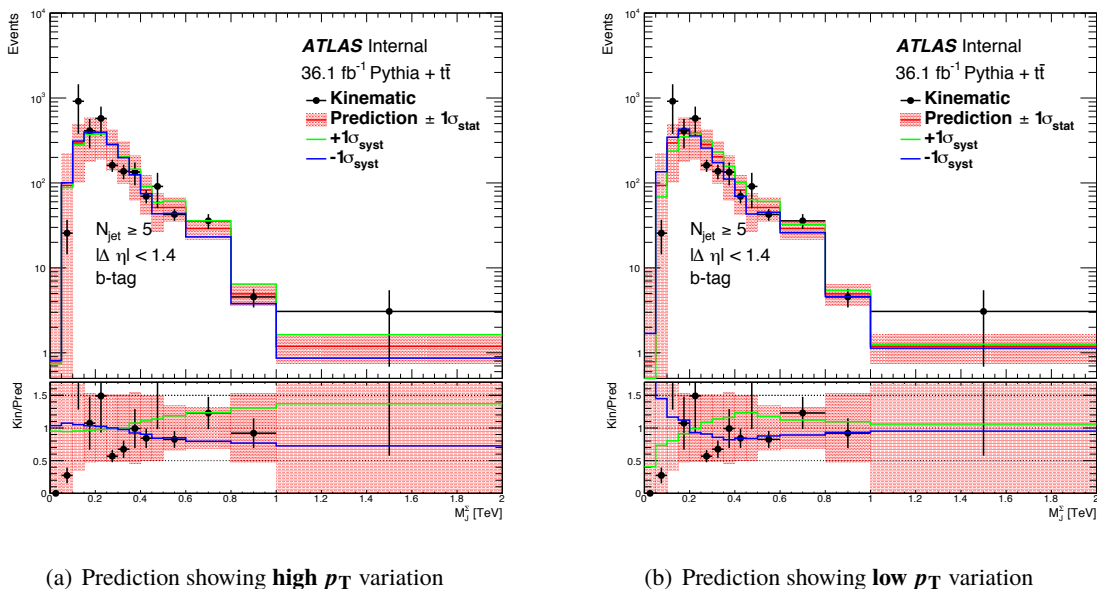


Figure 26: Predicted and observed M_j^Σ distributions in PYTHIA8 multijet and $t\bar{t}$ Monte Carlo background samples. The events are selected by requiring five or more large- R jets and a leading large- R jet with $p_T > 400$ GeV. The $|\Delta\eta_{12}|$ of the event is required to be less than 1.4. At least one b-tagged jet is required to be present in the event. The black dots with error bars indicate the observed M_j^Σ distribution and its statistical uncertainty. The solid red histogram with shaded bands indicate the predicted M_j^Σ distribution and its statistical uncertainty. The green and blue histograms correspond to $\pm 1 \sigma$ variation of one of the systematic uncertainties identified in the analysis. Subfigure (a) shows variations of the “high p_T ” systematic uncertainty, while subfigure (b) shows variations of the “low p_T ” systematic uncertainty. The bottom pane show the ratio of the observed M_j^Σ distribution over the expected M_j^Σ distribution or its systematic variations. The PYTHIA8 multijet MC samples are a combination of samples with different leading jet p_T requirements (known as the JZW samples in ATLAS), and the lowest MC luminosity of these samples is 1.8 fb^{-1} .

Not reviewed, for internal circulation only

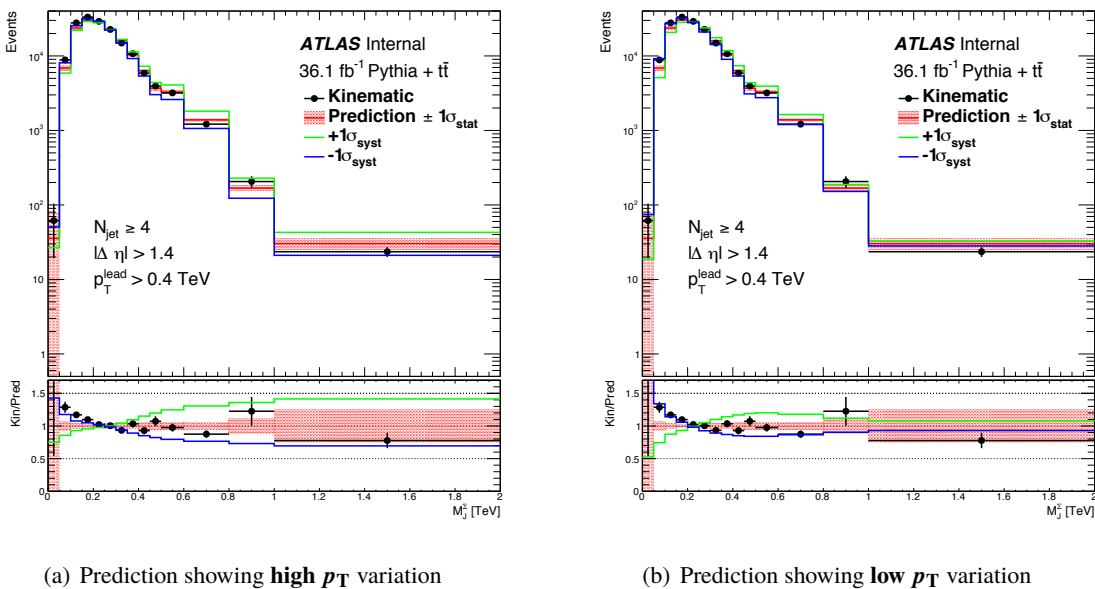


Figure 27: Predicted and observed M_j^Σ distributions in PYTHIA8 multijet and $t\bar{t}$ Monte Carlo background samples. The events are selected by requiring four or more large- R jets and a leading large- R jet with $p_T > 400$ GeV. The $|\Delta\eta_{12}|$ of the event is required to be greater than 1.4. There is no requirement on the presence of a b-tagged jet. The black dots with error bars indicate the observed M_j^Σ distribution and its statistical uncertainty. The solid red histogram with shaded bands indicate the predicted M_j^Σ distribution and its statistical uncertainty. The green and blue histograms correspond to $\pm 1 \sigma$ variation of one of the systematic uncertainties identified in the analysis. Subfigure (a) shows variations of the “high p_T ” systematic uncertainty, while subfigure (b) shows variations of the “low p_T ” systematic uncertainty. The bottom pane show the ratio of the observed M_j^Σ distribution over the expected M_j^Σ distribution or its systematic variations. The PYTHIA8 multijet MC samples are a combination of samples with different leading jet p_T requirements (known as the JZW samples in ATLAS), and the lowest MC luminosity of these samples is 1.8 fb^{-1} .

Not reviewed, for internal circulation only

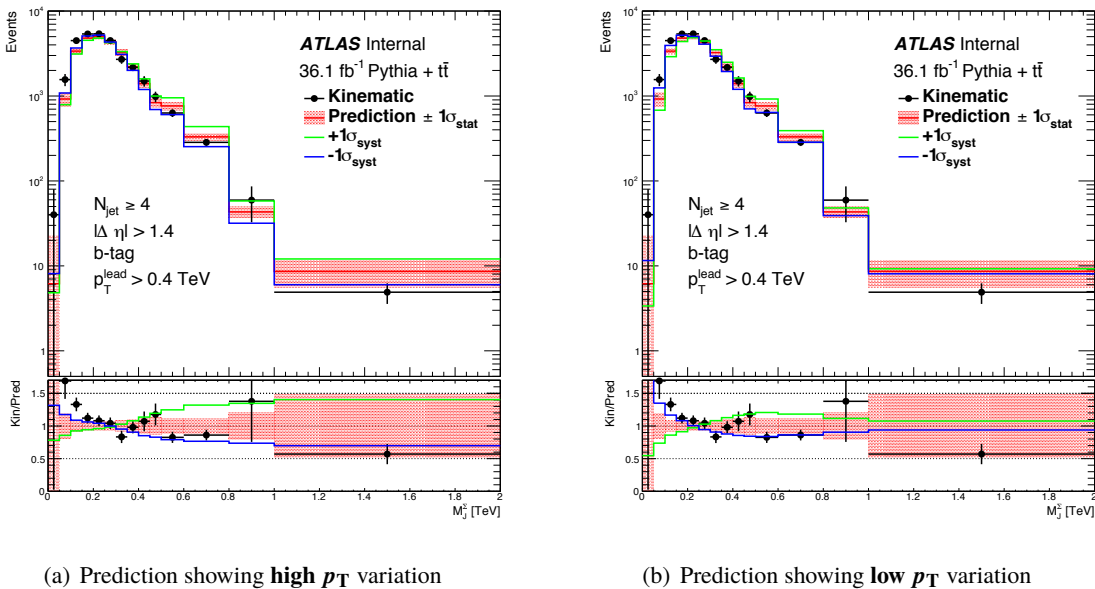


Figure 28: Predicted and observed M_j^Σ distributions in PYTHIA8 multijet and $t\bar{t}$ Monte Carlo background samples. The events are selected by requiring four or more large- R jets and a leading large- R jet with $p_T > 400$ GeV. The $|\Delta\eta_{12}|$ of the event is required to be greater than 1.4. At least one b-tagged jet is required to be present in the event. The black dots with error bars indicate the observed M_j^Σ distribution and its statistical uncertainty. The solid red histogram with shaded bands indicate the predicted M_j^Σ distribution and its statistical uncertainty. The green and blue histograms correspond to $\pm 1 \sigma$ variation of one of the systematic uncertainties identified in the analysis. Subfigure (a) shows variations of the “high p_T ” systematic uncertainty, while subfigure (b) shows variations of the “low p_T ” systematic uncertainty. The bottom pane show the ratio of the observed M_j^Σ distribution over the expected M_j^Σ distribution or its systematic variations. The PYTHIA8 multijet MC samples are a combination of samples with different leading jet p_T requirements (known as the JZW samples in ATLAS), and the lowest MC luminosity of these samples is 1.8 fb^{-1} .

Not reviewed, for internal circulation only

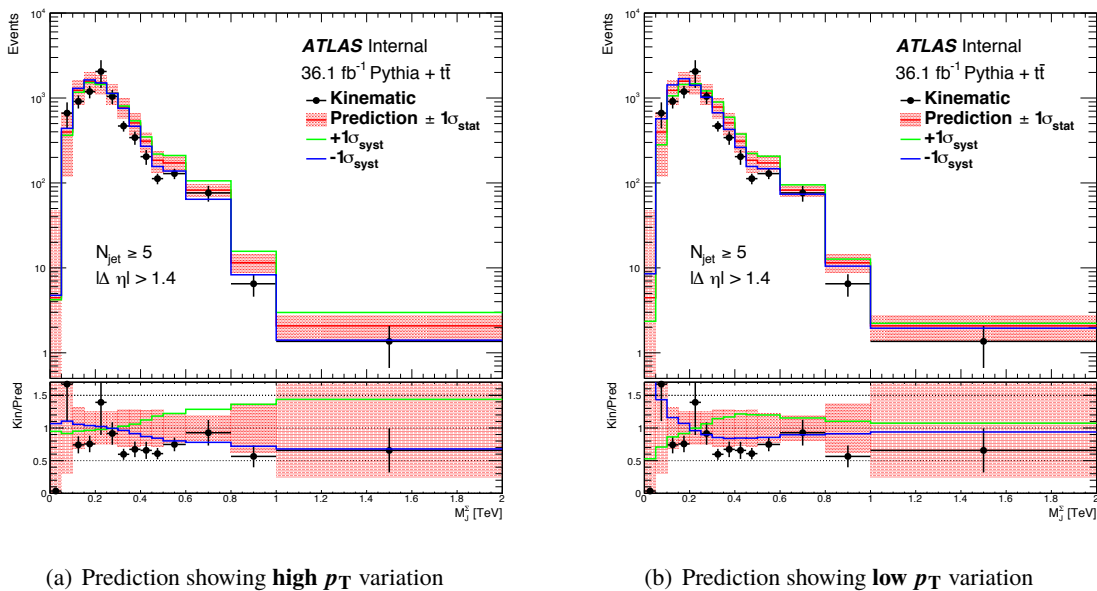


Figure 29: Predicted and observed M_j^Σ distributions in PYTHIA8 multijet and $t\bar{t}$ Monte Carlo background samples. The events are selected by requiring five or more large- R jets and a leading large- R jet with $p_T > 400$ GeV. The $|\Delta\eta_{12}|$ of the event is required to be greater than 1.4. There is no requirement on the presence of a b-tagged jet. The black dots with error bars indicate the observed M_j^Σ distribution and its statistical uncertainty. The solid red histogram with shaded bands indicate the predicted M_j^Σ distribution and its statistical uncertainty. The green and blue histograms correspond to $\pm 1 \sigma$ variation of one of the systematic uncertainties identified in the analysis. Subfigure (a) shows variations of the “high p_T ” systematic uncertainty, while subfigure (b) shows variations of the “low p_T ” systematic uncertainty. The bottom pane show the ratio of the observed M_j^Σ distribution over the expected M_j^Σ distribution or its systematic variations. The PYTHIA8 multijet MC samples are a combination of samples with different leading jet p_T requirements (known as the JZW samples in ATLAS), and the lowest MC luminosity of these samples is 1.8 fb^{-1} .

Not reviewed, for internal circulation only

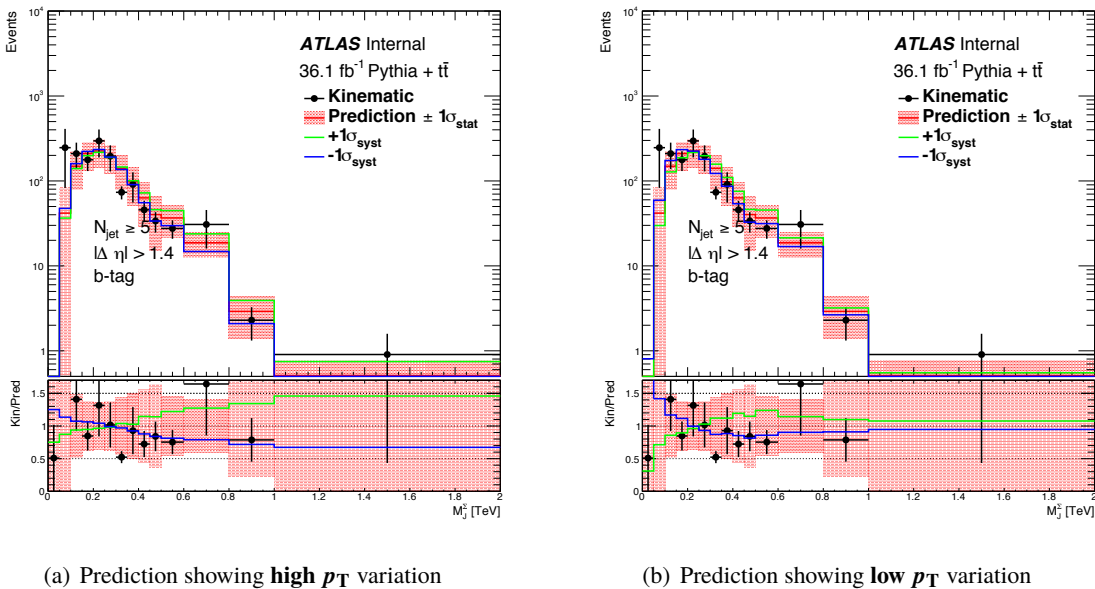


Figure 30: Predicted and observed M_j^Σ distributions in PYTHIA8 multijet and $t\bar{t}$ Monte Carlo background samples. The events are selected by requiring five or more large- R jets and a leading large- R jet with $p_T > 400$ GeV. The $|\Delta\eta_{12}|$ of the event is required to be greater than 1.4. At least one b-tagged jet is required to be present in the event. The black dots with error bars indicate the observed M_j^Σ distribution and its statistical uncertainty. The solid red histogram with shaded bands indicate the predicted M_j^Σ distribution and its statistical uncertainty. The green and blue histograms correspond to $\pm 1 \sigma$ variation of one of the systematic uncertainties identified in the analysis. Subfigure (a) shows variations of the “high p_T ” systematic uncertainty, while subfigure (b) shows variations of the “low p_T ” systematic uncertainty. The bottom pane show the ratio of the observed M_j^Σ distribution over the expected M_j^Σ distribution or its systematic variations. The PYTHIA8 multijet MC samples are a combination of samples with different leading jet p_T requirements (known as the JZW samples in ATLAS), and the lowest MC luminosity of these samples is 1.8 fb^{-1} .

Region	$\geq M_J^\Sigma$ [TeV]	Observed	Expected (\pm (Stat.) \pm (High p_T) \pm (Low p_T))
5jSRb	0.6	61	$44.0 \pm 7.5 \pm 11.2 \pm 7.2$
5jSRb	0.8	10	$7.0 \pm 2.4 \pm 1.9 \pm .7$
5jSR	0.8	31	$18.0 \pm 3.7 \pm 4.6 \pm 1.5$
4jSRb	1.0	15	$23.6 \pm 4.6 \pm 6.1 \pm 1.7$
4jSR	1.0	82	$68.2 \pm 7.6 \pm 15.8 \pm 4.4$

Table 9: Predicted and observed yields in various search regions in data for a number of different M_J^Σ cuts

Region	$\geq M_J^\Sigma$ [TeV]	Observed	Expected (\pm (Stat.) \pm (High p_T) \pm (Low p_T))
4jSRb	0.8	- ± -	$121.9 \pm 10.0 \pm 32.5 \pm 13.4$
5jSRb	0.8	- ± -	$7.0 \pm 2.4 \pm 1.9 \pm .7$
4jSR	0.8	- ± -	$325.1 \pm 16.7 \pm 85.0 \pm 33.5$
5jSR	0.8	- ± -	$18.0 \pm 3.7 \pm 4.6 \pm 1.5$
4jSRb	0.9	- ± -	$53.6 \pm 6.9 \pm 13.4 \pm 4.6$
5jSRb	0.9	- ± -	$3.0 \pm 1.7 \pm .7 \pm .3$
4jSR	0.9	- ± -	$142.4 \pm 12.9 \pm 35.0 \pm 11.3$
5jSR	0.9	- ± -	$8.9 \pm 2.5 \pm 1.8 \pm .5$
4jSRb	1.0	- ± -	$23.6 \pm 4.6 \pm 6.1 \pm 1.7$
5jSRb	1.0	- ± -	$1.3 \pm 1.0 \pm .3 \pm .1$
4jSR	1.0	- ± -	$68.2 \pm 7.6 \pm 15.8 \pm 4.4$
5jSR	1.0	- ± -	$4.8 \pm 1.9 \pm .9 \pm .2$
4jSRb	1.1	- ± -	$11.4 \pm 3.1 \pm 3.1 \pm .8$
4jSR	1.1	- ± -	$35.8 \pm 4.9 \pm 7.6 \pm 1.8$
4jSRb	1.2	- ± -	$5.5 \pm 2.6 \pm 1.3 \pm .3$
4jSR	1.2	- ± -	$21.0 \pm 3.8 \pm 3.5 \pm .8$

Table 10: Predicted and observed yields in various search regions in data for a number of different M_J^Σ cuts

544 4.6. Prediction in data

545 The determination of systematic uncertainty on the jet mass prediction is presented in Table 4 in Sec-
 546 tion 4.4.3.

547 The predicted M_J^Σ distributions for validation and signal regions with ≥ 4 or 5 jets are shown in Fig-
 548 ures 31, 32 33 and 34. For all signal regions, the observed distribution beyond $M_J^\Sigma > 0.6$ TeV is blinded.

549 Table 10 shows the predicted background yields in four different signal regions with a number of M_J^Σ cuts,
 550 which are used to determine the optimal signal region selection.

Not reviewed, for internal circulation only

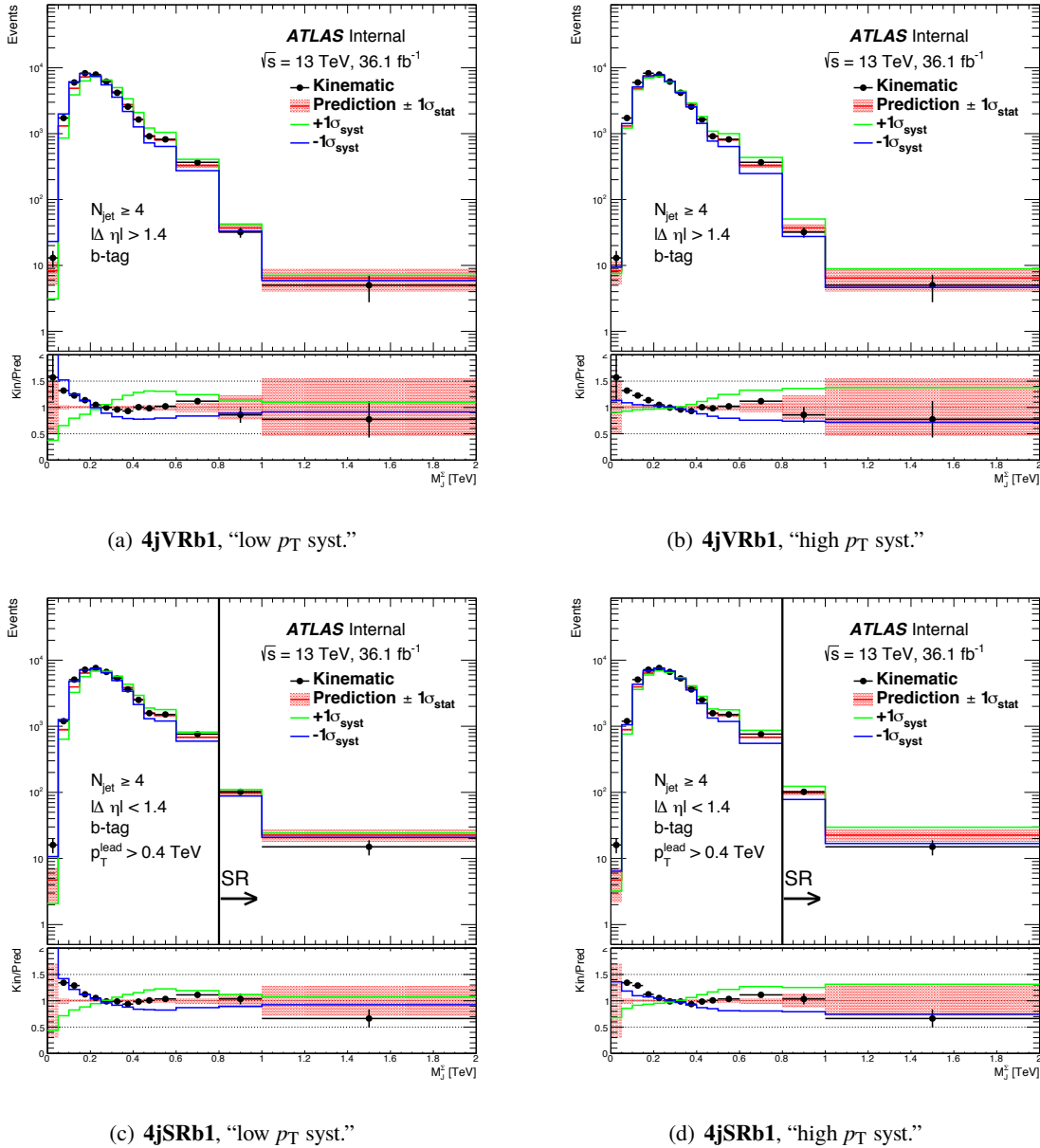


Figure 31: $M_j^\Sigma \geq 0.6 \text{ TeV}$ blinded for SRs Predicted and observed M_j^Σ distributions in the 4-jet b-tag events in data. The two subfigures on the top row are from the **VR**, while the two subfigures on the bottom row are from the **SR**. Subfigures on the left column show the systematic variations of the “**low p_T** ” systematic uncertainty in the jet mass estimation, while subfigures on the right column show systematic variations of the “**high p_T** ” systematic uncertainty. For the same region (SR or VR), the observed data, nomination background prediction and its statistical uncertainty, are the same between subfigures showing different systematic variations.

Not reviewed, for internal circulation only

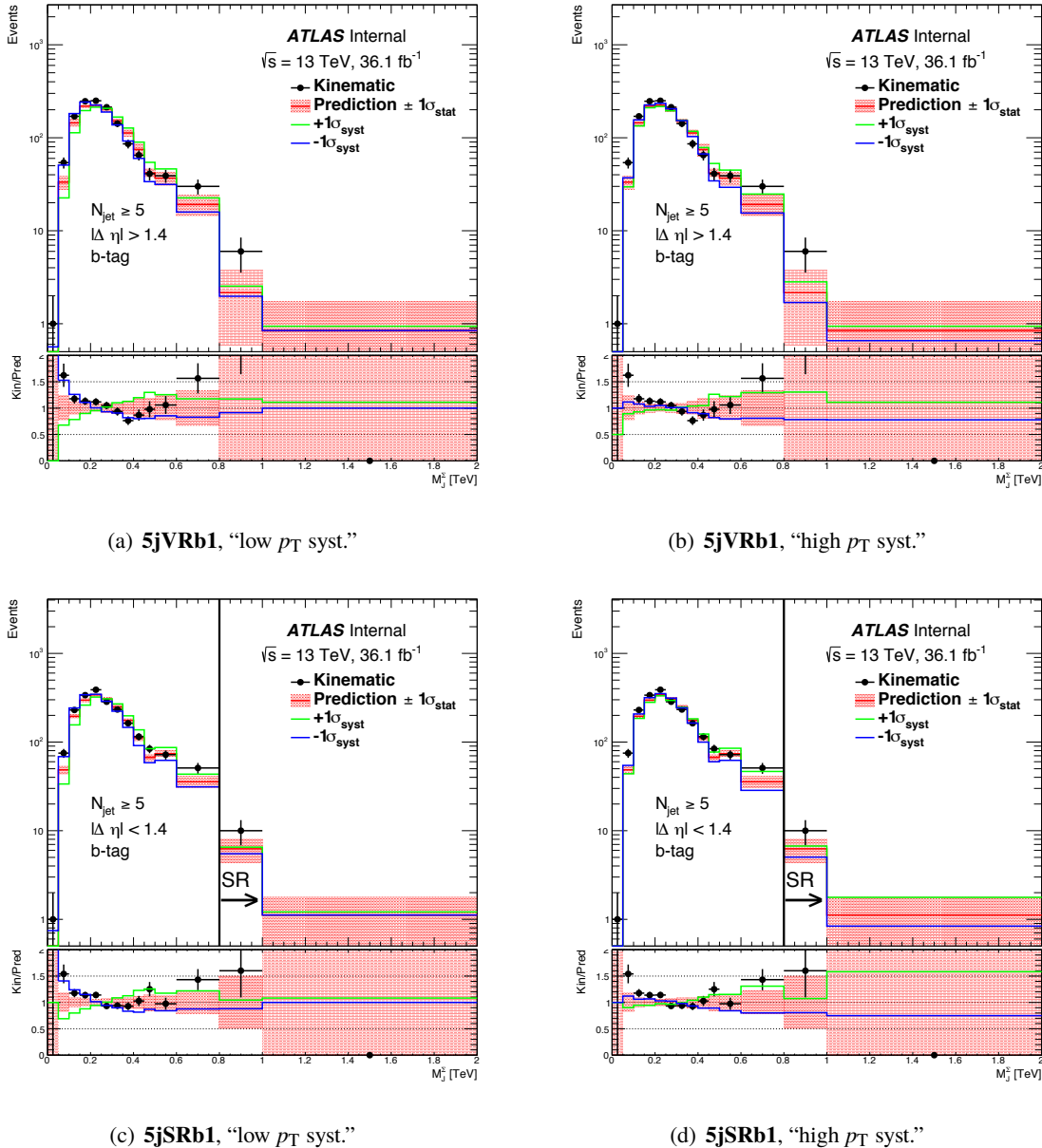


Figure 32: $M_j^\Sigma \geq 0.6$ TeV blinded for SRs Predicted and observed M_j^Σ distributions in the 5-jet b-tag events in data. The two subfigures on the top row are from the **VR**, while the two subfigures on the bottom row are from the **SR**. Subfigures on the left column show the systematic variations of the “**low p_T** ” systematic uncertainty in the jet mass estimation, while subfigures on the right column show systematic variations of the “**high p_T** ” systematic uncertainty. For the same region (SR or VR), the observed data, nomination background prediction and its statistical uncertainty, are the same between subfigures showing different systematic variations.

Not reviewed, for internal circulation only

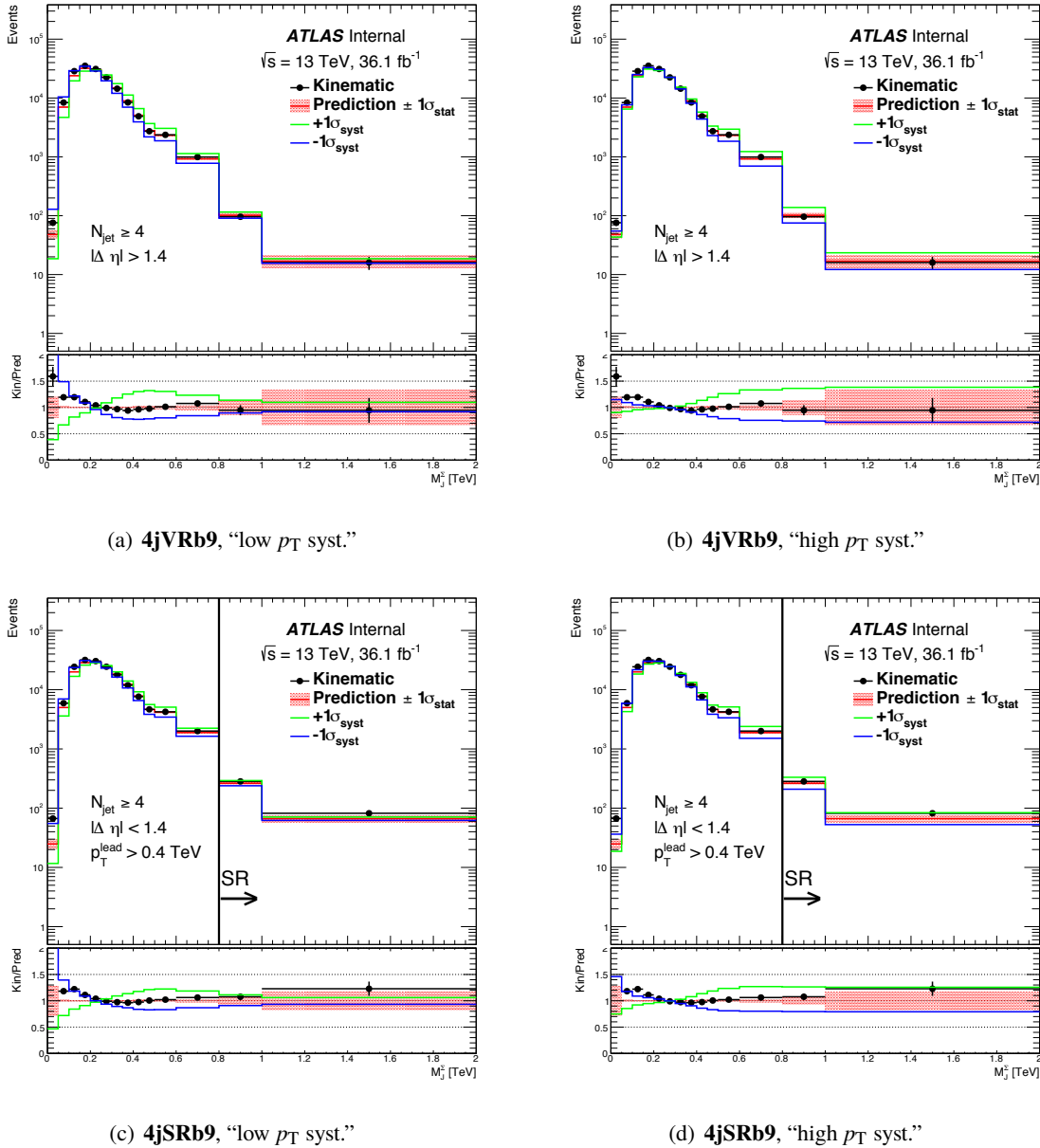


Figure 33: $M_j^\Sigma \geq 0.6$ TeV blinded for SRs Predicted and observed M_j^Σ distributions in the 4-jet b-tag events in data. The two subfigures on the top row are from the **VR**, while the two subfigures on the bottom row are from the **SR**. Subfigures on the left column show the systematic variations of the “**low p_T** ” systematic uncertainty in the jet mass estimation, while subfigures on the right column show systematic variations of the “**high p_T** ” systematic uncertainty. For the same region (SR or VR), the observed data, nomination background prediction and its statistical uncertainty, are the same between subfigures showing different systematic variations.

Not reviewed, for internal circulation only

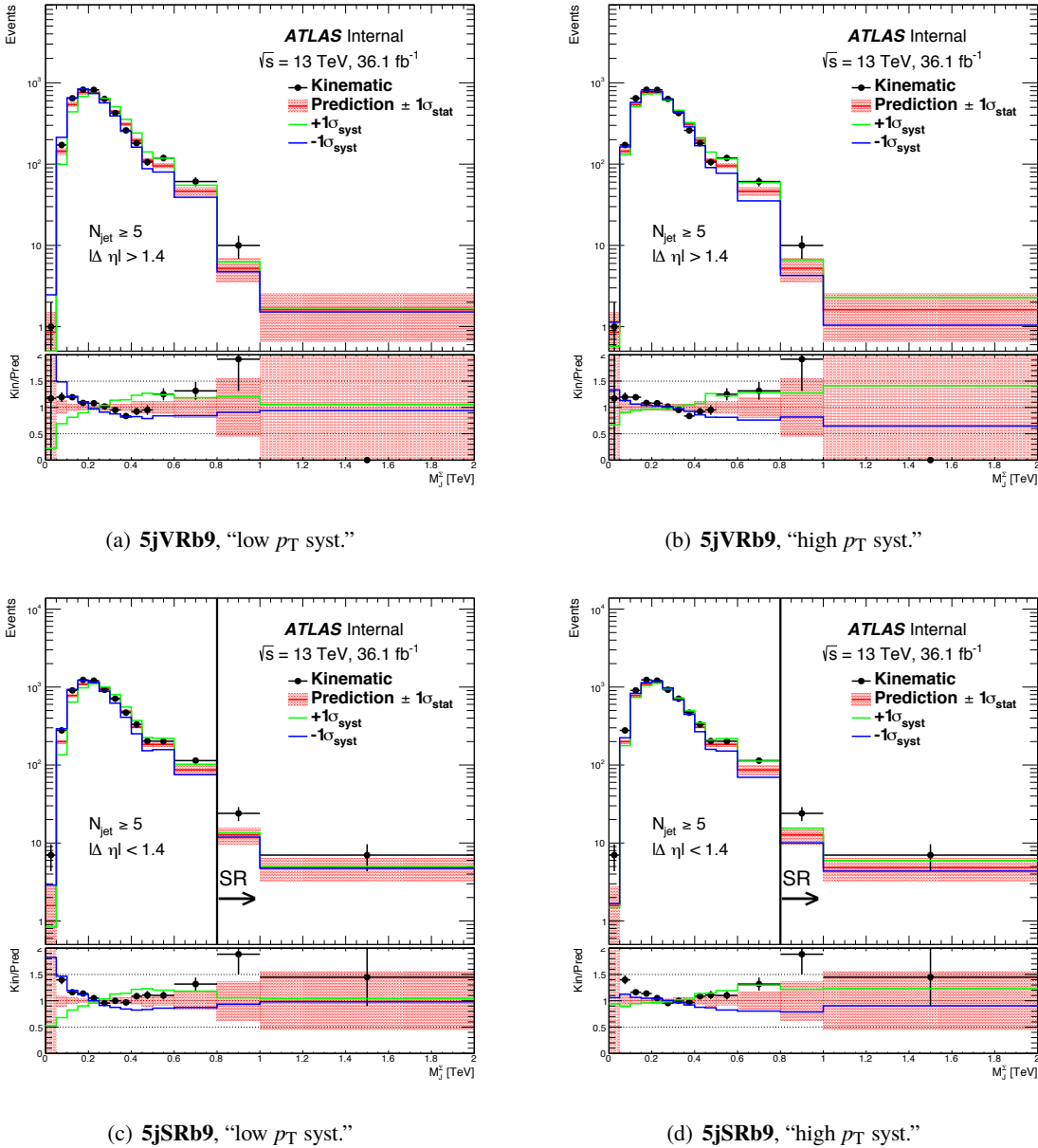


Figure 34: $M_j^\Sigma \geq 0.6$ TeV blinded for SRs Predicted and observed M_j^Σ distributions in the 5-jet b-tag events in data. The two subfigures on the top row are from the **VR**, while the two subfigures on the bottom row are from the **SR**. Subfigures on the left column show the systematic variations of the “**low p_T** ” systematic uncertainty in the jet mass estimation, while subfigures on the right column show systematic variations of the “**high p_T** ” systematic uncertainty. For the same region (SR or VR), the observed data, nomination background prediction and its statistical uncertainty, are the same between subfigures showing different systematic variations.

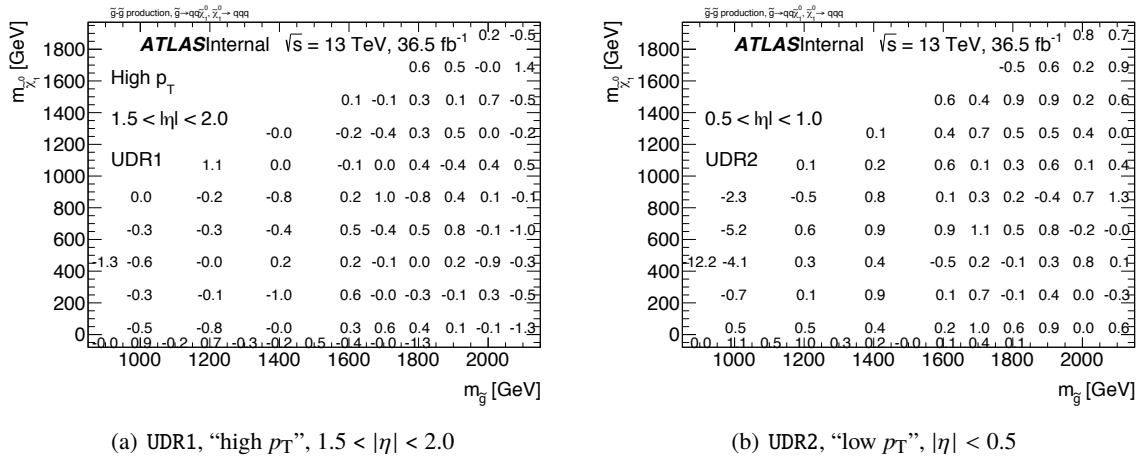


Figure 35: Variation in the jet mass prediction uncertainty due to the injection of signal events. (a) shows the “high p_T ” region of UDR1, with jets in $1.5 < |\eta| < 2.0$, and (b) shows the “low p_T ” region of UDR2, with jets in $|\eta| < 0.5$. The entry shown in the plot represents the change in the jet mass prediction uncertainty normalized to the nominal uncertainty, and this change is shown in percentage, i.e., the absolute change in the systematic uncertainty is the product of the entry shown in here and the uncertainty shown in Table 4.

551 4.7. Signal contamination

552 The presence of signal events in the data sample may impact both the central value and the uncertainty of
 553 the predicted background yields.

554 To understand the impact on the jet mass prediction uncertainty, a series of signal injection tests are
 555 performed. In each injection test, a signal MC sample corresponding to a particular 10-quark model or
 556 6-quark model is injected to data and the background estimation procedure is carried out. The jet mass
 557 prediction uncertainty is determined in the data sample injected with signal events, and the uncertainty is
 558 compared to the uncertainty determined without signal contamination. Figure 35 shows the variation in
 559 two regions as example, and the full set of plots can be found in the Appendix F. It is evident that the jet
 560 mass prediction uncertainty is not affected by the presence of signal events.

561 The signal contamination of the kinematic sample may bias the predicted background yield due to the
 562 differences in the observables (p_T , $|\eta|$, and b-tag, etc.) used to bin jets in the control region between the
 563 signal events and background events. The level of signal contamination can be studied with signal Monte
 564 Carlo samples. The jet mass PDFs as well as the uncertainties determined from data are applied to the
 565 kinematic sample of signal events. The predicted yield in the signal region represents the bias due to the
 566 presence of signal events, which can vary from signal point to signal point because of the differences in
 567 signal cross section as well as kinematics.

568 Tables 11 and 12 show the predicted event yield in the signal region of 5jSRb with an M_J^Σ cut of 0.8
 569 TeV due to the presence of signal event. This number is compared to the predicted background yield of
 570 7.0 events presented in Section 4.5. In the statistics interpretation, this contribution can be accounted in
 571 the likelihood function when a specific signal hypothesis is tested. Specifically, the event yield expectation

DSID	$m_{\tilde{g}}$	$m_{\tilde{\chi}}$	Δb	f_{sig}	f_{bkg}
403550	700	450	2.58	0.05	0.36
403551	800	450	3.14	0.06	0.44
403552	900	450	3.31	0.05	0.47
403553	1000	50	4.18	0.30	0.59
403554	1000	250	2.54	0.08	0.36
403555	1000	450	3.10	0.05	0.44
403556	1000	650	3.34	0.06	0.47
403557	1000	850	3.26	0.08	0.46
403558	1200	50	3.39	0.32	0.48
403559	1200	250	3.16	0.12	0.45
403560	1200	450	2.99	0.06	0.42
403561	1200	650	3.85	0.06	0.55
403562	1200	850	2.97	0.05	0.42
403563	1200	1050	2.69	0.10	0.38
403564	1400	50	2.41	0.45	0.34
403565	1400	250	2.16	0.16	0.30
403566	1400	450	2.60	0.08	0.37
403567	1400	650	2.98	0.06	0.42
403568	1400	850	2.88	0.06	0.41
403569	1400	1050	2.53	0.07	0.36
403570	1400	1250	2.18	0.12	0.31
403571	1600	50	1.55	0.45	0.22
403572	1600	250	1.57	0.18	0.22
403573	1600	450	1.89	0.10	0.27
403574	1600	650	2.10	0.08	0.30
403575	1600	850	2.18	0.07	0.31
403576	1600	1050	2.06	0.07	0.29
403577	1600	1250	1.75	0.08	0.25
403578	1600	1450	1.50	0.15	0.21

Table 11: Table of Δb , the predicted event yield in the signal region of 5jSRb with an M_j^Σ cut of 0.8 TeV due to the presence of signal event (**Part one**). Also shown here are f_{bkg} , the predicted yield normalized to the total predicted yield in data, and f_{sig} , the predicted yield normalized to the total signal yield.

Not reviewed, for internal circulation only

DSID	$m_{\tilde{g}}$	$m_{\tilde{\chi}}$	Δb	f_{sig}	f_{bkg}
403579	1700	50	1.28	0.49	0.18
403580	1700	250	1.26	0.21	0.18
403581	1700	450	1.39	0.11	0.19
403582	1700	650	1.65	0.09	0.23
403583	1700	850	1.76	0.08	0.25
403584	1700	1050	1.68	0.07	0.24
403585	1700	1250	1.59	0.08	0.22
403586	1700	1450	1.29	0.11	0.18
403587	1800	50	.98	0.48	0.14
403588	1800	250	1.01	0.21	0.14
403589	1800	450	1.18	0.13	0.16
403590	1800	650	1.36	0.10	0.19
403591	1800	850	1.42	0.09	0.20
403592	1800	1050	1.39	0.08	0.19
403593	1800	1250	1.36	0.09	0.19
403594	1800	1450	1.19	0.11	0.17
403595	1800	1650	.90	0.18	0.12
403597	1900	250	.74	0.23	0.10
403598	1900	450	.91	0.15	0.13
403599	1900	650	1.05	0.11	0.15
403601	1900	1050	1.14	0.09	0.16
403602	1900	1250	1.06	0.09	0.15
403603	1900	1450	.96	0.10	0.13
403615	2000	50	.53	0.56	0.07
403616	2000	250	.59	0.26	0.08
403617	2000	450	.66	0.16	0.09
403618	2000	650	.78	0.13	0.11
403619	2000	850	.85	0.11	0.12
403620	2000	1050	.86	0.10	0.12
403621	2000	1250	.85	0.10	0.12
403622	2000	1450	.79	0.11	0.11
403624	2000	1850	.52	0.20	0.07
403626	2100	250	.41	0.27	0.05
403627	2100	450	.49	0.17	0.07
403628	2100	650	.57	0.15	0.08
403629	2100	850	.64	0.13	0.09
403982	2100	1250	.66	0.11	0.09
403983	2100	1450	.61	0.11	0.08
403984	2100	1650	.55	0.13	0.07

Table 12: Table of Δb , the predicted event yield in the signal region of 5jSRb with an M_J^Σ cut of 0.8 TeV due to the presence of signal event (**Part two**). Also shown here are f_{bkg} , the predicted yield normalized to the total predicted yield in data, and f_{sig} , the predicted yield normalized to the total signal yield.

572 is written as

$$\lambda = \mu \times s + b \quad (2)$$

573 where s and b are expected signal yield and expected background yield, respectively; μ is the signal
 574 strength. When the contribution to the expected background yield from the presence of signal events, Δb
 575 is considered, Equation 2 becomes

$$\lambda = \mu \times s + b - \mu \times \Delta b \quad (3)$$

$$\lambda = \mu \times (s - \Delta b) + b. \quad (4)$$

576 Equation 4 indicates that the effect of the signal contamination is equivalent to a reduction of the expected
 577 signal yield. The ratio of Δb over the expected signal yield, f_{sig} , is also shown in Tables 11 and 12 for
 578 various signal points, in the region of 5jSRb with an M_J^Σ cut of > 0.8 TeV. For signal points with relatively
 579 large $m_{\tilde{\chi}}$, the contamination corresponds to $\approx 10\%$ level of reduction in the expected signal yield. For
 580 signal points with $m_{\tilde{\chi}} < 450$ GeV, the reduction can be significant, ranging from $\approx 16\%$ at $m_{\tilde{\chi}} = 450$ GeV
 581 to $\approx 45\%$ at $m_{\tilde{\chi}} = 50$ GeV. This effect needs to be taken into account when the M_J^Σ cut is optimized.

582 The numbers corresponding to other signal regions or a different M_J^Σ cut are also available [in the svn](#).

583 5. Signal systematic uncertainties

584 A number of systematic uncertainties affect the prediction of signal yield. Samples with systematic
 585 variations are generated following various performance group recommendations (see Appendix R for
 586 details). The uncertainty on the predicted signal yield is evaluated by comparing the nominal signal
 587 sample with signal samples with systematic variations. While Tables 17 and 18 provide a breakdown of
 588 the systematic uncertainty values evaluated for the signal region (5jSRb) with an M_J^Σ cut of 0.8 TeV for
 589 various signal samples, main findings of the systematic uncertainty study are summarized here.

- 590 • **b-tagging uncertainty** is found to have an impact on the expected signal yield at the level of 15%
 591 - 20% for signal regions with a b-jet requirement.
- 592 • **largeR jet uncertainty** has four components. The uncertainty of the **baseline** component ranges
 593 from $\approx 10\%$ at $m_{\tilde{g}} = 1.0$ TeV to $\approx 4\%$ at $m_{\tilde{g}} = 2.0$ TeV. The **modeling** component ranges from $\approx 6\%$
 594 at $m_{\tilde{g}} = 1.0$ TeV to $\approx 3\%$ at $m_{\tilde{g}} = 2.0$ TeV. The **statistical** component ranges from $\approx 8\%$ at $m_{\tilde{g}} =$
 595 1.0 TeV to $\approx 5\%$ at $m_{\tilde{g}} = 2.0$ TeV. The **tracking** component ranges from $\approx 17\%$ at $m_{\tilde{g}} = 1.0$ TeV to
 596 $\approx 9\%$ at $m_{\tilde{g}} = 2.0$ TeV.
- 597 • **luminosity uncertainty** is found to be 3.2 % for the 2015 and 2016 data sets.
- 598 • **Jet energy scale and resolution uncertainties.** The jet energy scale uncertainty is found to have
 599 negligible impact on the predicted signal yield, so is the jet energy resolution uncertainty. Therefore,
 600 these two uncertainties are not included in the final statistical interpretation.

Not reviewed, for internal circulation only

- **Pile-up effect on jets** are found to have negligible impact on the analysis, and therefore not included in the final statistical interpretation.
- **PDF, α_s , QCD scale uncertainties** are evaluated by checking the variation of truth level signal acceptance when varying these configurations are changed. Specifically, the PDF uncertainty is calculated using the event internal weights of the PDFset NNPDF 3.0; the QCD scale and α_s uncertainties are calculated by varying these parameters in the event generation.

The breakdown of each systematic uncertainty for all the RPV signal points are documented in the Appendix I. Table ?? summarizes the expected signal yield and its total systematic uncertainty at 36.1 fb^{-1} .

DSID	$m_{\tilde{g}}$	$m_{\tilde{\chi}_1^0}$	4jSRb, MJ > 1.0 TeV	4jSR, MJ > 1.0 TeV	5jSRb, MJ > 0.8 TeV	5jSR, MJ > 0.8 TeV
403553	1000	50	22.1 ± 8.4	36.2 ± 13.0	13.8 ± 5.1	24.7 ± 8.4
403554	1000	250	37.7 ± 16.5	54.7 ± 22.0	28.4 ± 9.6	42.7 ± 15.4
403555	1000	450	73.2 ± 22.5	89.6 ± 27.4	52.5 ± 18.6	59.9 ± 21.1
403556	1000	650	90.2 ± 32.1	114.1 ± 39.3	54.6 ± 20.5	64.3 ± 23.4
403557	1000	850	48.8 ± 19.6	59.6 ± 23.9	40.1 ± 15.1	47.9 ± 18.0
403558	1200	50	15.4 ± 5.2	26.6 ± 9.8	10.6 ± 3.8	16.8 ± 5.3
403559	1200	250	36.4 ± 12.1	49.3 ± 16.5	25.7 ± 8.6	33.6 ± 10.5
403560	1200	450	61.1 ± 18.9	78.9 ± 22.6	45.1 ± 13.8	59.7 ± 16.7
403561	1200	650	74.8 ± 23.5	96.7 ± 30.7	63.5 ± 20.3	77.0 ± 23.3
403562	1200	850	67.4 ± 20.8	84.8 ± 24.9	53.7 ± 16.3	68.0 ± 20.2
403563	1200	1050	40.5 ± 12.8	52.6 ± 15.9	26.7 ± 8.2	32.7 ± 9.6
403564	1400	50	9.9 ± 3.1	17.0 ± 4.8	5.3 ± 1.5	9.0 ± 2.7
403565	1400	250	21.9 ± 6.1	31.5 ± 8.5	12.9 ± 4.0	19.3 ± 5.8
403566	1400	450	36.9 ± 9.1	49.5 ± 11.8	30.1 ± 8.0	40.2 ± 10.6
403567	1400	650	49.4 ± 11.3	61.3 ± 14.2	42.8 ± 10.8	51.4 ± 13.3
403568	1400	850	51.3 ± 11.7	64.7 ± 14.8	46.4 ± 11.4	58.3 ± 14.1
403569	1400	1050	43.2 ± 9.7	55.1 ± 12.7	35.8 ± 9.6	43.6 ± 11.8
403570	1400	1250	24.6 ± 7.1	30.7 ± 9.1	17.6 ± 5.1	22.0 ± 6.3
403571	1600	50	6.3 ± 1.7	10.9 ± 3.0	3.4 ± 1.1	5.9 ± 1.8
403572	1600	250	13.3 ± 3.2	18.7 ± 4.5	8.7 ± 2.6	11.7 ± 3.3
403573	1600	450	22.5 ± 4.4	29.4 ± 5.8	17.3 ± 4.1	22.2 ± 5.4
403574	1600	650	26.2 ± 4.9	34.1 ± 6.4	24.1 ± 4.7	31.7 ± 6.1
403575	1600	850	30.6 ± 5.7	39.8 ± 7.3	29.9 ± 5.2	37.4 ± 6.4
403576	1600	1050	30.1 ± 6.0	38.1 ± 7.4	27.7 ± 5.4	35.0 ± 6.9
403577	1600	1250	25.1 ± 4.8	32.1 ± 5.8	21.0 ± 4.4	26.6 ± 5.4
403578	1600	1450	14.0 ± 3.3	18.3 ± 4.1	9.6 ± 2.6	12.5 ± 3.4
403579	1700	50	4.9 ± 1.3	8.1 ± 2.1	2.6 ± 0.7	4.3 ± 1.2
403580	1700	250	9.7 ± 2.0	13.5 ± 2.7	5.9 ± 1.4	8.4 ± 2.0
403581	1700	450	15.9 ± 2.8	21.0 ± 3.7	11.7 ± 2.5	15.5 ± 3.4
403582	1700	650	20.0 ± 3.4	25.3 ± 4.4	17.8 ± 3.1	22.6 ± 3.8
403583	1700	850	22.0 ± 3.6	27.9 ± 4.6	21.7 ± 3.8	26.9 ± 4.8
403584	1700	1050	22.6 ± 3.5	28.5 ± 4.4	22.1 ± 3.6	27.5 ± 4.7
403585	1700	1250	21.0 ± 3.3	26.3 ± 4.2	18.9 ± 3.8	23.4 ± 4.6
403586	1700	1450	14.8 ± 2.8	19.2 ± 3.5	10.9 ± 2.4	13.8 ± 2.9
403587	1800	50	3.4 ± 0.8	5.9 ± 1.4	2.0 ± 0.6	3.4 ± 1.0

Not reviewed, for internal circulation only

403588	1800	250	7.4 ± 1.4	10.1 ± 1.9	4.7 ± 1.1	6.5 ± 1.4
403589	1800	450	12.0 ± 2.1	15.8 ± 2.7	8.9 ± 1.6	11.5 ± 2.1
403590	1800	650	14.8 ± 2.2	19.1 ± 2.8	13.0 ± 2.0	16.5 ± 2.6
403591	1800	850	16.3 ± 2.2	20.6 ± 2.8	15.6 ± 2.2	19.6 ± 2.8
403592	1800	1050	16.6 ± 2.4	21.3 ± 3.0	16.0 ± 2.3	20.3 ± 2.9
403593	1800	1250	16.5 ± 2.3	20.8 ± 2.9	15.0 ± 2.2	19.0 ± 2.8
403594	1800	1450	12.9 ± 2.1	16.7 ± 2.7	10.7 ± 2.0	13.7 ± 2.5
403595	1800	1650	7.6 ± 1.4	10.1 ± 2.0	4.9 ± 1.1	6.6 ± 1.4
403596	1900	50	2.6 ± 0.6	4.6 ± 1.0	1.3 ± 0.3	2.3 ± 0.6
403597	1900	250	5.4 ± 0.9	7.4 ± 1.2	3.1 ± 0.7	4.4 ± 1.0
403598	1900	450	8.5 ± 1.2	11.2 ± 1.6	6.0 ± 1.0	7.9 ± 1.3
403599	1900	650	10.3 ± 1.4	13.3 ± 1.8	9.0 ± 1.3	11.4 ± 1.6
403600	1900	850	11.7 ± 1.4	14.9 ± 1.8	11.0 ± 1.5	13.7 ± 1.8
403601	1900	1050	12.0 ± 1.5	15.3 ± 1.9	11.8 ± 1.5	15.1 ± 1.8
403602	1900	1250	11.8 ± 1.5	15.1 ± 1.9	11.2 ± 1.4	14.2 ± 1.7
403603	1900	1450	10.4 ± 1.4	13.4 ± 1.8	8.8 ± 1.3	11.3 ± 1.6
403604	1900	1650	7.5 ± 1.1	9.7 ± 1.5	5.5 ± 0.9	7.1 ± 1.2
403615	2000	50	1.9 ± 0.4	3.3 ± 0.6	0.9 ± 0.2	1.6 ± 0.4
403616	2000	250	3.8 ± 0.6	5.2 ± 0.9	2.2 ± 0.4	3.1 ± 0.6
403617	2000	450	5.8 ± 0.8	7.7 ± 1.0	4.0 ± 0.6	5.2 ± 0.8
403618	2000	650	7.2 ± 0.9	9.3 ± 1.1	5.9 ± 0.8	7.5 ± 1.0
403619	2000	850	7.8 ± 0.9	10.0 ± 1.1	7.5 ± 0.9	9.5 ± 1.1
403620	2000	1050	8.3 ± 1.0	10.8 ± 1.2	8.2 ± 0.9	10.3 ± 1.1
403621	2000	1250	8.3 ± 0.9	10.7 ± 1.1	8.0 ± 1.0	10.2 ± 1.2
403622	2000	1450	7.9 ± 0.9	10.1 ± 1.2	7.0 ± 0.9	8.9 ± 1.1
403623	2000	1650	6.3 ± 0.8	8.3 ± 1.0	5.0 ± 0.7	6.5 ± 0.9
403624	2000	1850	3.7 ± 0.6	5.0 ± 0.9	2.5 ± 0.5	3.4 ± 0.7
403625	2100	50	1.3 ± 0.3	2.3 ± 0.5	0.7 ± 0.2	1.2 ± 0.3
403626	2100	250	2.6 ± 0.4	3.7 ± 0.5	1.5 ± 0.3	2.1 ± 0.4
403627	2100	450	4.0 ± 0.5	5.4 ± 0.6	2.8 ± 0.4	3.6 ± 0.5
403628	2100	650	4.7 ± 0.5	6.1 ± 0.7	3.8 ± 0.4	4.9 ± 0.6
403629	2100	850	5.3 ± 0.6	6.9 ± 0.7	4.9 ± 0.5	6.3 ± 0.6
403981	2100	1050	5.8 ± 0.5	7.4 ± 0.7	5.5 ± 0.5	7.0 ± 0.7
403982	2100	1250	5.8 ± 0.6	7.4 ± 0.7	5.7 ± 0.6	7.2 ± 0.7
403983	2100	1450	5.6 ± 0.5	7.3 ± 0.7	5.1 ± 0.5	6.6 ± 0.6
403984	2100	1650	4.8 ± 0.5	6.4 ± 0.7	4.1 ± 0.5	5.3 ± 0.6
403985	2100	1850	3.5 ± 0.5	4.7 ± 0.6	2.6 ± 0.4	3.4 ± 0.5
403605	900	-	29.6 ± 14.4	41.9 ± 19.4	16.4 ± 8.0	21.8 ± 10.2
403606	1000	-	20.6 ± 7.9	26.9 ± 11.1	17.7 ± 7.5	20.5 ± 8.6
403607	1100	-	27.6 ± 9.1	33.3 ± 11.4	15.3 ± 5.9	18.8 ± 7.5
403608	1200	-	20.8 ± 7.3	27.1 ± 9.5	13.6 ± 5.6	19.1 ± 7.5
403609	1300	-	15.6 ± 4.8	21.5 ± 6.3	10.9 ± 3.7	14.1 ± 4.8
403610	1400	-	13.6 ± 4.2	18.1 ± 5.4	8.8 ± 2.4	11.2 ± 3.1
403611	1500	-	10.4 ± 2.9	14.2 ± 3.9	6.5 ± 1.9	9.1 ± 2.5
403612	1600	-	8.2 ± 1.9	11.0 ± 2.6	6.1 ± 1.7	7.6 ± 2.1
403613	1700	-	6.2 ± 1.7	8.2 ± 2.2	3.7 ± 1.0	4.9 ± 1.3
403614	1800	-	4.8 ± 1.0	6.7 ± 1.4	2.8 ± 0.7	3.9 ± 1.0

Region	$\geq M_J^\Sigma$ [TeV]	Observed	Expected (\pm (Stat.) \pm (High p_T) \pm (Low p_T))
5jSRb	0.8	10	$7.0 \pm 2.4 \pm 1.9 \pm .7$
5jSR	0.8	31	$18.0 \pm 3.7 \pm 4.6 \pm 1.5$
4jSRb	1.0	15	$23.6 \pm 4.6 \pm 6.1 \pm 1.7$
4jSR	1.0	82	$68.2 \pm 7.6 \pm 15.8 \pm 4.4$

Table 14: Predicted and observed yields in various search regions in data for a number of different M_J^Σ cuts

6. Results

This section presents the following results. First, p-values of observed data in the four signal regions are reported. Second, the model-dependent limits on the 10-quark and 6-quark models are presented. The model-dependence in the likelihood model is primarily resulted from the correction term due to the signal contamination, although signal systematic uncertainties also contribute to a lesser extent. For the 10-quark model, the limit is presented as exclusion contours on the $m_{\tilde{g}}\text{-}m_{\tilde{\chi}}$ grid; for the 6-quark model, the limit is set on the cross section times branching ratio as a function of $m_{\tilde{g}}$. Third, model-independent limits are reported for the four signal regions, assuming no contribution to the background expectation from signal contaminations. This is a reasonable assumption given that no signal events are observed in data. The limits are set on the cross section times efficiency times acceptance.

As explained in Section 4.3, four overlapping signal regions are investigated. For each signal region, a M_J^Σ cut is determined so that the sensitivity to RPV signals is maximized, and the region with the best sensitivity is chosen for the model-dependent interpretation. Table 10 presents the predicted background yields in these signal regions for a number of candidate M_J^Σ cuts.

In general, signal regions with a b-tag requirement perform better for the RPV signal models, and they are used for model-dependent interpretation. The 5jSRb with an M_J^Σ cut of > 0.8 TeV is found to be the most sensitive signal region for most 10-quark models and all 6-quark models, while 5jSR with an M_J^Σ cut of > 0.8 TeV is found to be the most sensitive signal region for RPV signals with $m_{\tilde{\chi}} = 50$ GeV.

Model-independent limit and p-value are reported for all four signal regions. For 4j signal regions, $M_J^\Sigma > 1.0$ TeV is found to be most sensitive to RPV signal models and therefore is chosen as the cut used for the model-independent interpretation.

6.1. Summary of unblinded M_J^Σ distributions and event yields in the SRs

Figure 37 shows the predicted and observed M_J^Σ distributions in signal regions, and Figure 36 shows the predicted and observed M_J^Σ distributions in validation regions.

Table 14 summarizes the predicted and observed event yields in the signal regions.

Not reviewed, for internal circulation only

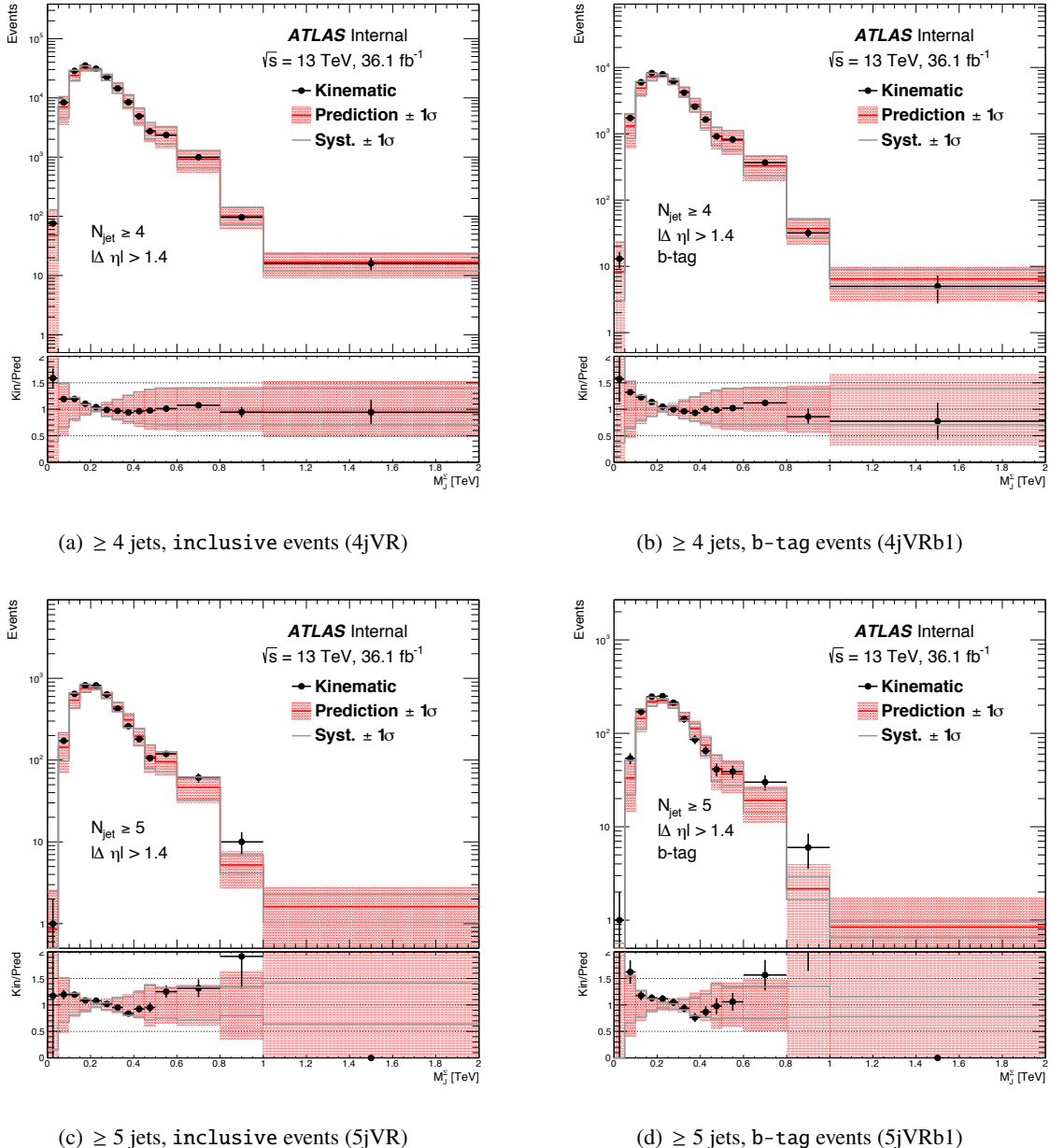


Figure 36: Predicted (solid line) and observed (dots) M_j^Σ distributions for validation regions 4jVR (a), 4jVRb1 (b), 5jVR (c), and 5jVRb1 (d). The shaded area surrounding the predicted M_j^Σ distribution represents the systematic uncertainty of the background estimation, predicted M_j^Σ distribution, and the residual p_T -dependent uncertainty. The predicted M_j^Σ distribution is normalized to data in $0.2 \text{ TeV} < M_j^\Sigma < 0.6 \text{ TeV}$, where expected contamination from signals of gluino direct or cascade decay models not excluded by the Run-1 analysis [1] is negligible compared to the background statistical uncertainty. The expected contribution from two RPV signal samples are also shown.

Not reviewed, for internal circulation only

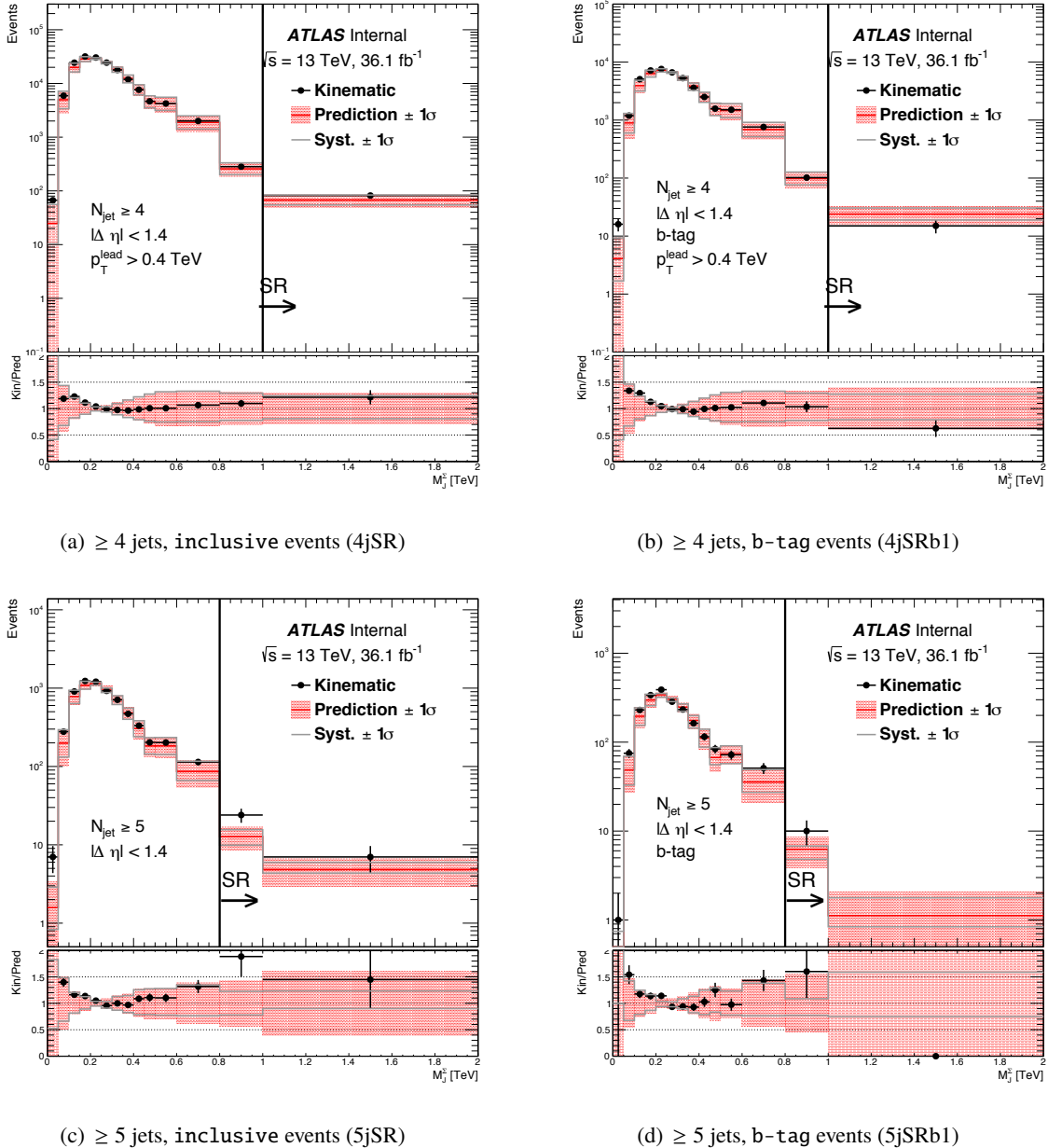


Figure 37: Predicted (solid line) and observed (dots) M_J^Σ distributions for signal regions 4jSR (a), 4jSRb1 (b), 5jSR (c), and 5jSRb1 (d). The shaded area surrounding the predicted M_J^Σ distribution represents the systematic uncertainty of background estimation. The predicted M_J^Σ distribution is normalized to data in $0.2 \text{ TeV} < M_J^\Sigma < 0.6 \text{ TeV}$, where expected contamination from signals of gluino direct or cascade decay models not excluded by the Run-1 analysis [1] is negligible compared to the background statistical uncertainty. The expected contribution from two RPV signal samples are also shown.

635 6.2. Likelihood function and statistical interpretation procedure

636 A frequentist approach is used to interpret data. A likelihood is built from the event yield expectation and
 637 observation in the signal region, and the associated systematic uncertainties. In a given inclusive n_{jet} bin,
 638 the expected event yield in the signal region can be written as:

$$\lambda = \mu \prod_i (1 + \theta_i \sigma_i) S_0 + B_0 \prod_j (1 + \theta_{b,j} \sigma_{b,j}) \quad (5)$$

639 where S_0 is the nominal signal yield, μ is the signal strength parameter, i is the index that labels signal
 640 systematic uncertainty, θ_i is the nuisance parameter associated with the systematic uncertainty i , σ_i is the
 641 size of the systematic uncertainty i , B_0 is the expected background yield predicted by the fit extrapolation,
 642 $\theta_{b,j}$ is the nuisance parameter associated with the background extrapolation uncertainty component j , and
 643 $\sigma_{b,j}$ is the size of the background extrapolation uncertainty component j .

644 Given an observed number of events k and the expected event yield λ , the likelihood function can be
 645 written as:

$$L(\mu) = P(k|\lambda) \prod_l G(0|\theta_l, 1) \quad (6)$$

646 where $P(k|\lambda)$ is the Poisson term of the event count and $G(0|\theta_l, 1)$ is the constraint term associated with
 647 a systematic uncertainty l . The standard procedure recommended in ATLAS uses LogNormal as the
 648 constraint term, which protects against large negative deviation of nuisance parameter in the case where
 649 the size of the uncertainty is large.

650 As discussed in Section 4.7, the background expectation receives a contribution from the presence of
 651 signal events and needs to be corrected. The event yield expectation (Eq. 5) then becomes

$$\lambda = \mu \left(\prod_i (1 + \theta_i \sigma_i) S_0 - \Delta b (1 + \theta_{b,stat} \sigma_{b,stat}) \right) + B_0 \prod_j (1 + \theta_{b,j} \sigma_{b,j}). \quad (7)$$

652 The correction is a negative term in the event yield expectation and scales with the signal strength μ , and
 653 therefore the effect of the signal contamination is equivalent to a reduction of the expected signal yield.
 654 The only uncertainty associated with the correction term is its statistical uncertainty, as the low p_T and
 655 high p_T jet mass prediction uncertainties, which are introduced to cover discrepancy between the true
 656 background yield and the expected background yield, do not apply.

$$q_\mu = -2 \ln \frac{L(\mu, \hat{\theta})}{L(\hat{\mu}, \hat{\theta})} \quad (8)$$

657 The Profile Likelihood Ratio (PLR) is shown in Eq. 8, and it is constructed by two maximum likelihood
 658 fits. The numerator of the PLR corresponds to a fit of the likelihood model to data, where the parameter of
 659 interest μ is fixed the value being tested; the denominator of the PLR corresponds to a fit where μ is free.
 660 In the limit setting procedure, a μ times signal plus background hypothesis is tested, and μ in the numerator
 661 of PLR is fixed to 1. Since the correction term is signal point dependent, the statistical test cannot yield
 662 a model independent limit on the number of signal events. However, in the p-value calculation, the
 663 hypothesis being tested is the background only hypothesis, i.e., $\mu = 0$, therefore the likelihood function
 664 does not have a model dependent contribution from the correction term. The model dependent correction
 665 term that appears in the denominator of the PLR does not affect the p-value calculation, as it only alters
 666 the total expected signal yield, which has no role in the p-value calculation.

Not reviewed, for internal circulation only

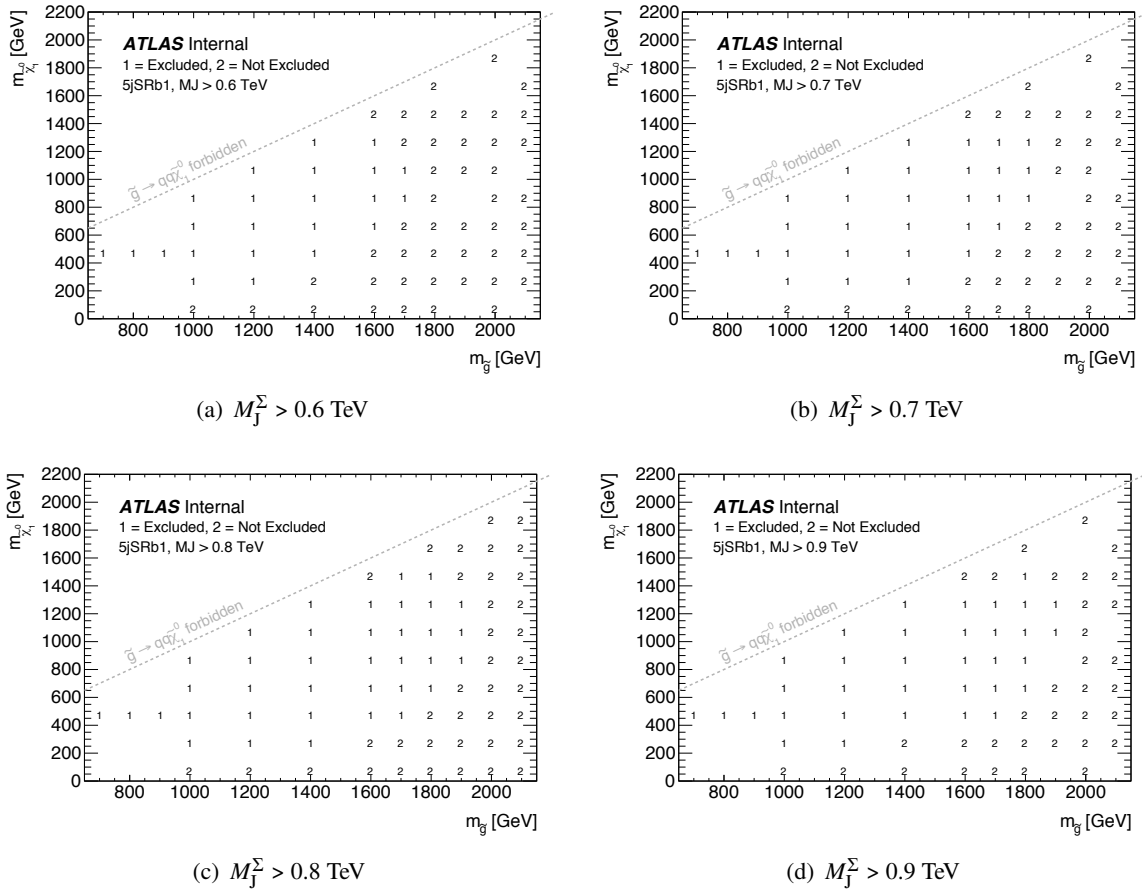


Figure 38: Expected exclusion for RPV 10-quark signal models. (a), (b), (c), and (d) show the result for $M_J^\Sigma > 0.6$ TeV, 0.7 TeV, 0.8 TeV, and 0.9 TeV, respectively. Results are available only for signal points where simulation samples exist.

This likelihood function, saved as `RooWorkspace` object is then passed to the `RooStats` package, to construct the profile likelihood ratio, which is used to calculate the p_0 -value and limit. Pseudo experiments are generated for calculating p_0 -value and limit. This procedure is implemented in a package that is previously used for $H \rightarrow \gamma\gamma$ and black hole multijet analyses. The package can be found in [research].

6.3. Expected sensitivity

Table 10 shows the predicted and observed event yields in various search regions. These results are used in the model dependent and model independent interpretations.

Figure 6.3 shows the expected exclusion for RPV 10-quark models with a number of candidate M_J^Σ cuts. The exclusion is only shown for signal points where simulated samples exist. The entries in the figure indicates whether or not the signal point is excluded at 95% CL. The best performance is achieved with $M_J^\Sigma > 0.8$ TeV cut, and the $M_J^\Sigma > 0.9$ TeV cut achieves slightly looser exclusion for $m_{\tilde{\chi}} = 250$ GeV signal points. For the 5jSRb, $M_J^\Sigma > 0.8$ TeV is adopted for the model dependent interpretation.

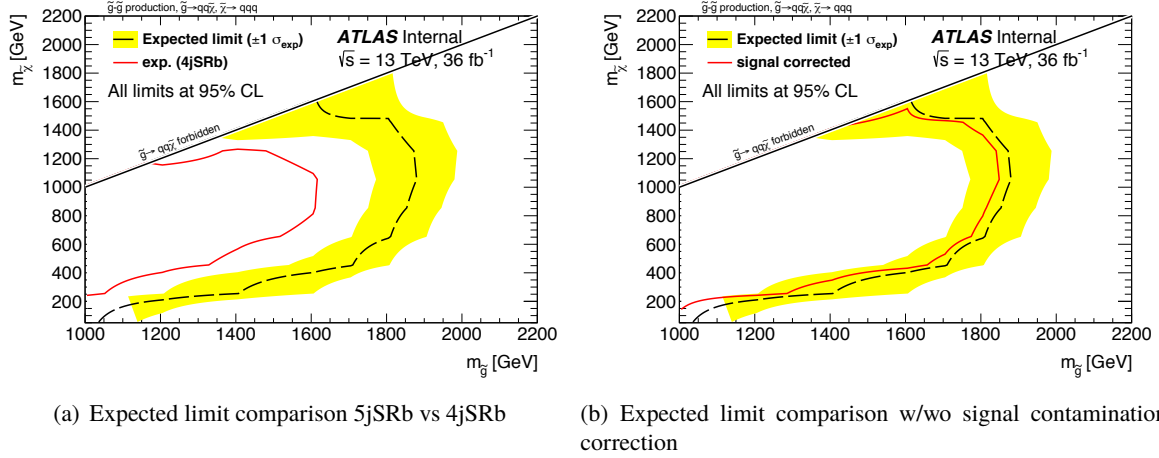


Figure 39: Expected 95% CL limit for the RPV 10-quark model. The signal region of 5jSRb combined with an $M_J^\Sigma > 0.8$ TeV cut is used for the interpretation. The long-dashed line indicates the expected limit, while the yellow area indicates its $\pm 1 \sigma$ variations. Figure (a) compares the results from 5jSRb with the expected limit from signal region of 4jSRb combined with an $M_J^\Sigma > 1.2$ TeV cut. Figure (b) compares the results from 5jSRb with the expected limit from the same signal region but accounting for a correction due to the signal contamination.

679 Figure 39(a) compares the results from 5jSRb with the expected limit from signal region of 4jSRb
 680 combined with an $M_J^\Sigma > 1.2$ TeV cut, which is found to be the most optimal for 4jSRb. This demonstrates
 681 that the 5jSRb is the most sensitive signal region for the 10-quark model, as found in the previous analysis
 682 ⁴. Figure 39(b) compares the results from 5jSRb with the expected limit from the same signal region but
 683 accounting for a correction due to the signal contamination. Since the correction of the signal contamination
 684 is essentially a reduction of the signal yield, the expected limit accounting for the signal contamination is
 685 slightly weaker than the one without accounting for the contamination.

686 6.4. Interpolation of result

687 Since simulated signal samples only exist for a limited number of points, an interpolation is needed to
 688 produce limit contours. In the ICHEP CONF note, a limit is set on the number of signal yield, the expected
 689 signal yield is interpolated in $m_{\tilde{g}}$ and $m_{\tilde{\chi}}$, and then the limit contour is drawn using the limit on the signal
 690 yield and the interpolated signal yield in $m_{\tilde{g}}$ and $m_{\tilde{\chi}}$.

691 This procedure is no longer applicable since the event expectation now includes a correction term that
 692 depends on the signal point and therefore the limit setting procedure needs to be performed at every signal
 693 point. Two interpolation procedures are studied. The results shown in the current note are based on an
 694 interpolation of the CL_s value in the $m_{\tilde{g}} - m_{\tilde{\chi}}$ plane (Figures 39(a) and 39(b)). Since the CL_s value variation
 695 as a function of $m_{\tilde{g}}$ and $m_{\tilde{\chi}}$ has a much larger slope compared to the yield variation, the interpolated
 696 contours are not smooth and show some artifact.

697 A new interpolation procedure is being developed. This procedure interpolates both the expected signal
 698 yield and the expected correction term in $m_{\tilde{g}}$ and $m_{\tilde{\chi}}$, and therefore create inputs for the statistical

⁴ Results shown in Figures 39(a) and 39(b) do not account for the correction of the signal contamination. They are presented to show the relative sensitivity between different setups

Signal Region	M_J^Σ cut	Expected limit (fb)	Observed Limit (fb)	p_0 -value
4jSRb	> 1.0 TeV	$0.53^{+0.20}_{-0.12}$	0.37	0.86
4jSR		$1.12^{+0.56}_{-0.32}$	1.50	0.24
5jSRb	> 0.8 TeV	$0.24^{+0.10}_{-0.06}$	0.34	0.26
5jSR		$0.43^{+0.08}_{-0.06}$	0.84	0.062

Table 15: Expected and observed limits on the signal production cross-section for the four signal regions, and p_0 -values of excesses in the 5-jet signal regions.

interpretation at a much finer $m_{\tilde{g}}$ and $m_{\tilde{\chi}}$ grid. Then the CL_s values are calculated on this fine $m_{\tilde{g}}$ and $m_{\tilde{\chi}}$ grid.

6.5. Unblinded statistical interpretation

The p-value is calculated for each of the four overlapping signal regions, in order to quantify the significance of an excess or deficit. The observed p-value does not depend on the signal model, and a test finds that the observed p-value calculated from likelihood models built using different signal hypotheses return the same p-value within numerical precision of RooFit. Table 15 shows the observed p-value in the four signal regions. The most significant excess is seen in 5jSR with a p-value of 0.062, corresponding to a statistical significance of 1.54σ . The 5jSRb and 4jSR saw small excess, and the 4jSRb saw a deficit at 1σ level.

Since no significant excess is seen in any of the four signal regions, limits are set on the production of RPV signals in the context of gluino direct and cascade decay models. The limit contours for the 10-quark model are derived from 5jSRb, with $M_J^\Sigma > 0.8$ TeV, while the limits for the 6-quark model are a combination of limits derived from 5jSRb with two different M_J^Σ cuts. For $m_{\tilde{g}} \leq 1050$ GeV, the limit is calculated from 5jSRb with $M_J^\Sigma > 0.6$ TeV, and for $m_{\tilde{g}} \geq 1050$ GeV, the limit is calculated from 5jSRb with $M_J^\Sigma > 0.8$ TeV.

For the 10-quark model, the exclusion on $m_{\tilde{g}}$ strongly depends on the $m_{\tilde{\chi}}$. Gluinos with a mass of less than 1920 GeV is excluded for a neutralino mass of 1050 GeV, and this constraint is weakened for heavier neutralino, an exclusion of $m_{\tilde{g}} < 1150$ GeV is achieved when the $m_{\tilde{\chi}}$ is very close to $m_{\tilde{g}}$. For light neutralinos down to 170 GeV, the exclusion only reaches $m_{\tilde{g}} = 1000$ GeV; and for neutralino with lighter masses no exclusion is achieved. The observed exclusion is weaker than the expected exclusion.

Figure 40 also shows the limit placed on the 6-quark model. The expected exclusion on $m_{\tilde{g}}$ is around 1150 GeV; however, due to the observed excess in the 5jSRb, the observed limit does not exclude any 6-quark signal considered in the analysis. The observed limit on the cross section of 6-quark model varies between 0.95 fb^{-1} at $m_{\tilde{g}} = 900$ GeV and 0.022 fb^{-1} at $m_{\tilde{g}} = 1800$ GeV. A comparison of the current limit on the 6-quark model and the limit reported in Ref. [25] is documented in the Appendix S.

Model independent limit is also reported. The signal correction term is removed from the likelihood model in the calculation of the model independent limit, so are signal theoretical uncertainties such as PDF and QCD scale uncertainties. A limit on the number of signal events in the signal region can be calculated and converted to a limit on the cross section times acceptance times efficiency. The experimental uncertainties also vary as a function of $m_{\tilde{g}}$ and $m_{\tilde{\chi}}$, and the largest signal uncertainties are chosen in the calculation. The expected and observed model independent limits are shown in Table 15.

Not reviewed, for internal circulation only

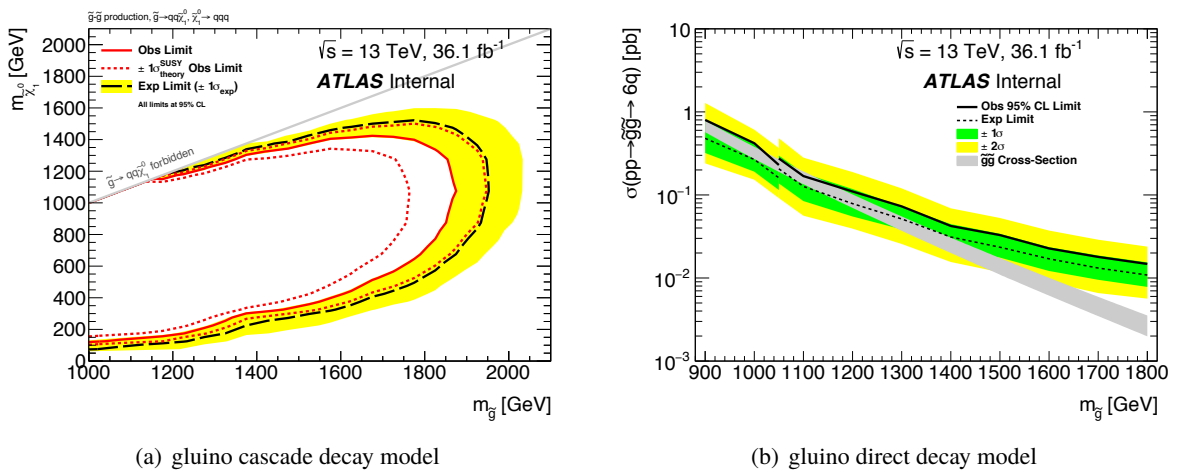


Figure 40: (a) Expected and observed exclusion limits in the $(m_{\tilde{g}}, m_{\tilde{\chi}})$ plane for the gluino cascade decay model. Limits are obtained by using the signal region with the best expected sensitivity for every signal point (5jSRb1 with $M_J^\Sigma > 0.6 \text{ TeV}$). The dashed black lines show the expected limits at 95% CL, with the light (yellow) bands indicating the 1σ excursions due to experimental uncertainties. Observed limits are indicated by medium dark (maroon) curves, where the solid contour represents the nominal limit, and the dotted lines are obtained by varying the signal cross-section by the renormalization and factorization scale and PDF uncertainties. The observed limit from the Run-1 analysis [1] is also shown as a solid line. (b) Expected and observed cross-section limits for the gluino direct decay model gluino models.

730 7. Conclusion

731 A search for *R*-Parity Violating SUSY signals in events with multiple jets is conducted. Distributions of
732 events as a function of total jet mass are examined. No significant excess is seen in any signal regions.
733 Limits are set on the production of gluinos in the gluino direct and cascade decay models in the UDD
734 scenarios of RPV SUSY. In the gluino cascade decay model, gluinos with masses up to 1000 GeV -
735 1920 GeV are excluded, depending on the neutralino mass; For the gluino direct decay model, the limit on
736 the cross section times branching ratio varies between 0.80 fb^{-1} at $m_{\tilde{g}} = 900 \text{ GeV}$ and 0.011 fb^{-1} at $m_{\tilde{g}} =$
737 1800 GeV . Model independent limits on the cross section of signal in the defined SRs are also reported.

738 Acknowledgements

739 **Appendix**

740 **A. M_J^Σ , p_T , and η distributions vs $m_{\tilde{\chi}}$**

741 This section presents plots that show how observables, e.g., M_J^Σ , p_T , and η vary between signal points
 742 with different $m_{\tilde{\chi}}$ but the same $m_{\tilde{g}}$.

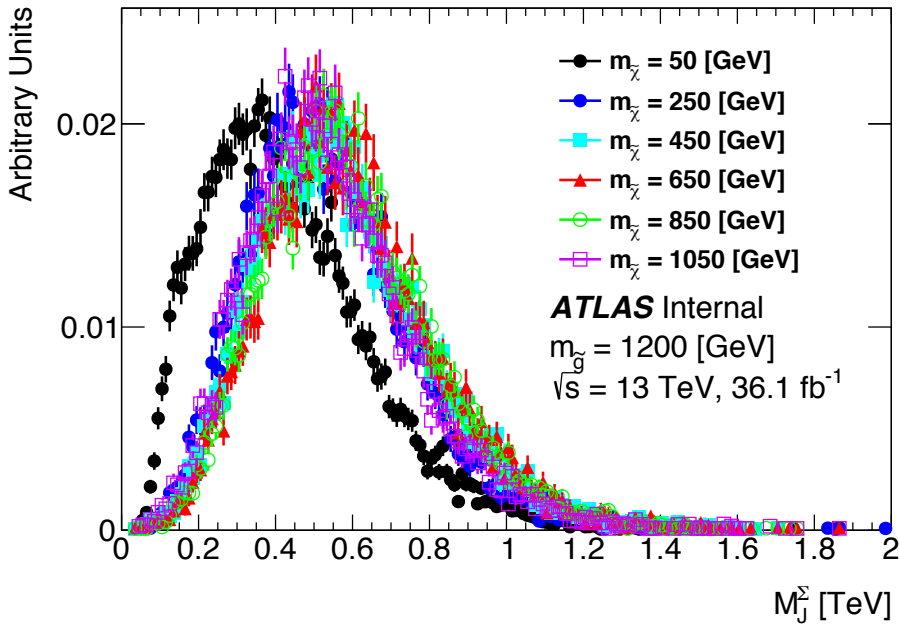


Figure 41: M_J^Σ distributions for RPV signals with $m_{\tilde{g}} = 1200$ GeV and different $m_{\tilde{\chi}}$.

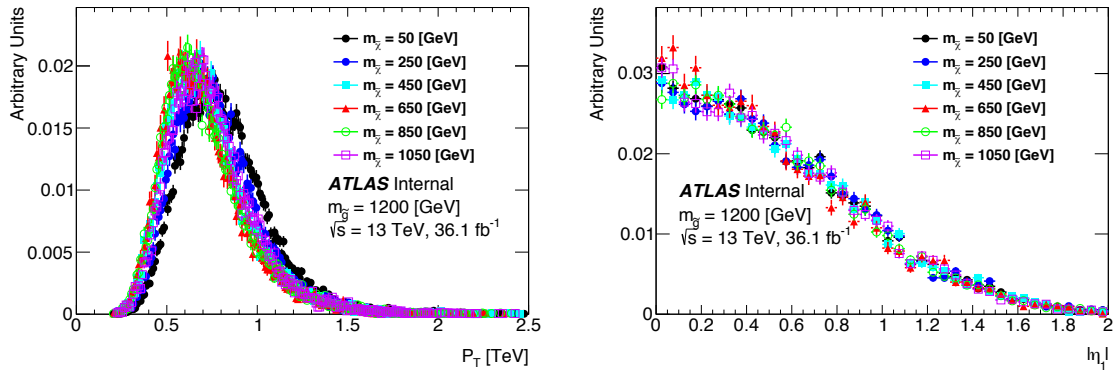


Figure 42: Leading jet p_T (left) and η (right) distributions for RPV signals with $m_{\tilde{g}} = 1200$ GeV and different $m_{\tilde{\chi}}$.

Not reviewed, for internal circulation only

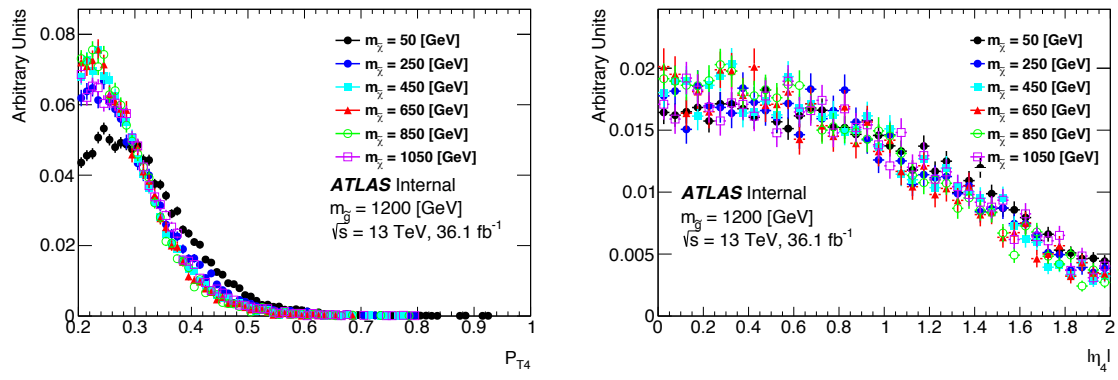


Figure 43: Fourth leading jet p_T (left) and η (right) distributions for RPV signals with $m_{\tilde{g}} = 1200$ GeV and different $m_{\tilde{\chi}}$.

Not reviewed, for internal circulation only

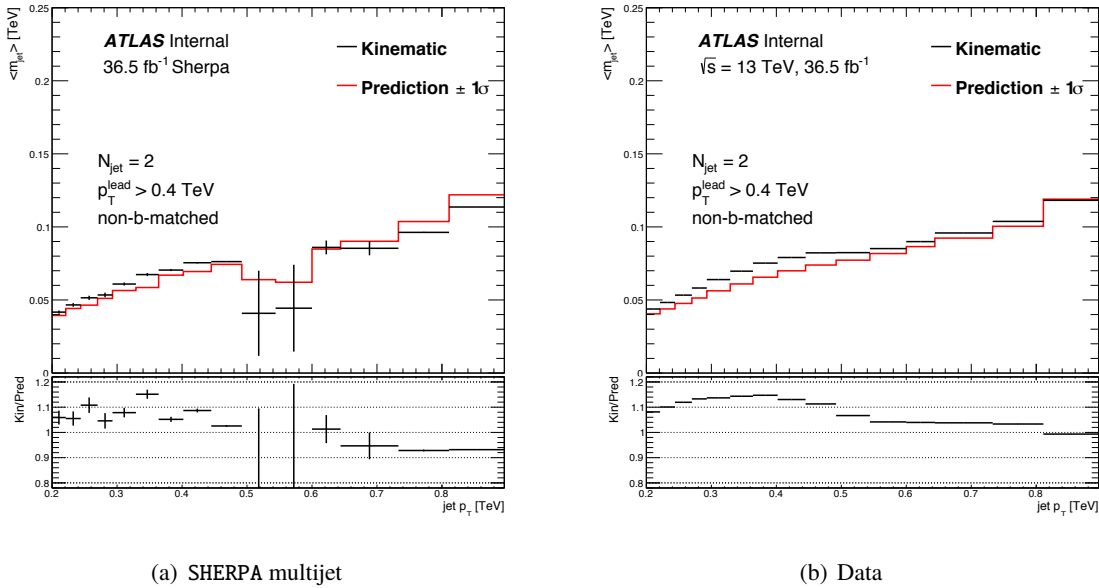


Figure 44: Jet mass response comparison in UDR1 with non-matched jets between SHERPA multijet sample(left) and data(right).

743 B. Background estimation result in Sherpa multijet sample

744 SHERPA multijet sample is studied in this analysis, but it is disfavored due to low MC statistics and
 745 mis-modeling data.

746 Figures 44 - 47 compare the jet mass response between the SHERPA multijet sample and data in
 747 UDR1 and UDR2, for non-matched jets and b-matched jets. In the sample with highest statisti-
 748 cs, the non-matched jetsample in the UDR1, SHERPA shows qualitatively similar behavior in the ratio
 749 of observation over prediction as data for the p_T range of < 500 GeV; for $p_T > 600$ GeV the discrepancy in
 750 SHERPA is opposite the one seen in data. For b-matched jets in the UDR1, the result in SHERPA sample
 751 is statistically inconclusive. For jets in the UDR2, SHERPA appears to show an under-prediction while the
 752 discrepancy in data is the opposite.

Not reviewed, for internal circulation only

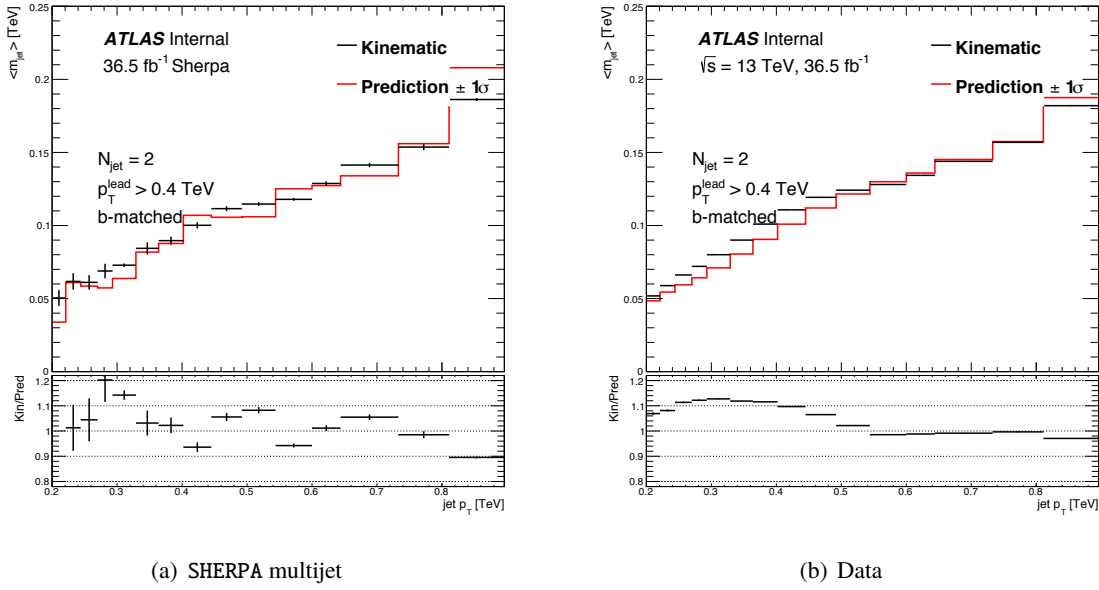


Figure 45: Jet mass response comparison in UDR1 with b-matched jets between SHERPA multijet sample(left) and data(right).

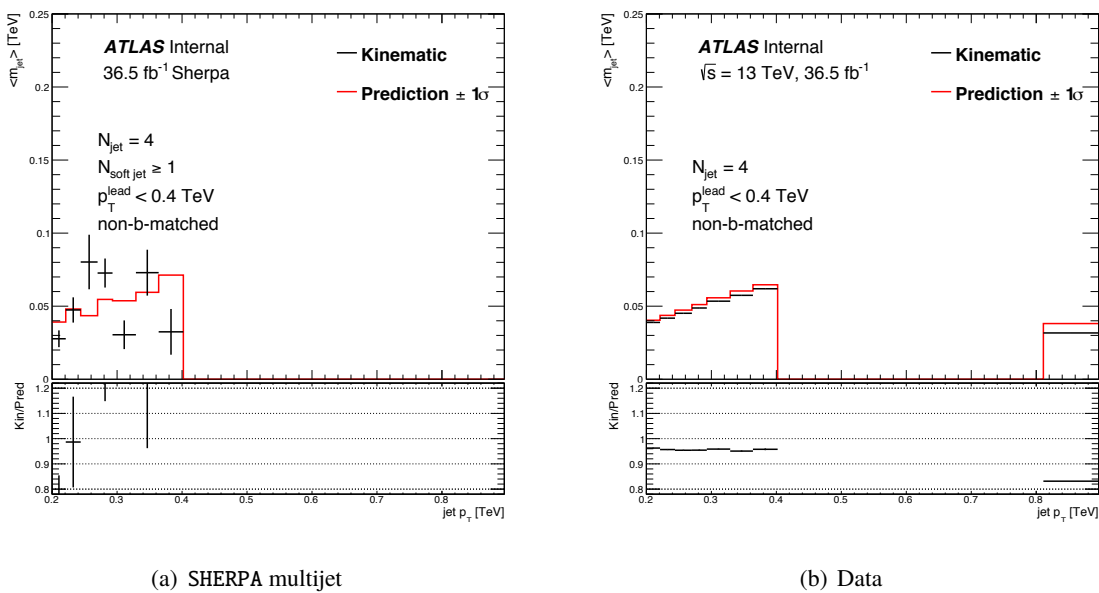


Figure 46: Jet mass response comparison in UDR2 with non-matched jets between SHERPA multijet sample(left) and data(right).

Not reviewed, for internal circulation only

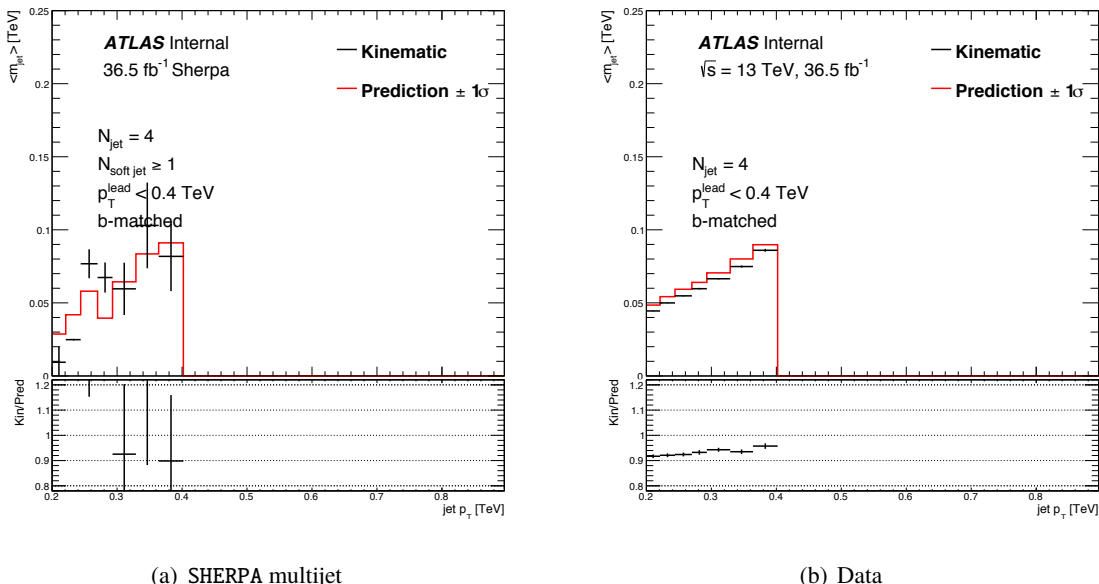


Figure 47: Jet mass response comparison in UDR2 with b-matched jets between SHERPA multijet sample(left) and data(right).

Not reviewed, for internal circulation only

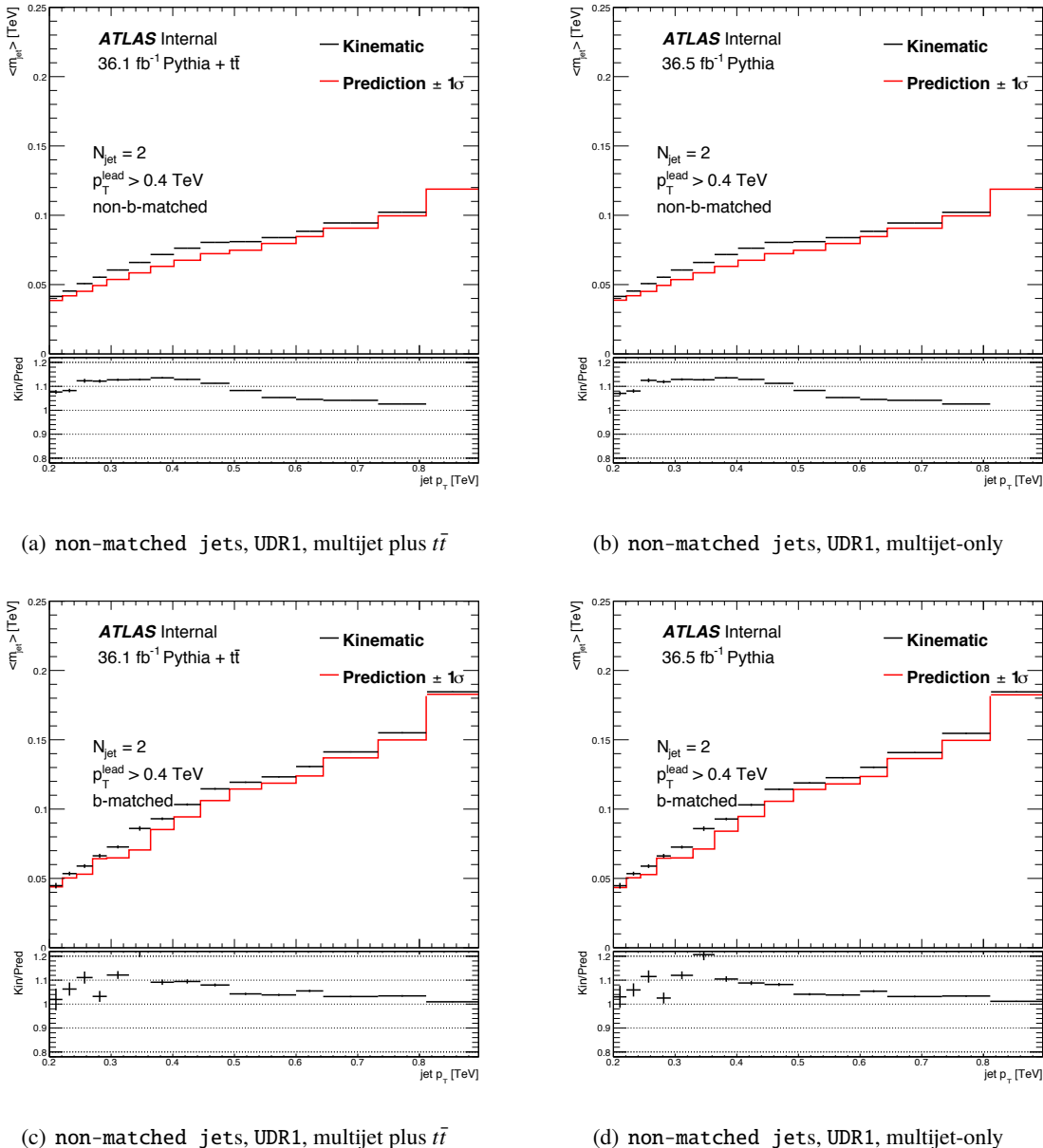


Figure 48: Jet mass response in the UDR1. Left column shows results from PYTHIA8 multijet plus $t\bar{t}$ sample; right column shows results from PYTHIA8 multijet sample only.

753 C. Impact of $t\bar{t}$ events on the background estimation performance

754 Jet mass response plots are compared between PYTHIA8 multijet only sample and PYTHIA8 multijet plus
 755 $t\bar{t}$ sample, for the UDR1 (Figure 48) and the UDR2 (Figure 49). It is shown that the presence of $t\bar{t}$ events
 756 does not change the jet mass prediction uncertainty in any significant way.

Not reviewed, for internal circulation only

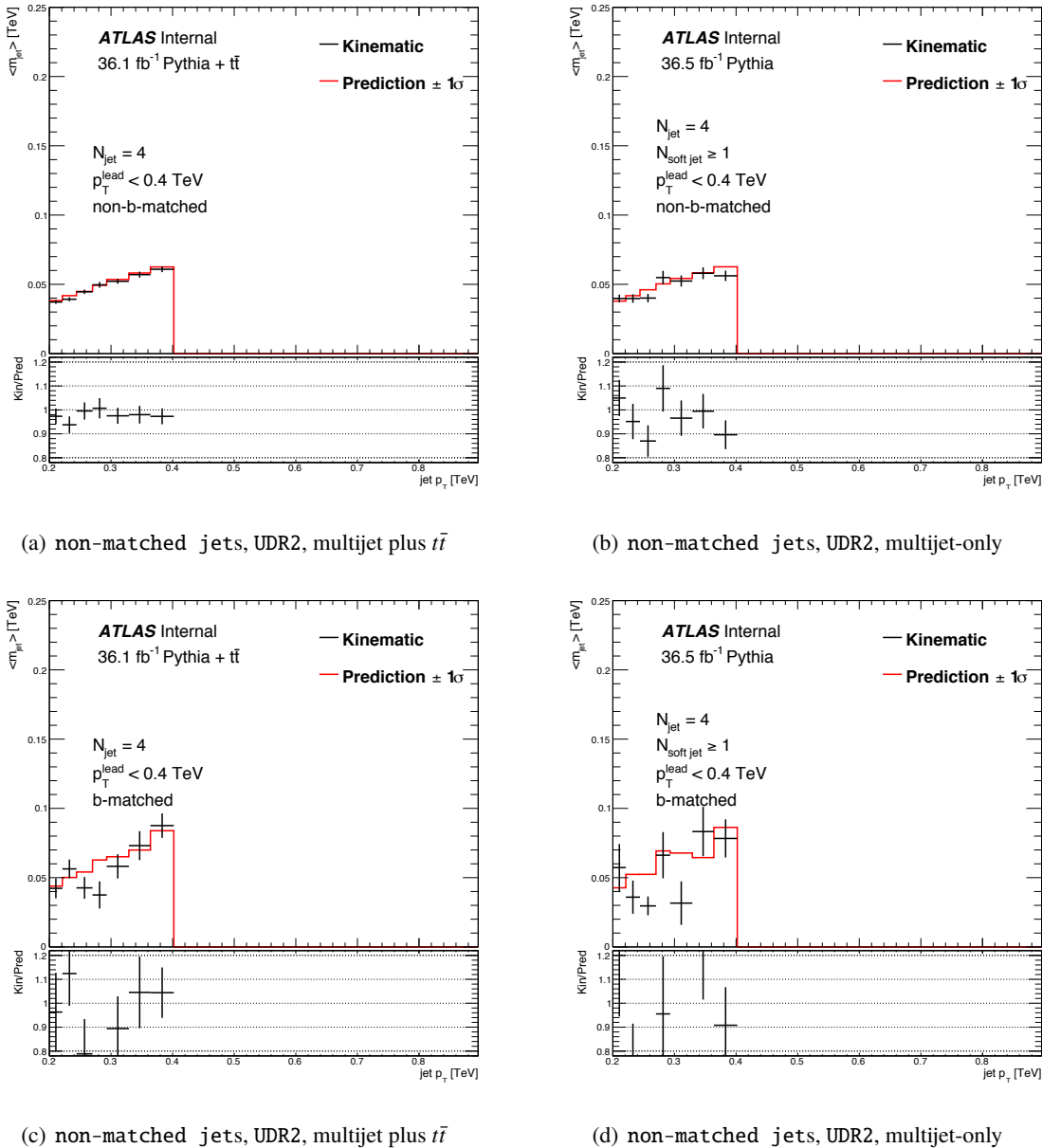


Figure 49: Jet mass response in the UDR2. Left column shows results from PYTHIA8 multijet plus $t\bar{t}$ sample; right column shows results from PYTHIA8 multijet sample only.

Not reviewed, for internal circulation only

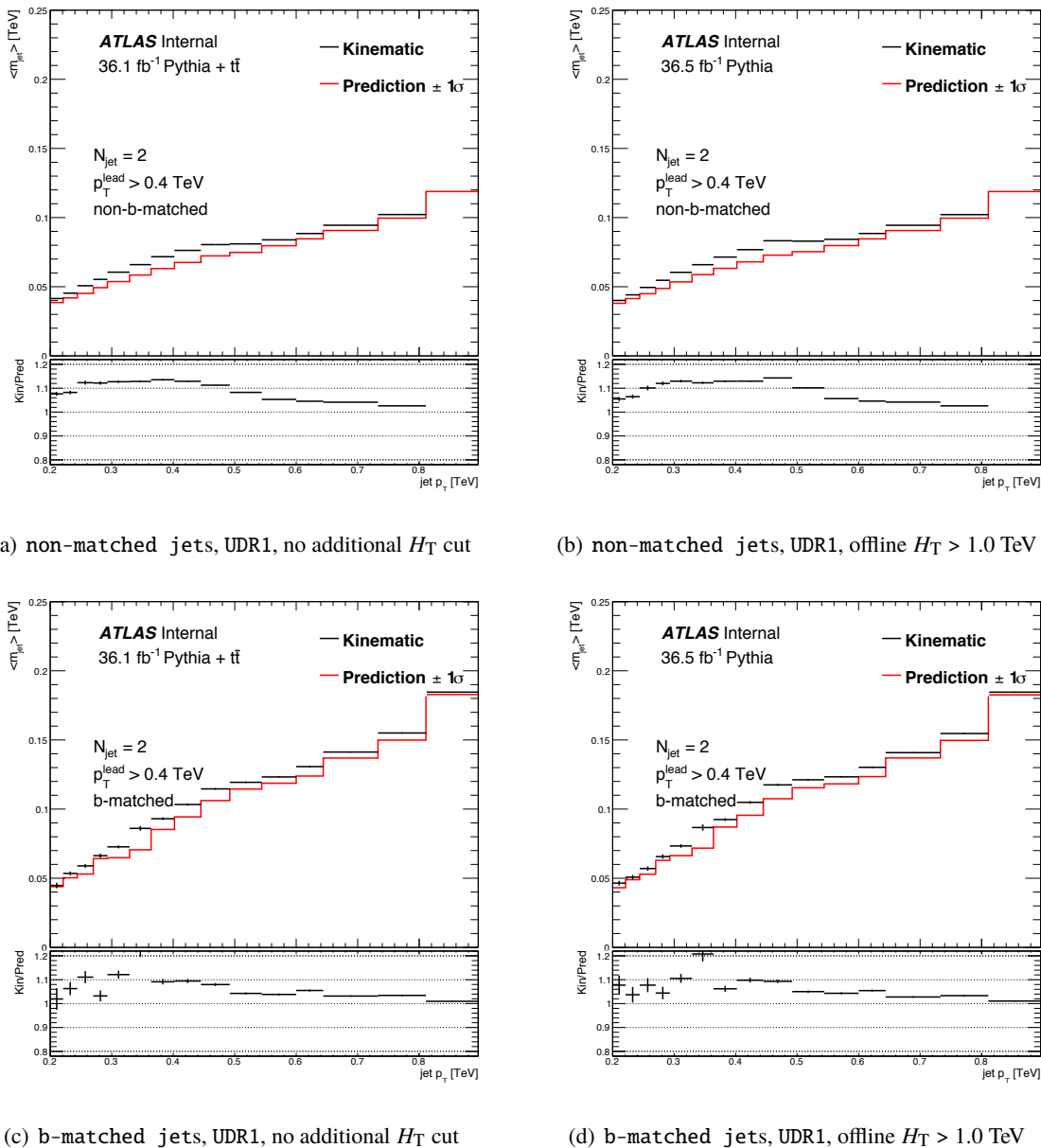


Figure 50: Jet mass response in the UDR1. Left column shows results from standard analysis of PYTHIA8 multijet plus $t\bar{t}$ MC sample; right column shows results from the analysis with additional offline cut of $H_T > 1.0$ TeV.

⁷⁵⁷ **D. Trigger impact on the UDR**

Not reviewed, for internal circulation only

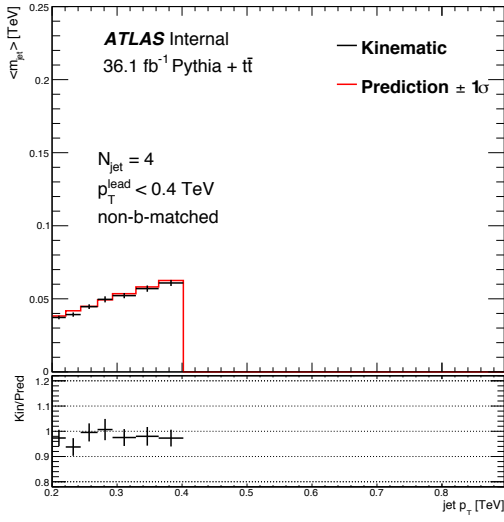
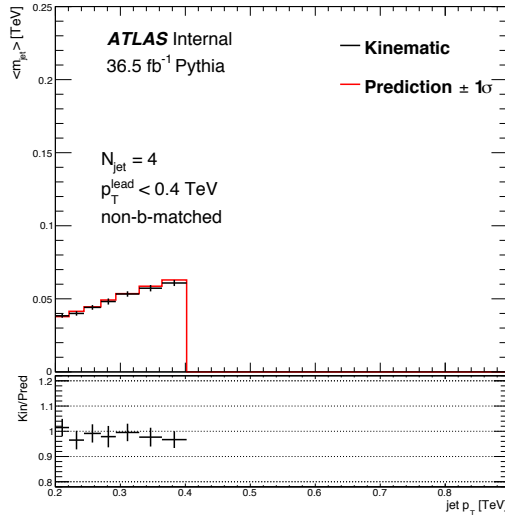
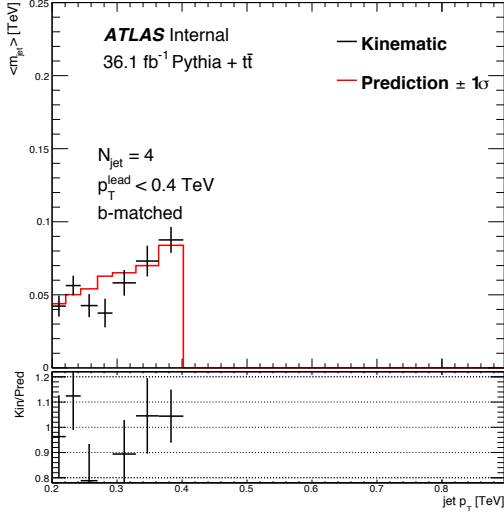
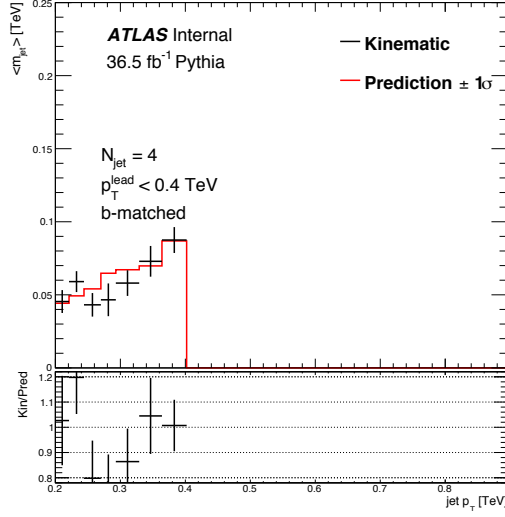
(a) non-matched jets, UDR2, no additional H_T cut(b) non-matched jets, UDR2, offline $H_T > 1.0 \text{ TeV}$ (c) b-matched jets, UDR2, no additional H_T cut(d) b-matched jets, UDR2, offline $H_T > 1.0 \text{ TeV}$

Figure 51: Jet mass response in the UDR2. Left column shows results from standard analysis of PYTHIA8 multijet plus t̄t MC sample; right column shows results from the analysis with additional offline cut of $H_T > 1.0 \text{ TeV}$.

Not reviewed, for internal circulation only

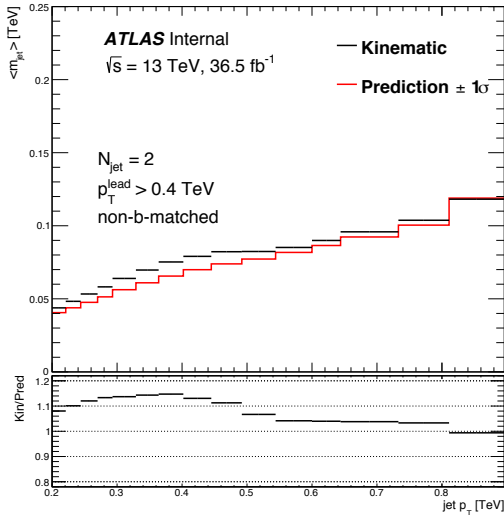
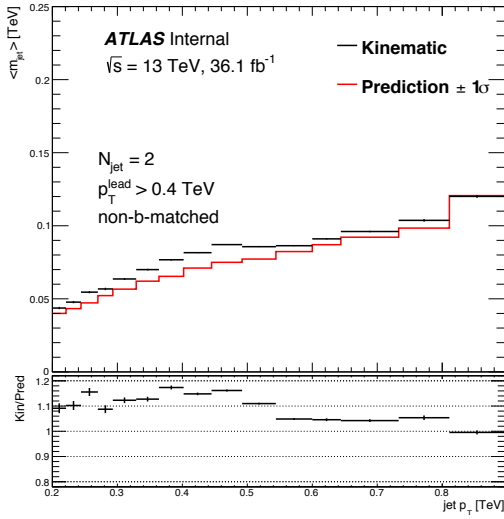
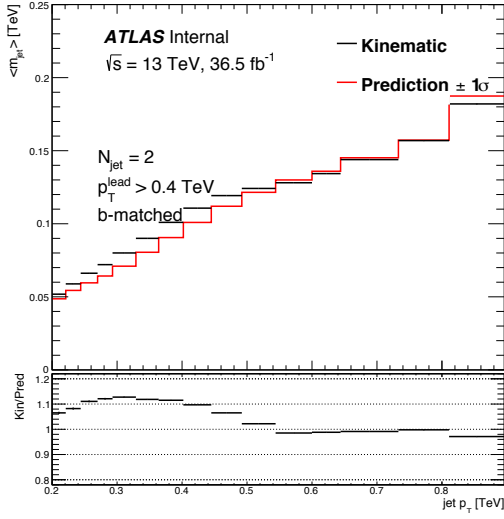
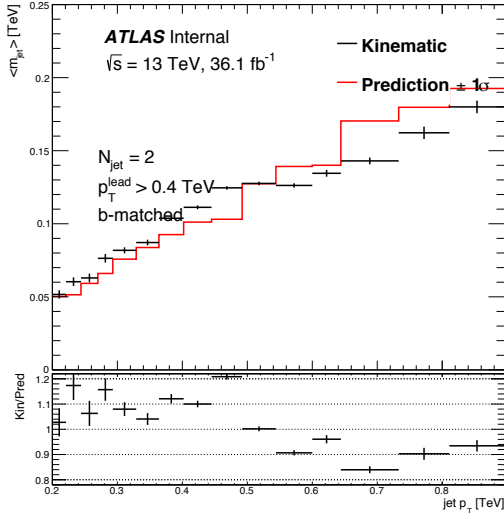
(a) non-matched jets, UDR1, no additional H_{T} cut(b) non-matched jets, UDR1, offline $H_{\text{T}} > 1.0 \text{ TeV}$ (c) b-matched jets, UDR1, no additional H_{T} cut(d) b-matched jets, UDR1, offline $H_{\text{T}} > 1.0 \text{ TeV}$

Figure 52: Jet mass response in the UDR1. Left column shows results from standard analysis of data; right column shows results from the analysis with additional offline cut of $H_{\text{T}} > 1.0 \text{ TeV}$.

Not reviewed, for internal circulation only

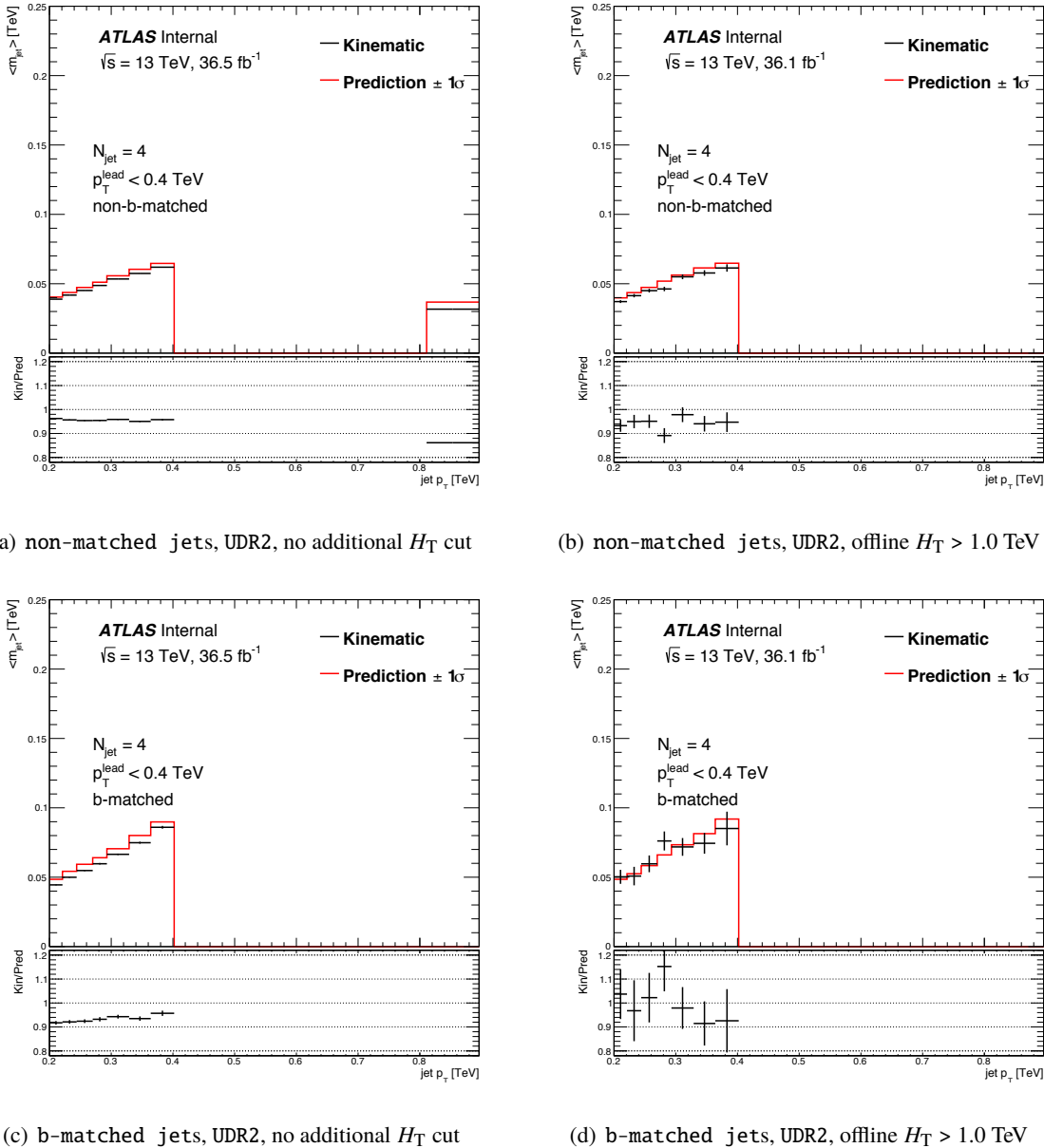


Figure 53: Jet mass response in the UDR2. Left column shows results from standard analysis of data; right column shows results from the analysis with additional offline cut of $H_T > 1.0$ TeV.

Not reviewed, for internal circulation only

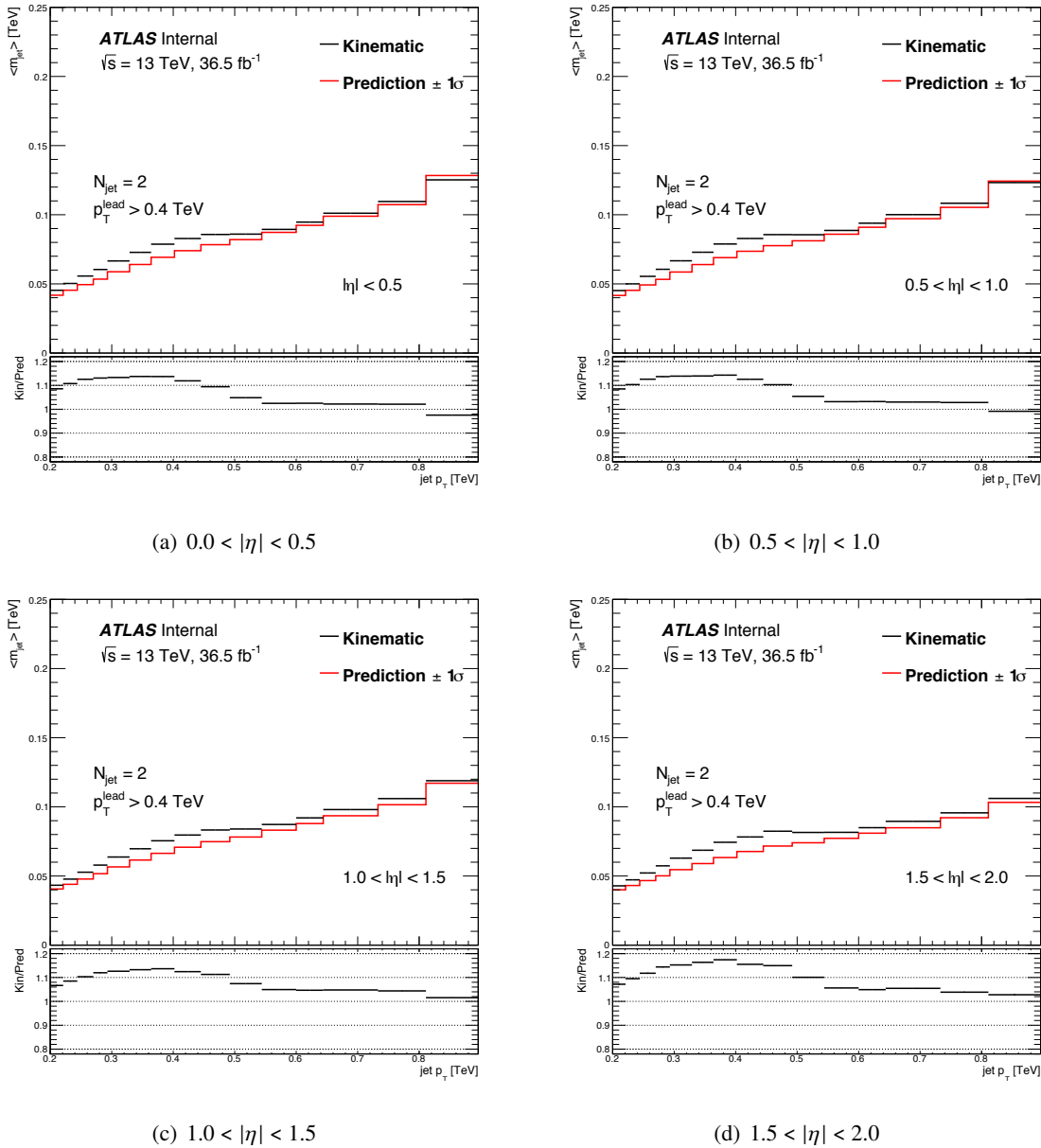


Figure 54: Jet mass response in four different $|\eta|$ regions in the UDR1 using data.

Not reviewed, for internal circulation only

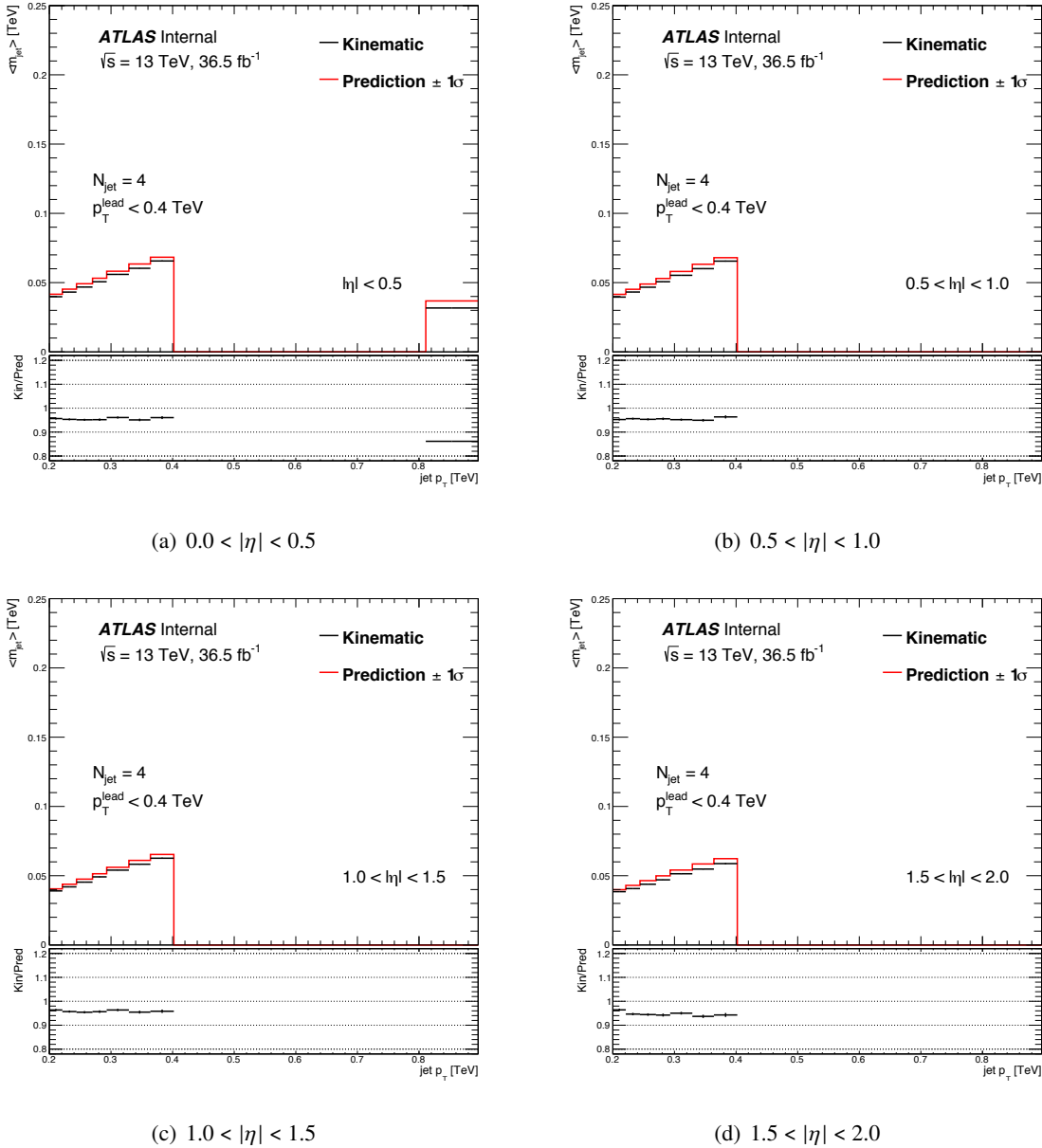


Figure 55: Jet mass response in four different $|\eta|$ regions in the UDR2 using data.

Not reviewed, for internal circulation only

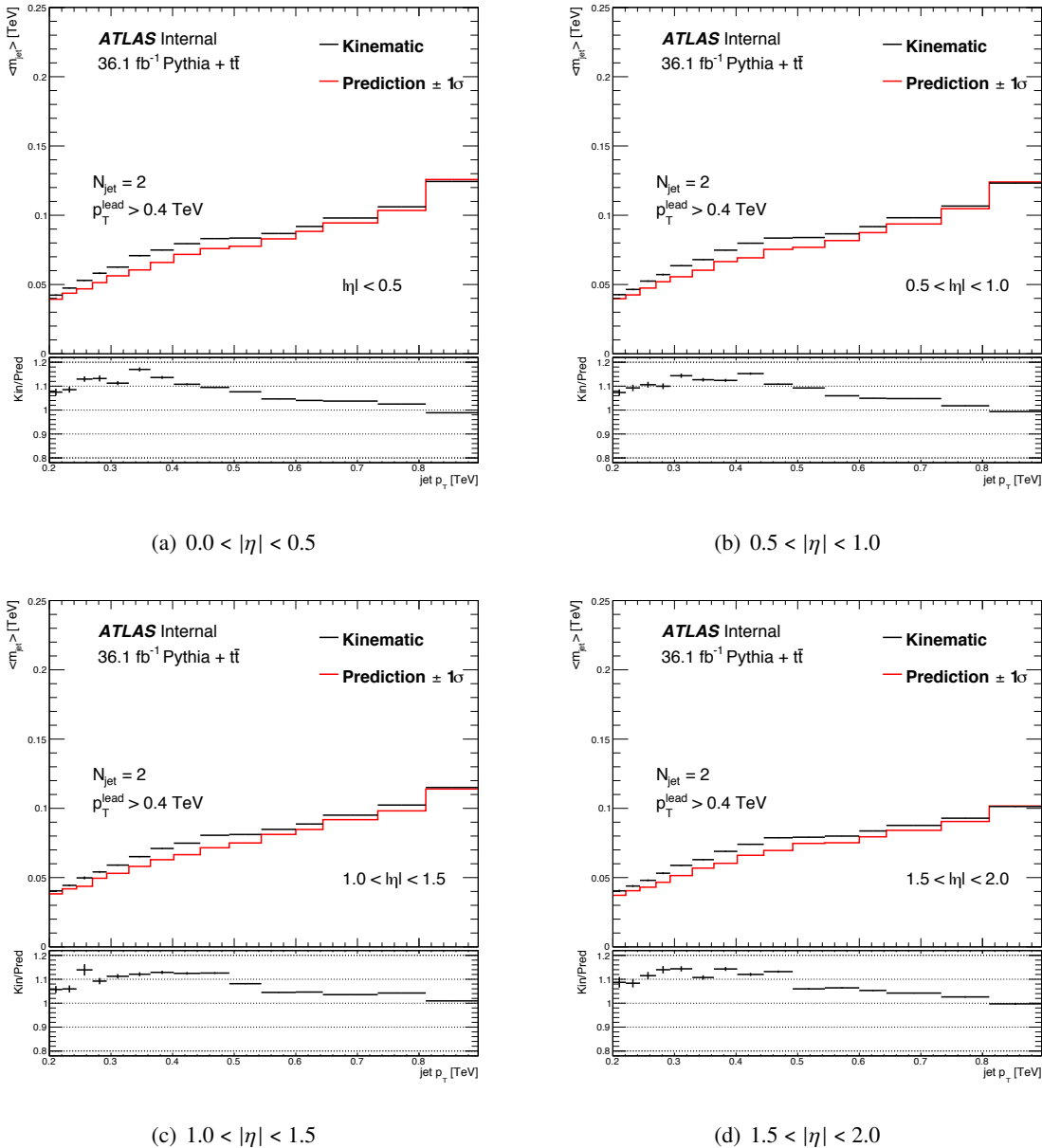


Figure 56: Jet mass response in four different $|\eta|$ regions in the UDR1 using PYTHIA8 multijet plus $t\bar{t}$ sample.

Not reviewed, for internal circulation only

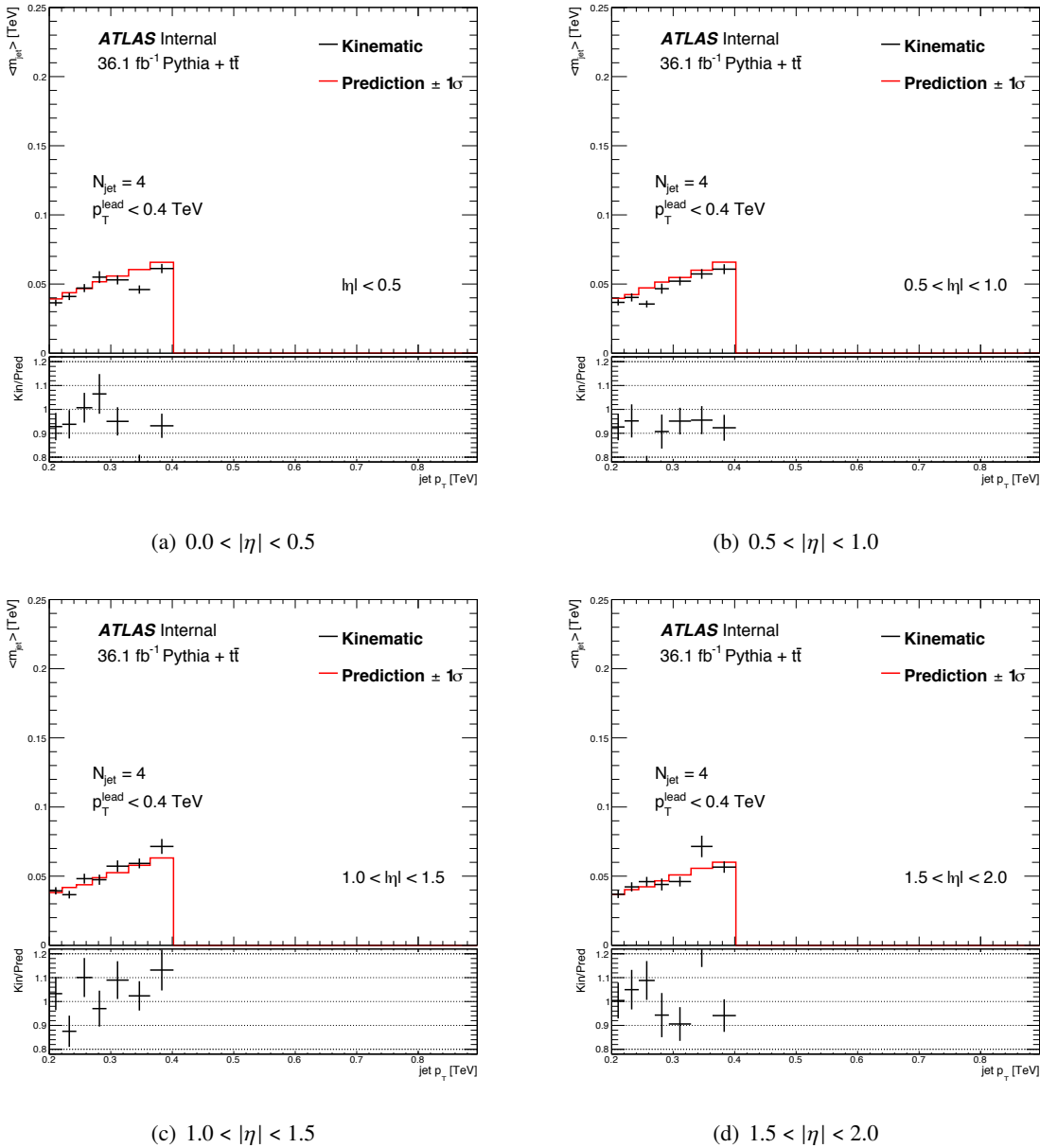


Figure 57: Jet mass response in four different $|\eta|$ regions in the UDR2 using PYTHIA8 multijet plus $t\bar{t}$ sample.

Not reviewed, for internal circulation only

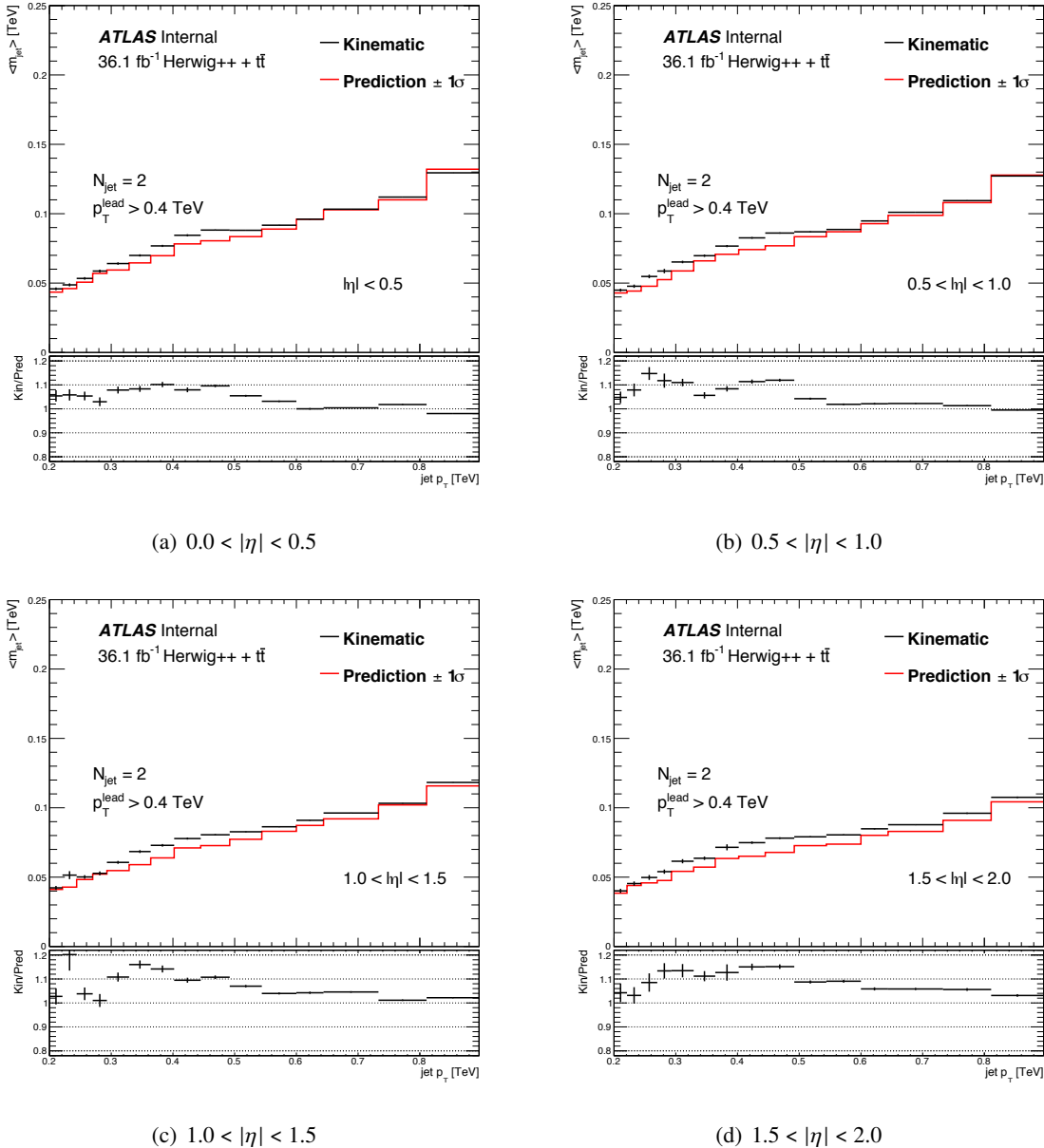


Figure 58: Jet mass response in four different $|\eta|$ regions in the UDR1 using Herwigpp multijet plus $t\bar{t}$ sample.

Not reviewed, for internal circulation only

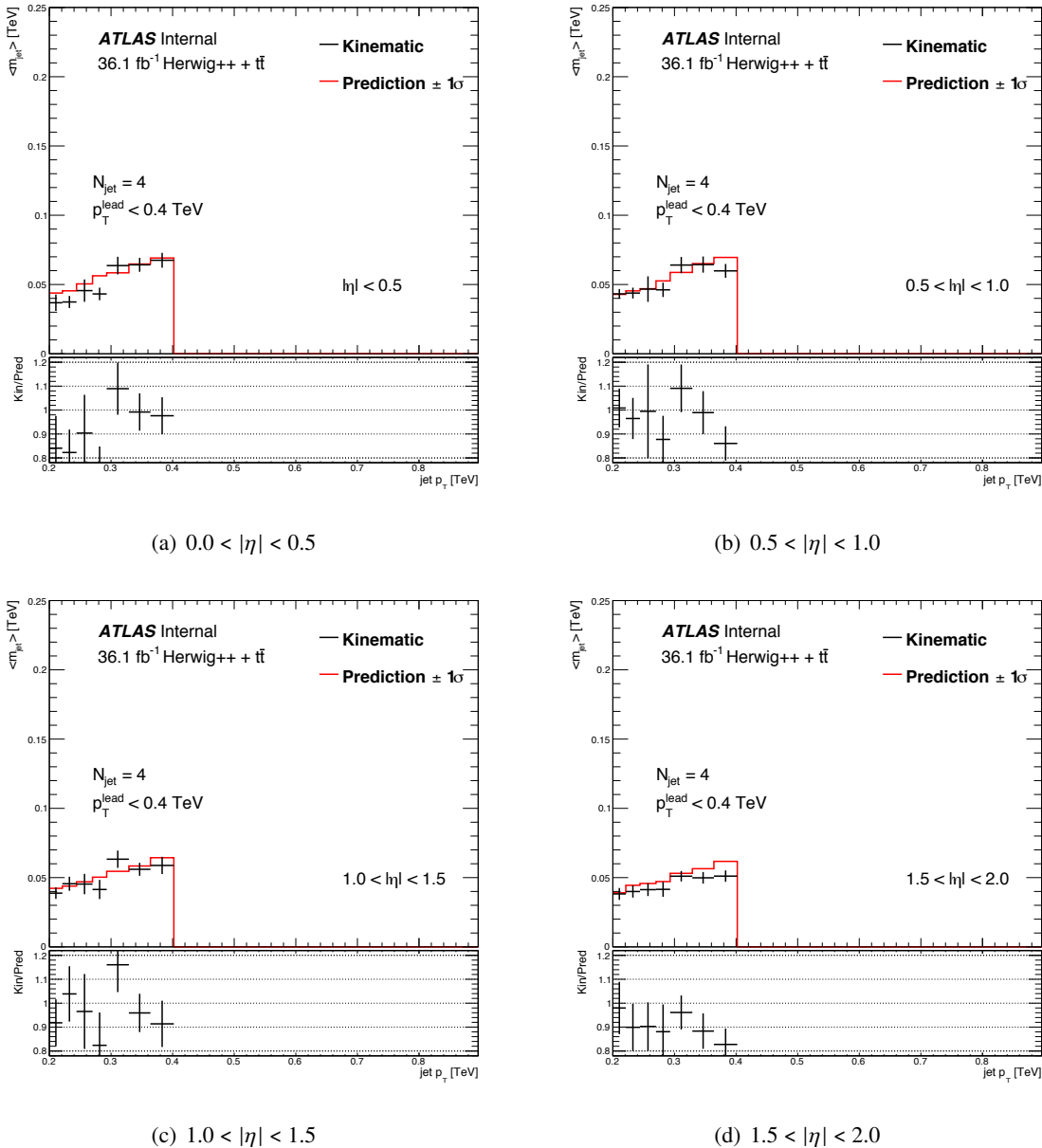


Figure 59: Jet mass response in four different $|\eta|$ regions in the UDR2 using Herwigpp multijet plus $t\bar{t}$ sample.

758 **E. Jet mass response in the UDR**

759 **E.1. Data**

760 **E.2. PYTHIA8 multijet plus $t\bar{t}$ sample**

761 **E.3. Herwigpp multijet plus $t\bar{t}$ sample**

762 **E.4. SHERPA multijet sample**

Not reviewed, for internal circulation only

Not reviewed, for internal circulation only

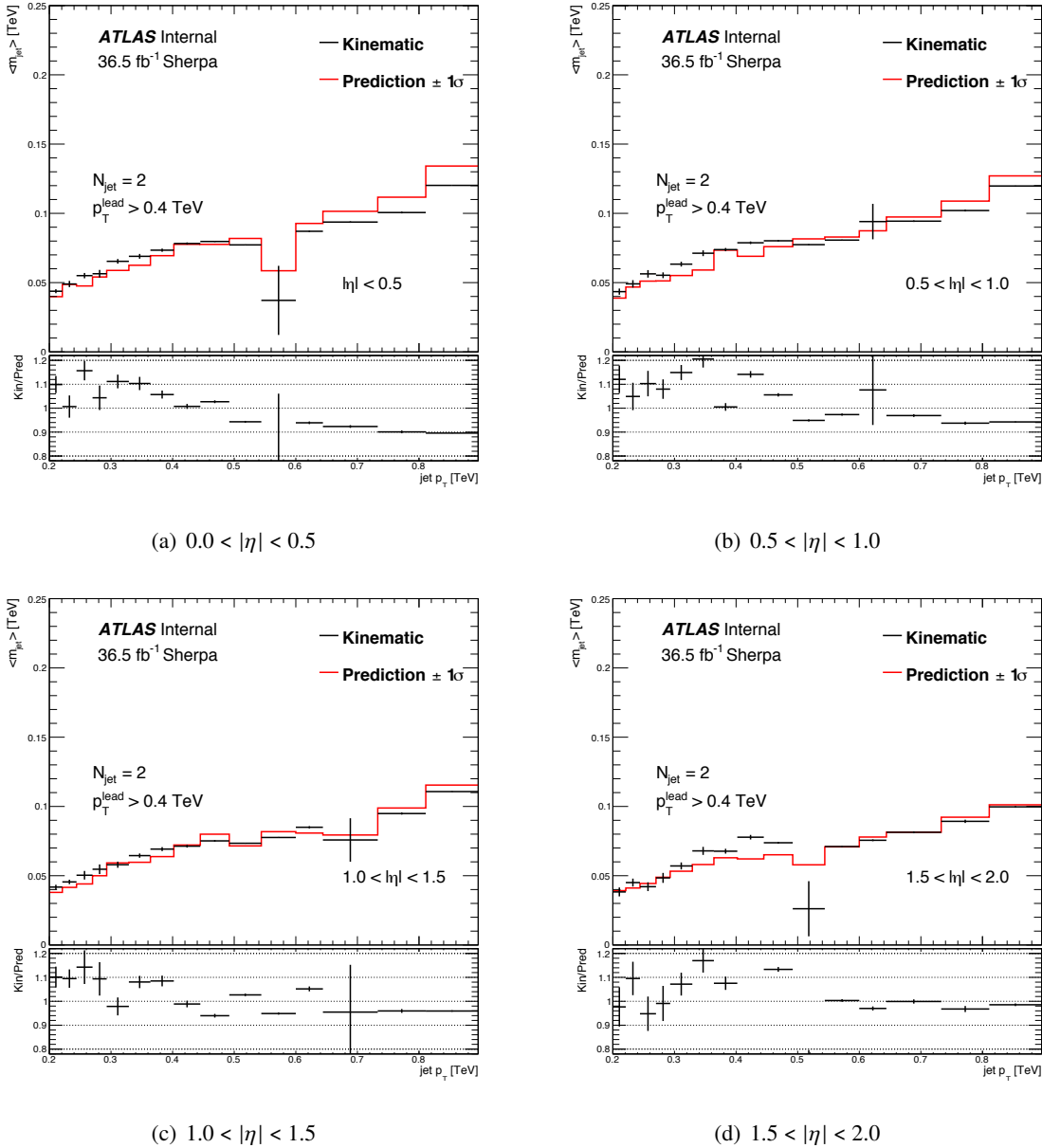


Figure 60: Jet mass response in four different $|\eta|$ regions in the UDR1 using SHERPA multijet sample.

Not reviewed, for internal circulation only

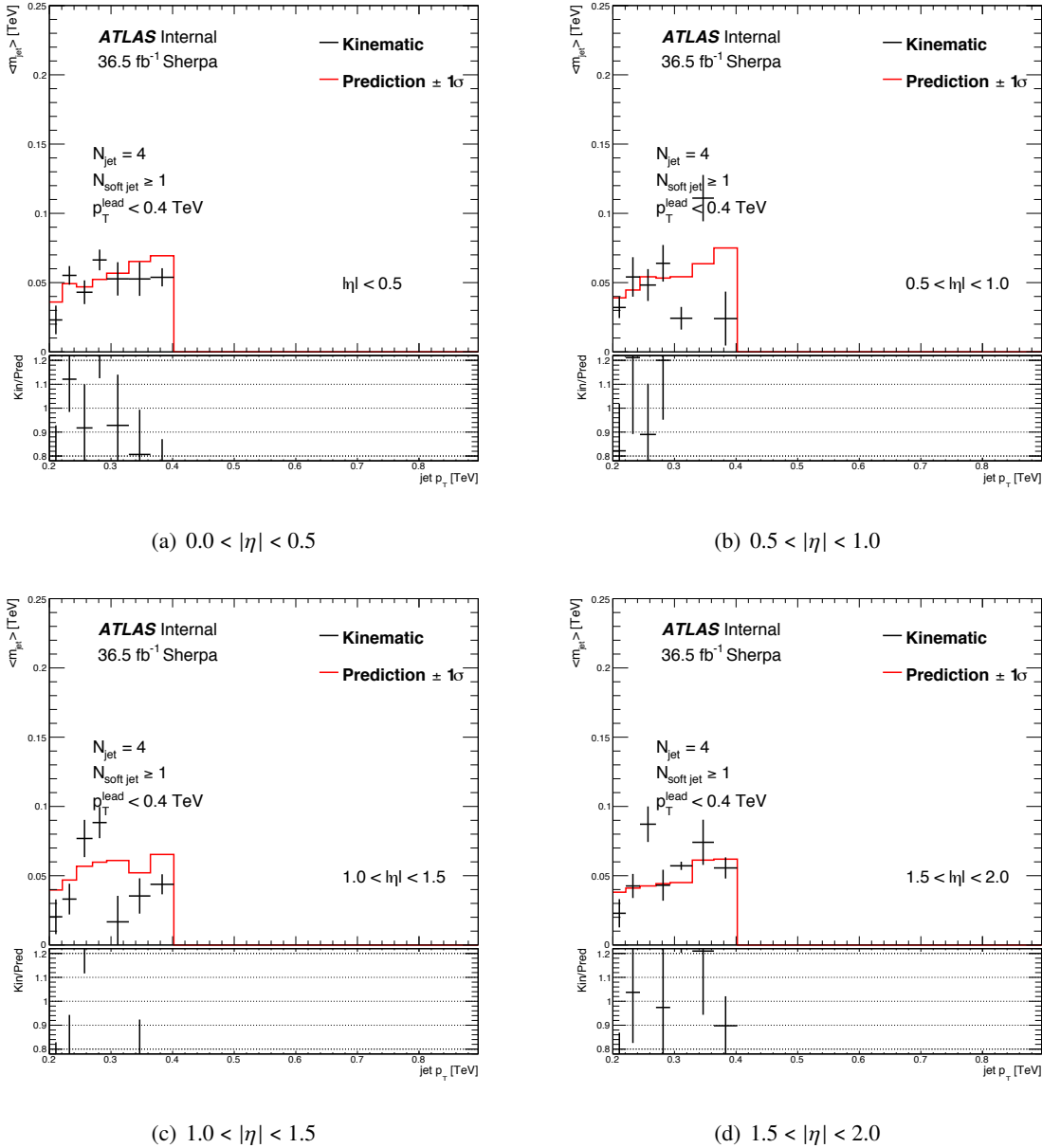


Figure 61: Jet mass response in four different $|\eta|$ regions in the UDR2 using SHERPA multijet sample.

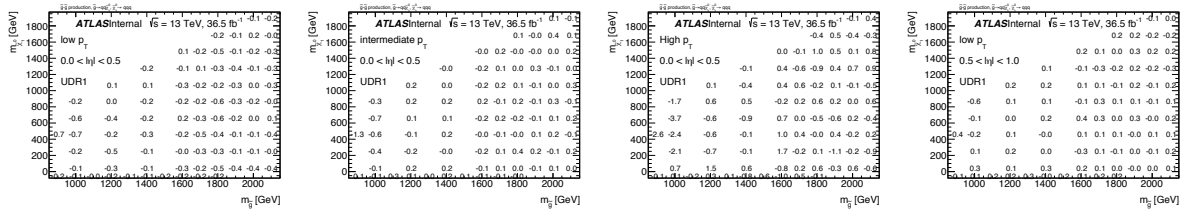


Figure 62: Variation in the jet mass prediction uncertainty due to the injection of signal events for low p_T jets in the UDR1. The four plots correspond to four different η regions where the jet mass prediction uncertainty is determined separately. The entry shown in the plot represents the change in the jet mass prediction uncertainty normalized to the nominal uncertainty, and this change is shown in percentage, i.e., the absolute change in the systematic uncertainty is the product of the entry shown in here and the uncertainty shown in Table 4.

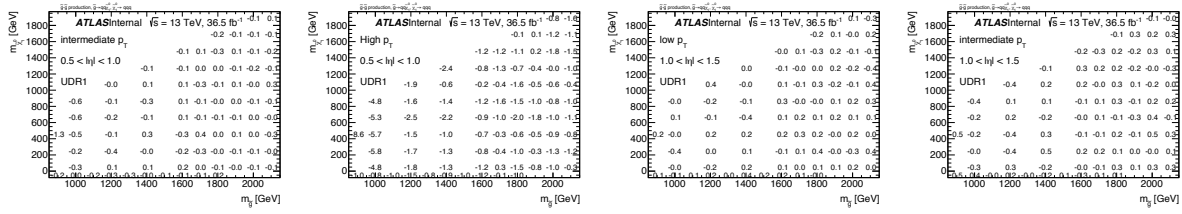


Figure 63: Variation in the jet mass prediction uncertainty due to the injection of signal events for intermediate p_T jets in the UDR1. The four plots correspond to four different η regions where the jet mass prediction uncertainty is determined separately. The entry shown in the plot represents the change in the jet mass prediction uncertainty normalized to the nominal uncertainty, and this change is shown in percentage, i.e., the absolute change in the systematic uncertainty is the product of the entry shown in here and the uncertainty shown in Table 4.

763 F. Systematic uncertainty vs signal injection

764 The presence of signal events in the UDRs may affect the estimation of jet mass prediction uncertainty.
 765 To check this potential effect, a series of signal injection tests are done using the 10-quark and 6-quark
 766 signal samples. In each injection test, a signal sample is injected to data, and the background estimation
 767 procedure is carried out. The jet mass prediction uncertainty is determined in the data sample injected with
 768 signal events, and the uncertainty is compared to the uncertainty determined without signal contamination.
 769 Figures 62 - 65 show the change in the jet mass prediction uncertainty normalized to its nominal value,
 770 and it is evident that the jet mass prediction uncertainty is not affected by the presence of signal events.

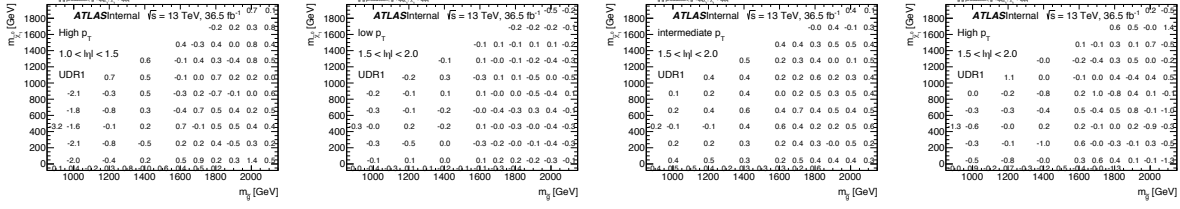


Figure 64: Variation in the jet mass prediction uncertainty due to the injection of signal events for high p_T jets in the UDR1. The four plots correspond to four different η regions where the jet mass prediction uncertainty is determined separately. The entry shown in the plot represents the change in the jet mass prediction uncertainty normalized to the nominal uncertainty, and this change is shown in percentage, i.e., the absolute change in the systematic uncertainty is the product of the entry shown in here and the uncertainty shown in Table 4.

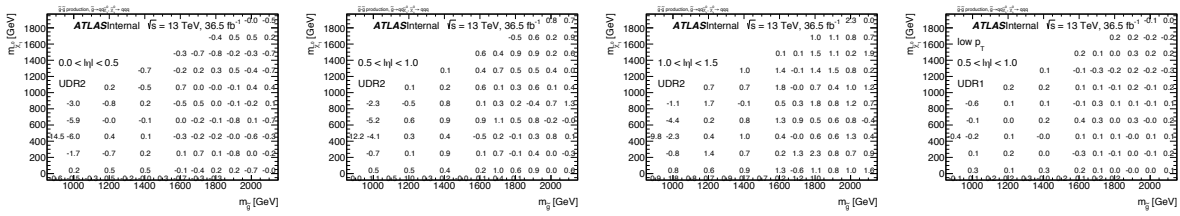


Figure 65: Variation in the jet mass prediction uncertainty due to the injection of signal events for low p_T jets in the UDR2. The four plots correspond to four different η regions where the jet mass prediction uncertainty is determined separately. The entry shown in the plot represents the change in the jet mass prediction uncertainty normalized to the nominal uncertainty, and this change is shown in percentage, i.e., the absolute change in the systematic uncertainty is the product of the entry shown in here and the uncertainty shown in Table 4.

Not reviewed, for internal circulation only

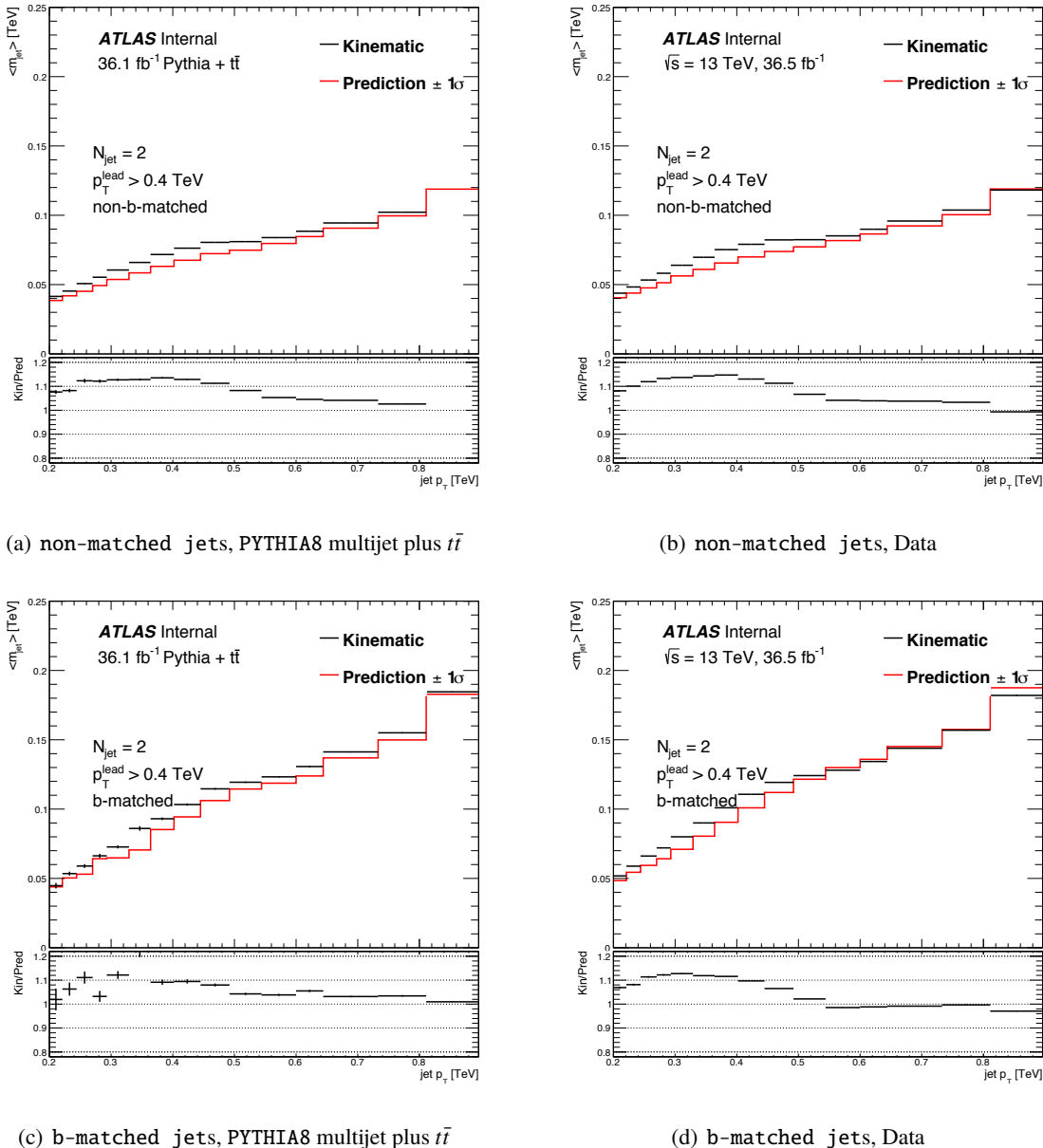


Figure 66: Jet mass response comparison in UDR1 with non-matched jets between PYTHIA8 multijet plus $t\bar{t}$ sample(left) and data(right).

G. Jet mass response between non-matched jets and b-matched jets

Not reviewed, for internal circulation only

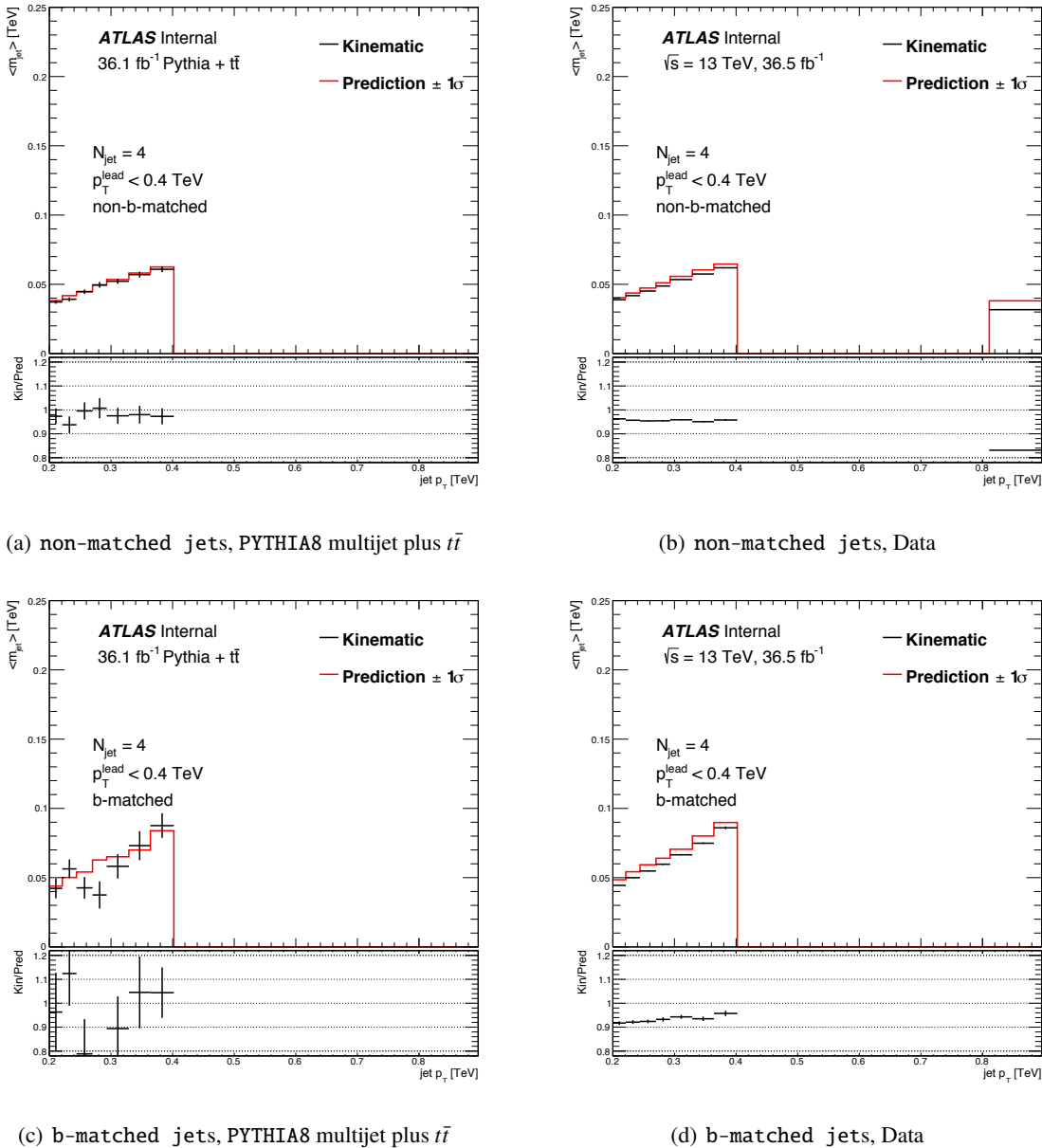


Figure 67: Jet mass response comparison in UDR2 with non-matched jets between PYTHIA8 multijet plus $t\bar{t}$ sample(left) and data(right).

Not reviewed, for internal circulation only

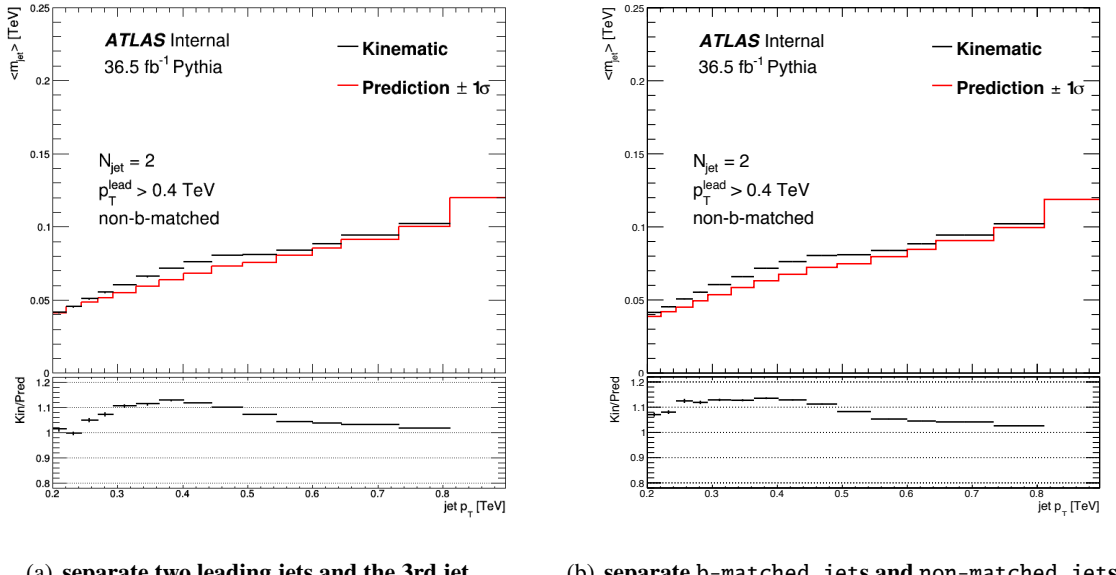


Figure 68: Jet mass response of non-matched jets in the UDR1 using PYTHIA8 multijet sample. (a) shows the result when the jet mass templates are separately made for two leading jets and the third leading jet. (b) shows the result when jet mass templates are separately made for b-matched jets and non-matched jets.

772 H. Background estimation performance with alternative binning for 773 control region

774 The jet mass template paper suggested the ordering of jets in p_T can serve as one observable that the
775 jet mass PDF can have a dependency [2]. It is believed that the leading jet in p_T in the event may have
776 different quark or gluon origin than jets trailing in p_T . The Run-1 analysis found that the jet mass PDFs
777 are similar between the leading jet and the subleading jet while the jet mass PDFs are more different
778 between the two leading jet and the third and the fourth leading jets. In response to this observation, the
779 Run-1 analysis binned control region jets not only in p_T and η but also between the two leading jets and
780 the third and fourth leading jets. In the Run-2 study, the separation between two leading jets and the third
781 and fourth leading jets is found not to improve the prediction of jet mass response and the M_J^Σ distribution,
782 and as a result, this separation is not included in the binning of control region jets.

783 Figure 71 (69) show the jet mass response for non-matched jets in the UDR1 (UDR2) using PYTHIA8 multijet
784 sample under two different binnings for the jet mass templates. Figure 70 shows the predicted and
785 observed M_J^Σ distributions in the 4jSR region using PYTHIA8 multijet sample under two different binnings
786 for the jet mass templates. The jet mass response and M_J^Σ prediction are checked in all regions defined in
787 the analysis, no significant improvement in the result is seen due to the separation in the jet mass templates
788 between the two leading jets and the third leading jet.

789 However, there is some indication that the binning used in the Run-2 analysis does not result in a full
790 closure in the prediction of control region jet masses, if the prediction and observation are compared
791 separately for leading jets and trailing jets. This non-closure can be due to either that control region

Not reviewed, for internal circulation only

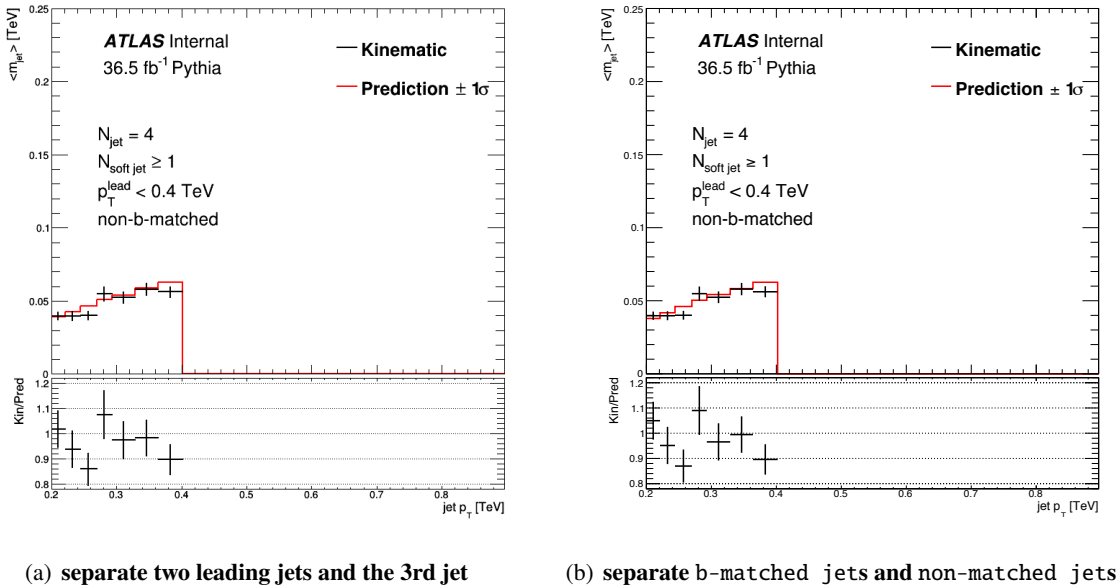


Figure 69: Jet mass response of non-matched jets in the UDR2 using PYTHIA8 multijet sample. (a) shows the result when the jet mass templates are separately made for two leading jets and the third leading jet. (b) shows the result when jet mass templates are separately made for b-matched jets and non-matched jets.

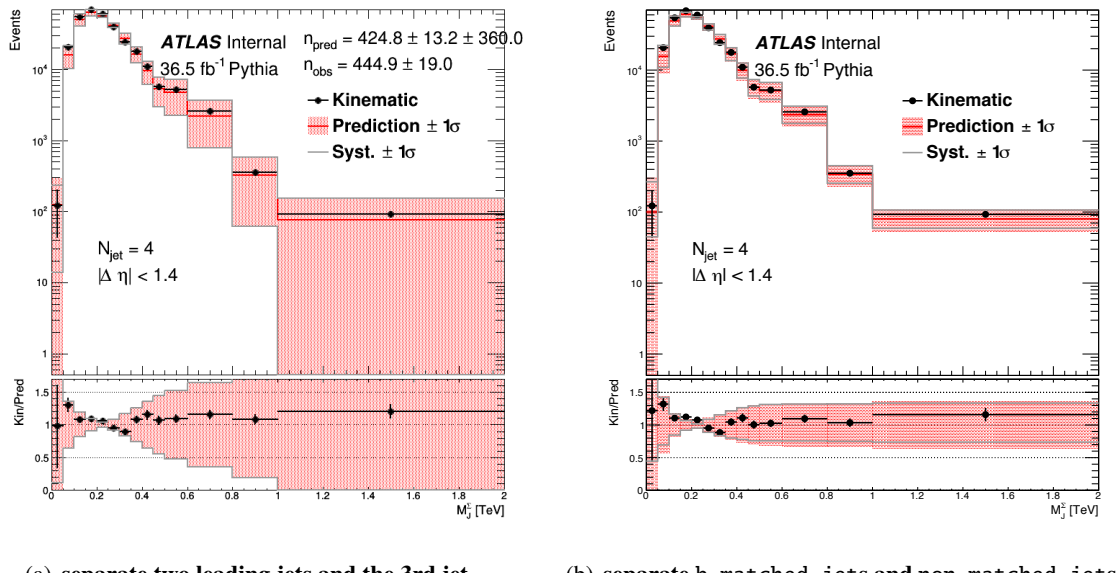
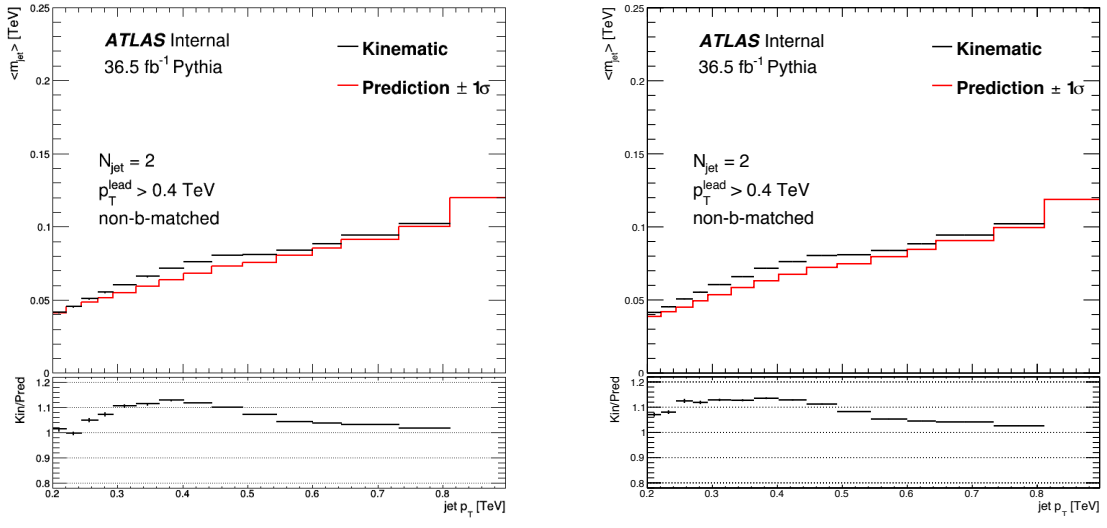


Figure 70: Predicted and observed M_J^Σ distributions in 4jSR using PYTHIA8 multijet sample. (a) shows the result when the jet mass templates are separately made for two leading jets and the third leading jet. (b) shows the result when jet mass templates are separately made for b-matched jets and non-matched jets.

Not reviewed, for internal circulation only



(a) separate two leading jets and the 3rd jet

(b) separate b-matched jets and non-matched jets

Figure 71: Jet mass response of non-matched jets in the UDR1 using PYTHIA8 multijet sample. (a) shows the result when the jet mass templates are separately made for two leading jets and the third leading jet. (b) shows the result when jet mass templates are separately made for b-matched jets and non-matched jets.

792 jets are not binned with the right list of observables or that correlations between jets are not taken into
793 account.

Not reviewed, for internal circulation only

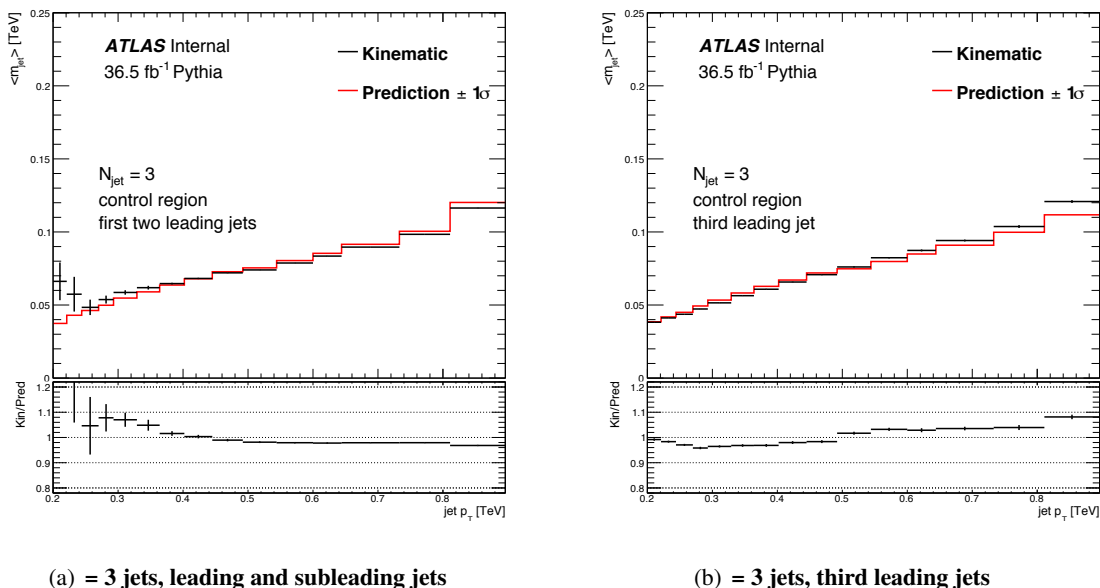


Figure 72: Jet mass response of 3-jet events for the two leading jets (15(a)) and the third leading jets (15(b)) in PYTHIA8 multijet MC sample.

794 I. Signal systematic uncertainties

795 This section presents the signal systematic uncertainties evaluated for every signal point in the 10-quark
796 and 6-quark models.

Not reviewed, for internal circulation only

1800	650	13.0	+0.4	+11.7	+1.3	+11.8
1800	850	15.6	-0.2	+11.6	+1.3	+11.3
1800	1050	16.0	-0.2	-10.6	+1.4	+10.6
1800	1250	15.0	+0.1	+10.7	1.4	+10.8
1800	1450	10.7	-0.3	-10.8	+1.2	+11.0
1800	1650	4.9	+0.1	+10.9	+1.1	+11.0
1900	50	1.3	-0.1	+13.1	+1.1	+12.7
1900	250	3.1	-0.0	-10.5	+1.3	+13.1
1900	450	6.0	-0.5	+15.8	2.6	+10.8
1900	650	9.0	+0.3	-13.4	+1.5	+15.8
1900	850	11.0	-0.2	+11.7	+1.5	+13.9
1900	1050	11.8	-0.1	-10.3	+1.8	+11.9
1900	1250	11.2	+0.2	+10.8	1.8	+10.4
1900	1450	8.8	+0.2	-10.2	+1.4	+10.9
1900	1650	5.5	+0.1	+9.3	1.4	+9.4
2000	50	0.9	-0.3	-10.6	+1.4	+10.7
2000	250	2.2	+0.0	+9.7	+1.2	+9.8
2000	450	4.0	-0.2	-9.3	1.2	-9.4
2000	650	5.9	+0.3	+9.4	+1.3	+9.5
2000	850	7.5	-0.2	-9.3	1.3	-9.4
2000	1050	8.2	+0.1	+12.0	+1.3	+12.0
2000	1250	8.0	-0.2	-11.1	1.3	-11.2
2000	1450	7.0	+0.1	+12.6	+0.9	+12.6
2000	1650	5.0	-0.3	-12.3	+5.0	+12.3
2000	1850	2.5	+0.0	+11.2	5.0	-13.4
2100	50	0.7	-0.4	-12.4	+1.4	+10.6
2100	250	1.5	+0.2	+10.5	-8.7	-8.8
2100	450	2.8	-0.4	+10.1	1.4	+10.2
2100	650	3.8	+0.4	-10.3	+1.5	+10.9
2100	850	4.9	-0.2	+10.8	+1.2	-9.7
2100	1050	5.5	+0.1	-9.0	1.4	-9.1
2100	1250	5.7	-0.2	+9.3	+1.4	+8.3
2100	1450	5.1	+0.1	-7.4	1.4	+8.9
2100	1650	4.1	-0.1	+9.2	+1.3	+9.4
2100	1850	2.6	+0.2	-9.3	+1.3	-7.6
			-0.1	+10.8	+1.4	+13.5
			-0.1	-9.3	1.4	-9.3
			-0.1	+10.8	+1.0	+10.9
			-0.1	-11.1	1.0	-11.2
			-0.1	+11.6	+1.5	+11.7
			-0.1	-12.6	1.5	-12.7
			-0.1	+12.4	+5.2	+13.5
			-0.1	-11.8	5.2	-12.9
			-0.1	+10.1	+2.0	+10.3
			-0.1	-12.8	2.0	-13.0
			-0.1	+9.3	+1.7	+9.5
			-0.1	-10.3	1.7	-10.4
			-0.1	+7.7	+1.5	+7.8
			-0.1	-8.9	1.5	-9.0
			-0.1	+8.3	+1.2	+8.4
			-0.1	-7.8	1.2	-7.9
			-0.1	+7.8	+1.5	+8.0
			-0.1	-7.9	1.5	-8.0
			-0.1	+6.2	+1.0	+6.3
			-0.1	-8.1	1.0	-8.2
			-0.1	+7.1	+1.0	+7.2
			-0.1	-7.5	1.0	-7.6
			-0.1	+9.4	+0.9	+9.5
			-0.1	-8.8	0.9	-8.9
			-0.1	+10.4	+1.3	+10.5
			-0.1	-11.4	1.3	-11.4

$m_{\tilde{g}}$	$m_{\tilde{\chi}}$	yield	NP1	NP2	NP3	Baseline	Modeling	Stat.	Tracking	b-tagging	JER
1000	50	9568	+0	+0	+0	+9.92126	+6.59674	+7.72605	+17.1342	+19.0886	+0
1000	250	7016	0	0	0	-1.0603	0	-4.61731	-7.94586	-18.7538	0
1000	450	0.0283	+1.34419	+0	+1.34419	-12.5288	-9.13083	-7.7059	-18.7155	-17.0376	0
1000	650	1553	+0	+0	+0	+15.7229	+7.26627	+8.62344	+15.4911	+18.2239	+1.34419
1000	850	49.5058	+0.499982	+0.499982	+0	-10.5864	-4.4484	-5.52358	-15.152	-14.3225	+0
1200	50	6603	+0	0	0	-13.2442	-7.76541	-7.92841	-19.0671	-15.7007	0.499982
1200	250	9358	-1.14237	0	0	+11.9454	+8.89238	+11.212	+16.4068	+20.5419	+1.14237
1200	450	45.5436	-0.657532	0	0	-11.1805	-4.59111	-5.15661	-15.6552	-20.1806	-1.14237
1200	650	64.0737	+0.342709	+0	+0	+6.84794	+3.33118	+3.20893	+11.333	+16.8085	+0
1200	850	54.2682	-0.287612	0	0	-12.2674	-8.41613	-8.30266	-17.4709	-16.5355	0
1200	1050	26.996	+0	+0	+0	+11.0349	+5.63919	+4.42583	+17.5407	+16.2848	+0.342709
1400	50	5.32206	0	0	0	-10.5915	-5.60195	-6.65214	-12.5952	-16.0936	0.342709
1400	250	13.0419	+0.707038	+0.353523	+0.353523	+9.1827	+7.37842	+8.86569	+16.8898	+16.2082	+0.0398369
1400	450	30.3609	+0.680577	+0	+0	+13.6515	+2.98881	+3.89766	+13.4692	+17.26	+0.8663
1400	650	43.2508	-0.16873	0	-0.16873	-7.37048	-4.13589	-5.51762	-11.4765	-16.4381	+1.05224
1400	850	46.8191	+0.117441	+0	+0	+9.30254	+4.86148	+5.75051	+12.3135	+17.0725	+0.106599
1400	1050	36.1507	-0.224616	0	0	-9.29045	-3.89626	-5.17957	-11.8859	-17.1412	-0.106599
1400	1250	17.7803	+0.314833	+0.0984747	+0	+10.0729	+4.67039	+5.17772	+14.2632	+17.9466	+0.190623
1400	1450	-0.196949	0	0	+0	-10.2292	-5.01723	-5.82069	-12.4677	-17.8982	-0.190623
1400	1600	-0.430188	+0	+0	+0	-11.8271	+6.34944	+7.28154	+16.0652	+16.4809	+0.127535
1400	1800	-0.127535	+0	+0.127535	+0	-10.2984	-6.51655	-6.47378	-12.6511	-16.4098	0.127535
1400	2000	-0.403088	0	0	+0	+9.82518	+3.72301	+6.15608	+12.5966	+18.3653	+0
1400	2200	-0.102022	+0	+0	+0	-10.8054	-5.05572	-6.01951	-14.7181	-18.0728	0
1600	50	3.43774	0	0	0	+6.22217	+4.52736	+6.19098	+12.8495	+18.865	+0
1600	250	8.75381	+1.07022	+0.193995	+0.193995	+8.2618	+6.20538	+6.91587	+17.2264	+18.6648	+0
1600	450	17.4806	-0.699078	0	-0.337316	-8.14852	-4.70221	-6.5702	-13.9361	-18.5724	0
1600	650	24.3764	+0.188661	+0.104201	+0.104201	+7.7825	+4.62298	+4.70744	+12.1973	+17.3675	+0.112428
1600	850	30.1695	-0.267949	0	0	-7.63052	-4.85109	-5.52267	-11.891	-17.3183	-0.112428
1600	1050	27.993	+0.434246	+0.0708677	+0.13143	+7.02068	+4.20445	+4.27551	+10.6304	+17.8815	+0.182849
1600	1250	21.2404	-0.121129	0	0	-6.88794	-4.42195	-4.28531	-9.58554	-17.6199	0.182849
1600	1450	9.71014	+0.0978705	+0	+0	+6.76672	+3.41227	+3.99773	+9.81728	+17.8316	+0.158674
1600	1600	-0.0472896	-0.0472896	-0.0472896	+0	-6.86537	-3.46826	-3.91721	-9.82335	-17.6153	0.158674
1600	1800	+0.263705	+0	+0	+0	+6.44743	+3.80735	+3.94616	+9.36692	+17.6285	+0.00171829
1600	2000	-0.158222	0	-0.0527382	+0	-7.74471	-4.66849	-4.65473	-10.5567	-17.5539	-0.00171829
1600	2200	+0.139018	+0	+0.139018	+0	+7.27931	+4.00618	+4.28647	+10.9937	+17.9287	+0.0723481
1600	2400	-0.0695045	-0.0695045	-0.0695045	+0	-8.6574	-4.498	-4.81661	-11.7942	-17.8335	-0.0723481
1600	2600	+0.324733	+0	+0.152037	+0	+6.19071	+7.29001	+6.43851	+14.6492	+17.7443	+0.324733
1600	2800	-0.18457	0	0	+0	-7.24729	-4.29783	-5.03074	-10.7466	-18.2399	0.324733

Table 17: Expected signal yield (normalized to 36.1 fb^{-1}) and systematic uncertainties (in percentage) for various signal points.

$m_{\tilde{g}}$	$m_{\tilde{\chi}}$	yield	NP1	NP2	NP3	Baseline	Modeling	Stat.	Tracking	b-tagging	JER
1700	50	23.3076	+0 -0.34298 +0.144489	+0 0 +0.144489	+0 0 +0.144489	+6.00431 -5.32507 +6.92585	+3.90336 -3.31421 +4.35479	+8.74344 -6.05798 +5.08608	+10.8286 -8.17634 +10.0404	+17.6677 -17.4235 +18.5893	+0.34298 -0.34298 +0.000804674
1700	250	5.96515	-0.287386 +0.527124	0 +0.0723514	-0.143701 +0.0895803	-8.15383 +6.57429	-4.17971 +4.10297	-5.28911 +3.94158	-12.4553 +9.76422	-18.3837 +18.0842	0.000804674 +0.221292
1700	450	1.8463	+0.0954299 -0.244061	+0.0477177 -0.0953854	-0.0677339 -0.0476676	-6.99605 +6.49726	-3.95041 +4.10297	-4.08211 +3.94158	-11.4772 +9.76422	-17.2851 +18.0842	+0.0476676 +0.15947
1700	650	1.964	-0.244061 +0	-0.0953854 +0	-0.0476676 +0	-6.39547 +6.71587	-3.879 +3.76349	-4.2695 +4.27939	-9.41534 +11.0089	-18.0123 +17.8748	-0.0476676 +0.15947
1700	850	2.8893	-0.0391561 +0.0384597	0 +0.0384597	0 +0	-6.40035 +6.23038	-3.25202 +3.60714	-3.9233 +3.82953	-9.4533 +9.32174	-17.6833 +17.7188	-0.15947 +0.192289
1700	1050	2.2883	-0.155876 +0.144243	-0.0384552 +0.0448087	-0.0769149 +0	-5.74032 +5.56817	-3.44758 +4.44509	-4.54326 +5.38779	-9.34053 +11.6582	-17.5793 +17.8156	-0.192289 +0.196114
1700	1250	1.1302	-0.137892 +0.156294	0 +0.156294	0 +0.0781469	-5.98555 +8.02214	-3.3928 +4.26262	-4.00434 +5.35662	-10.0708 +11.676	-17.7816 +18.0507	-0.196114 +0.156294
1700	1450	1.9691	-0.0781377 +0	0 +0	0 +0	-7.59694 +6.48747	-4.78658 +4.00964	-5.42074 +5.97193	-10.2901 +10.6589	-17.8717 +20.3841	0.156294 +0
1800	50	2.96136	+0 0	+0 0	+0 +0	-8.39383 +7.83083	-4.44779 +4.47659	-6.97588 +5.81027	-12.75 +11.4347	-19.9478 +18.8096	0 +0.222284
1800	250	4.6642	+0.111132 -0.111132	+0.111132 0	+0.111132 0	-8.15411 +5.73372	-4.97967 +3.77446	-6.24697 +4.96756	-10.9817 +8.94801	-18.6787 +18.4663	-0.222284 +0.00329588
1800	450	8.9809	+0.398401 -0.168112	+0.286319 -0.0560411	+0.225378 0	+5.73372 -5.79242	-3.02421 +3.1305	-4.38701 +3.47139	-8.95407 +9.14944	-18.2645 +18.1584	0.00329588 +0.0769454
1800	650	15.0807	+0.311512 -0.161383	+0.115422 -0.0459608	+0.192367 -0.0459608	+5.64986 -5.61618	-3.36782 +3.01303	-3.86226 +3.3792	-8.78644 +8.77497	-17.9602 +17.8526	0.0769454 +0.0159727
1800	850	15.7394	+0.191844 -0.159873	+0.0319772 0	+0.0319772 -0.063948	+5.37046 -5.1814	-3.86226 +3.3792	-8.78644 +8.77497	-17.8326 +17.8526	0.0159727 +0.0739014	
1800	1050	16.1553	-0.0664797 +0.0333319	-0.032788 +0	-0.0664797 +0	-5.23343 +4.95029	-2.9956 +3.10778	-3.68929 +3.48306	-8.14463 +8.53644	-17.6747 +18.3532	-0.0739014 +0.266629
1800	1250	15.0996	-0.16664 +0.0464736	-0.0333253 +0.0464736	-0.0333253 +0	-5.43091 +6.452	-2.85379 +3.43248	-3.4751 +4.33726	-8.161 +9.92289	-18.2112 +18.6192	-0.266629 +0.000664832
1800	1450	10.8298	-0.188424 +0.434277	-0.0464736 +0.107323	0 +0	-6.11882 +7.25314	-3.88584 +3.37897	-4.10318 +4.55322	-9.43109 +11.0629	-18.6249 +18.4292	-0.000664832 +0.098388
1800	1650	4.93556	0 +0	0 0	0 0	-6.07951 +7.03734	-3.44826 +3.85246	-4.55687 +5.49527	-9.67582 +12.4242	-18.4954 +18.6592	+0.098388 +0.0356473
1900	250	3.13067	+0.285626 -0.482197	+0.0951872 -0.194271	+0 0	-6.31452 +6.31452	-3.36736 +3.22265	-6.25795 +4.7282	-9.49068 +8.7282	-18.4333 +18.2011	-0.0356473 +0.10423
1900	450	6.04433	+0.295881 -0.14794	+0.049319 -0.0493024	+0.049319 -0.0493024	+5.89957 -5.38308	-2.98954 +2.71473	-3.15145 +3.37897	-7.62054 +4.55322	-18.8921 +11.0629	-0.10423 +0.136013
1900	650	9.05133	-0.164661 +0.174538	0 +0.0498728	0 +0.0498728	-4.93055 +4.77695	-2.74067 +2.67764	-3.20811 +3.18969	-7.58327 +3.49499	-18.2049 +8.93226	-0.136013 +0.0242337
1900	1050	11.9544	-0.224402 +0.0790188	-0.024928 +0.0263337	-0.0498644 +0	-4.56125 +4.57323	-2.46205 +2.66984	-3.1565 +2.79082	-7.10717 +7.304	-18.4949 +18.652	0.0242337 +0.133551
1900	1250	11.3163	-0.131695 +0.0670707	-0.0263425 +0.0335354	-0.0263425 +0.0335354	-4.63671 +6.16808	-2.4279 +3.27656	-2.72268 +4.01307	-7.15217 +8.85653	-18.5907 +18.5674	0.133551 +0.169477
1900	1450	8.88912	-0.100595 +0	-0.0670595 +0	0 +0	-5.4409 +4.75916	-2.78945 +1.94621	-4.00169 +4.9756	-8.41542 +8.66672	-18.3797 +21.2918	-0.169477 +0
2000	50	0.944348	-0.195691 +0.426838	0 +0.174698	0 +0.0790784	-4.40854 +5.09375	-2.94108 +2.38637	-6.01823 +3.74605	-9.50021 +8.03707	-20.9505 +19.9156	0 +0.409235
2000	250	2.26105	-0.237235 +0.308774	0 +0.132332	0 +0.0441106	-3.80081 +4.70269	-2.37235 +2.84151	-3.01228 +4.02709	-6.75974 +7.44505	-19.6077 +18.8949	0.409235 +0.132332
2000	450	4.05344	-0.178885 +0.282782	0 +0.0628367	0 +0.0628367	-5.19805 +5.38701	-2.48825 +2.95989	-3.00602 +3.71802	-6.70445 +8.09759	-18.7063 +18.6055	0.132332 +0.0566766
2000	650	5.99013	-0.131834 +0.21451	0 +0.047188	0 +0.0729462	-4.76699 +4.27937	-2.72729 +2.793	-3.42644 +3.29302	-7.19158 +6.63332	-18.4241 +18.79	0.0566766 +0.0510676
2000	850	7.57819	-0.188752 +0.067116	-0.0943761 +0.0434323	-0.047188 -0.0434323	-4.13266 +3.9738	-2.43838 +2.21217	-3.25169 +2.64471	-6.82688 +6.2091	-18.7553 +18.7138	-0.0510676 +0.0651485
2000	1050	8.2335	-0.217162 +0.19841	-0.0434323 +0.0661365	-0.0434323 +0.0881821	-4.37353 +4.38058	-2.56377 +2.59042	-3.00602 +3.05901	-6.49254 +7.11383	-18.6765 +18.7417	-0.0651485 +0.0220455
2000	1250	8.11049	-0.176364 +0.0253256	-0.0220455 +0.0253256	-0.0220455 +0.0253256	-3.57767 +4.66199	-1.87553 +2.53326	-2.52093 +3.24636	-5.71823 +6.80568	-18.6097 +18.8145	-0.0220455 +0.133016
2000	1450	7.06006	-0.0812316 +0.212452	0 +0.0354086	0 +0.0354086	-4.5399 +5.1817	-2.66843 +2.64159	-3.39392 +3.38594	-6.92474 +8.46959	-18.7614 +19.389	-0.133016 +0.0354086
2000	1650	5.04962	-0.106226 +0.212452	-0.0354086 +0	-0.0354086 +0	-5.60837 +5.99186	-3.31306 +5.21343	-3.88255 +4.07278	-8.1424 +8.43247	-19.2099 +18.7489	-0.0354086 +0.00472563
2000	1850	2.51818	-0.355018 +0	-0.0710036 +0	-0.0710036 +0	-5.52279 -3.73337	-3.73337 -5.15467	-5.15467 -9.34741	-9.34741 -18.9577	-18.9577 -0.00472563	

Table 18: **continued from Table 17** Expected signal yield (normalized to 36.1 fb⁻¹) and systematic uncertainties (in percentage) for various signal points.

DSID	$m_{\tilde{g}}$	$m_{\tilde{\chi}}$	4jSRb (%)	4jSR (%)	5jSRb (%)	5jSR (%)
403550	700	450	0.236624	0.236819	0.308249	0.277641
403551	800	450	0.27918	0.249127	0.294387	0.28902
403552	900	450	0.234498	0.225028	0.199591	0.185502
403553	1000	50	0.225741	0.25638	0.250047	0.264714
403554	1000	250	0.209673	0.215408	0.206608	0.189883
403555	1000	450	0.208957	0.207684	0.185579	0.177785
403556	1000	650	0.196782	0.192365	0.244046	0.263884
403557	1000	850	0.224021	0.228428	0.241838	0.241219
403558	1200	50	0.203403	0.215866	0.219683	0.237405
403559	1200	250	0.203227	0.210131	0.205529	0.211705
403560	1200	450	0.194538	0.195742	0.191454	0.202765
403561	1200	650	0.185178	0.176881	0.187564	0.186292
403562	1200	850	0.20197	0.206697	0.189673	0.190681
403563	1200	1050	0.19102	0.185923	0.216026	0.222248
403564	1400	50	0.192773	0.196036	0.231155	0.203585
403565	1400	250	0.172009	0.164512	0.179917	0.190101
403566	1400	450	0.152216	0.142841	0.175889	0.169058
403567	1400	650	0.143855	0.144749	0.149313	0.153336
403568	1400	850	0.140294	0.137299	0.149739	0.150202
403569	1400	1050	0.155632	0.156696	0.149016	0.145901
403570	1400	1250	0.185034	0.184522	0.196556	0.192621
403571	1600	50	0.177965	0.165404	0.227007	0.21367
403572	1600	250	0.148996	0.148041	0.193514	0.195676
403573	1600	450	0.121962	0.12176	0.15579	0.156931
403574	1600	650	0.120264	0.118353	0.130474	0.133179
403575	1600	850	0.110106	0.106116	0.110396	0.11106
403576	1600	1050	0.122558	0.121997	0.121356	0.121321
403577	1600	1250	0.11099	0.112479	0.131765	0.130103
403578	1600	1450	0.137892	0.138825	0.170557	0.172584
403579	1700	50	0.140821	0.149835	0.19214	0.186207
403580	1700	250	0.119502	0.116116	0.166172	0.160268
403581	1700	450	0.106901	0.100312	0.15247	0.145359
403582	1700	650	0.100844	0.0965058	0.1148	0.111538
403583	1700	850	0.0901765	0.0931163	0.100439	0.0999855
403584	1700	1050	0.0906817	0.0899911	0.100769	0.0971868
403585	1700	1250	0.0953923	0.0939165	0.12235	0.120566
403586	1700	1450	0.117725	0.119581	0.151816	0.154949
403587	1800	50	0.122812	0.117751	0.208666	0.212758
403588	1800	250	0.113594	0.114736	0.144148	0.145294
403589	1800	450	0.086218	0.0844961	0.129716	0.131807
403590	1800	650	0.0849159	0.0829334	0.103732	0.0994394
403591	1800	850	0.0805418	0.0817488	0.0833116	0.0848519
403592	1800	1050	0.0827547	0.0823001	0.0895339	0.0875088
403593	1800	1250	0.0770665	0.0784044	0.097701	0.0984775
403594	1800	1450	0.0989083	0.101447	0.122089	0.119335

Not reviewed, for internal circulation only

Not reviewed, for internal circulation only

403595	1800	1650	0.117695	0.119435	0.155718	0.157358
403596	1900	50	0.12367	0.117766	0.202181	0.198077
403597	1900	250	0.0894459	0.0832758	0.156728	0.147307
403598	1900	450	0.0793711	0.0789673	0.116667	0.116381
403599	1900	650	0.0762129	0.0777106	0.089842	0.0896488
403600	1900	850	0.0661505	0.0659411	0.0784583	0.0796338
403601	1900	1050	0.062224	0.0623871	0.0727556	0.0727169
403602	1900	1250	0.0691312	0.0681364	0.0782443	0.0771157
403603	1900	1450	0.067924	0.0687919	0.085014	0.0828698
403604	1900	1650	0.0893179	0.087497	0.118957	0.115981
403605	900	-	0.279386	0.280273	0.224981	0.240588
403606	1000	-	0.229607	0.231146	0.157095	0.159549
403607	1100	-	0.226276	0.232722	0.258429	0.271138
403608	1200	-	0.239368	0.237869	0.250437	0.256864
403609	1300	-	0.209871	0.20765	0.22563	0.22664
403610	1400	-	0.196773	0.197528	0.221672	0.223218
403611	1500	-	0.160614	0.158983	0.223195	0.220001
403612	1600	-	0.144304	0.143509	0.201267	0.202456
403613	1700	-	0.141125	0.141093	0.19898	0.201755
403614	1800	-	0.129563	0.126698	0.176546	0.174071
403615	2000	50	0.105598	0.118347	0.200052	0.212375
403616	2000	250	0.0938572	0.0906801	0.143678	0.144153
403617	2000	450	0.0693571	0.0686977	0.103049	0.100368
403618	2000	650	0.0639893	0.064938	0.0763289	0.0767481
403619	2000	850	0.057722	0.0586827	0.0647408	0.0644235
403620	2000	1050	0.0558919	0.0549441	0.0628274	0.0623307
403621	2000	1250	0.0522671	0.0533018	0.062553	0.0613861
403622	2000	1450	0.0578024	0.0569448	0.0748852	0.0768788
403623	2000	1650	0.0638951	0.0640528	0.0850755	0.0868447
403624	2000	1850	0.0948428	0.0949894	0.144849	0.145075
403625	2100	50	0.0878434	0.0832108	0.178234	0.158416
403626	2100	250	0.0684991	0.0676035	0.116253	0.119274
403627	2100	450	0.0578327	0.0543384	0.086814	0.0835584
403628	2100	650	0.0514231	0.0505085	0.0712988	0.0700441
403629	2100	850	0.0436191	0.044406	0.0579108	0.0565892
403981	2100	1050	0.0424189	0.0404847	0.0527266	0.0498703
403982	2100	1250	0.0429578	0.0422897	0.0559083	0.0541256
403983	2100	1450	0.0478182	0.0470562	0.0552312	0.0527911
403984	2100	1650	0.0474111	0.0471178	0.0638693	0.0650037
403985	2100	1850	0.0692943	0.0707137	0.101532	0.103373

Table 19: QCD scale, α_s uncertainties.

DSID	$m_{\tilde{g}}$	$m_{\tilde{\chi}}$	4jSRb (%)	4jSR (%)	5jSRb (%)	5jSR (%)
403550	700	450	0.360206	0.360206	0.412338	0.412338
403551	800	450	0.102777	0.102777	0.207427	0.207427

403552	900	450	0.126069	0.126069	0.155417	0.155417
403553	1000	50	0.160333	0.160333	0.130914	0.130914
403554	1000	250	0.144998	0.144998	0.108043	0.108043
403555	1000	450	0.0964474	0.0964474	0.175025	0.175025
403556	1000	650	0.0923077	0.0923077	0.0730694	0.0730694
403557	1000	850	0.0318233	0.0318233	0.12871	0.12871
403558	1200	50	0.0751647	0.0751647	0.0735415	0.0735415
403559	1200	250	0.10388	0.10388	0.0826058	0.0826058
403560	1200	450	0.0521002	0.0521002	0.0660822	0.0660822
403561	1200	650	0.113108	0.113108	0.0798755	0.0798755
403562	1200	850	0.0370598	0.0370598	0.071088	0.071088
403563	1200	1050	0.0801567	0.0801567	0.101411	0.101411
403564	1400	50	0.071718	0.071718	0.10235	0.10235
403565	1400	250	0.0616935	0.0616935	0.145871	0.145871
403566	1400	450	0.0260102	0.0260102	0.0579708	0.0579708
403567	1400	650	0.0534314	0.0534314	0.0994129	0.0994129
403568	1400	850	0.0778691	0.0778691	0.0417791	0.0417791
403569	1400	1050	0.0386117	0.0386117	0.0338794	0.0338794
403570	1400	1250	0.0646494	0.0646494	0.0735857	0.0735857
403571	1600	50	0.084153	0.084153	0.0945781	0.0945781
403572	1600	250	0.0341451	0.0341451	0.065537	0.065537
403573	1600	450	0.0608412	0.0608412	0.0825174	0.0825174
403574	1600	650	0.0226267	0.0226267	0.023287	0.023287
403575	1600	850	0.0314268	0.0314268	0.026356	0.026356
403576	1600	1050	0.0583082	0.0583082	0.045578	0.045578
403577	1600	1250	0.0143696	0.0143696	0.0339898	0.0339898
403578	1600	1450	0.0688314	0.0688314	0.0770537	0.0770537
403579	1700	50	0.144724	0.144724	0.148742	0.148742
403580	1700	250	0.0469454	0.0469454	0.0399466	0.0399466
403581	1700	450	0.0428287	0.0428287	0.0472713	0.0472713
403582	1700	650	0.0337162	0.0337162	0.0249037	0.0249037
403583	1700	850	0.0305686	0.0305686	0.0344235	0.0344235
403584	1700	1050	0.0207023	0.0207023	0.0400941	0.0400941
403585	1700	1250	0.0181012	0.0181012	0.022123	0.022123
403586	1700	1450	0.0306521	0.0306521	0.0111622	0.0111622
403587	1800	50	0.0320123	0.0320123	0.112356	0.112356
403588	1800	250	0.0367441	0.0367441	0.0667025	0.0667025
403589	1800	450	0.0560918	0.0560918	0.036927	0.036927
403590	1800	650	0.0304842	0.0304842	0.0258506	0.0258506
403591	1800	850	0.02256	0.02256	0.0179578	0.0179578
403592	1800	1050	0.0283868	0.0283868	0.0273356	0.0273356
403593	1800	1250	0.0200056	0.0200056	0.0216611	0.0216611
403594	1800	1450	0.0140548	0.0140548	0.047995	0.047995
403595	1800	1650	0.0602605	0.0602605	0.039856	0.039856
403596	1900	50	0.0672439	0.0672439	0.0509026	0.0509026
403597	1900	250	0.0509805	0.0509805	0.0713956	0.0713956
403598	1900	450	0.0142215	0.0142215	0.037855	0.037855

Not reviewed, for internal circulation only

403599	1900	650	0.0264694	0.0264694	0.0213384	0.0213384
403600	1900	850	0.00674613	0.00674613	0.0137325	0.0137325
403601	1900	1050	0.025343	0.025343	0.0119476	0.0119476
403602	1900	1250	0.0133266	0.0133266	0.00888444	0.00888444
403603	1900	1450	0.0180073	0.0180073	0.0195517	0.0195517
403604	1900	1650	0.0138375	0.0138375	0.0155516	0.0155516
403605	900	-	0.276289	0.276289	0.28537	0.28537
403606	1000	-	0.122065	0.122065	0.280728	0.280728
403607	1100	-	0.139437	0.139437	0.130411	0.130411
403608	1200	-	0.117504	0.117504	0.0680283	0.0680283
403609	1300	-	0.0623218	0.0623218	0.176242	0.176242
403610	1400	-	0.0784532	0.0784532	0.0540231	0.0540231
403611	1500	-	0.127603	0.127603	0.0737305	0.0737305
403612	1600	-	0.047918	0.047918	0.0519771	0.0519771
403613	1700	-	0.0959545	0.0959545	0.0987689	0.0987689
403614	1800	-	0.0815708	0.0815708	0.123194	0.123194
403615	2000	50	0.0551004	0.0551004	0.054329	0.054329
403616	2000	250	0.0360785	0.0360785	0.0614247	0.0614247
403617	2000	450	0.0462708	0.0462708	0.0423031	0.0423031
403618	2000	650	0.0215806	0.0215806	0.0379579	0.0379579
403619	2000	850	0.0194308	0.0194308	0.0256588	0.0256588
403620	2000	1050	0.0379085	0.0379085	0.0151485	0.0151485
403621	2000	1250	0.0350613	0.0350613	0.0444129	0.0444129
403622	2000	1450	0.0267852	0.0267852	0.0282129	0.0282129
403623	2000	1650	0.00985944	0.00985944	0.0461824	0.0461824
403624	2000	1850	0.0532942	0.0532942	0.0872003	0.0872003
403625	2100	50	0.0632303	0.0632303	0.0923489	0.0923489
403626	2100	250	0.0579379	0.0579379	0.0511582	0.0511582
403627	2100	450	0.0398985	0.0398985	0.0292309	0.0292309
403628	2100	650	0.0445307	0.0445307	0.0294402	0.0294402
403629	2100	850	0.0373669	0.0373669	0.0191655	0.0191655
403981	2100	1050	0.013561	0.013561	0.0276069	0.0276069
403982	2100	1250	0.0207286	0.0207286	0.0160121	0.0160121
403983	2100	1450	0.0184458	0.0184458	0.0132499	0.0132499
403984	2100	1650	0.0243378	0.0243378	0.0176747	0.0176747
403985	2100	1850	0.0232052	0.0232052	0.0376339	0.0376339

Table 20: PDF uncertainties.

⁷⁹⁷ **J. Expected signal yields in various regions at 36.1 fb^{-1}**

Not reviewed, for internal circulation only

Not reviewed, for internal circulation only

DSID	$m_{\tilde{g}}$	$m_{\tilde{\chi}}$	3jCR	UDR1	UDR2	5jSRb1	5jSRb1, $M_J^\Sigma > 0.8 \text{ TeV}$
403550	700	450	18007.19	26226.63	3563.41	1169.78	135.94
403551	800	450	8253.4	9748.88	2300.64	1262.93	220.71
403552	900	450	3641.39	3585.51	1099.23	1109.54	243.94
403553	1000	50	2546.68	1128.03	121.9	700.45	54.06
403554	1000	250	2021.49	1426.57	220.77	650.93	123.28
403555	1000	450	1581.89	1312.7	420.08	892.14	207.88
403556	1000	650	1474.7	1257.77	456.77	902.57	230.1
403557	1000	850	1599.84	1495.83	265.92	713.35	152.81
403558	1200	50	555.11	188.16	8.51	286.99	38.6
403559	1200	250	428.14	227.17	20.23	292.95	81.45
403560	1200	450	315.81	179.95	36.58	416.51	142.5
403561	1200	650	257.48	153.09	46.23	518.47	207.7
403562	1200	850	285.37	183.29	44.9	460.86	167.06
403563	1200	1050	354.18	232.89	25.72	327.94	92.95
403564	1400	50	138.21	37.3	0.55	114.33	20.02
403565	1400	250	105.07	43.95	1.98	117.48	40.26
403566	1400	450	71.65	34.02	3.03	178.68	81.21
403567	1400	650	55.12	26.19	4.16	223.07	108.39
403568	1400	850	52.25	25.28	3.82	237.66	119.47
403569	1400	1050	67.22	32.58	4.14	193.63	92.77
403570	1400	1250	84.69	45.63	2.25	139.2	49.37
403571	1600	50	37.28	9.77	0.1	42.95	9.98
403572	1600	250	28.18	10.73	0.04	48.54	23.17
403573	1600	450	19.54	7.54	0.33	68.67	36.47
403574	1600	650	13.83	4.89	0.32	90.01	51.77
403575	1600	850	10.95	3.82	0.38	99.26	61.03
403576	1600	1050	12.56	4.7	0.25	93.74	57.29
403577	1600	1250	17.92	6.49	0.41	74.82	43.55
403578	1600	1450	23.94	10.47	0.3	55.94	25.04

Table 21: Expected signal yield (normalized to 36.1 fb^{-1}) and systematic uncertainties (in percentage) for various signal points.

Not reviewed, for internal circulation only

DSID	$m_{\tilde{g}}$	$m_{\tilde{\chi}}$	3jCR	UDR1	UDR2	5jSRb1	5jSRb1, $M_J^\Sigma > 0.8 \text{ TeV}$
403579	1700	50	20.6	4.72	0.03	27.12	6.96
403580	1700	250	15.55	5.36	0.06	30.36	14.7
403581	1700	450	10.8	4.15	0.09	40.59	24.02
403582	1700	650	7.31	2.17	0.15	55.12	34.57
403583	1700	850	6.06	1.67	0.1	62.45	40.99
403584	1700	1050	5.7	1.77	0.07	62.22	41.47
403585	1700	1250	7.71	2.46	0.13	55.07	35.58
403586	1700	1450	11.16	4.58	0.18	40.12	22.78
403587	1800	50	10.83	2.47	0.02	16.84	5.06
403588	1800	250	8.82	2.91	0.02	19.2	10.1
403589	1800	450	6.08	2.06	0.03	25.6	16.09
403590	1800	650	3.85	1.1	0.05	34.15	22.81
403591	1800	850	2.88	0.78	0.03	38.69	26.86
403592	1800	1050	2.87	0.76	0.01	39.95	28.37
403593	1800	1250	3.6	0.91	0.01	36.63	26.07
403594	1800	1450	5.14	1.5	0.05	29.38	19.53
403595	1800	1650	7.37	2.64	0.02	21.0	10.39
403597	1900	250	4.7	1.56	0.0	12.01	6.56
403598	1900	450	3.39	1.16	0.02	15.84	10.61
403599	1900	650	2.25	0.57	0.0	21.15	15.0
403601	1900	1050	1.37	0.29	0.01	25.11	18.95
403602	1900	1250	1.77	0.37	0.01	24.14	17.95
403603	1900	1450	2.25	0.59	0.0	20.33	14.7
403615	2000	50	3.74	0.75	0.0	6.32	2.18
403616	2000	250	2.91	0.87	0.0	7.6	4.41
403617	2000	450	2.04	0.6	0.0	9.68	6.72
403618	2000	650	1.34	0.32	0.0	12.99	9.43
403619	2000	850	0.9	0.19	0.0	14.95	11.43
403620	2000	1050	0.84	0.2	0.0	15.66	12.3
403621	2000	1250	0.84	0.19	0.0	15.56	12.18
403622	2000	1450	1.13	0.26	0.0	13.94	10.71
403623	2000	1650	1.64	0.48	0.0	11.34	8.28
403624	2000	1850	2.5	0.77	0.0	8.38	4.83
403626	2100	250	1.64	0.47	0.0	4.65	2.8
403627	2100	450	1.13	0.35	0.0	6.0	4.35
403628	2100	650	0.7	0.18	0.0	7.77	5.76
403629	2100	850	0.5	0.11	0.0	9.26	7.28
403982	2100	1250	0.46	0.11	0.0	10.01	8.17
403983	2100	1450	0.48	0.09	0.0	9.19	7.35
403984	2100	1650	0.72	0.15	0.0	7.81	6.12

Table 22: Expected signal yield (normalized to 36.1 fb^{-1}) and systematic uncertainties (in percentage) for various signal points.

DSID	$m_{\tilde{g}}$	$m_{\tilde{\chi}}$	4jVR	5jVR	4jVRb	5jVRb
403550	700	450	2164.7	411.5	1652.6	335.1
403551	800	450	1535.5	444.4	1174.8	330.7
403552	900	450	1048.3	307.1	776.2	229.7
403553	1000	50	866.4	263.0	466.5	147.8
403554	1000	250	705.4	215.3	489.6	157.1
403555	1000	450	676.6	233.0	515.7	181.4
403556	1000	650	618.7	222.5	480.1	172.0
403557	1000	850	681.1	206.5	528.5	165.3
403558	1200	50	273.4	98.4	151.6	56.4
403559	1200	250	238.9	79.3	168.0	55.4
403560	1200	450	233.0	104.2	175.3	77.8
403561	1200	650	230.7	116.5	181.3	90.5
403562	1200	850	222.4	103.2	176.7	81.3
403563	1200	1050	227.2	83.3	181.1	67.8
403564	1400	50	83.7	33.7	45.0	19.4
403565	1400	250	74.4	27.9	53.0	19.9
403566	1400	450	73.7	35.5	54.4	25.6
403567	1400	650	74.2	41.0	57.5	31.6
403568	1400	850	71.6	41.5	57.0	33.3
403569	1400	1050	73.8	37.7	58.0	30.7
403570	1400	1250	73.6	30.1	56.8	23.1
403571	1600	50	26.2	11.2	14.8	6.2
403572	1600	250	25.6	10.9	18.1	7.7
403573	1600	450	25.3	13.3	19.2	10.2
403574	1600	650	23.7	14.8	18.9	11.5
403575	1600	850	23.5	15.7	18.5	12.4
403576	1600	1050	23.2	14.7	18.2	11.6
403577	1600	1250	23.3	13.0	18.3	10.2
403578	1600	1450	24.4	10.2	18.7	7.8

Table 23: Expected signal yield (normalized to 36.1 fb^{-1}) for validation regions (**Part 1**).

Not reviewed, for internal circulation only

DSID	$m_{\tilde{g}}$	$m_{\tilde{\chi}}$	4jVR	5jVR	4jVRb	5jVRb
403579	1700	50	15.2	7.0	8.3	4.0
403580	1700	250	14.6	6.2	10.5	4.7
403581	1700	450	15.2	8.3	11.3	6.2
403582	1700	650	14.1	9.0	11.2	7.2
403583	1700	850	13.1	8.6	10.2	6.7
403584	1700	1050	13.2	9.0	10.4	7.1
403585	1700	1250	13.4	8.5	10.3	6.8
403586	1700	1450	13.7	7.1	10.8	5.5
403587	1800	50	9.0	4.2	4.9	2.2
403588	1800	250	8.5	3.8	6.0	2.7
403589	1800	450	8.3	4.5	6.3	3.5
403590	1800	650	7.9	5.2	6.1	4.0
403591	1800	850	7.7	5.4	6.1	4.4
403592	1800	1050	7.1	5.2	5.7	4.2
403593	1800	1250	7.7	5.3	6.0	4.2
403594	1800	1450	8.0	4.8	6.1	3.7
403595	1800	1650	8.4	4.0	6.4	3.0
403596	1900	50	5.2	2.5	3.0	1.4
403597	1900	250	5.1	2.4	3.6	1.7
403598	1900	450	5.0	2.8	3.7	2.0
403599	1900	650	4.7	3.2	3.7	2.5
403600	1900	850	4.5	3.3	3.5	2.6
403601	1900	1050	4.2	3.1	3.3	2.5
403602	1900	1250	4.3	3.1	3.4	2.4
403603	1900	1450	4.8	3.2	3.7	2.4
403615	2000	50	3.1	1.5	1.7	0.8
403616	2000	250	2.8	1.3	2.0	0.9
403617	2000	450	2.9	1.6	2.2	1.2
403618	2000	650	2.8	1.8	2.1	1.4
403619	2000	850	2.6	1.9	2.0	1.4
403620	2000	1050	2.5	1.9	1.9	1.5
403621	2000	1250	2.4	1.8	1.8	1.4
403622	2000	1450	2.7	1.9	2.1	1.5
403623	2000	1650	2.9	1.8	2.2	1.3
403624	2000	1850	2.9	1.4	2.1	1.0
403625	2100	50	1.8	0.8	1.0	0.5
403626	2100	250	1.8	0.9	1.3	0.6
403627	2100	450	1.8	1.0	1.3	0.8
403628	2100	650	1.7	1.1	1.4	0.9
403629	2100	850	1.6	1.1	1.2	0.9
403981	2100	1050	1.4	1.1	1.1	0.8
403982	2100	1250	1.4	1.1	1.1	0.9
403983	2100	1450	1.5	1.1	1.1	0.8
403984	2100	1650	1.7	1.2	1.3	0.9
403985	2100	1850	1.7	0.9	1.2	0.7

Table 24: Expected signal yield (normalized to 36.1 fb^{-1}) for validation regions (**Part 2**).

Not reviewed, for internal circulation only

DSID	$m_{\tilde{g}}$	$m_{\tilde{\chi}}$	UDR1	UDR2	3jCR	3jCRb
403550	700	450	2164.7	411.5	1652.6	335.1
403551	800	450	1535.5	444.4	1174.8	330.7
403552	900	450	1048.3	307.1	776.2	229.7
403553	1000	50	866.4	263.0	466.5	147.8
403554	1000	250	705.4	215.3	489.6	157.1
403555	1000	450	676.6	233.0	515.7	181.4
403556	1000	650	618.7	222.5	480.1	172.0
403557	1000	850	681.1	206.5	528.5	165.3
403558	1200	50	273.4	98.4	151.6	56.4
403559	1200	250	238.9	79.3	168.0	55.4
403560	1200	450	233.0	104.2	175.3	77.8
403561	1200	650	230.7	116.5	181.3	90.5
403562	1200	850	222.4	103.2	176.7	81.3
403563	1200	1050	227.2	83.3	181.1	67.8
403564	1400	50	83.7	33.7	45.0	19.4
403565	1400	250	74.4	27.9	53.0	19.9
403566	1400	450	73.7	35.5	54.4	25.6
403567	1400	650	74.2	41.0	57.5	31.6
403568	1400	850	71.6	41.5	57.0	33.3
403569	1400	1050	73.8	37.7	58.0	30.7
403570	1400	1250	73.6	30.1	56.8	23.1
403571	1600	50	26.2	11.2	14.8	6.2
403572	1600	250	25.6	10.9	18.1	7.7
403573	1600	450	25.3	13.3	19.2	10.2
403574	1600	650	23.7	14.8	18.9	11.5
403575	1600	850	23.5	15.7	18.5	12.4
403576	1600	1050	23.2	14.7	18.2	11.6
403577	1600	1250	23.3	13.0	18.3	10.2
403578	1600	1450	24.4	10.2	18.7	7.8

Table 25: Expected signal yield (normalized to 36.1 fb^{-1}) for UDRs and control regions (**Part 1**).

Not reviewed, for internal circulation only

DSID	$m_{\tilde{g}}$	$m_{\tilde{\chi}}$	UDR1	UDR2	3jCR	3jCRb
403579	1700	50	15.2	7.0	8.3	4.0
403580	1700	250	14.6	6.2	10.5	4.7
403581	1700	450	15.2	8.3	11.3	6.2
403582	1700	650	14.1	9.0	11.2	7.2
403583	1700	850	13.1	8.6	10.2	6.7
403584	1700	1050	13.2	9.0	10.4	7.1
403585	1700	1250	13.4	8.5	10.3	6.8
403586	1700	1450	13.7	7.1	10.8	5.5
403587	1800	50	9.0	4.2	4.9	2.2
403588	1800	250	8.5	3.8	6.0	2.7
403589	1800	450	8.3	4.5	6.3	3.5
403590	1800	650	7.9	5.2	6.1	4.0
403591	1800	850	7.7	5.4	6.1	4.4
403592	1800	1050	7.1	5.2	5.7	4.2
403593	1800	1250	7.7	5.3	6.0	4.2
403594	1800	1450	8.0	4.8	6.1	3.7
403595	1800	1650	8.4	4.0	6.4	3.0
403596	1900	50	5.2	2.5	3.0	1.4
403597	1900	250	5.1	2.4	3.6	1.7
403598	1900	450	5.0	2.8	3.7	2.0
403599	1900	650	4.7	3.2	3.7	2.5
403600	1900	850	4.5	3.3	3.5	2.6
403601	1900	1050	4.2	3.1	3.3	2.5
403602	1900	1250	4.3	3.1	3.4	2.4
403603	1900	1450	4.8	3.2	3.7	2.4
403615	2000	50	3.1	1.5	1.7	0.8
403616	2000	250	2.8	1.3	2.0	0.9
403617	2000	450	2.9	1.6	2.2	1.2
403618	2000	650	2.8	1.8	2.1	1.4
403619	2000	850	2.6	1.9	2.0	1.4
403620	2000	1050	2.5	1.9	1.9	1.5
403621	2000	1250	2.4	1.8	1.8	1.4
403622	2000	1450	2.7	1.9	2.1	1.5
403623	2000	1650	2.9	1.8	2.2	1.3
403624	2000	1850	2.9	1.4	2.1	1.0
403625	2100	50	1.8	0.8	1.0	0.5
403626	2100	250	1.8	0.9	1.3	0.6
403627	2100	450	1.8	1.0	1.3	0.8
403628	2100	650	1.7	1.1	1.4	0.9
403629	2100	850	1.6	1.1	1.2	0.9
403981	2100	1050	1.4	1.1	1.1	0.8
403982	2100	1250	1.4	1.1	1.1	0.9
403983	2100	1450	1.5	1.1	1.1	0.8
403984	2100	1650	1.7	1.2	1.3	0.9
403985	2100	1850	1.7	0.9	1.2	0.7

Table 26: Expected signal yield (normalized to 36.1 fb^{-1}) for UDRs and control regions (**Part 2**).

798 K. Implemnetation of the background estimation method

799 A data-driven method is used to predict the background yield in the signal regions, as well as the uncer-
 800 tainties on those predictions. First, jet mass templates are created from control region jets. Randomized
 801 jet masses, called dressed masses, are generated from these templates for each jet in the kinematic sample.
 802 Summing the dressed masses for each of the up to four leading jets in an event gives the dressed M_j^Σ for
 803 that event. The dressed M_j^Σ distribution for each signal region is used to estimate the expected background
 804 contribution to that region.

805 K.1. Jet mass templates

806 Separate templates are created for b-matched and non-b-matched jets. A b-matched jet is defined as a
 807 large-R jet within $\Delta R = 1.0$ of a b-tagged small-R jet. For the b-matched templates, only events with
 808 $|\Delta\eta_{1,2}| > 1.4$ are included in the templates.

809 Templates are binned in p_T and $|\eta|$. The p_T bins are approximately logarithmic, while the $|\eta|$ bin
 810 boundaries are at 0.0, 0.5, 1.0, and 1.5.

811 The template binning and number of jets contributing to each bin are shown in figure 73.

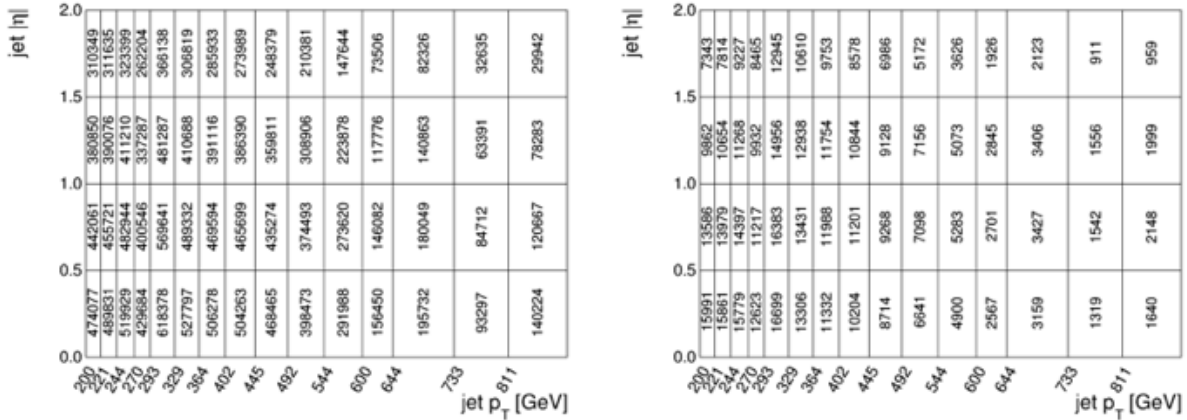


Figure 73: Number of jets contributing to each template bin for the non-b-matched (left) and b-matched (right) templates.

812 Each template is a one-dimensional histogram of $\log(m/p_T)$, with 50 bins. Jets with $\log(m/p_T) < -7$
 813 are excluded from the templates.

814 K.2. Jet mass randomization

815 For each jet in the kinematic region, a dressed mass is generated by sampling from the template corres-
 816 ponding to its p_T , $|\eta|$ and b-match bin. To generate a dressed mass, the empirical cumulative distribution
 817 function (ECDF) is calculated for the template. A uniform random number, y , in the range $[0, 1)$ is then
 818 generated. The inverse of the ECDF, $\Phi^{-1}(y)$, gives a randomized $\log(m/p_T)$ bin. A second uniform

random number, x , is sampled from the range $[x_1, x_2]$, where x_1, x_2 are the edges of the selected bin. The dressed mass is then computed as $m_{dressed} = p_T \exp(x)$.

To obtain a dressed M_J^Σ for an event, one dressed mass is generated for each jet, and the dressed masses are summed. For events with more than four jets, only the first four leading jets are included in the sum.

K.3. Dressed mass response

Dressed mass response plots are created by plotting the average dressed and kinematic jet mass in each p_T bin. The dressed mass response for the control region is shown in figure 74. A Good agreement between average dressed and kinematic masses is observed.

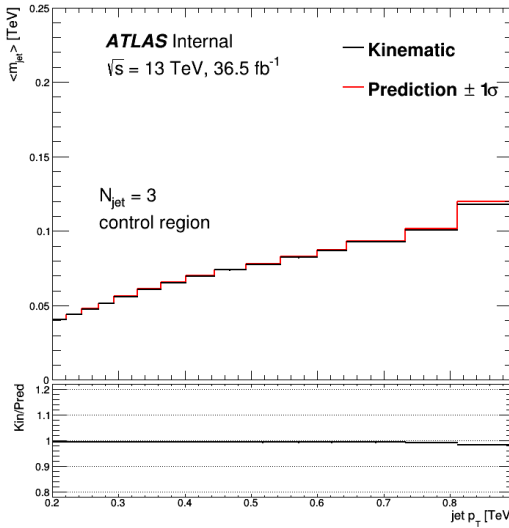


Figure 74: Average dressed and kinematic jet masses for each p_T bin in the control region

K.4. Dressed M_J^Σ distributions

To obtain the nominal dressed M_J^Σ distribution, n_{toys} histograms of M_J^Σ are created, where each histogram is generated by dressing all events in the sample once. For each M_J^Σ bin, the average bin content over all histograms is taken as the nominal value, and the standard deviation of bin contents is taken as the statistical uncertainty.

The M_J^Σ histograms are binned in the following manner. There are ten equal-width bins covering the range $0 \text{ TeV} \leq M_J^\Sigma < 0.5 \text{ TeV}$. The next three bins cover the ranges $0.5 \text{ TeV} \leq M_J^\Sigma < 0.6 \text{ TeV}$, $0.6 \text{ TeV} \leq M_J^\Sigma < 0.8 \text{ TeV}$, and $0.8 \text{ TeV} \leq M_J^\Sigma < 1.0 \text{ TeV}$. The final bin is $M_J^\Sigma \geq 1.0 \text{ TeV}$

835 K.5. Normalization

836 The dressed M_J^Σ distributions are scaled such that the dressed yield in the range $0.2 \text{ TeV} < M_J^\Sigma < 0.4 \text{ TeV}$
 837 is equal to the kinematic yield in the same range. Separate scale factors are derived for each of the validation
 838 and signal regions.

839 K.6. Systematic uncertainty

840 Systematic uncertainties are derived from the dressed mass response in the UDRs. Systematic uncertainties
 841 are binned in p_T and $|\eta|$. The lowest p_T bin is for jets with $p_T < 402 \text{ GeV}$. The second bin is for jets
 842 with $402 \text{ GeV} \leq p_T < 544 \text{ GeV}$, and the highest bin is for jets with $p_T \geq 544 \text{ GeV}$. For jets with
 843 $p_T \geq 402 \text{ GeV}$, uncertainties are derived only from UDR1.

844 For jets with $p_T < 402 \text{ GeV}$, uncertainties are derived from both UDR1 and UDR2, and the maximum
 845 uncertainty is used.

846 For each p_T bin in the UDR dressed mass response, a fractional error is calculated as $e_i = (\langle m_{kin} \rangle - \langle m_{dressed} \rangle) / \langle m_{dressed} \rangle$.

848 For the lowest and highest p_T systematic bins, the root-mean-square of fractional errors is taken as the
 849 systematic error. For the intermediate systematic bin, the maximum fractional error is taken

850 K.7. Propagation of uncertainty

851 Two separate systematic uncertainties are derived. The first uncertainty accounts for the discrepancy
 852 between dressed and kinematic masses for jets with $p_T \geq 402 \text{ GeV}$, and the second accounts for the
 853 discrepancy for jets with $p_T < 402 \text{ GeV}$.

854 To propagate the low- p_T systematic, two shifted M_J^Σ values are calculated for each dressed M_J^Σ . The first
 855 shifted value is obtained by increasing the dressed mass of every low- p_T jet by its corresponding fractional
 856 uncertainty. This yields n_{toys} histograms of shifted M_J^Σ . The average value of each bin content over all
 857 toys is taken to obtain the systematically-shifted M_J^Σ distribution.

858 The second shifted distribution is obtained by decreasing the dressed mass of every low- p_T jet by its
 859 corresponding fractional uncertainty, and averaging over all the toys to obtain a downwards-shifted
 860 distribution of M_J^Σ .

861 The same procedure is used to propagate the high- p_T systematic, but the high- p_T jets are shifted instead
 862 of the low- p_T jets.

863 K.8. Determining predicted M_J^Σ and uncertainties

864 To determine the nominal predicted background yield, one thousand toys are generated, where a toy
 865 consists of a dressed M_J^Σ value for each event in the kinematic sample. For each toy, the number of events
 866 with dressed M_J^Σ greater than the signal region M_J^Σ cut are counted, giving a distribution of one thousand
 867 dressed background yields. The central value of this distribution is multiplied by the scale factor to obtain

Not reviewed, for internal circulation only

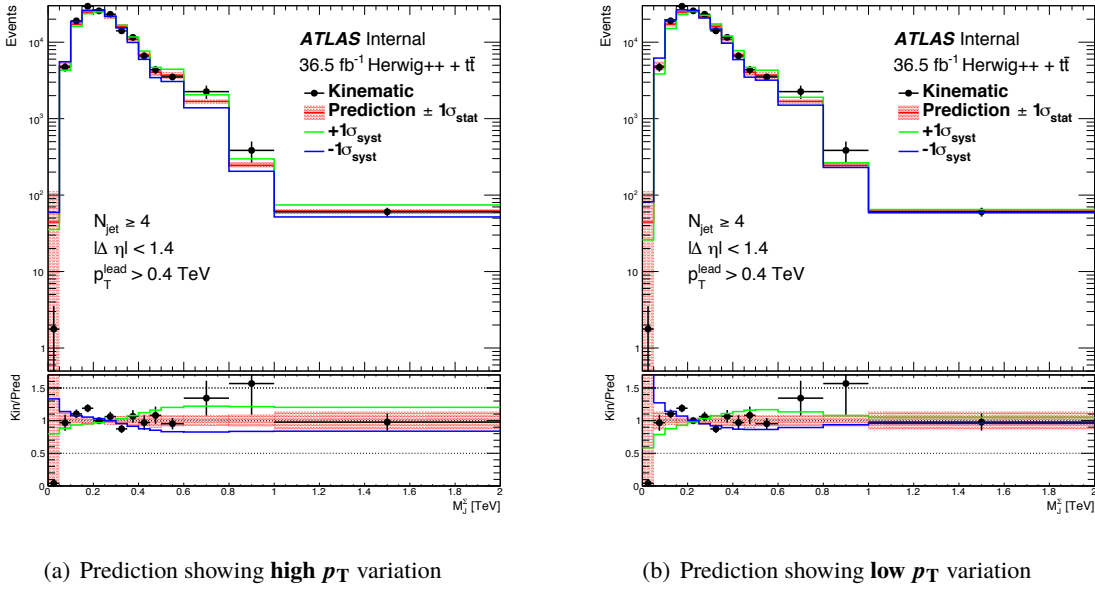


Figure 75: Predicted and observed M_J^Σ distributions in Herwigpp multijet and $t\bar{t}$ Monte Carlo background samples. The events are selected by requiring four or more large- R jets and a leading large- R jet with $p_T > 400$ GeV. The $|\Delta\eta_{12}|$ of the event is required to be less than 1.4. There is no requirement on the presence of a b-tagged jet. The black dots with error bars indicate the observed M_J^Σ distribution and its statistical uncertainty. The solid red histogram with shaded bands indicate the predicted M_J^Σ distribution and its statistical uncertainty. The green and blue histograms correspond to $\pm 1 \sigma$ variation of one of the systematic uncertainties identified in the analysis. Subfigure (a) shows variations of the “high p_T ” systematic uncertainty, while subfigure (b) shows variations of the “low p_T ” systematic uncertainty. The bottom pane show the ratio of the observed M_J^Σ distribution over the expected M_J^Σ distribution or its systematic variations. The Herwigpp multijet MC samples are a combination of samples with different leading jet p_T requirements (known as the JZW samples in ATLAS), and the lowest MC luminosity of these samples is 3.6 fb^{-1} .

- 868 the nominal background prediction. The standard deviation of this distribution is multiplied by the scale
869 factor to obtain the statistical uncertainty on the background prediction.
- 870 Systematically-shifted background yield predictions are determined by repeating the above procedure for
871 the systematically-shifted dressed M_J^Σ values. The systematic uncertainties are taken as the difference
872 between the nominal and systematically-shifted background yield predictions. Scale factors are only
873 derived from the nominal M_J^Σ distributions and applied to both the nominal and systematically-shifted
874 predictions.
- 875 The two systematic uncertainties are symmetrized by taking the maximum of the downward-shifted and
876 upward-shifted uncertainties.

Not reviewed, for internal circulation only

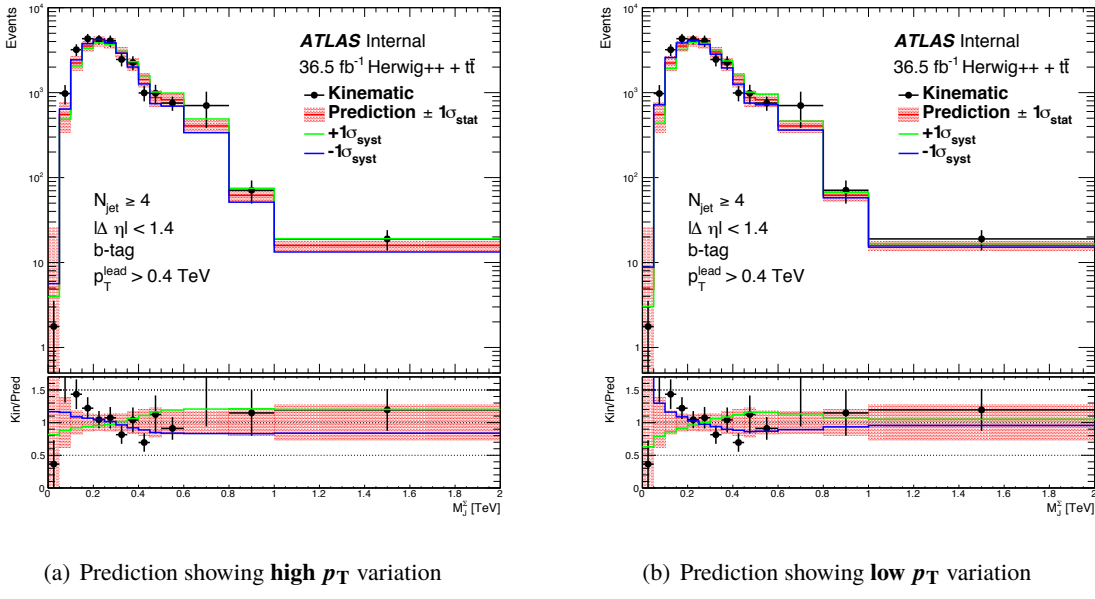


Figure 76: Predicted and observed M_J^Σ distributions in Herwigpp multijet and $t\bar{t}$ Monte Carlo background samples. The events are selected by requiring four or more large- R jets and a leading large- R jet with $p_T > 400$ GeV. The $|\Delta\eta_{12}|$ of the event is required to be less than 1.4. At least one b-tagged jet is required to be present in the event. The black dots with error bars indicate the observed M_J^Σ distribution and its statistical uncertainty. The solid red histogram with shaded bands indicate the predicted M_J^Σ distribution and its statistical uncertainty. The green and blue histograms correspond to $\pm 1 \sigma$ variation of one of the systematic uncertainties identified in the analysis. Subfigure (a) shows variations of the “high p_T ” systematic uncertainty, while subfigure (b) shows variations of the “low p_T ” systematic uncertainty. The bottom pane show the ratio of the observed M_J^Σ distribution over the expected M_J^Σ distribution or its systematic variations. The Herwigpp multijet MC samples are a combination of samples with different leading jet p_T requirements (known as the JZW samples in ATLAS), and the lowest MC luminosity of these samples is 3.6 fb^{-1} .

L. Predicted and observed M_J^Σ distributions in Herwigpp multijet plus $t\bar{t}$ MC samples

M. Trigger impact on CR and UDRs

Figure 7 in Section 3.2 demonstrates the HLT_ht1000_L1J100 trigger is fully efficient for the signal and validation regions used in the analysis. Further checks are made to understand if the trigger turn-on has any effect on the jet mass response in the CR and UDRs. Figures 83, 84, and 85 compare the jet mass response between two versions of the same analysis, one with the current analysis selection, and one with an additional offline H_T requirement so that the HLT_ht1000_L1J100 trigger is fully efficient for the UDRs and CR. It is seen that the additional H_T requirement does not change the jet mass response in any significant way. Small variations are seen in the comparison, but these variations are within the level of jet mass systematic uncertainty.

Not reviewed, for internal circulation only

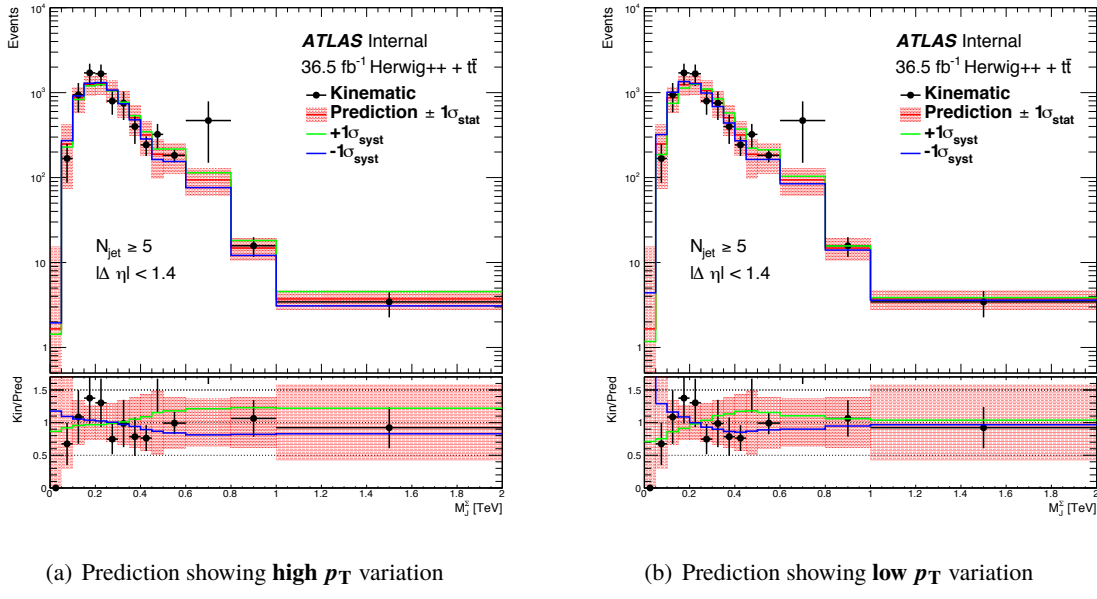


Figure 77: Predicted and observed M_J^Σ distributions in Herwigpp multijet and $t\bar{t}$ Monte Carlo background samples. The events are selected by requiring five or more large- R jets and a leading large- R jet with $p_T > 400$ GeV. The $|\Delta\eta_{12}|$ of the event is required to be less than 1.4. There is no requirement on the presence of a b-tagged jet. The black dots with error bars indicate the observed M_J^Σ distribution and its statistical uncertainty. The solid red histogram with shaded bands indicate the predicted M_J^Σ distribution and its statistical uncertainty. The green and blue histograms correspond to $\pm 1 \sigma$ variation of one of the systematic uncertainties identified in the analysis. Subfigure (a) shows variations of the “high p_T ” systematic uncertainty, while subfigure (b) shows variations of the “low p_T ” systematic uncertainty. The bottom pane show the ratio of the observed M_J^Σ distribution over the expected M_J^Σ distribution or its systematic variations. The Herwigpp multijet MC samples are a combination of samples with different leading jet p_T requirements (known as the JZW samples in ATLAS), and the lowest MC luminosity of these samples is 3.6 fb^{-1} .

N. Jet mass templates comparison between the b-matched jets and non-matched jets

Not reviewed, for internal circulation only

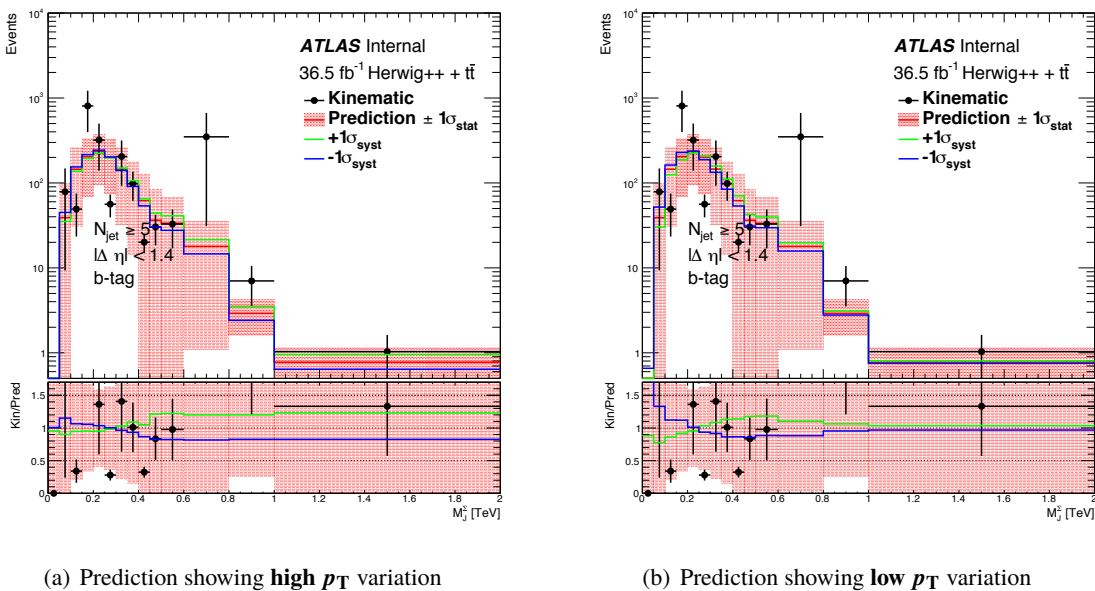


Figure 78: Predicted and observed M_j^Σ distributions in Herwigpp multijet and $t\bar{t}$ Monte Carlo background samples. The events are selected by requiring five or more large- R jets and a leading large- R jet with $p_T > 400$ GeV. The $|\Delta\eta_{12}|$ of the event is required to be less than 1.4. At least one b-tagged jet is required to be present in the event. The black dots with error bars indicate the observed M_j^Σ distribution and its statistical uncertainty. The solid red histogram with shaded bands indicate the predicted M_j^Σ distribution and its statistical uncertainty. The green and blue histograms correspond to $\pm 1 \sigma$ variation of one of the systematic uncertainties identified in the analysis. Subfigure (a) shows variations of the “high p_T ” systematic uncertainty, while subfigure (b) shows variations of the “low p_T ” systematic uncertainty. The bottom pane show the ratio of the observed M_j^Σ distribution over the expected M_j^Σ distribution or its systematic variations. The Herwigpp multijet MC samples are a combination of samples with different leading jet p_T requirements (known as the JZW samples in ATLAS), and the lowest MC luminosity of these samples is 3.6 fb^{-1} .

Not reviewed, for internal circulation only

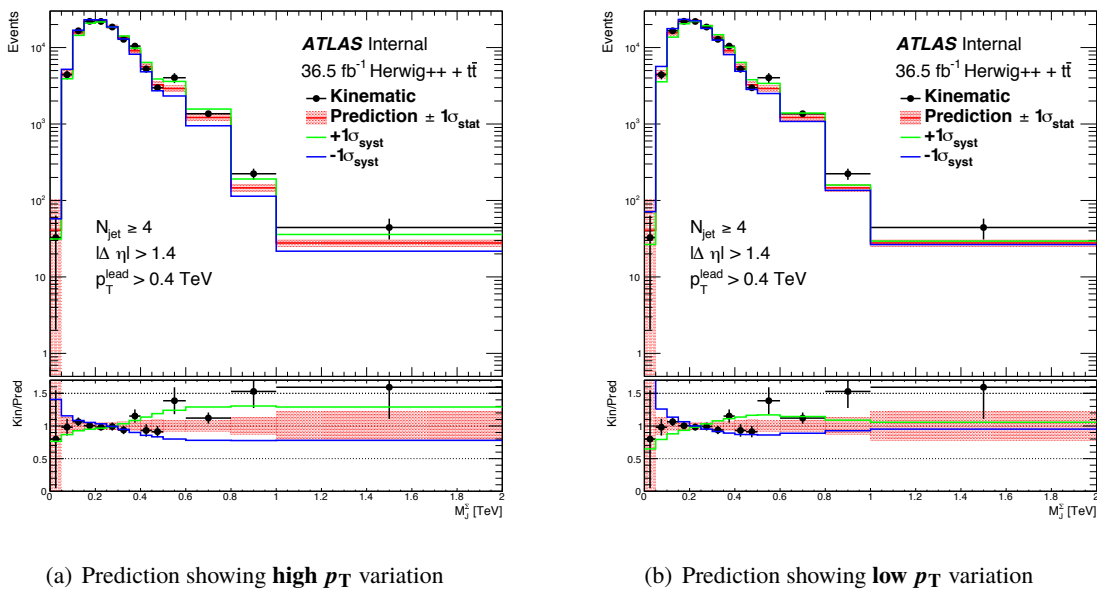


Figure 79: Predicted and observed M_j^Σ distributions in Herwigpp multijet and $t\bar{t}$ Monte Carlo background samples. The events are selected by requiring four or more large- R jets and a leading large- R jet with $p_T > 400$ GeV. The $|\Delta\eta_{12}|$ of the event is required to be greater than 1.4. There is no requirement on the presence of a b-tagged jet. The black dots with error bars indicate the observed M_j^Σ distribution and its statistical uncertainty. The solid red histogram with shaded bands indicate the predicted M_j^Σ distribution and its statistical uncertainty. The green and blue histograms correspond to $\pm 1 \sigma$ variation of one of the systematic uncertainties identified in the analysis. Subfigure (a) shows variations of the “high p_T ” systematic uncertainty, while subfigure (b) shows variations of the “low p_T ” systematic uncertainty. The bottom pane show the ratio of the observed M_j^Σ distribution over the expected M_j^Σ distribution or its systematic variations. The Herwigpp multijet MC samples are a combination of samples with different leading jet p_T requirements (known as the JZW samples in ATLAS), and the lowest MC luminosity of these samples is 3.6 fb^{-1} .

Not reviewed, for internal circulation only

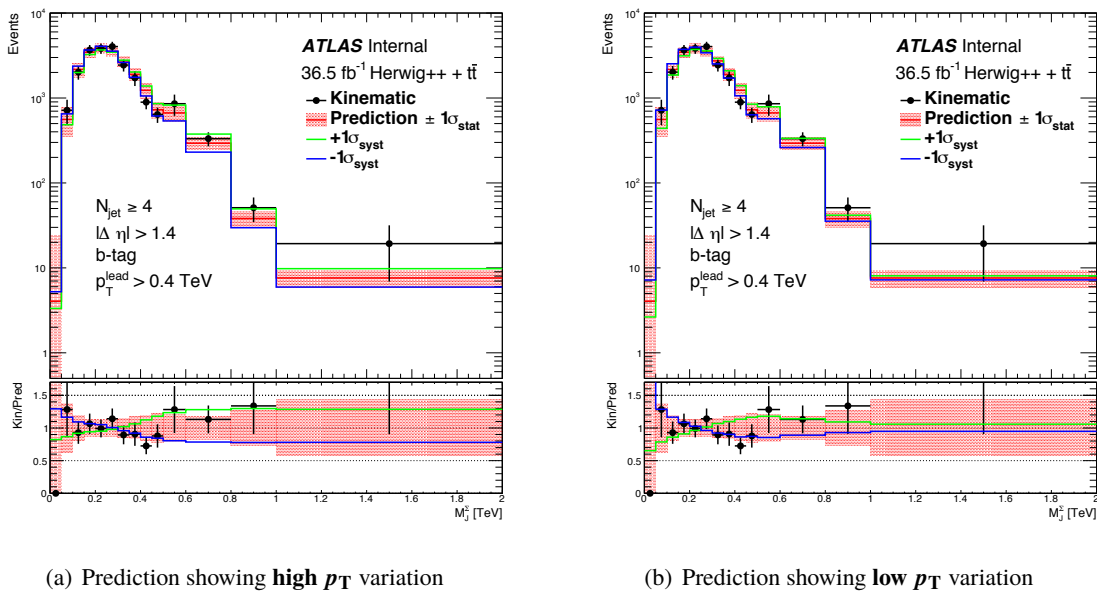


Figure 80: Predicted and observed M_j^Σ distributions in Herwigpp multijet and $t\bar{t}$ Monte Carlo background samples. The events are selected by requiring four or more large- R jets and a leading large- R jet with $p_T > 400$ GeV. The $|\Delta\eta_{12}|$ of the event is required to be greater than 1.4. At least one b-tagged jet is required to be present in the event. The black dots with error bars indicate the observed M_j^Σ distribution and its statistical uncertainty. The solid red histogram with shaded bands indicate the predicted M_j^Σ distribution and its statistical uncertainty. The green and blue histograms correspond to $\pm 1 \sigma$ variation of one of the systematic uncertainties identified in the analysis. Subfigure (a) shows variations of the “high p_T ” systematic uncertainty, while subfigure (b) shows variations of the “low p_T ” systematic uncertainty. The bottom pane show the ratio of the observed M_j^Σ distribution over the expected M_j^Σ distribution or its systematic variations. The Herwigpp multijet MC samples are a combination of samples with different leading jet p_T requirements (known as the JZW samples in ATLAS), and the lowest MC luminosity of these samples is 3.6 fb^{-1} .

Not reviewed, for internal circulation only

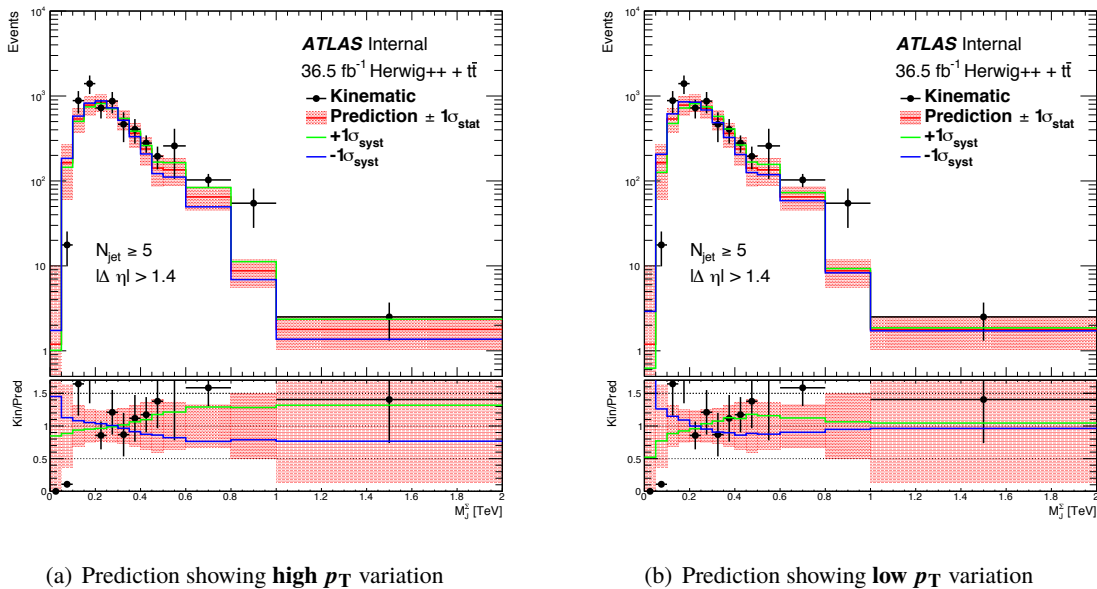


Figure 81: Predicted and observed M_j^Σ distributions in Herwigpp multijet and $t\bar{t}$ Monte Carlo background samples. The events are selected by requiring five or more large- R jets and a leading large- R jet with $p_T > 400$ GeV. The $|\Delta\eta_{12}|$ of the event is required to be greater than 1.4. There is no requirement on the presence of a b-tagged jet. The black dots with error bars indicate the observed M_j^Σ distribution and its statistical uncertainty. The solid red histogram with shaded bands indicate the predicted M_j^Σ distribution and its statistical uncertainty. The green and blue histograms correspond to $\pm 1 \sigma$ variation of one of the systematic uncertainties identified in the analysis. Subfigure (a) shows variations of the “high p_T ” systematic uncertainty, while subfigure (b) shows variations of the “low p_T ” systematic uncertainty. The bottom pane show the ratio of the observed M_j^Σ distribution over the expected M_j^Σ distribution or its systematic variations. The Herwigpp multijet MC samples are a combination of samples with different leading jet p_T requirements (known as the JZW samples in ATLAS), and the lowest MC luminosity of these samples is 3.6 fb^{-1} .

Not reviewed, for internal circulation only

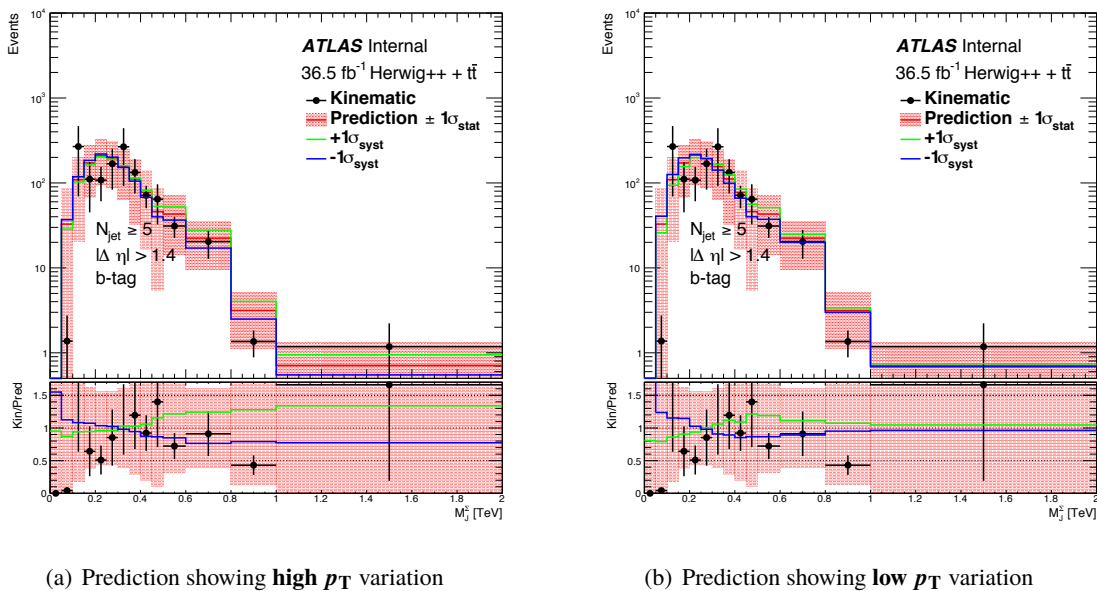


Figure 82: Predicted and observed M_j^Σ distributions in Herwigpp multijet and $t\bar{t}$ Monte Carlo background samples. The events are selected by requiring five or more large- R jets and a leading large- R jet with $p_T > 400$ GeV. The $|\Delta\eta_{12}|$ of the event is required to be greater than 1.4. At least one b-tagged jet is required to be present in the event. The black dots with error bars indicate the observed M_j^Σ distribution and its statistical uncertainty. The solid red histogram with shaded bands indicate the predicted M_j^Σ distribution and its statistical uncertainty. The green and blue histograms correspond to $\pm 1 \sigma$ variation of one of the systematic uncertainties identified in the analysis. Subfigure (a) shows variations of the “high p_T ” systematic uncertainty, while subfigure (b) shows variations of the “low p_T ” systematic uncertainty. The bottom pane show the ratio of the observed M_j^Σ distribution over the expected M_j^Σ distribution or its systematic variations. The Herwigpp multijet MC samples are a combination of samples with different leading jet p_T requirements (known as the JZW samples in ATLAS), and the lowest MC luminosity of these samples is 3.6 fb^{-1} .

Not reviewed, for internal circulation only

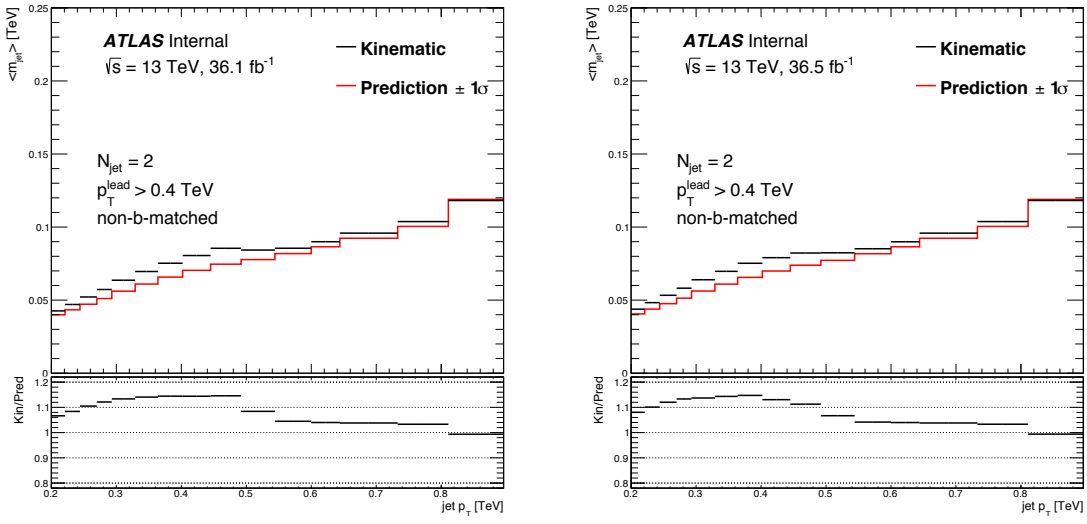


Figure 83: Trigger efficiency is shown as a function of large- R jet p_T threshold for events with our or more large- R jets events with five or more large- R jets.

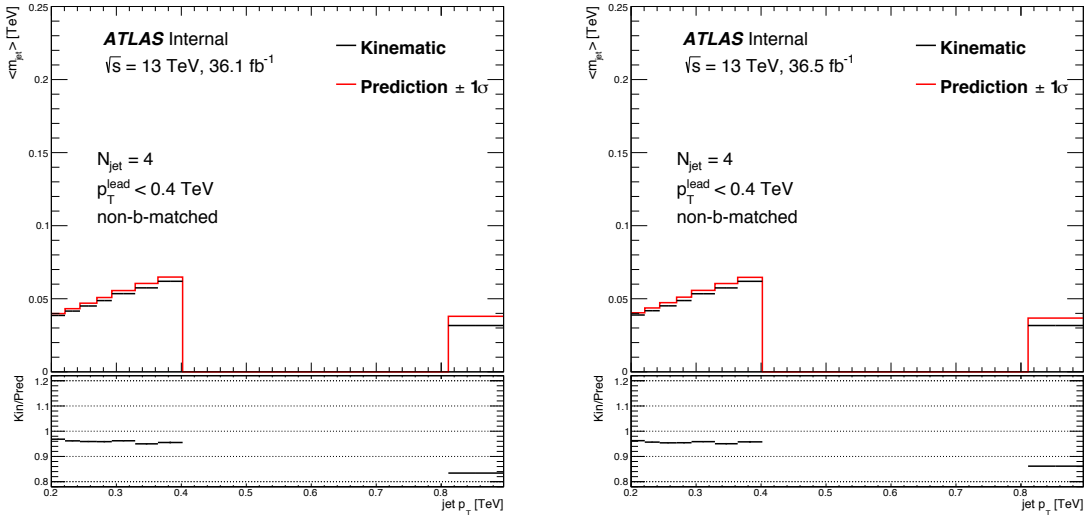


Figure 84: Trigger efficiency is shown as a function of large- R jet p_T threshold for events with our or more large- R jets events with five or more large- R jets.

Not reviewed, for internal circulation only

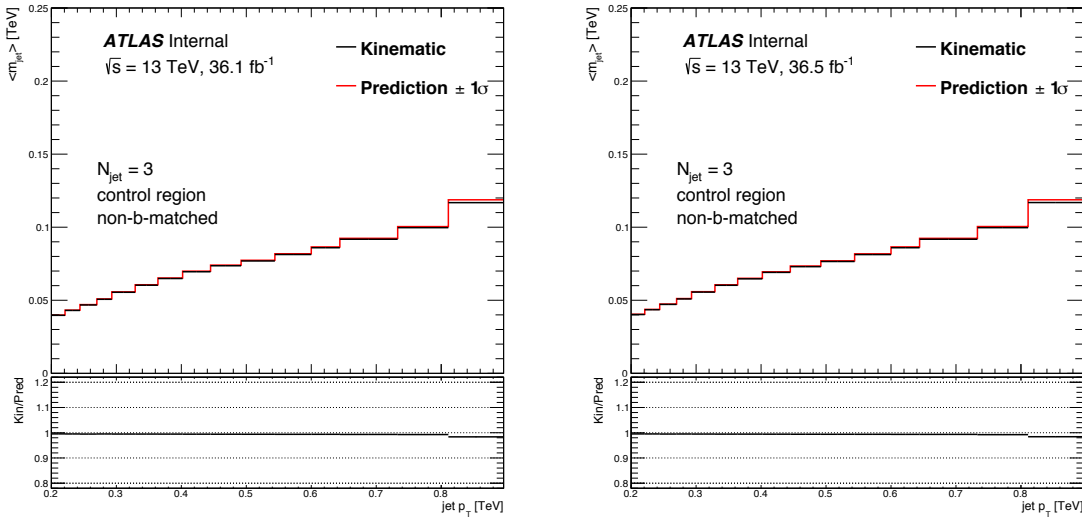


Figure 85: Trigger efficiency is shown as a function of large- R jet p_T threshold for events with our or more large- R jets events with five or more large- R jets.

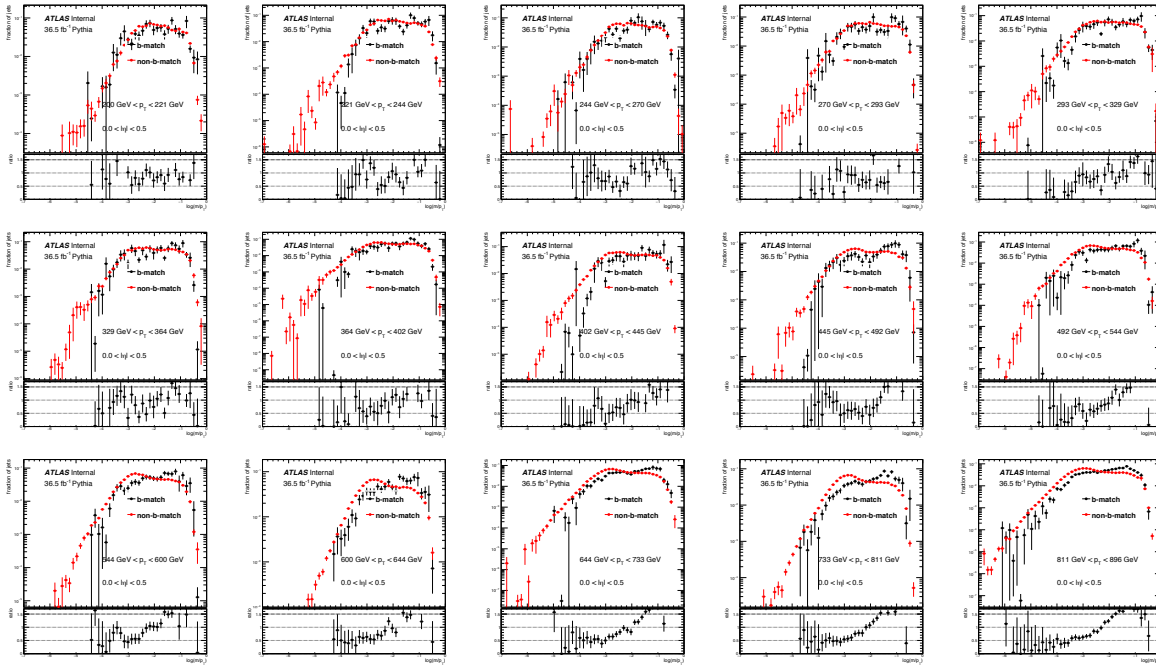


Figure 86: Jet mass templates comparison between b-matched jets and non-matched jets in the η region between 0 and 0.5. PYTHIA8 multijet sample is used for this comparison.

Not reviewed, for internal circulation only

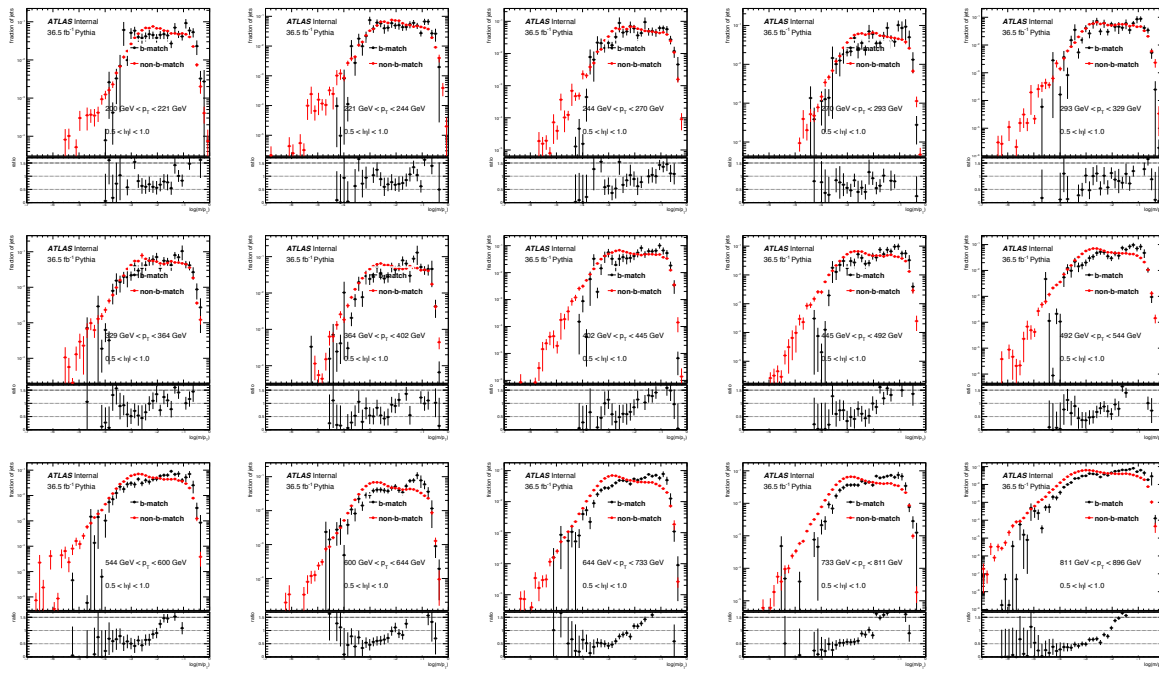


Figure 87: Jet mass templates comparison between b-matched jets and non-matched jets in the η region between 0.5 and 1.0. PYTHIA8 multijet sample is used for this comparison.

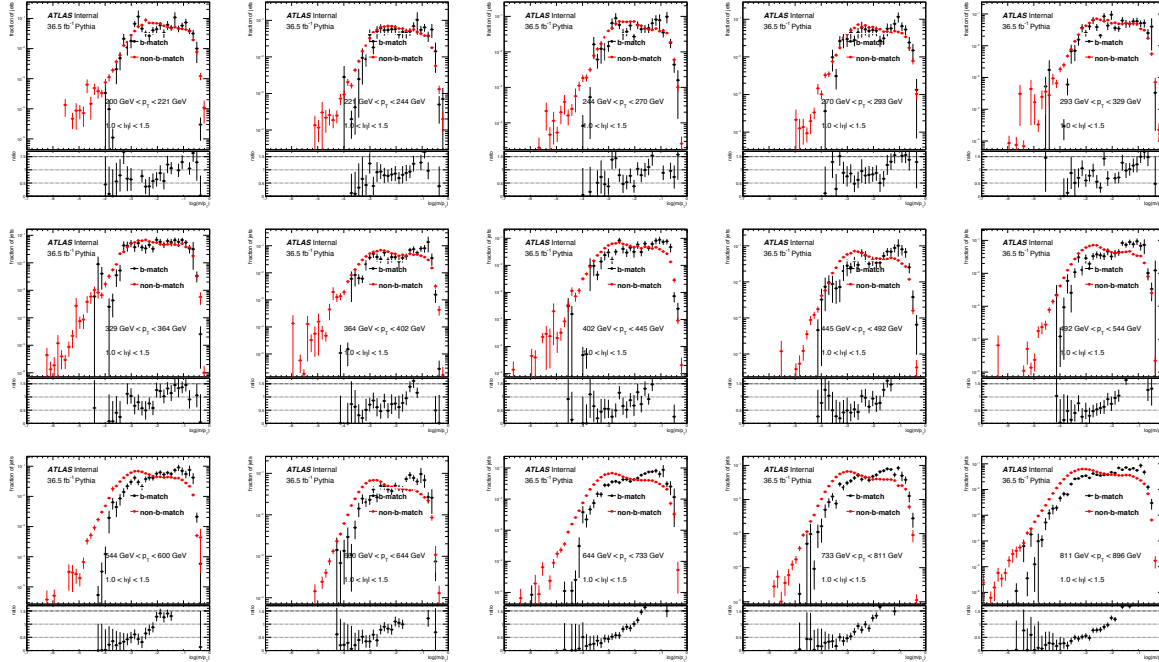


Figure 88: Jet mass templates comparison between b-matched jets and non-matched jets in the η region between 1.0 and 1.5. PYTHIA8 multijet sample is used for this comparison.

Not reviewed, for internal circulation only

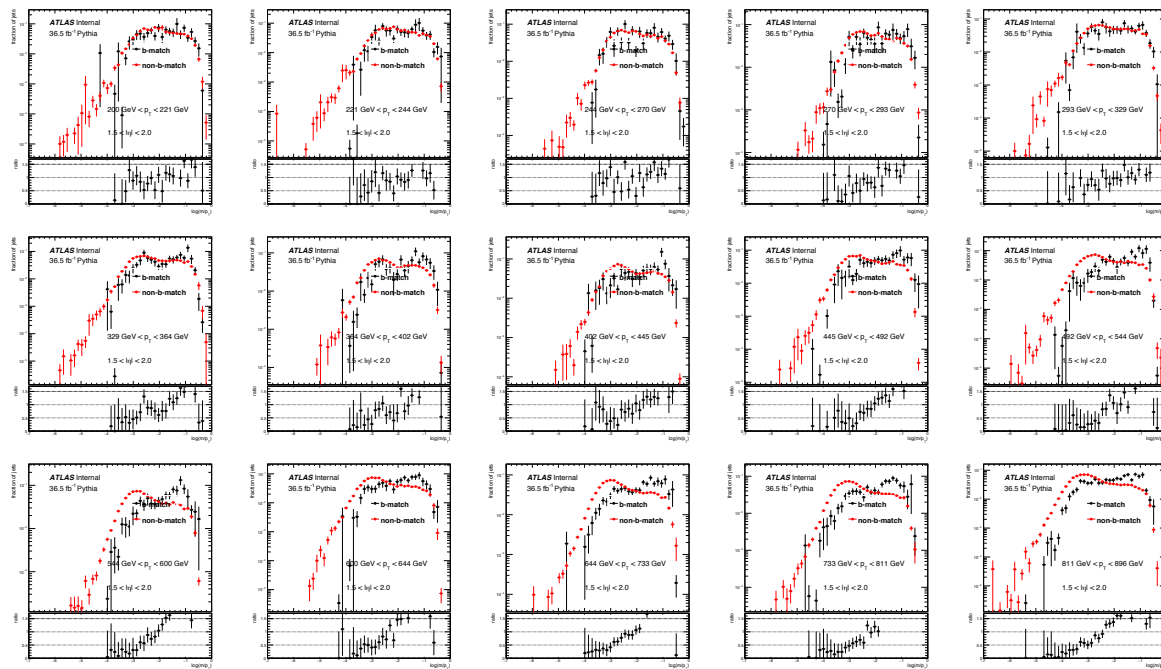


Figure 89: Jet mass templates comparison between b-matched jets and non-matched jets in the η region between 1.5 and 2.0. PYTHIA8 multijet sample is used for this comparison.

Not reviewed, for internal circulation only

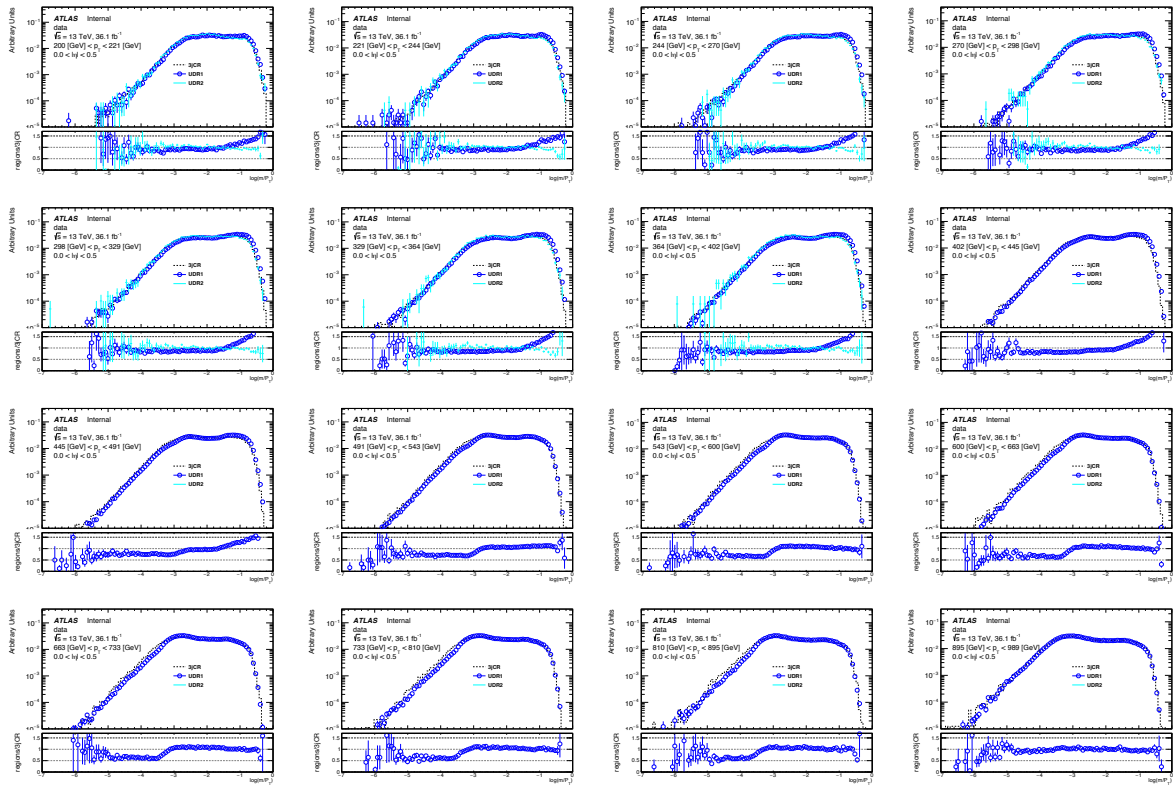


Figure 90: Jet mass PDFs comparison between CR and UDRs. Jets with $0.0 < |\eta| < 0.5$ from data are used.

890 O. Jet mass PDFs comparison between CR and UDRs

891 Figures 90 - 93 show the comparison of jet mass PDF between the control region and the two UDRs using
 892 data. Figures 94 - 97 show the same comparison plots for the jet mass distributions.

Not reviewed, for internal circulation only

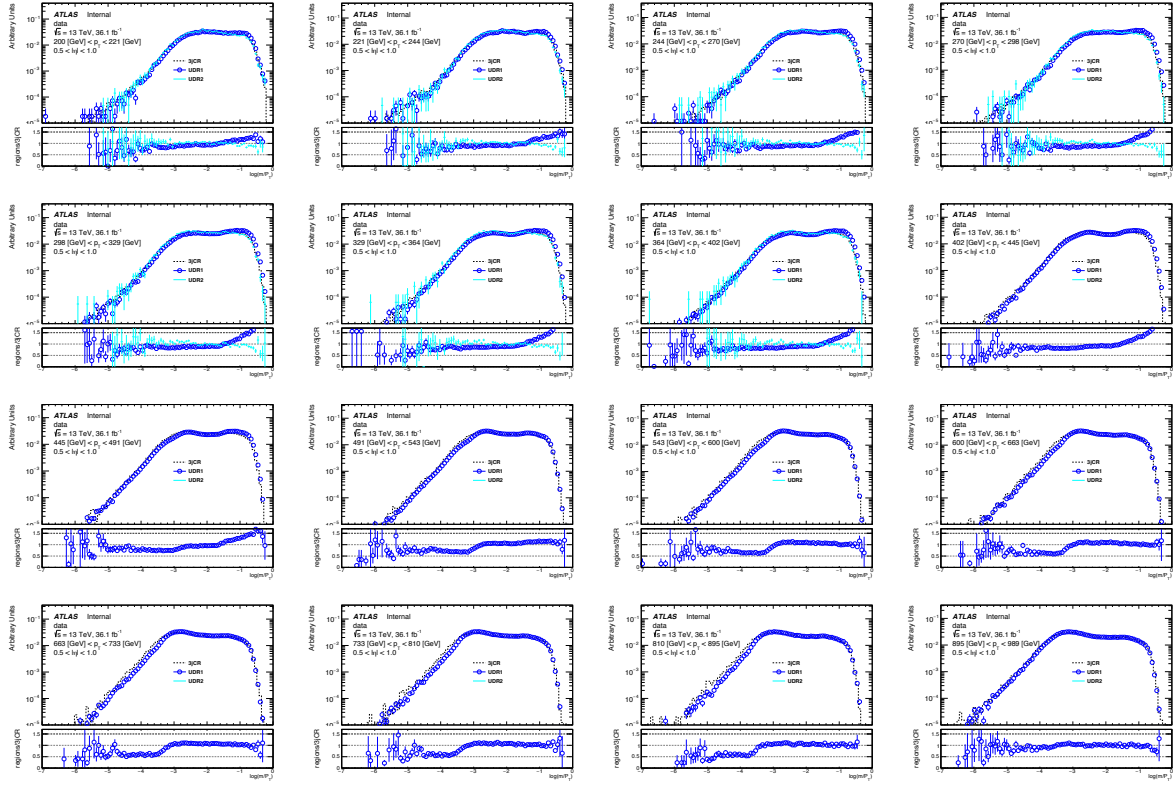


Figure 91: Jet mass PDFs comparison between CR and UDRs. Jets with $0.5 < |\eta| < 1.0$ from data are used.

Not reviewed, for internal circulation only

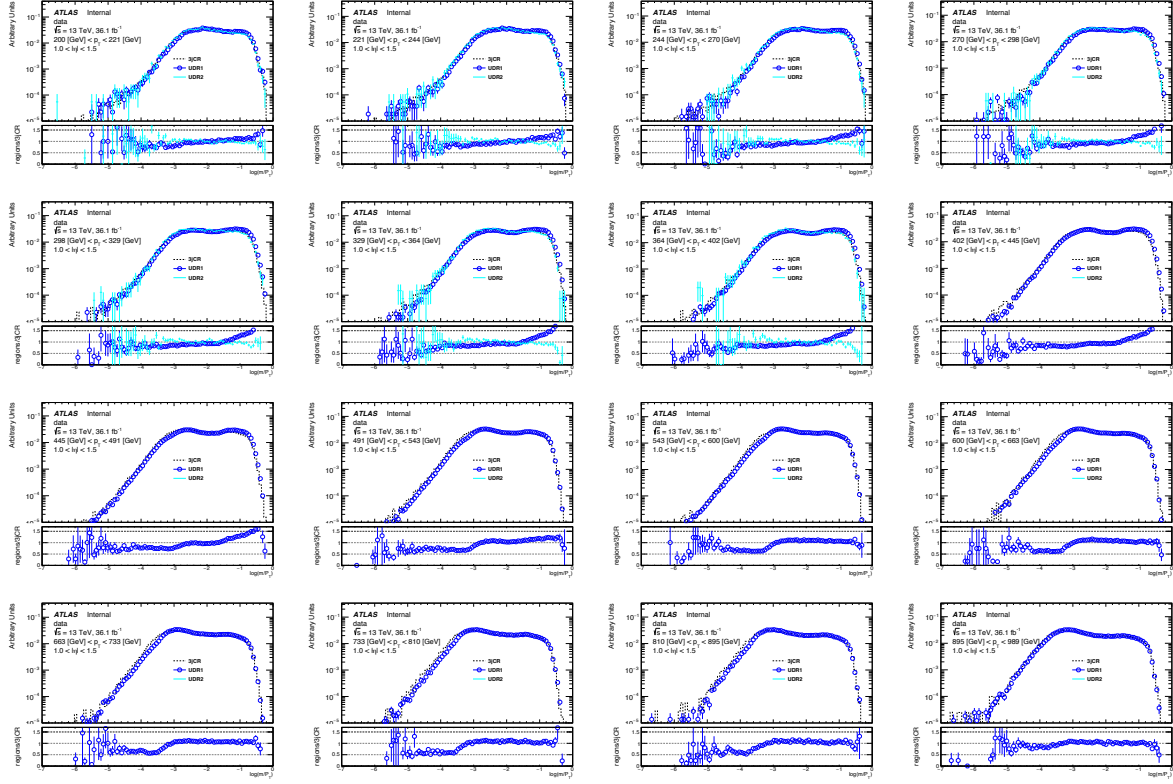


Figure 92: Jet mass PDFs comparison between CR and UDRs. Jets with $1.0 < |\eta| < 1.5$ from data are used.

Not reviewed, for internal circulation only

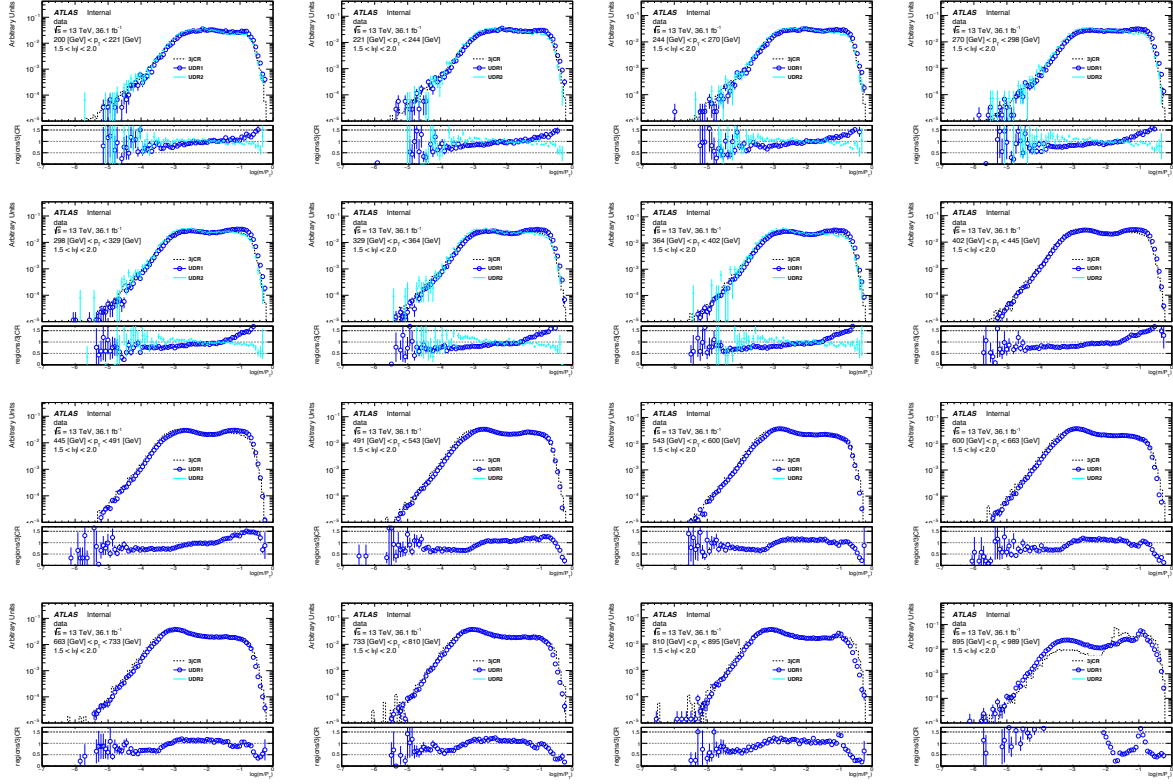


Figure 93: Jet mass PDFs comparison between CR and UDRs. Jets with $1.5 < |\eta| < 2.0$ from data are used.

Not reviewed, for internal circulation only

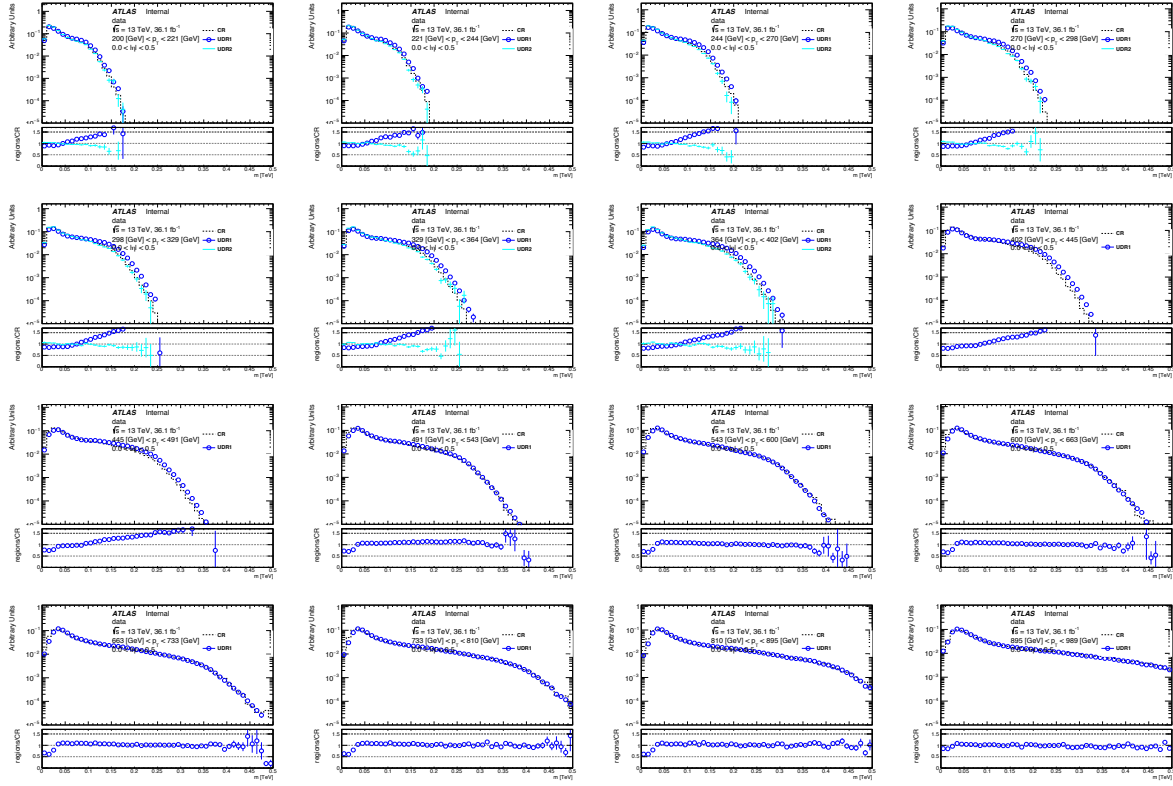


Figure 94: Jet mass distributions comparison between CR and UDRs. Jets with $0.0 < |\eta| < 0.5$ from data are used.

Not reviewed, for internal circulation only

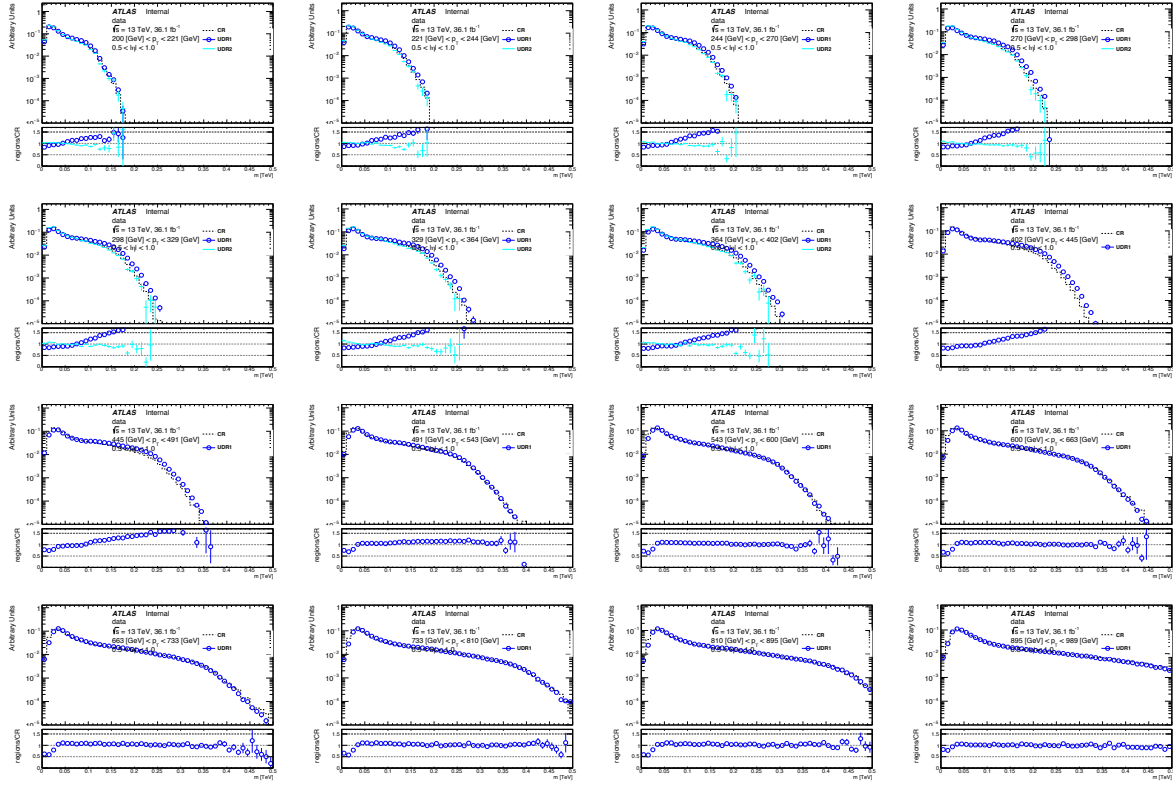


Figure 95: Jet mass distributions comparison between CR and UDRs. Jets with $0.5 < |\eta| < 1.0$ from data are used.

Not reviewed, for internal circulation only

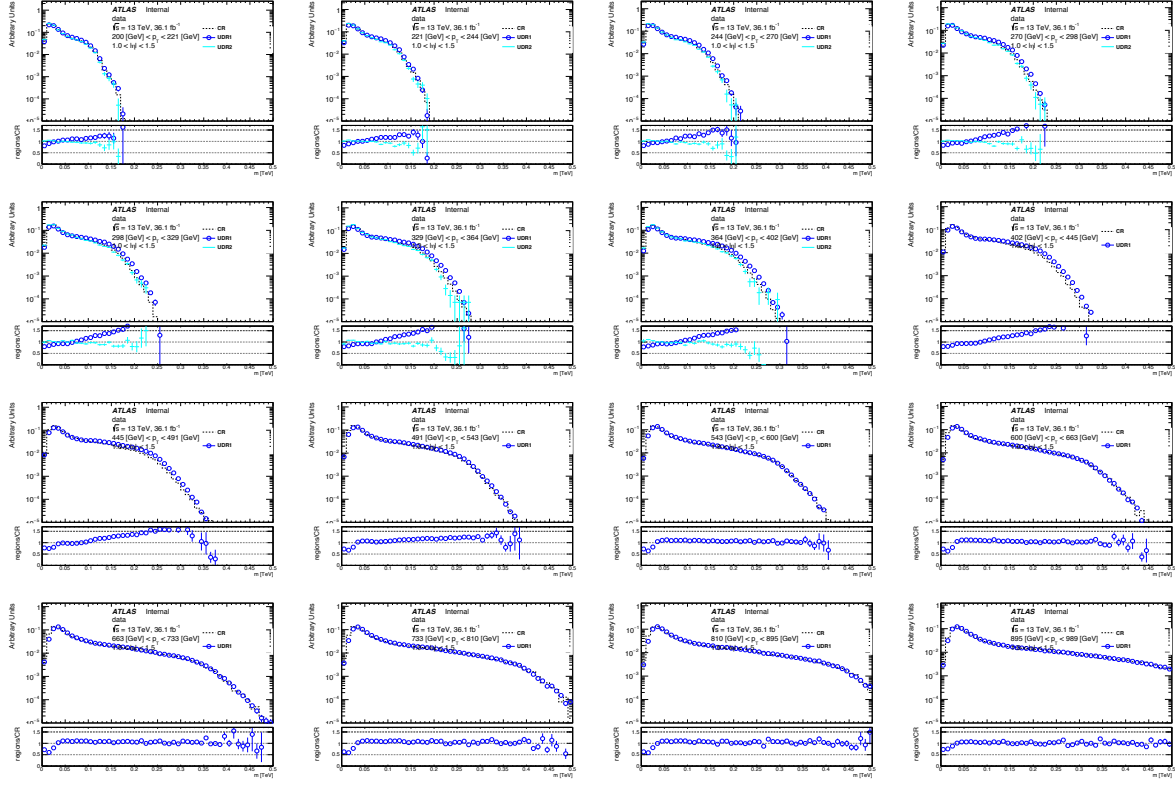


Figure 96: Jet mass distributions comparison between CR and UDRs. Jets with $1.0 < |\eta| < 1.5$ from data are used.

Not reviewed, for internal circulation only

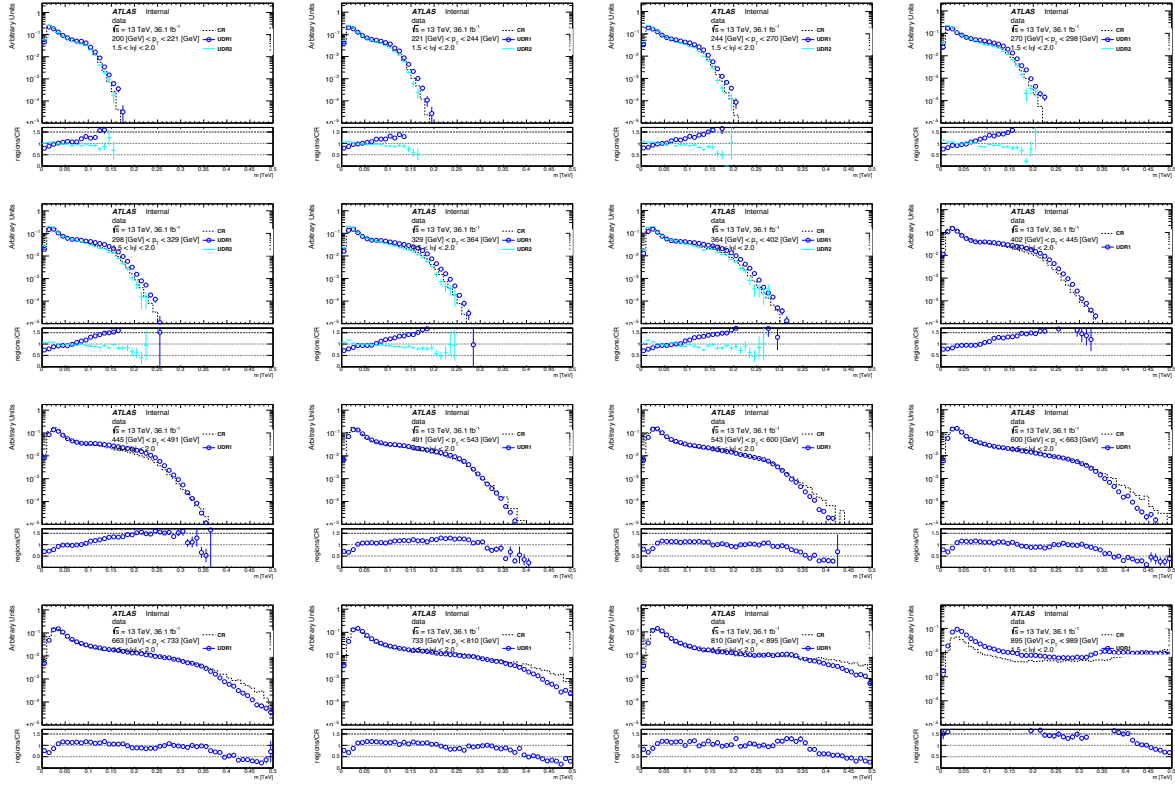


Figure 97: Jet mass distributions comparison between CR and UDRs. Jets with $1.5 < |\eta| < 2.0$ from data are used.

Not reviewed, for internal circulation only

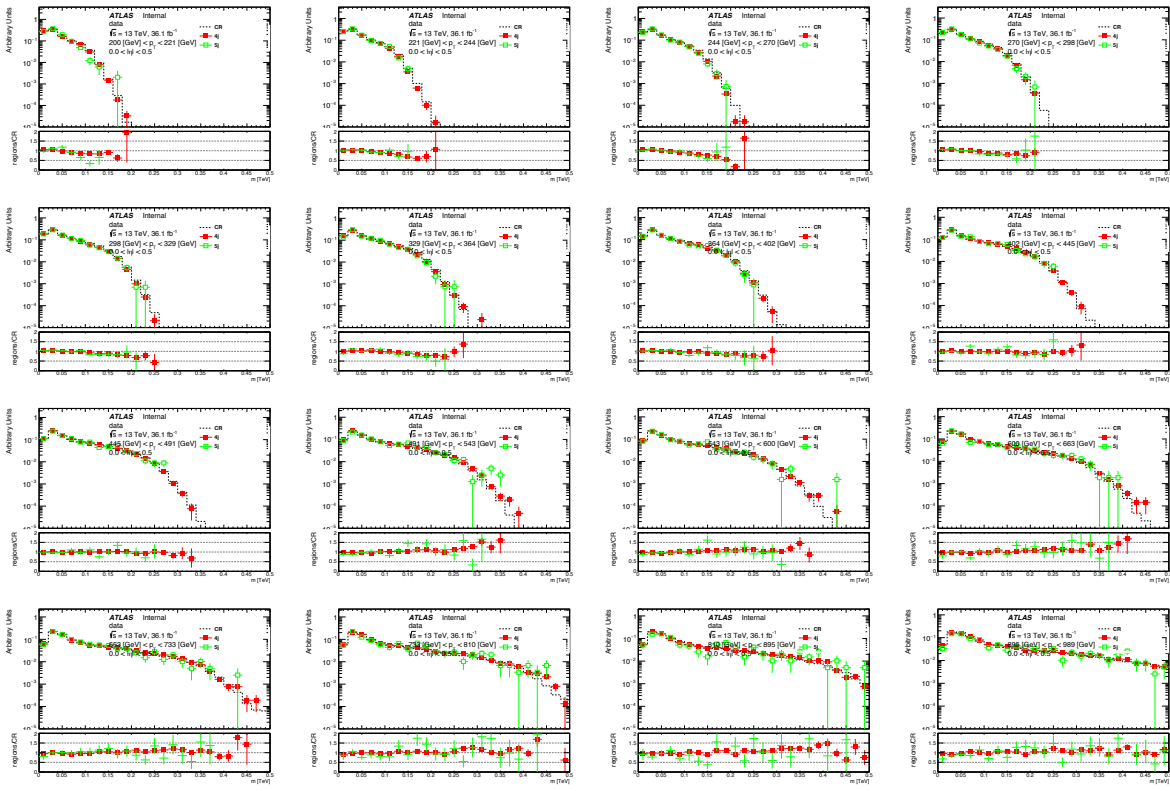


Figure 98: Jet mass PDFs comparison between CR and UDRs. Jets with $0.0 < |\eta| < 0.5$ from data are used.

893 P. Jet mass PDFs comparison between CR and 4j and 5j regions

894 Figures 98 to 101 show the comparison of jet mass distributions between the control region and regions
 895 with ≥ 4 jets or ≥ 5 jets.

Not reviewed, for internal circulation only

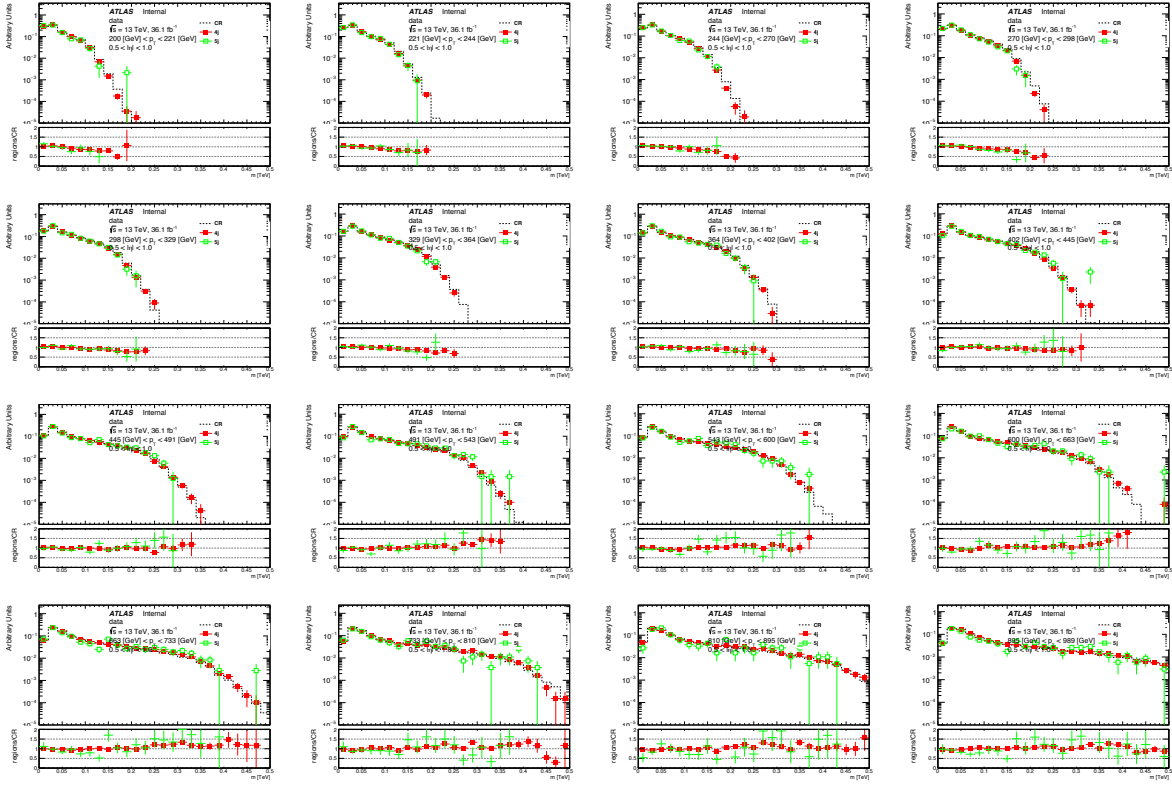


Figure 99: Jet mass PDFs comparison between CR and UDRs. Jets with $0.5 < |\eta| < 1.0$ from data are used.

Not reviewed, for internal circulation only

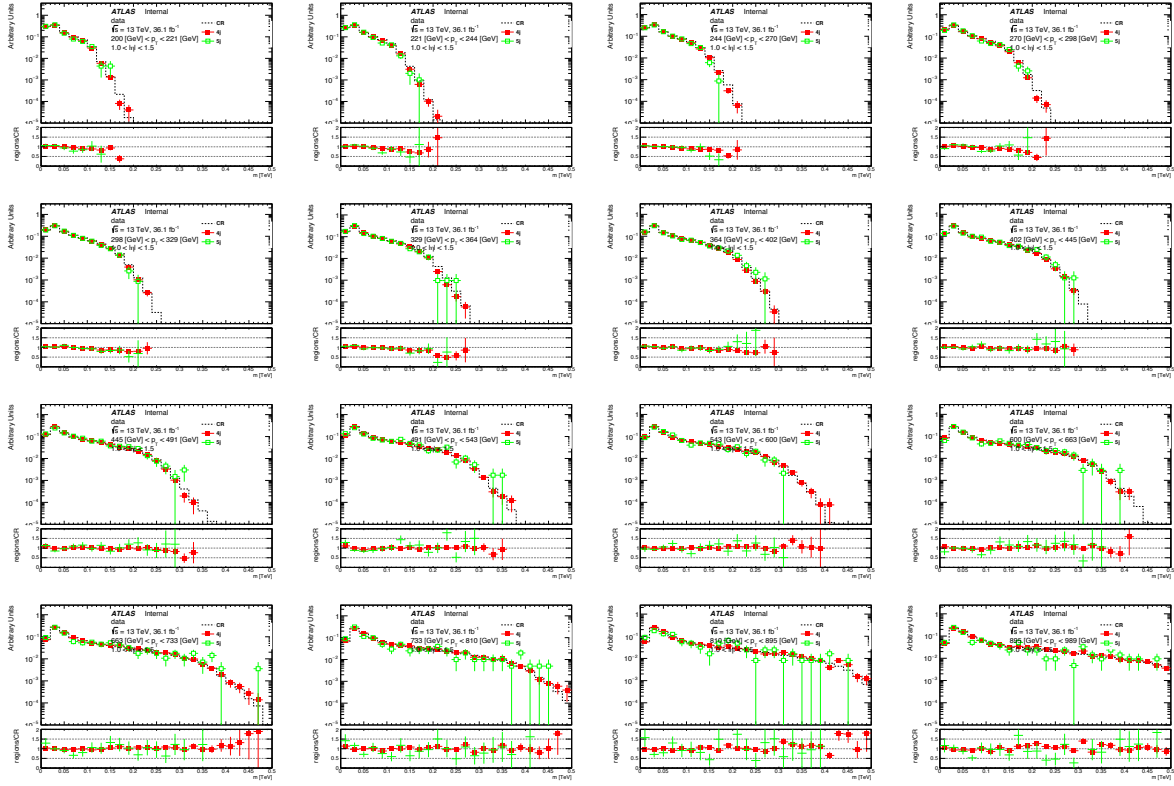


Figure 100: Jet mass PDFs comparison between CR and UDRs. Jets with $1.0 < |\eta| < 1.5$ from data are used.

Not reviewed, for internal circulation only

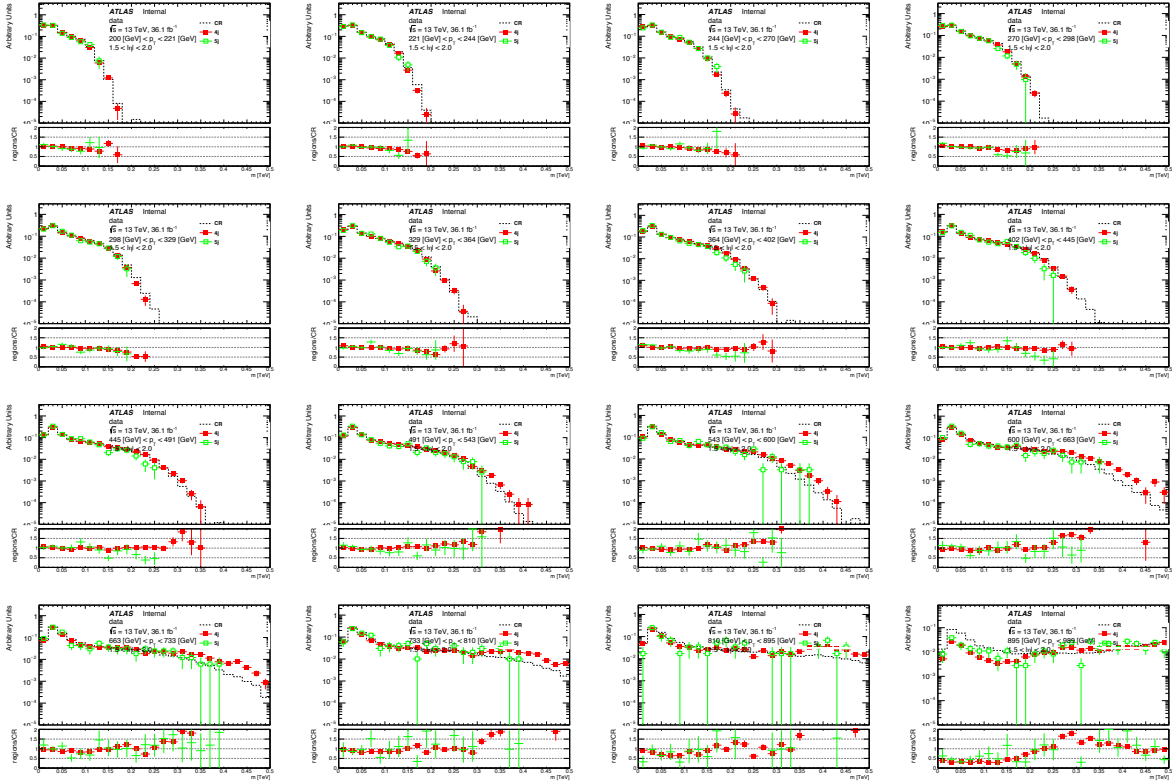


Figure 101: Jet mass PDFs comparison between CR and UDRs. Jets with $1.5 < |\eta| < 2.0$ from data are used.

Not reviewed, for internal circulation only

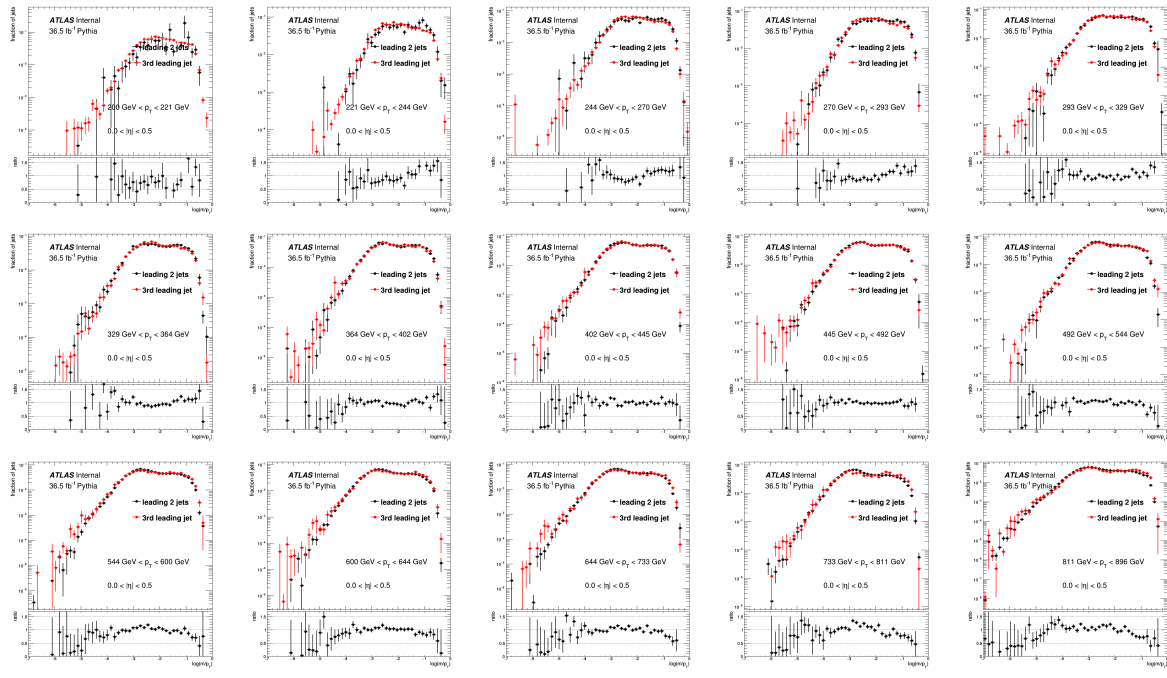


Figure 102: Jet mass templates comparison between the two leading jets and the third and fourth leading jets in the η region between 0 and 0.5. PYTHIA8 multijet sample is used for this comparison.

896 **Q. Jet mass templates comparison between the two leading jets and the
897 third and fourth leading jets**

Not reviewed, for internal circulation only

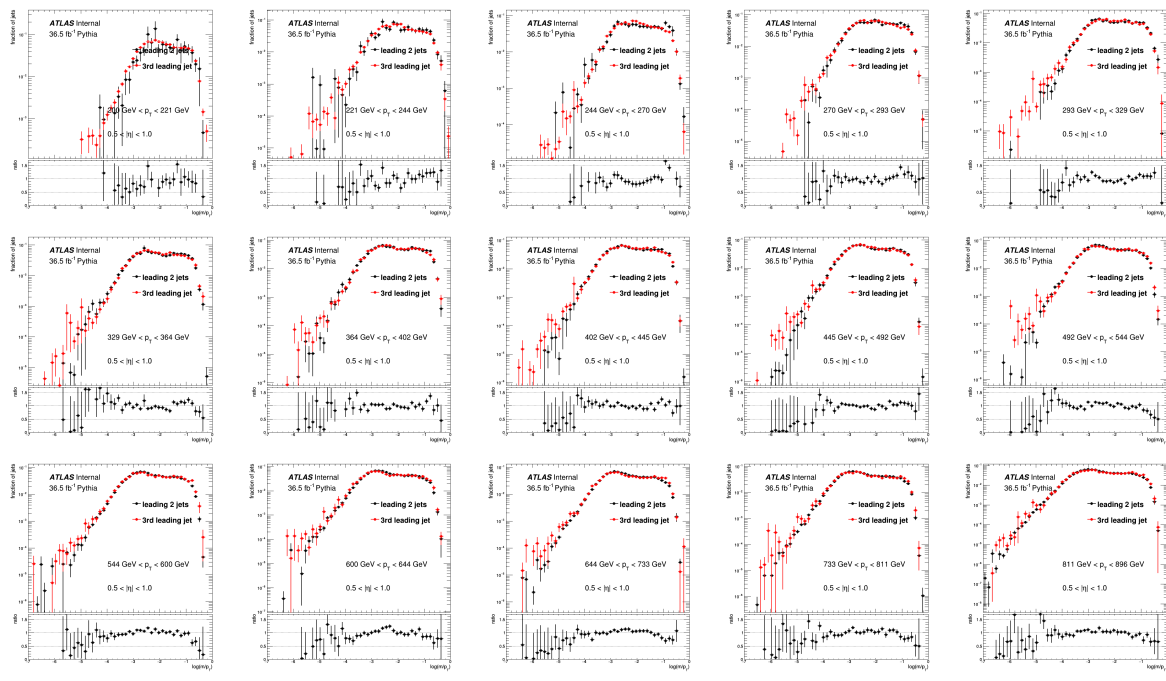


Figure 103: Jet mass templates comparison between the two leading jets and the third and fourth leading jets in the η region between 0.5 and 1.0. PYTHIA8 multijet sample is used for this comparison.

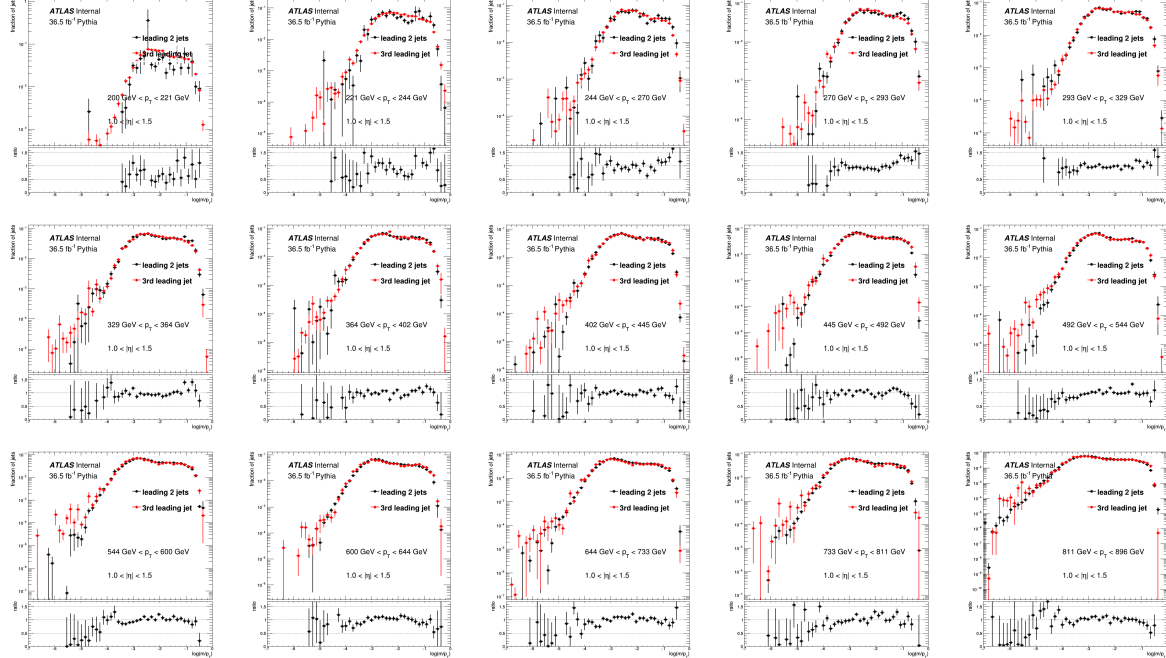


Figure 104: Jet mass templates comparison between the two leading jets and the third and fourth leading jets in the η region between 1.0 and 1.5. PYTHIA8 multijet sample is used for this comparison.

Not reviewed, for internal circulation only

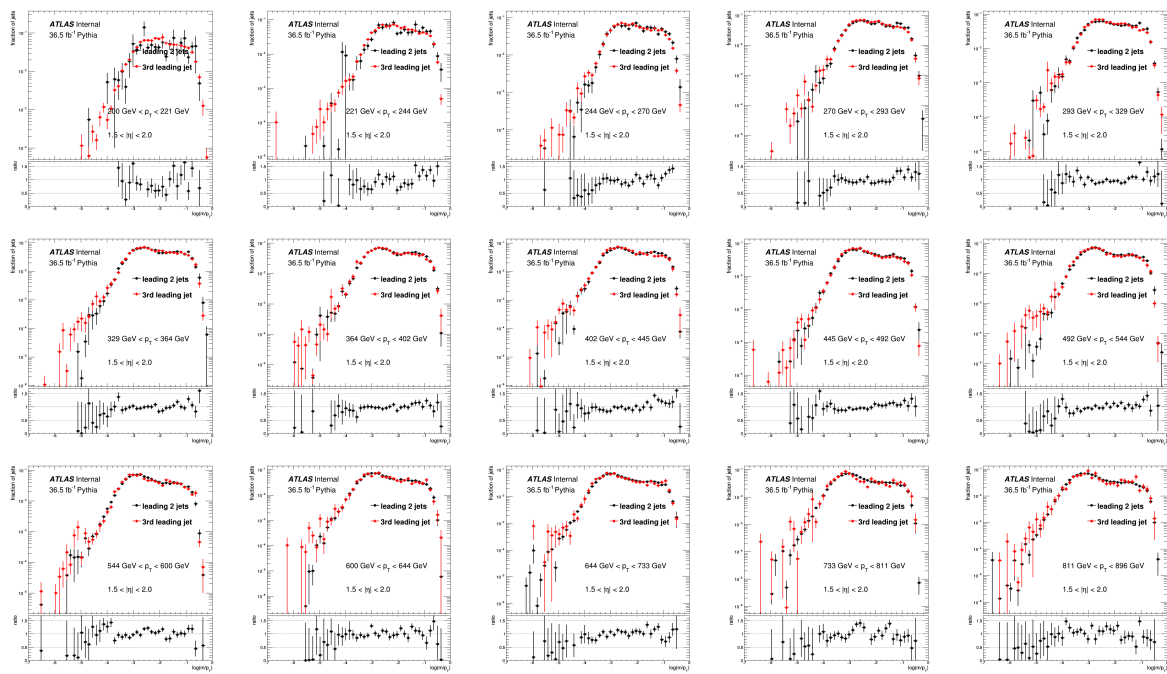


Figure 105: Jet mass templates comparison between the two leading jets and the third and fourth leading jets in the η region between 1.5 and 2.0. PYTHIA8 multijet sample is used for this comparison.

898 R. Packages and performance recommendations

899 Small-R JER

- 900 • Package tag: JetResolution-03-00-49
- 901 • configuration: JetResolution/Prerec2015_xCalib_2012JER_ReducedTo9NP_Plots_v2.root
- 902 • nuisance parameters: 1
- 903 • purpose: account for uncertainty on jet energy resolution by smearing jet energy

904 Large-R JMS

- 905 • Package tag: JetUncertainties-00-09-63
- 906 • configuration: UJ_2015/ICHEP2016/TopTagging_CombMass_strong.config
- 907 • Nuisance parameters: 4
- 908 • purpose: account for uncertainty on large-R jet mass and pT scales using Rtrk method

909 Small-R JES

- 910 • package tag: JetUncertainties-00-09-63
- 911 • configuration: JES_2015/ICHEP2016/JES2015_SR_Scenario1.config
- 912 • nuisance parameters: 4
- 913 • purpose: account for small-R jet JES uncertainty

914 b-tagging efficiency

- 915 • package tag: xAODBTaggingEfficiency-00-00-34
- 916 • configuration: 2016-20_7-13TeV-MC15-CDI-2016-11-25_v1.root
- 917 • nuisance paramters: 25
- 918 • purpose: account for uncertainty on b-tagging efficiency

S. Sensitivity to the 6-quark model

Figure ?? compares the expected sensitivity to the 6-quark model between the result of Ref. [25] and results from the current data sample with a few different setups. The nominal results implement the correction of signal contamination in the likelihood function, which was not done for Ref. [25]. To understand the impact of the correction of signal contamination on the sensitivity to the 6-quark model, expected limits are also calculated using likelihood functions where the correction is removed. In Ref. [25], the signal region is defined as 5jSRb, $M_J^\Sigma > 0.6$ TeV, and the expected background yield in the SR is $18.2 \pm 4.2 \pm 2.5 \pm 3.0$. The current background prediction in this region is 44.0 ± 7.5 (stat.) ± 11.2 (low p_T) ± 7.2 (high p_T). The central value between these two results scales with luminosity, the current result has slightly larger systematic uncertainty and lower statistical uncertainty, and the total uncertainty is similar between these two results. Consequently, the expected limit is compatible between Ref. [25] and the current analysis using 5jSRb, $M_J^\Sigma > 0.6$ TeV and without correction of signal contamination. Once the correction is included, the expected limit is weaker.

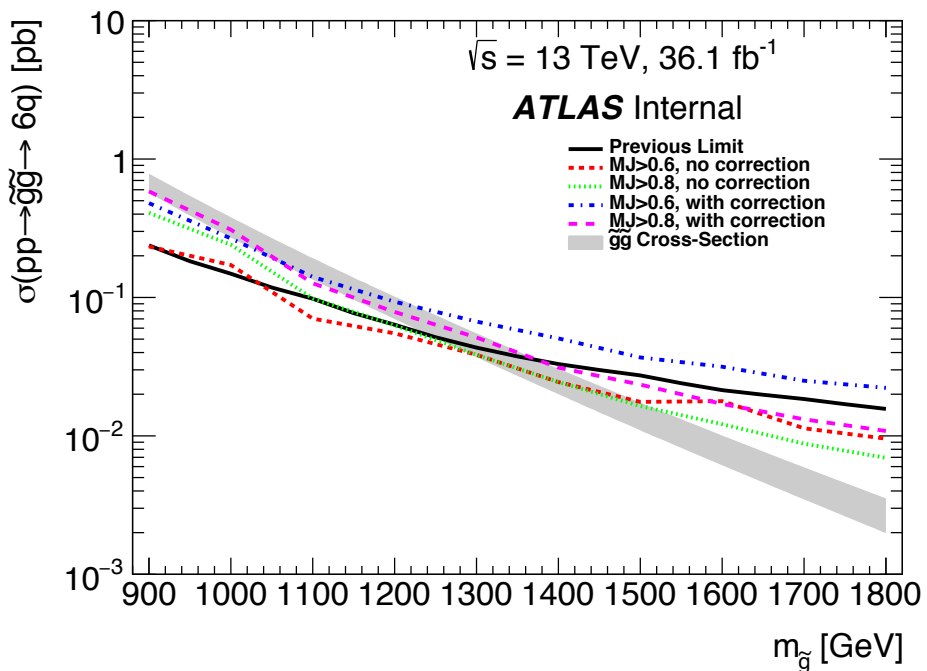


Figure 106: The expected limits on the RPV6 models in different setups are compared. The solid line shows the expected limit using 14.8 fb^{-1} data, reported in [25]. The expected limits calculated from two different signal regions (5jSRb, $M_J^\Sigma > 0.6$ TeV, and 5jSRb, $M_J^\Sigma > 0.8$ TeV) are also shown. For each of these two signal regions, an expected limit calculated without the signal contamination correction is also presented.

932 References

- [1] G. Aad et al., *Search for massive supersymmetric particles decaying to many jets using the ATLAS detector in pp collisions at $\sqrt{s} = 8 \text{ TeV}$,*

- 935 *Phys. Rev.* **D91**.11 (2015) 112016, [Erratum: *Phys. Rev.*D93,no.3,039901(2016)],
 936 arXiv: [1502.05686 \[hep-ex\]](#).
- 937 [2] T. Cohen et al., *Jet Substructure Templates: Data-driven QCD Backgrounds for Fat Jet Searches*,
 938 *JHEP* **05** (2014) 005, arXiv: [1402.0516 \[hep-ph\]](#).
- 939 [3] J. Alwall et al., *The automated computation of tree-level and next-to-leading order differential*
 940 *cross sections, and their matching to parton shower simulations*, *JHEP* **07** (2014) 079,
 941 arXiv: [1405.0301 \[hep-ph\]](#).
- 942 [4] T. Sjöstrand et al., *An Introduction to PYTHIA 8.2*, *Comput. Phys. Commun.* **191** (2015) 159,
 943 arXiv: [1410.3012 \[hep-ph\]](#).
- 944 [5] The ATLAS Collaboration, tech. rep.
- 945 [6] R. D. Ball et al., *Parton distributions with LHC data*, *Nucl. Phys.* **B867** (2013) 244,
 946 arXiv: [1207.1303 \[hep-ph\]](#).
- 947 [7] D. J. Lange, *The EvtGen particle decay simulation package*,
 948 *Nucl. Instrum. Meth.* **A462** (2001) 152.
- 949 [8] T. Gleisberg et al., *Event generation with SHERPA 1.1*, *JHEP* **02** (2009) 007,
 950 arXiv: [0811.4622 \[hep-ph\]](#).
- 951 [9] W. Beenakker et al., *Squark and gluino production at hadron colliders*,
 952 *Nucl. Phys.* **B492** (1997) 51, arXiv: [hep-ph/9610490 \[hep-ph\]](#).
- 953 [10] A. Kulesza and L. Motyka,
 954 *Threshold resummation for squark-antisquark and gluino-pair production at the LHC*,
 955 *Phys. Rev. Lett.* **102** (2009) 111802, arXiv: [0807.2405 \[hep-ph\]](#).
- 956 [11] A. Kulesza and L. Motyka, *Soft gluon resummation for the production of gluino-gluino and*
 957 *squark-antisquark pairs at the LHC*, *Phys. Rev.* **D80** (2009) 095004,
 958 arXiv: [0905.4749 \[hep-ph\]](#).
- 959 [12] W. Beenakker et al., *Soft-gluon resummation for squark and gluino hadroproduction*,
 960 *JHEP* **12** (2009) 041, arXiv: [0909.4418 \[hep-ph\]](#).
- 961 [13] W. Beenakker et al., *Squark and Gluino Hadroproduction*, *Int. J. Mod. Phys.* **A26** (2011) 2637,
 962 arXiv: [1105.1110 \[hep-ph\]](#).
- 963 [14] M. Kramer et al., *Supersymmetry production cross sections in pp collisions at $\sqrt{s} = 7$ TeV* (2012),
 964 arXiv: [1206.2892 \[hep-ph\]](#).
- 965 [15] e. a. Brian Amadio, *Large-R Jets in AFII Fast and Full Sim Comparison for RPV Multijet Search*,
 966 2016, URL: [https://indico.cern.ch/event/525351/contributions/2151621/](https://indico.cern.ch/event/525351/contributions/2151621/attachments/1265515/1873280/presentation_v2.pdf)
 attachments/1265515/1873280/presentation_v2.pdf.
- 968 [16] S. Alioli et al., *A general framework for implementing NLO calculations in shower Monte Carlo*
 969 *programs: the POWHEG BOX*, *JHEP* **06** (2010) 043, arXiv: [1002.2581 \[hep-ph\]](#).
- 970 [17] H.-L. Lai et al., *New parton distributions for collider physics*, *Phys. Rev.* **D82** (2010) 074024,
 971 arXiv: [1007.2241 \[hep-ph\]](#).
- 972 [18] A. Hook et al., *High Multiplicity Searches at the LHC Using Jet Masses*,
 973 *Phys. Rev.* **D85** (2012) 055029, arXiv: [1202.0558 \[hep-ph\]](#).
- 974 [19] S. El Hedri et al., *Learning How to Count: A High Multiplicity Search for the LHC*,
 975 *JHEP* **08** (2013) 136, arXiv: [1302.1870](#).

Not reviewed, for internal circulation only

- 976 [20] R. S. Chivukula and H. Georgi, *Composite Technicolor Standard Model*,
977 [Phys. Lett. B188 \(1987\) 99](#).
- 978 [21] L. J. Hall and L. Randall, *Weak scale effective supersymmetry*, [Phys. Rev. Lett. 65 \(1990\) 2939](#).
- 979 [22] A. J. Buras et al., *Universal unitarity triangle and physics beyond the standard model*,
980 [Phys. Lett. B500 \(2001\) 161](#), arXiv: [hep-ph/0007085 \[hep-ph\]](#).
- 981 [23] G. D'Ambrosio et al., *Minimal flavor violation: An Effective field theory approach*,
982 [Nucl. Phys. B645 \(2002\) 155](#), arXiv: [hep-ph/0207036 \[hep-ph\]](#).
- 983 [24] C. Csaki, Y. Grossman and B. Heidenreich, *MFV SUSY: A Natural Theory for R-Parity Violation*,
984 [Phys. Rev. D85 \(2012\) 095009](#), arXiv: [1111.1239 \[hep-ph\]](#).
- 985 [25] The ATLAS collaboration, *Search for massive supersymmetric particles in multi-jet final states*
986 *produced in pp collisions at $\sqrt{s} = 13$ TeV using the ATLAS detector at the LHC* (2016).